



**University of
Nottingham**
UK | CHINA | MALAYSIA

EPSRC

Engineering and Physical Sciences
Research Council

**CDT in Advanced Therapeutics
and Nanomedicines**



AstraZeneca



GlaxoSmithKline

Targeted bio-distribution of drugs to the lymphatic system

Adelaide Marie Jewell (BSc)

Thesis submitted to the University of Nottingham for the degree
of Doctor of Philosophy

March 2022

Academic supervisors: Dr. Pavel Gershkovich, Prof. Peter Fischer, Prof.
Michael Stocks, Dr. David Scurr.

Industrial affiliations: Dr. Paul Gellert (AstraZeneca), Dr. Marianne Ashford
(AstraZeneca), Dr. James Butler (GlaxoSmithKline).

COVID-19 impact statement

- I spent 6 months with either no or extremely limited lab access (March-September 2020). During this time I was unable to carry out the laboratory experiments I had planned, including animal experiments, or undertake analyses of samples I collected from previous animal experiments by specialized analytical methods (HPLC, OrbiSIMS, histology, or MRI analysis).
- In addition, I was initially delayed by not having a remote access connection to University computers set up to use from home. This included computers containing IonToF software for Secondary Ion Mass Spectrometry data analysis.
- Following this 6 month period, laboratory access remained limited (from September 2020 to April 2021). When the laboratories re- opened, reduced capacities and shorter access times, due to COVID-19 measures, resulted in a lower level of activity and hence slower progress of experimental work. Inevitably, the COVID-19 measures have made laboratory working conditions significantly more stressful to work under.
- For extended periods I did not have access to the OrbiSIMS instrument which is located in UoN Nano and Micro Research Centre (nmRC). Although a new member of staff had been trained to run the instrument on my behalf, physically not being present resulted, at times, in difficulty communicating and suboptimal data.
- I have also not been able to arrange experiments which were planned to be undertaken at the University of Birmingham using a relevant model of Multiple Sclerosis which could have been valuable for my project. Furthermore, MRI studies at the UoN Sir Peter Mansfield imaging centre

could not be performed under COVID restrictions. This meant that, following initial feasibility studies, work to improve the experimental method and increase sample size could not be achieved.

Abstract

Targeted drug delivery to the intestinal lymphatic system has emerged as an important goal in drug development for the treatment of a number of clinical indications. These include, cancers, inflammatory disorders and infectious diseases. Following oral administration, small molecule drugs with specific physiochemical properties, have been shown to associate with lipoproteins called chylomicrons in the enterocytes of the small intestine. Chylomicron associated drugs then bypass hepatic uptake and enter the mesenteric lymph nodes (MLN). Oral co-administration of highly lipophilic small molecule drugs with lipids had subsequently been identified as an effective mechanism for delivering highly lipophilic small molecule drugs to the MLN in high concentrations. One example is Cannabidiol (CBD), which was shown to undergo lymphatic transport following oral administration with lipids and has received significant research interest for the treatment of inflammatory disorders.

The overarching aim of this thesis was to determine how small molecule drugs distribute in the lymphatic system following oral delivery. More specifically, work in this thesis was divided into two main research questions; 1) where within the cellular structures of lymph nodes drugs distribute and 2) which specific individual lymph nodes can be targeted. For the purposes of this thesis, CBD was selected as a model drug, with which drug distribution in the lymphatics was investigated.

Lymph nodes are comprised of distinct anatomical and function regions. The flow of lymph and lymph bourn molecules within lymph nodes is highly regulated. This aids appropriate immune surveillance. Based on this, it was

hypothesised that small molecule drugs, such as CBD, may preferentially distribute in some regions of lymph nodes more than others.

Mass spectrometry imaging (MSI) has been adapted over recent years to enable detailed tissue analysis. However, so far, MSI had only been applied to image drug distribution in tissues at mg/g concentrations, following topical administration. A method using a hybrid instrument comprising a time-of-flight analyser with an Orbitrap mass spectrometer, termed OrbiSIMS, to image CBD in MLN tissues at *in vivo* relevant concentrations was described. The estimated limit of sensitivity for the [M-H]⁻ ion of CBD was in the range of 5-10 µg/g, which correlates to concentrations observed *in vivo*. Subsequently, OrbiSIMS imaging of sectioned MLNs from rats dosed orally with CBD in sesame oil was performed. Critically, CBD could be visualised primarily in the paracortex of the lymph node, which is known to be dominated by T-cells. This work represents the first evidence of label- and matrix-free imaging of drug distribution at the time of peak absorption into intestinal lymph nodes. Although imaging reproducibility and drug-cell interaction would need to be confirmed, this work may therefore support the hypothesis that CBD exerts its immunoregulatory effects *in vivo* primarily through T-cells. This is likely aided through cross-talk with conduit resident dendritic cells of the paracortex. Assuming other lipophilic small molecule drugs are also distributed in the paracortex, this finding could have wider clinical implications for diseases where T-cells are primarily involved.

The MLNs are a large group of lymph nodes which drain lymph from the small intestine. Lipid uptake is understood to vary across the length of the small intestine. Based on this it was also hypothesised that individual nodes within the chain of MLNs may be exposed to differing concentrations of orally administered drugs entering the lymphatics via chylomicron association. In addition, following

collection in the MLN, lymph is understood to drain into the retroperitoneal lymph nodes (RPLN) before entering the cisterna chyli and ultimately systemic circulation. Subsequently, it was also hypothesised that the RPLN may also be exposed to drugs undergoing lymphatic transport.

The second major research question of this project, relating to which specific lymph nodes can be targeted following oral delivery and to what extent, was addressed using two main approaches. Firstly, in a rat model, CBD concentrations in individual lymph nodes from animals dosed orally with CBD were determined using high-performance liquid chromatography (HPLC). It was shown that, at the time of peak absorption, drug concentrations were significantly higher in the upper middle nodes of the mesenteric chain and distribution was therefore non-uniform within the MLNs. Another key finding was that the RPLN could also be targeted. Moreover, at time points after 2 hours post administration, at which absorption into the MLN reaches a peak, concentrations were similar in RPLN and MLN. Concentrations in RPLN were also more than 20 times higher than previously reported in plasma, indicating lymphatic transport of drug rather than redistribution from systemic circulation. This widespread delivery of drugs to multiple groups of lymph nodes following oral administration had not previously been demonstrated and indicates the clinical potential of oral drug administration for diseases where lymphatic involvement is widespread. This includes inflammatory diseases and cancer metastases.

Finally, the question of which lymph nodes can be targeted using orally delivered lipid-based formulations was assessed in a human setting. It was hypothesised that MRI may be used to identify changes in lymph nodes as dietary lipids are absorbed. Subsequently, these changes could be used to map lipid uptake into individual lymph nodes and thus which nodes may be exposed to chylomicron

associated drugs. An assessment of the feasibility of a label free, non-invasive MRI method for this indication was also performed. Repeated identification of individual lymph nodes at baseline and following a high fat meal was achieved in 3 healthy human volunteers. In all participants, the apparent diffusion coefficient (ADC) of lymph nodes was shown to increase following a high fat meal. The timings of these changes correlated with expected lymphatic lipid uptake. Based on this, increases in ADC may represent a novel measurable indicator for lipid tracking in the intestinal lymphatics in future work.

In conclusion, the work in this thesis has provided preliminary evidence that the paracortex is the predominant target following oral delivery of small molecule drugs. In addition, novel data support the notion that the MLN are differentially exposed to lymph associated drugs and that the RPLN may also be targeted.

Publications

Jewell, A., Williams, H., Hoad, C. L., Gellert, P. R., Ashford, M. B., Butler, J., Stolnik, S., Scurr, D., Stocks, M. J., Marciana, L., Gowland, P. A. & Gershkovich, P. Assessing Lymphatic Uptake of Lipids Using Magnetic Resonance Imaging: A Feasibility Study in Healthy Human Volunteers with Potential Application for Tracking Lymph Node Delivery of Drugs and Formulation Excipients. *Pharmaceutics*, 2021; 13 (9), 1343

Jewell, A., Brookes, A., Feng, W., Ashford, M., Gellert, P., Butler, J., Fischer, P. M., Scurr, D. J., Stock, M. J. & Gershkovich, P. Distribution of a highly lipophilic drug cannabidiol into different lymph nodes following oral administration in lipidic vehicle. *Eur J Pharm Biopharm*, 2022; 174: 29-34.

Acknowledgements

I would like to firstly express my immense gratitude to my academic supervisors, Dr. Pavel Gershkovich, Dr. David Scurr and Prof. Michael Stocks. Firstly to Pavel for his unmatched time, energy and commitment to my PhD project and PhD process overall. His can-do attitude and determination to progress in research was incredibly inspiring, especially during difficult times, and his dry sense of humour was also greatly appreciated. Particularly his invaluable network of contacts proved pivotal to the success of the collaborative aspects of the project. I am also extremely grateful to David for his patience and refreshing approach to research. His impressive knowledge of SIMS has been invaluable. I am also very grateful for the support of my industry supervisors, Dr. Marianne Ashford and Dr. Paul Gellert at AstraZeneca and Dr. James Butler at GlaxoSmithKline. Their input in supervision meetings was highly stimulating and allowed me to consider perspectives I wouldn't have without their expertise.

I am indebted to the EPSRC and CDT for their financial support, without which the project would not have been possible. The extracurricular support from the CDT helped make the PhD experience a well-rounded process which will undoubtedly support me in my future career. The school of Pharmacy is friendly and collaborative environment which I will truly miss. My sincerest thanks also to my fellow CDT cohort Isobel Holden, Paula Muresan, Lorenzo Schiazza, Steven Gibney, Ania Kotowska and George Papakostos, Liisa Nitsou and Clarissa Harmen and members of other cohorts; Catherine Vasey, Akosua Anane-Adjei, Sadie Swainson, Amy Nash, Oran Maguire for their continued support and comradeship throughout the 4 years. A special thanks should go to Ania Kotowska for her

unwavering patience and support. Thanks also to Claudia Matz for her palliative support.

I must also acknowledge the members of the Gershkovich group, Alice Brookes, Wanshan Feng, YenJu Chu, Chalong Qin, Carlos Sanders, Haojie Chen, Abby Wong. Lab work would have undoubtedly proved much more difficult without their team spirit. I am also hugely grateful for the technical support I have received. This includes individuals at the Sir Peter Mansfield imaging centre, Hannah Williams, Penny Gowland, Luca Marciani, who were so welcoming and enthusiastic throughout our collaborative work. Thanks also to the incredible hard work of the staff at the NMRC, particularly Steffi Kern and Julie Watts. Thanks also to Ian Ward and Denise Mclean at the SLIM lab for donating their time and their friendly approach to supporting me technically. Thanks also to Helen Richards, Mark Trussell and Ian Devonshire at the BSU who were always incredibly professional and helpful.

Finally an enormous thank you to my family. To Richard, for his grounding and calming influence and of course my parents, Clare and James, for their ongoing love, emotional support and belief in my success.

Table of contents

1. Introduction	29
1.1. Structure and function of the intestinal lymphatic system	29
1.1.1. Lymph.....	29
1.1.2. Terminal lymphatics and lymphatic vessels.....	30
1.1.3. Lymph nodes.....	31
1.2. Role of the intestinal lymphatic system in disease.....	37
1.2.1. Immune tolerance and inflammatory disease.....	37
1.2.2. Infectious disease.....	39
1.2.3. Lymphoma	39
1.2.4. Metastasis from solid tumours	40
1.2.5. Metabolic disease	42
1.2.6. Lymphoedema	43
1.3. Drug delivery to the intestinal lymphatic system	43
1.3.1. Rationale for targeted drug delivery.....	43
1.3.2. Access to the lymph nodes	44
1.3.3. Approaches to enhancing uptake into the intestinal lymphatics following oral delivery	46
1.4. Imaging the intestinal lymphatic system	51
1.4.1. Imaging as a tool in drug development	51
1.4.2. Imaging drug delivery to intestinal lymph nodes	53

1.4.3. Imaging drug distribution within intestinal lymph nodes.....	54
1.5. Cannabidiol as a model drug for lymphatic delivery	60
1.5.1. Cannabis as medicine.....	60
1.5.2. Endocannabinoid system	61
1.5.3. Pharmacokinetics of orally administered cannabinoids	61
1.5.4. Real world-data.....	64
1.6. Scope of thesis	68
2. Development of a Mass spectrometry imaging method for determining the distribution of cannabidiol in lymph nodes	70
2.1. Introduction	70
2.2. Chapter aims and objectives.....	72
2.3. Materials and Methods	74
2.3.1 Materials	74
2.3.2 Animals.....	74
2.3.3 Tissue collection and preparation.....	75
2.3.4. Analytical methods	78
2.3.5 Data processing and analysis	81
2.4. Results and Discussion	82
2.4.1. Method development for ToF-SIMS detection of CBD in lymph node tissue	82
2.4.2 Method development for OrbiSIMS detection of CBD in lymph node tissue	93

2.4.3 Optimising tissue sectioning	103
2.5. Conclusions	104
3. Distribution of cannabidiol and other lipophilic molecules within intestinal lymph nodes.....	107
3.1. Introduction	107
3.2. Chapter aims and objectives.....	109
3.3. Materials and methods.....	109
3.3.1. Sectioned MLN tissue	109
3.3.2. Analytical methods	110
3.3.3. Determination of tissue matrix effects	113
3.4. Results and Discussion	114
3.4.1. Characterisation of innate lymph node tissue using OrbiSIMS imaging	114
3.4.2. Imaging the distribution of CBD in sectioned lymph nodes	125
3.4.3. Investigation of tissue matrix effects on CBD ionisation	136
3.4.4. Imaging the distribution of components of the orally administered lipidic formulation in sectioned lymph nodes	138
3.5. Conclusions	154
4. Determination of which individual lymph nodes can be targeted following oral administration of drugs using an animal model	156
4.1. Introduction	156
4.2. Chapter aims and objectives.....	157
4.3. Methods and materials.....	158

4.3.1	Detection and quantification of CBD in rat lymphatic tissue.....	158
4.4.	Results and Discussion	162
4.4.1.	Bio-distribution of CBD into different lymph nodes following oral administration in lipidic vehicles in rats.....	162
4.5	Conclusions	174
5.	Assessing lymphatic uptake of lipids in healthy human volunteers using Magnetic Resonance Imaging	175
5.1.	Introduction	175
5.2.	Chapter aims and objectives.....	176
5.3.	Methods and materials	176
5.3.1.	Magnetic resonance imaging in human volunteers.....	176
5.4.	Results and Discussion	181
5.4.1.	Assessment of lymphatic uptake of lipids using MRI in healthy human volunteers	181
5.5.	Conclusions	194
6.	General Discussion and Further Work	195
6.1.	Key findings and implications	195
6.2.	Future work.....	200
6.2.1.	Confirmation of drug distribution within lymph nodes.....	200
6.2.2.	Assessing which lymph nodes can be targeted by oral delivery.....	202

List of figures

Figure 1.1. Proposed lymphatic drainage routes in the human abdomen in accordance with current literature. Arrows indicate direction of lymph flow. Tissues are shown in red. LN; lymph nodes.

Figure 1.2. Schematic showing the major groups of lymph nodes in the human mesentery. The mesentery contains blood vessels, lymphatic vessels and approximately 150-200 lymph nodes. Nodes commonly lie in close proximity to major vessels which are also indicated. Right colic (dark green), superior mesenteric (light blue), middle coelic (light green), paracolic (red), left colic (pink), sigmoid (purple), inferior mesenteric (orange) and ileocolic (yellow) [1] with permission.

Figure 1.3. Schematic showing the structure of a lymph node containing 3 lobules. Arterioles are shown in red, venules in blue and capillaries in purple. The right lobule is a micrograph from a section of rat mesenteric lymph node stained with H&E. Adapted from [2] with permission.

Figure 1.4. Mesenteric lymphadenopathy in a 38-year-old man with carcinoid tumour. a) CT image shows a primary soft-tissue mass (arrows). b) Non-enhanced CT image obtained 1 year later shows recurrence in a mesenteric lymph node (arrows). Taken from [3] with permission.

Figure 1.5. Schematic showing the mechanism by which chylomicron associated drugs can be directed to the intestinal lymphatic system following oral delivery.

Figure 1.6. Schematic illustrating the primary components of a ToF-SIMS Orbitrap analyser hybrid instrument termed an OrbiSIMS and data processing for imaging.

Figure 1.7. Structure of the two major chemical constituents of cannabis; a) THC and b) CBD.

Figure 2.1. Schematic showing experimental workflow for Chapter 2.

Figure 2.2. Static ToF-SIMS spectra of CBD powder in a) negative mode and b) positive mode.

Figure 2.3. Proposed fragmentation patterns for CBD.

Figure 2.4. Overlaid static ToF-SIMS spectra of blank MLN tissue homogenate (black) and MLN tissue homogenate spiked with 5 mg/g CBD (red) in the a) negative spectra and b) positive spectra.

Figure 2.5. Dynamic SIMS negative mode depth profile data of MLN tissue homogenate spiked with 5 mg/g CBD.

Figure 2.6. ToF-SIMS spectra of MLN tissue homogenate spiked with 5 mg/g using static SIMS (purple) and dynamic SIMS (green). Data shown in the negative mode.

Figure 2.7. Overlaid Dynamic ToF-SIMS spectra of blank MLN tissue homogenate (black) and MLN tissue homogenate spiked with 10 µg/g CBD (red) CBD cannot be

deciphered against the matrix of homogenised MLN tissue at *in vivo* relevant concentrations. Data shown in the negative mode.

Figure 2.8. ToF-SIMS images of $[M-H]^-$ CBD $C_{21}H_{29}O_2^-$ in MLN tissue homogenates spiked at a range of concentrations.

Figure 2.9. ToF-SIMS images of sectioned lymph nodes from animals dosed with CBD. a) total ion counts, b) Overlay red, PO_3^- a tissue fragment, blue, $SiHO_3^-OCT$, green $SiCH_5N^-$ glass, c) $C_{21}H_{29}O_2^-$ $[M-H]^-$ CBD. The outline of the node is indicated in each image by a dashed white line.

Figure 2.10. Calibration curve showing the intensity of the $[M-H]^-$ for CBD spiked at various concentrations in homogenised MLN tissue using dynamic SIMS. $R^2 = 0.9955$. $n=1$. Data is presented using a log scale.

Figure 2.11. Overlaid dynamic ToF-SIMS spectra of blank MLN tissue homogenate (black) and MLN tissue homogenate spiked with $10 \mu\text{g/g}$ CBD (red) CBD in following exposure to TFA in the a) negative and b) positive mode.

Figure 2.12. Comparison of Total ion counts (TIC) using Ar_{5000}^+ and Ar_{3000}^+ beams to analyse MLN tissue homogenates. Data is shown as mean \pm SD $n = 13$ Ar_{3000}^+ and $n = 5$ for Ar_{5000}^+ . *Statistically significant, unpaired two-tailed t-test, $p < 0.05$.

Figure 2.13. Overlaid mass spectra of MLN tissue homogenate spiked with $10 \mu\text{g/g}$ CBD analysed with dynamic ToF-SIMS (black) and OrbiSIMS (blue).

Figure 2.14. OrbiSIMS spectra of blank MLN tissue homogenate (black) and MLN tissue homogenate spiked with 10 µg/g CBD (red). CBD can be clearly deciphered against the matrix of tissue homogenate.

Figure 2.15. Calibration curve showing the intensity of the [M-H]⁻ for CBD normalised to total counts spiked at various concentrations in homogenised MLN tissue using OrbiSIMS. Data is presented as mean ± SD, n=3. R² = 0.922.

Figure 2.16. Relative intensities of the CBD [M-1]⁻ fragment in homogenates from dosed animals and homogenates spiked with 10 µg/g CBD. Error bars represent mean ± SD. For dosed animals n represents samples from 4 separate animals and for spiked homogenates n represents 3 spiked systems. *Statistically significant, unpaired two-tailed t-test, p < 0.05.

Figure 2.17. OrbiSIMS Image of droplet of MLN tissue homogenate from an animal dosed with CBD. The periphery of the homogenate droplet is indicated by a dashed white line.

Figure 2.18. Average peak intensities for samples analysed under different conditions. Data is displayed as mean ± SD. n=4 *statistically significant p < 0.05. One- way ANOVA, with Tukey's multiple comparisons test.

Figure 2.19. 5x magnification light microscope images showing a comparison of the integrity of sectioned MLN following different methods of freezing following H&E

staining. Samples were frozen using a) liquid isopentane, b) freezing at -20 °C. Some of the major cellular regions can be deciphered in b) and are indicated; P, paracortex; HEV, high endothelial venuole; BCF, B-cell follicle; OC, outer cortex.

Figure 3.1. H&E stained images from a) Section 1 and b) Section 2 of MLN tissue. OrbiSIMS images showing total ion for c) Section 1 and d) Section 2, and overlays of $\text{Si}_2\text{O}_5\text{H}^-$, (red), $\text{C}_4\text{H}_9\text{O}_3^-$ (green) and $\text{C}_{47}\text{H}_{82}\text{O}_{13}\text{P}^-$ (blue) for e) Section 1 and f) Section 2. The 2 sections were generated from the same lymph node. The periphery of the tissue is indicated by a white dashed line.

Figure 3.2. OrbiSIMS images showing the spatial distribution of a) and b) Cholesterol sulphate $\text{C}_{27}\text{H}_{45}\text{SO}_4^-$, c) and d) Phosphoinositide head group $\text{C}_6\text{H}_{10}\text{PO}_8^-$ and e) and f) Diaminomaleonitrile $\text{C}_4\text{H}_3\text{N}_4^-$ in 2 sections of MLN tissue respectively. The sections imaged are the same as that in Figure 3.1. The periphery of the tissue is indicated by a blue dashed line.

Figure 3.3. Total ion count OrbiSIMS image showing the selected ROI compared by PCA for a) Section 1 and b) Section 2. The sections shown are the same as that in Figure 3.1. and Figure 3.2.

Figure 3.4. Scores plot for PC 1 generated from ROIs of sectioned lymph nodes tissue. The colours of the ROIs correspond with those in Figure 3.3.

Figure 3.5. Loadings plot for PC 1 generated from PCA of ROIs from sectioned lymph node tissue. The loadings plot corresponds to the score plot in figure 3.4 and ROIs in Figure 3.3.

Figure 3.6. OrbiSIMS images showing the spatial distribution of a) and b) taurine, $C_2H_6NO_3S^-$, deviation -0.2 ppm; and c) and d) adenine, $C_5H_4N_5^-$, deviation 0.0, in 2 sections of MLN respectively. The periphery of the tissue is indicated by a blue dashed line.

Figure 3.7. OrbiSIMS images of sectioned MLN tissue from animals dosed with CBD. Total ion counts for a) section 3, b) section 4, c) section 5. Overlays of $Si_2O_5H^-$ (red), $C_4H_9O_3^-$ (green) and $C_{47}H_{82}O_{13}P^-$ (blue) for d) section 3, e) section 4 and d) section 5. Overlays of CBD species $C_{21}H_{29}O_2^-$, $C_{21}H_{27}O_2^-$ and $C_{16}H_{21}O_2^-$ for g) section 3, h) section 4, i) section 5. The periphery of the tissue is indicated by a white dashed line.

Figure 3.8. OrbiSIMS image of sectioned MLN from a dosed animal (section 3) showing CBD, blue and cholesterol, green. The periphery of the tissue is indicated by a dashed white line.

Figure 3.9. Total ion count OrbiSIMS image showing the selected ROI which were compared by PCA. The sections shown are the same as that in Figure 3.7.

Figure 3.10. Scores plot for PC 1 generated from ROIs of sectioned lymph nodes tissue from animals dosed and not dosed with CBD. The colours for each group are

reflected in the ROIs drawn in Figures 3.3 for not dosed animals and 3.7 for dosed animals.

Figure 3.11. Loadings plot for PC 1 generated from PCA of ROIs from sectioned lymph nodes tissue from animals dosed and not dosed with CBD. The loadings plot corresponds to the score plot in Figure 3.9.

Figure 3.12. OrbiSIMS images of 3 sections of MLN tissue from dosed animals. Images show the distribution of cholesterol sulphate $C_{27}H_{45}SO_4^-$ in a) section 3, b) section 4 and c) section 5; Phosphoinositide head group $C_6H_{10}PO_8^-$ in d) section 3, e) section 4 and f) section 5 and Diaminomaleonitrile $C_4H_3N_4^-$ in g) section 3, h) section 4 and i) section 5. The sections imaged are the same as that in Figure 3.6. The periphery of the tissue is indicated by a blue dashed line.

Figure 3.13. Intensity of CBD in 2 sections of MLN tissue sprayed with CBD. 6 locations per region were analysed.

Figure 3.14. OrbiSIMS images of sectioned MLN tissue from an animal not dosed (a&b) and animals dosed with CBD in sesame oil (c-e). Red is the sum of the [M-H]⁻ fatty acids shown in Table 3.2 and blue is the sum of the fragments of CBD in Table 3.1. The periphery of each node is demonstrated using the dashed white line. Images are normalised by total ion counts.

Figure 3.15. OrbiSIMS images showing the distribution of the sum of alpha tocopherol, $C_{29}H_{49}O_2^-$ and gamma tocopherol, $C_{28}H_{47}O_2^-$ in sectioned MLN tissue

from an animals not dosed (a & b) and animals dosed with CBD in sesame oil (c- e). The periphery of the node is indicated by the dashed white line.

Figure 4.1. Anatomical localisation of the mesenteric lymph nodes and retroperitoneal lymph nodes collected as part of the bio-distribution study. Modified from [4].

Figure 4.2. Schematic of the rat intestines and mesentery. The lymph nodes collected in this study are depicted by the coloured circles. Blue, position 1; Green, position 2; Red, position 3 & purple, position 4. The anterior and posterior of the body are also indicated. Modified from [5].

Figure 4.3. Distribution of CBD in MLN and RPLN at various time points post oral administration in sesame oil. The bar colours in this figure correspond to the positions of lymph nodes collected in Figures 4.1 & 4.2. All data are presented as mean \pm SEM, $n = 3$. Statistical analysis was performed using one-way ANOVA with Tukey's multiple comparisons test. * $P < 0.05$. No outliers were identified (Grubb's test, alpha = 0.05).

Figure 4.4. Distribution of CBD at various time points post oral administration in sesame oil in MLN and RPLN at various positions (a-f). The data in this figure is the same as the data in Figure 4.4, presented differently. All data are presented as mean \pm SEM, $n = 3$. Statistical analysis was performed using one-way ANOVA with Tukey's multiple comparisons test. * $P < 0.05$. No outliers were identified (Grubb's test, alpha = 0.05).

Figure 4.5. Distribution of CBD in MLN and RPLN at various time points post oral administration in coconut oil. The bar colours in this figure correspond to the positions of lymph nodes collected in Figures 4.1 & 4.2. All data are presented as mean \pm SEM, $n = 3$. Statistical analysis was performed using one-way ANOVA with Tukey's multiple comparisons test. * $P < 0.05$. No outliers were identified (Grubb's test, $\alpha = 0.05$).

Figure 4.6. Distribution of CBD in MLN and RPLN at various time points post oral administration in rapeseed oil. The bar colours in this figure correspond to the positions of lymph nodes collected in Figures 4.1 & 4.2. All data are presented as mean \pm SEM, $n = 3$. Statistical analysis was performed using one-way ANOVA with Tukey's multiple comparisons test. * $P < 0.05$. No outliers were identified (Grubb's test, $\alpha = 0.05$).

Figure 4.7. Distribution of CBD at various time points post oral administration in coconut oil in MLN and RPLN at various positions (a-f). The data in this figure is the same as the data in Figure 4.6, presented differently. All data are presented as mean \pm SEM, $n = 3$. Statistical analysis was performed using one-way ANOVA with Tukey's multiple comparisons test. * $P < 0.05$. No outliers were identified (Grubb's test, $\alpha = 0.05$).

Figure 4.8. Distribution of CBD at various time points post oral administration in rapeseed oil in MLN and RPLN at various positions (a-f). The data in this figure is the same as the data in Figure 4.7, presented differently. All data are presented as

mean \pm SEM, $n = 3$. Statistical analysis was performed using one-way ANOVA with Tukey's multiple comparisons test. * $P < 0.05$. No outliers were identified (Grubb's test, $\alpha = 0.05$).

Figure 5.1. Anatomical planes of the human body [6].

Figure 5.2. a) Gastric volume and b) small bowel water content (SBWC) post high fat meal. Each line represents data from an individual participant.

Figure 5.3. Number of lymph nodes visible at each time point post meal. a) Data represents the combined total of nodes across all slices. Each line represents data from an individual participant. (mean \pm SEM).

Figure 5.4. Example Diffusion Weighted Image (DWI) showing how the vertebra of the spine can be used as an anatomical marker to allow for the same lymph nodes to be consistently imaged at multiple time-points pre and post meal. The first lumbar vertebra is indicated (L1) and lymph nodes are indicated by coloured arrows. Colours represent the same individual lymph at each time point. The anterior side (A) of the body is to the left of each image and the posterior side (P) is on the right.

Figure 5.5. Example Diffusion weighted Image (DWI). Lymph nodes can be seen along the spine at various distances from the spine. Lymph nodes are indicated with white arrows. The lumbar vertebra (L1-3) are also indicated.

Figure 5.6. Change in lymph node area, major and minor axis length relative to baseline post high fat meal. Data represents mean \pm SEM of all nodes that were consistently imaged across all time points. n=11 for participant 1, n=22 for participant 2 and n=33 for participant 3. Statistical analysis was performed using one-way ANOVA with Tukey's multiple comparisons test. *p<0.05.

Figure 5.7. Change in lymph node area, major and minor axis length relative to baseline post high fat meal. Data represents the average difference between individual lymph nodes at each vertebra level (mean \pm SEM). L = lumbar vertebra. The data in this figure is the same as in Figure 5.6, displayed differently. Statistical analysis comparing change in area and major and minor axis length was performed using one-way ANOVA with Tukey's multiple comparisons test. *p<0.05.

Figure 5.8. Change in lymph node Apparent Diffusion Coefficient post high fat meal. Data represents the average difference between individual lymph nodes (mean \pm SEM). b). n=11 for participant 1, n=22 for participant 2 and n=33 for participant 3.

Figure 5.9. Change in lymph node Apparent Diffusion Coefficient post high fat meal. Data represents the average difference between individual lymph nodes at each vertebra level (mean \pm SEM). L = lumbar vertebra. The data in this figure is the same as in Figure 5.8 displayed differently. Statistical analysis comparing change in ADC at each time point was performed using a one-way ANOVA with Tukey's multiple comparisons test. *p<0.05.

List of Tables

Table 1.1. Summary of recent clinical trials involving oral CBD.

Table 2.1. CBD fragments and their relative abundance in CBD powder in the negative mode analysed by static SIMS.

Table 2.2. CBD fragments and their relative abundance in tissue homogenates from CBD dosed animals in the negative mode analysed by OrbiSIMS.

Table 3.1. Relative abundances of CBD fragments and cholesterol sulphate in MLN sections.

Table 3.2. Concentrations of CBD in sectioned of MLN as estimated by SIMS data.

Table 3.3. Relative abundances of fatty acids in MLN sections from animals dosed with CBD in sesame oil (n=3 sections from 3 animals) and an animal not fasted or dosed (n=2 sections from 1 animal), as determined by OrbiSIMS. The relative abundances of fatty acids in sesame oil and chylomicrons from rats following oral administration of sesame oil were generated by a colleague using GC-MS analysis (Wanshan Feng, unpublished).

Table 3.4. Relative abundances of acylglycerides in MLN sections from animals dosed with CBD in sesame oil (n=3 sections from 3 animals) and an animal not dosed or fasted, as determined by OrbiSIMS. Data is presented as mean \pm SD.

Table 5.1. Vertebral level of nodes imaged across all time points. Data represents the mean across all participants \pm SEM.

Table 5.2. Relative standard deviation (RSD) and Relative Error (RE) for 15 nodes (n=3).

List of abbreviations

2-AG 2-arachidonoylglycerol

AEA Anandamide

CB1 Cannabinoid receptor type 1

CB2 Cannabinoid receptor type 2

CBD Cannabidiol

CT Computerised tomography

DESI Desorption electrospray ionisation

DLBCL Diffuse large B-cell lymphoma

FRC Fibroblastic reticular cell

GALT Gut-associated lymphoid tissue

H&E Hematoxylin and eosin

HEV High endothelial venules

HPLC High-performance liquid chromatography

IBD Inflammatory bowel disease

LAESI Laser ablation electrospray ionisation

LCMS Liquid chromatography- mass spectrometry

LCT Long chain triglyceride

M Microfold

MALDI Matrix-assisted laser desorption/ ionisation

MALT Mucosa-associated lymphoid tissue

MCT Medium chain triglyceride

MLN Mesenteric lymph node

MRI Magnetic resonance imaging

MS Mass spectrometry

MSI Mass spectrometry imaging

NHL Non-Hodgkin lymphoma

NLC Nanostructured lipid carriers

PP Peyer's patches

RPLN Retroperitoneal lymph nodes

SEDDS Self-emulsifying drug delivery systems

SIMS Secondary ion mass spectrometry

SMEDDS Self-microemulsifying drug delivery system

SNEDD Self-nanoemulsifying drug delivery systems

THC Tetrahydrocannabinol

ToF Time-of-flight

1. Introduction

1.1. Structure and function of the intestinal lymphatic system

Historically, the lymphatic system has been largely overlooked in terms of research interest [7]. This was likely due to difficulties in visualising the lymphatic system, leading to an incomplete understanding of function [8]. Consequently, the lymphatic system was previously thought of as simply the sewer of the body, with no major relevance in pathophysiology [9]. However, the lymphatic system is now understood to play a central role in a number of diseases and subsequently there is a current drive to develop novel approaches to targeted lymphatic drug delivery [10].

1.1.1. Lymph

The lymphatic system was first described in the 17th century, with the word lymph coming from the Latin word *lympa*, meaning “connected to water” [7]. Amongst the first to be described were the intestinal lymphatics [11], which are the most extensive and densely populated in the body [12, 13]. Lymphatic fluid, or lymph, is a mixture of excess fluid, waste material, proteins and lymphocytes formed in the interstitial spaces through extravasation from capillaries as a result of hydrostatic pressure [14]. Interstitial fluid pressure then contributes to the stretching of microfilaments of endothelial cells which act like a valve to allow unidirectional entry into bulbous sacs termed initial or terminal lymphatics [14]. Upon entry into the terminal lymphatics, fluid is termed lymph. The lymphatic system, in parallel to the blood venous system, therefore plays an integral role in the maintenance of fluid homeostasis.

1.1.2. Terminal lymphatics and lymphatic vessels

The terminal or initial lymphatics are blind ended vessels lacking contractile smooth muscle and valves. Subsequently, terminal lymphatics rely on extrinsic forces such as peristalsis to allow movement of lymph [15]. Terminal lymphatics in the gastrointestinal tract can be divided into those draining the villi which connect to the submucosal lymphatic network (lymphatic capillaries or lacteals) and those that drain the muscular layer of the intestine [16]. The mucosa associated lymphoid tissue (MALT) includes the gut associated lymphoid tissue (GALT), which makes up is the largest mass of lymphoid tissue in the body [13]. The GALT in turn includes diffuse immune cells throughout the GI tract, Peyer's patches (PPs) of the ileum, the isolated lymphoid follicles along the length of the intestine, the Colonic Patches and mesenteric lymph nodes (MLN). Other types of GALT are specific to the mammal including the appendix and presence of rectal lymphoid tissues [13].

From the terminal lymphatics, lymph is directed through an extensive network of progressively larger vessels and lymphatic tissues, flow of which is aided by the presence of a series of valves and smooth muscle contractions in the walls of lymphatic vessels [15]. These are lined with continuous cell-cell junctions to avoid lymph drainage [17]. Within the abdomen, the mesentery makes up a continuous folded double layer of the peritoneum membrane that suspends the intestines from the posterior wall. A number of major collecting lymphatic vessels are located throughout the mesentery [18]. These vessels direct lymph from regions of the GI tract to lymph nodes located in the mesentery [19, 20].

The location of the terminal lymphatics in the small intestine relates to the role of the intestinal lymphatics in the absorption of dietary lipids. Triglycerides are the most common lipids in both foods and pharmaceutical excipients. Lipids including triglycerides are partially digested in the stomach by gastric lipases,

producing free fatty acids and diglycerides. Together with bile salts and phospholipids, products of lipid digestion form mixed micelles. These micelles then diffuse to the membrane of the mucosal enterocytes on the apical membrane of the apical membrane. In the enterocytes they are reassembled into triglycerides in the endoplasmic reticulum [21-23]. Along with cholesterol, cholesterol esters, phospholipids and apoproteins, triglycerides are then packaged into large lipoproteins called chylomicrons [24]. Due to their large size, chylomicrons are not taken up into blood capillaries, but instead enter the intestinal lymphatic lacteals where they are directed into the MLN [25].

1.1.3. Lymph nodes

The thymus and bone marrow are considered primary / central lymphatic organs and are the site of lymphocyte maturation and entry into the lymphatic circulation. Via the lymphatic vessels, lymph is also channelled through a series of secondary lymphoid organs, which include lymph nodes, the spleen and tonsils [26]. Lymph nodes represent the primary location for immune regulation through antigen presentation, recognition and activation [27]. Lymph node resident cells therefore play critical roles in the generation of both humoral and adaptive immune responses.

1.1.3.1. Location

The abdomen and pelvis contain several large groups of lymph nodes which include those associated with the gastrointestinal tract [1]. Humans have approximately 150-200 lymph nodes contained within the mesentery including the superior and inferior mesenteric lymph nodes (Figure 1.1). Groups of nodes can be further categorised by their location relative to major blood vessels (Figure 1.2). Much of what is known about the flow of lymph from tissues and into lymph nodes

in the intestine originates from an anatomy book originally published in 1858 [28], but continues to be widely adhered to in the scientific community [29-32]. The superior MLN are understood to collectively receive efferent lymph from the jejunum, ileum and cecum, appendix, and the ascending and descending colon [33]. The efferent lymph from the superior MLN is then understood to be directed into the retroperitoneal lymph nodes (RPLN) before entry into the cisterna chyli, thoracic duct and systemic circulation [28]. However, RPLN are also a large group of nodes and include the pelvic lymph nodes and the para-aortic (also referred to as lumbar or periaortic) lymph nodes [28]. Each subgroup of lymph nodes drains lymph from specific tissues [20]. The preaortic nodes lie in front of the aorta and are understood to collect and filter efferent lymph from common iliac, celiac, superior and inferior mesenteric nodes. All lymph then collects into the cisterna chyli and ultimately is returned to the systemic circulation via the thoracic duct [28]. RPLN therefore represent major cross roads between lymph draining dietary lipids and lymph collected throughout the abdomen. The extent to which solutes draining from intestine enter RPLN have, however not before been investigated.

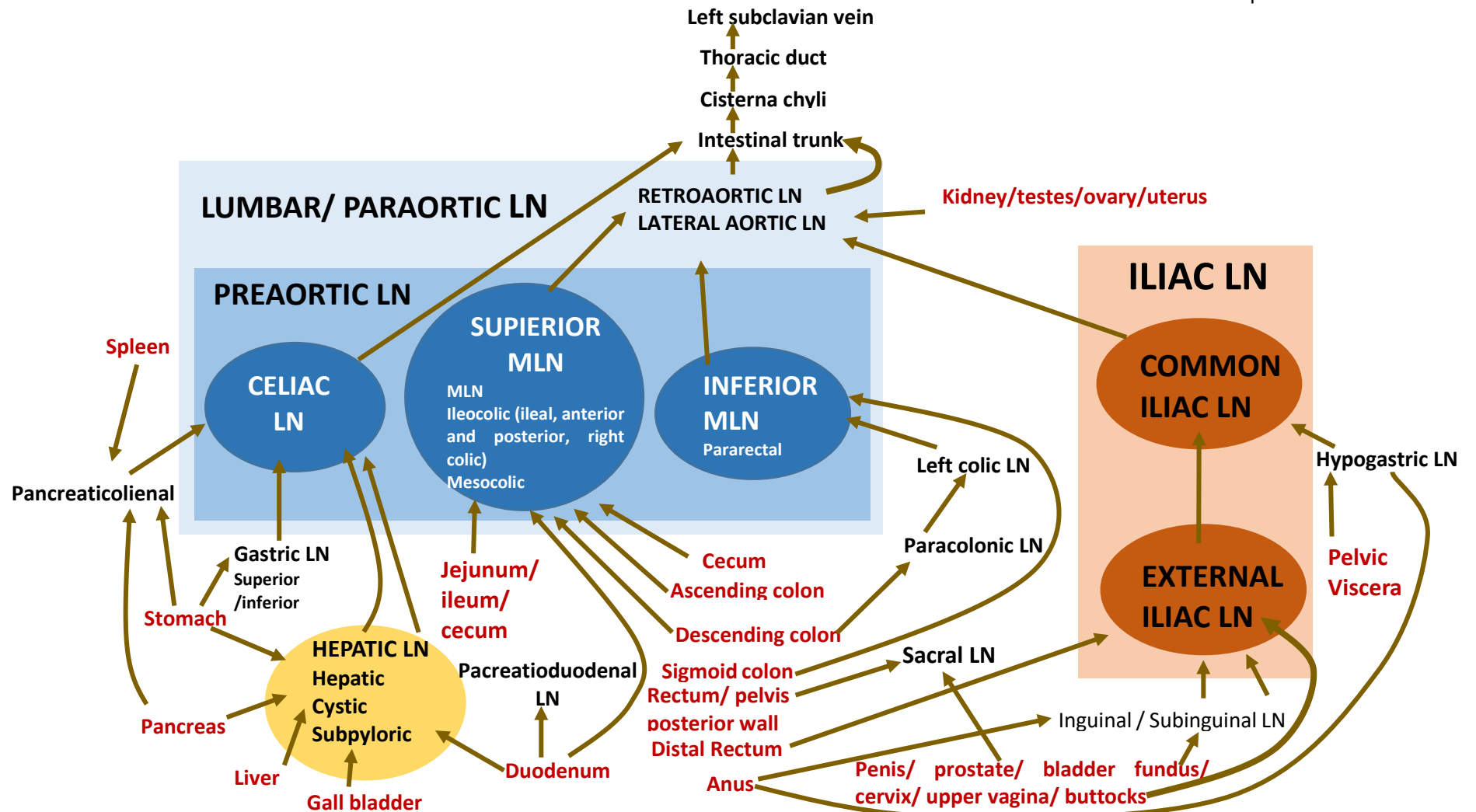


Figure 1.1. Proposed lymphatic drainage routes in the human abdomen in accordance with current literature. Arrows indicate direction of lymph flow. Tissues are shown in red. LN; lymph nodes.

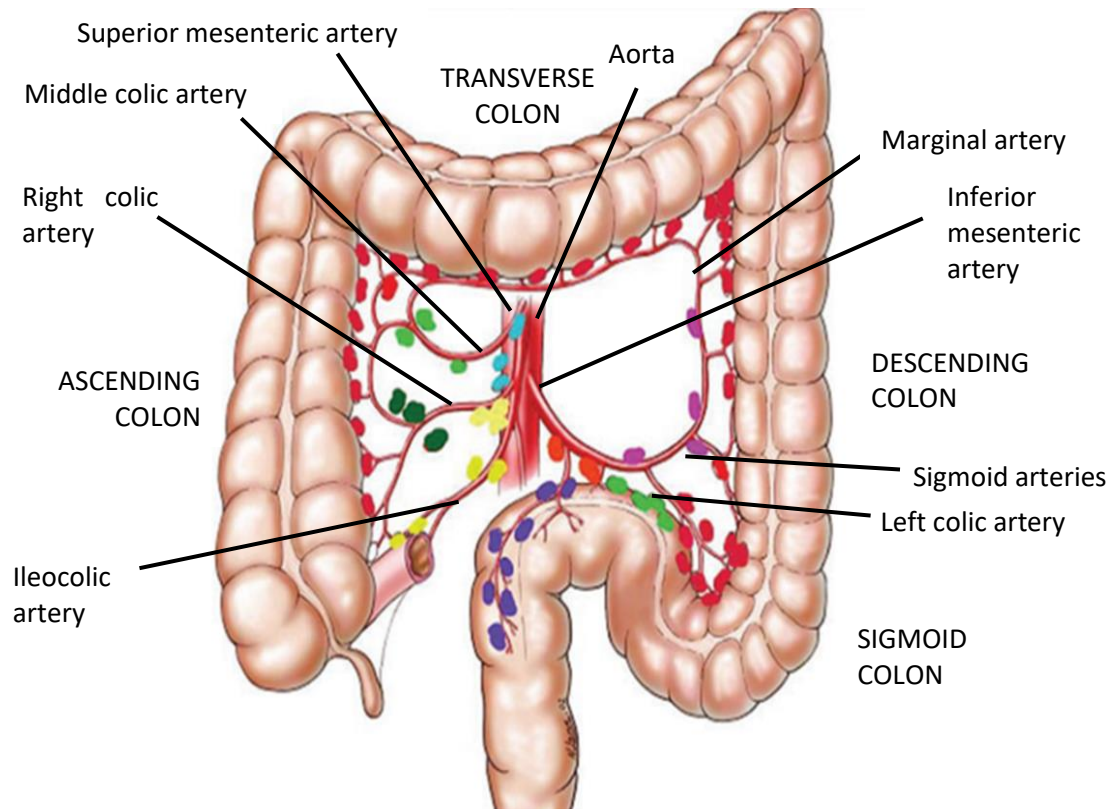


Figure 1.2. Schematic showing the major groups of lymph nodes in the human mesentery. The mesentery contains blood vessels, lymphatic vessels and approximately 150-200 lymph nodes. Nodes commonly lie in close proximity to major vessels which are also indicated. Right colic (dark green), superior mesenteric (light blue), middle colic (light green), paracolic (red), left colic (pink), sigmoid (purple), inferior mesenteric (orange) and ileocolic (yellow) [1] with permission.

1.1.3.2. Internal structure

All lymph nodes are comprised of distinct anatomical and functional regions, some of which may be visualized histologically and are generally well described [34-36] and (Figure 1.3). Each lymph node is comprised of functional units

called lobules each with its own afferent vessel in which lymph enters [34]. Lymph nodes can contain a single or multiple lobules. An outer capsule surrounds the node and channels lymph from afferent vessels. The distribution of lymph-borne solutes is dependent on the interfaces with structural components and resident cells of the lymph node [37]. Following entry via afferent vessels, lymph is known to be directed into the subcapsular sinus which contains macrophages and dendritic cells [38]. These 'barrier' cells can act to filter lymph of large particles and aid antigen presentation either to dendritic cells or to B-cells [10, 38, 39]. Remaining lymph is directed into transverse /trabecular sinuses and the reticular network [40]. The reticular network comprises a 3D scaffold of channels lined with lymphatic endothelial cells which serves to restrict access of lymph-borne material into the paracortex. Size has been described as a key factor for determining access across lymphatic endothelial cells (LECs), with cellular gaps of 0.1-1 μm excluding high molecular weight molecules of >70 kDa from conduit access [41-44]. Conversely, small molecular weight molecules, may then enter the conduit system within the paracortex, which is made up of collagen fibres lined with stromal cells called fibroblastic reticular cells (FRCs) [43, 45]. FRCs contain tight cell-cell junctions which limit access of lymph-borne solutes to the T-cell rich paracortex [46, 47].

High endothelial venules (HEVs) allow for the entry of blood bound leukocytes, via a 'multi-step adhesion cascade' [48, 49]. Within the T-cell dense areas surrounding HEVs, naive T-cells, undergo interaction with antigen presenting cells, the most abundant being mature DCs, which can present fragments of antigen and encourage T-cell stimulation [27, 50, 51]. B-cells are also believed to enter the lymph via HEVs. However, following entry, B-cells migrate towards the more superficial regions of cortex to form B-cell rich follicles [52]. In these absence of stimulation, primary follicles are composed of B-cells, which in turn may be 'virgin'

or recirculating memory B-cells. Upon activation, secondary follicles or germinal centres comprise of a mantle zone of transient lymphocytes which support proliferation, maturation and differentiation of B-cells and subsequent antibody production [53]. Medullary sinuses drain into the medullary trunk which extends into the hilus and the efferent vessels. Although the duration of time spent in the lymph is likely to be variable and multifactorial, it is understood that most lymphocytes are re-entered into the circulation, either via a network of venous blood-containing venules or in the lymph via the medullary sinuses [54].

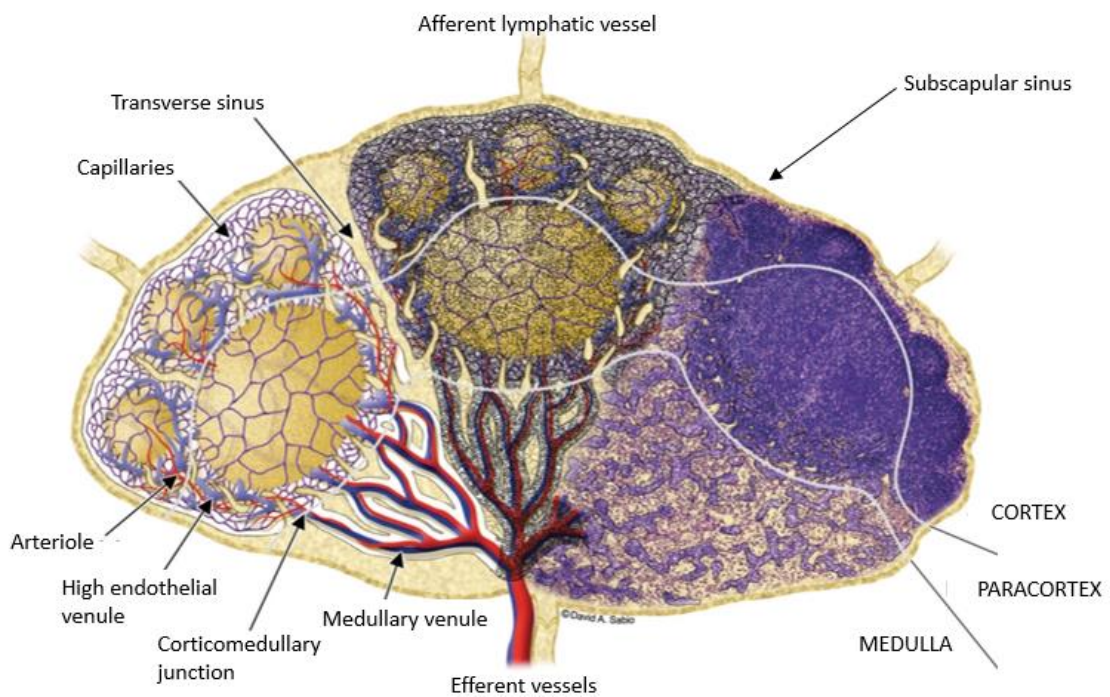


Figure 1.3. Schematic showing the structure of a lymph node containing 3 lobules.

Arterioles are shown in red, venules in blue and capillaries in purple. The right lobule is a micrograph from a section of rat mesenteric lymph node stained with H&E. Adapted from [2] with permission.

1.2. Role of the intestinal lymphatic system in disease

The fundamental roles of the intestinal lymphatic system in immune control, lipid absorption and fluid homeostasis mean that functional impairment can result in a number of diseases.

1.2.1. Immune tolerance and inflammatory disease

The intestines are consistently exposed to exogenous pathogens through the diet. It is therefore unsurprising that the GALT harbours approximately 50–70% of the entire body lymphocyte pool [55, 56]. However, the human gut also contains a diverse microbiota, which are essential to health through prevention of colonisation of pathogenic strains, metabolism of undigested carbohydrates, generation of essential metabolites and detoxification of bile acids [13]. Suitable immunosurveillance within lymph nodes is therefore essential for appropriate immune control and tolerance.

1.2.1.1. *Inflammatory bowel disease (IBD)*

Inappropriate activation of immune cells residing in the lymphatics to food and self-antigens can result in both acute inflammation and chronic inflammatory disorders and auto-immune disease [57]. IBD is the term commonly used to describe Crohn's disease and ulcerative colitis. The two diseases are distinguished by different locations in bowel, with ulcerative colitis being isolated to the colon, whereas inflammation can occur throughout the GI tract in Crohn's [58]. Symptoms of Crohn's disease and ulcerative colitis include chronic pain, diarrhoea, fatigue and weight loss which may be constant and worsen with periodic flare-ups. Many patients with IBD do not respond to currently available medications [59]. For example, real-world data indicates that current therapies such as the anti-TNF- α

monoclonal antibody infliximab, are only effective in 25 % of UC patients after a 12 month period of treatment [60]. Subsequently, it is estimated that 10-30 % and 50-80 % of people with ulcerative colitis and Crohn's disease respectively will require surgery to sections of GI tract in their life time [61]. Patients with IBD also have an increased risk of bowel cancer [62].

Both Crohn's disease and ulcerative colitis are considered autoimmune disease with unknown cause, but both hereditary and environmental factors are thought to play an etiological role [63]. Mesenteric lymphadenopathy associated with influx of immune cells is common in patients with IBD [3]. Patients with IBD were also recently shown to have different immune cell populations within MLN compared to healthy people [64]. In addition, lymphatic remodelling has been demonstrated in IBD, including hyperplasia and an expansion of surrounding adipose tissue, which are likely to impede lymphatic flow and function[65].

1.2.1.2. Other inflammatory diseases

The integral role of the intestinal lymphatic in systemic immune control means it has also been implicated in a number of other autoimmune diseases. Several microbes such as Zika virus and *Helicobacter pylori* present in the lymphatic system are known to have impact on neurological function and are linked to neuroinflammatory diseases [66]. For example, there is a growing body of evidence that the gut-brain axis, could play a role in pathology of multiple sclerosis (MS) [67-69]. Subsequently, immunomodulatory drugs which can be targeted to the intestinal lymphatics are being investigated for MS [70]. Gastrointestinal manifestations are also described in a number of other systemic autoimmune disease such as systemic lupus erythematosus, Sjögren's syndrome and polyarteritis nodeosa [71]. In addition, it has been hypothesised that the

pathogenesis of Rheumatoid Arthritis is initiated by dysregulated interactions between the mucosal immune system and local microbiota, which later transitions to the synovial joints [72].

1.2.2. Infectious disease

Despite being 'hot spots' for immune surveillance, a number of bacterial and viral pathogens have the ability to reside and propagate within the intestinal lymph nodes. These include, but are in no means limited to HIV [73, 74], hepatitis C virus [75], salmonella [76], anthrax [77], Filariasis [78, 79] and Ebola virus [80]. As a result, despite the ability of antiretroviral and antibiotics regimens to effectively irradiate antigen from the plasma, cessation of therapy often results in an inevitable rebound in pathogen. More specifically, in patients with HIV infection, the MLN are one of the main viral reservoirs in the body, with the highest viral load [81]. Correspondingly, concentrations of antiretroviral drugs within the lymphatics have been associated with persistent HIV-1 replication [9].

1.2.3. Lymphoma

Lymphoma is the term given collectively to a heterogeneous group of malignant neoplasms arising from the lymphocytes of lymphatic tissue. In total, lymphomas are believed to be responsible for 3% of new cancer diagnoses globally [82]. Lymph nodes are primarily affected by lymphoma and are the most common malignancy resulting in mesenteric lymphadenopathy or abnormal swelling seen at imaging [3]. Lymphoma in the intestinal lymph nodes can represent a solid primary tumour or be the result of disseminated disease affecting several groups of nodes [83]. Lymphoma can be loosely divided into Hodgkin lymphoma or non-Hodgkin lymphoma (NHL), depending on the histological appearance of affected cells.

Abdominal lymph node involvement is usually associated with NHL and as many as 30-50% of NHL patients have significant involvement of abdominal lymph nodes upon presentation [84]. NHLs themselves represent a diverse group of cancers, of which Diffuse large B-cell lymphoma (DLBCL) is the most common. Patients with abdominal nodal involvement in DLBCL have a poorer outcome compared to patients without [85]. Unfortunately, due to their central location in the body, mesenteric masses resulting from lymphoma can remain undetected until they reach a large size [84].

1.2.4. Metastasis from solid tumours

Cancer metastasis is widely understood to be responsible for around 90 % of cancer-related morbidities [86] and lymphatic involvement is commonly already present at the time of primary tumour diagnosis. The number of metastatic nodes and distance from the primary tumour are therefore major clinical considerations in staging and subsequent prognosis [87, 88]. The mechanisms of metastatic seeding via the lymphatics is not fully understood and remains an active and intensely debated area of research. Despite this both direct permeation and movement along chemotactic gradients have both been described [89]. Unsurprisingly, the first nodes in which oncological changes can be identified, termed the sentinel node or nodes, are almost always those in closest proximity to the primary tumour. In many cancers the pattern of lymph node metastasis from the primary tumours is therefore well described and predictable. Based on this, metastatic mesenteric lymph nodes are commonly described in gastric, small intestine endocrine, and colorectal cancers [90]. Of these, colonic carcinoma alone is one of the most common cancers occurring in both men and women [91].

Although more common in some malignancies, almost any malignancy may result in mesenteric lymphadenopathy. In addition to GI tract related cancers, metastasis from a number of primary tumours have been described in MLN. These include carcinomas in the ovaries, oesophagus, appendix, breast, lung, pancreas, bladder, melanoma and Kaposi sarcoma following HIV [90]. This highlights the incomplete understanding of metastatic processes from these areas.

Described sites of intranodal neoplasm are diverse and include cortical, paracortical and medullary regions [92] with the lymphatic sinuses common sites of metastasis, although expansion beyond sinusoidal walls and into the parenchyma is commonly rapid. In addition, as with many pathologies of the lymphatics, lymphangiogenesis and remodelling are characteristic of metastasis, with developmental cues such as VEGF-C recently being implicated [93]. This is likely to aid the possibility of lymphatic spread.

Although primary tumours can often be targeted via surgery, radiotherapy and chemotherapy, the extensive and complex structure of the lymphatic system makes lymphectomy more complex. The primary treatment for lymph node metastasis is lymphadenectomy surgery, in which the affected lymph nodes are excised, usually followed by adjuvant chemotherapy or radiotherapy. However, complexity surrounding the identification of sentinel nodes makes this difficult and often results in reoccurrence (Figure 1.4) and pathology associated with disruption in lymphatic flow including pain and oedema. In addition, the cytotoxic nature of most clinically relevant chemotherapeutic drugs results in a range of associated adverse effects. Moreover, permeability into affected lymph nodes is often poor [94]. Therefore, drugs that specifically target metastatic lymph nodes of the intestines have the potential for significant clinical impact.

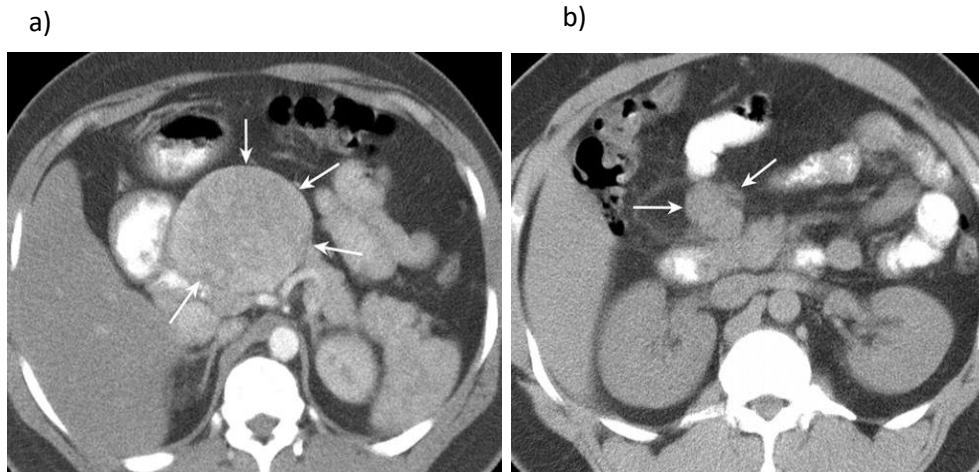


Figure 1.4. Mesenteric lymphadenopathy in a 38-year-old man with carcinoid tumour. a) CT image shows a primary soft-tissue mass (arrows). b) Non-enhanced CT image obtained 1 year later shows recurrence in a mesenteric lymph node (arrows). Taken from [3] with permission.

1.2.5. Metabolic disease

High fat diets promote a number of changes in the intestinal lymphatics. These include reduced contractibility of smooth muscle, changes to lymphatic permeability, vessel hyperplasia and dilation, altered lymph node structure and expansion of surrounding adipose tissue [9]. Although the mechanisms are not yet well understood, obesity is thought to result in dysregulation of lipid uptake by the intestinal lymphatic system [95]. This in turn has been linked to altered blood lipid levels and metabolic disease such as obesity, type 2 diabetes, hypertension and atherosclerosis [16] all of which pose an enormous health burden in the western world.

1.2.6. Lymphoedema

Disruption in lymph flow may occur for a number of reasons. These include malignancy, congenital malformations, thoracic and abdominal surgery or trauma and infectious diseases [96]. This can result in chronic fluid accumulation in tissues, termed oedema, which can be painful, debilitating, promote skin infections and lacks an effective drug treatment. Lymphoedema can be categorised into primary and secondary lymphoedema depending on their cause. Primary lymphoedema caused by genetic mutations usually starts in infancy but is rare [97]. Secondary lymphoedema is more common, with the primary cause being cancer. Secondary lymphoedema is most common in breast and pelvic cancers, but can also occur in the abdomen [98]. In addition, primary intestinal lymphangiectasia has an unknown cause and is characterised by a dilation in lymphatic vessels resulting in lymphoedema.

1.3. Drug delivery to the intestinal lymphatic system

1.3.1. Rationale for targeted drug delivery

The therapeutic potential of a drug is directly dependent on its engagement with the target, which in turn is dependent on both the affinity for the target and concentration at the site [99]. Bio-distribution is therefore a recognised fundamental pillar of drug discovery [99]. Recognition of the role of the lymphatics in various diseases has led to the appreciation of the large potential of targeted therapeutics and subsequent extensive research interest [9]. Subsequently, the efficacy of the immunomodulatory drug fingolimod has been linked to its accumulation in the lymphatics [100]. Despite this, active targeting of drugs to the lymphatics for better treatment of diseases of the lymphatics has not yet become

a key consideration in preclinical drug design. As a result, drug permeation into target tissues is often poor, which ultimately negatively impacts drug efficacy [101]. In addition, off target effects will contribute to a range of side effects.

In addition to improved treatment of diseases of the intestinal lymphatics, drug targeting to the intestinal lymphatic system can also promote improved oral bioavailability through reduced hepatic uptake and first pass metabolism in the liver. Furthermore, targeting vaccine antigens to lymph node antigen presenting cells (APCs) such as dendritic cells may also improve the efficacy [10]. Subsequently, the full extent to which targeted drug delivery could improve efficacy of a range of medicinal compounds could be great, however is yet to be determined.

1.3.2. Access to the lymph nodes

The structure and anatomy of the intestinal lymphatic system means targeted drug delivery to specific cell populations within lymph nodes can be a challenge. Since drugs can generally enter lymph nodes through various mechanisms (Figure 1.3), a number of approaches to lymphatic drug targeting have been proposed [10]. These include distribution from the circulation via HEVs, via cell-mediated pathways such as lymphocyte homing and direct lymph node injection. However, perhaps the most simplistic and effective approach is to exploit natural drainage mechanisms from interstitial fluid into lymph nodes via afferent lymph.

Entry into the interstitial fluid and subsequently lymph, requires drug delivery systems to overcome physical barriers. For access to peripheral lymph nodes, this can be achieved via subcutaneous and intradermal injection. However, for intestinal lymph nodes afferent lymph drains from interstitial fluid in the intestines (Figure 1.1). Drug delivery systems must therefore transverse the gut

mucosa following oral delivery. Opportunely, oral delivery remains the preferable route of administration due to convenience, patient compliance, flexibility and safety.

Following oral delivery, lymphatic uptake can be achieved via two major pathways which relate to the two independent subdivisions of the intestinal lymphatics [102] (Section 1.1.2). These are the M (microfold) cell pathway and the chylomicron pathway. Firstly, M cells are a mucosal antigen presenting cell and subtype of follicle associated epithelia, which cover Peyer's patches. M cells are responsible for the capture and delivery of intestinal antigens to underlying lymphoid follicles for surveillance and ultimate accumulation in MLNs. By increasing exposure to lymph node resident immune cells, exploitation of this method therefore has clinical potential for targeted delivery of biologics to the intestinal lymphatic system [10].

The chylomicron pathway is highly amenable to delivery of small molecule drugs to the intestinal lymphatics and therefore has great potential for a range of diseases in which they are implemented. In terms of drug delivery, the approach relies on exploitation of the mechanisms by which dietary lipids are absorbed from the gut by essentially hitchhiking drugs into the lymphatics through association with chylomicrons (Figure 1.5). Upon uptake into enterocytes, chylomicron-drug complexes are too large to penetrate blood capillaries so enter the lymphatic system. A relationship between chylomicron association and extent of lymphatic transport has been well established [103]. In addition, chylomicron association is known in turn to be dependent on the physicochemical properties of the drug, of which $\text{LogD}_{7.4} > 5$ and high triglyceride solubility are essential [104]. Orally administered drugs must also be stable during exposure to high pH and gastric enzymes and undergo epithelial penetration. This approach has also been utilised

to increase the oral bioavailability of drugs by bypassing the hepatic first pass metabolism.

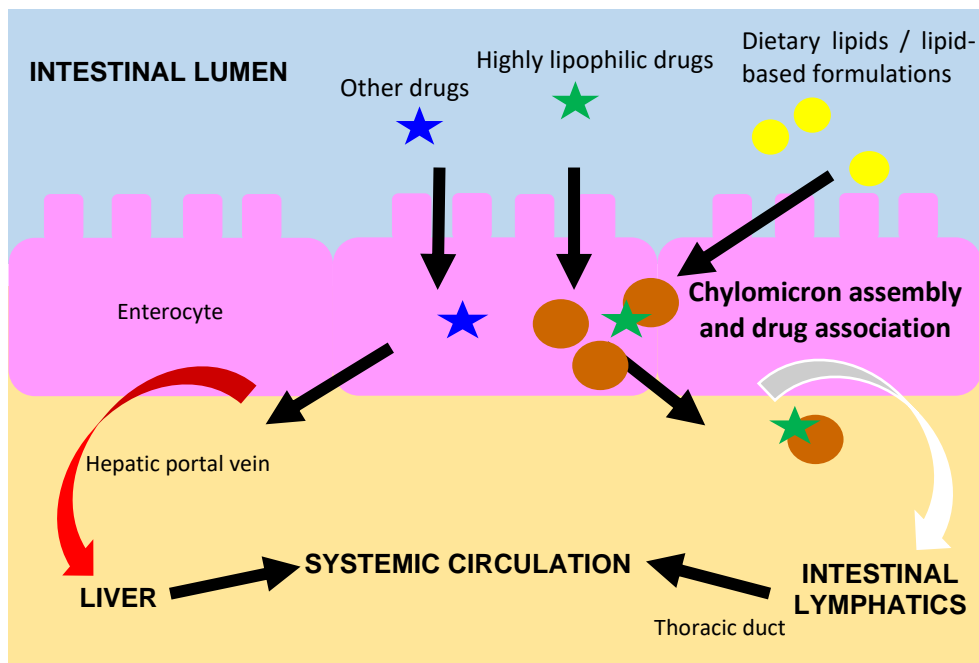


Figure 1.5. Schematic showing the mechanism by which chylomicron associated drugs can be directed to the intestinal lymphatic system following oral delivery.

1.3.3. Approaches to enhancing uptake into the intestinal lymphatics following oral delivery

1.3.3.1. Administration with lipids

Lipid droplets are emulsified in the intestinal tract with bile salts and phospholipids to form mixed micelles. Co-administration with lipids facilitates the uptake of lipophilic drugs into the intestinal lymphatics by improving luminal solubility and diffusion with enterocyte membranes as well as chylomicron formulation and rate of lymph flow rate [105, 106]. Concentrations in MLN of two Cannabinoids, cannabidiol (CBD) and tetrahydrocannabinol (THC) increased between 2 and 10 fold following administration in lipid-based formulations

compared to lipid-free [70]. Significant increases in lymphatic delivery when administered in lipidic formulations was also demonstrated *in vivo* for halofantrine [107]. In addition, the synthetic Cannabinoid PRS-211,220 was shown to undergo significant lymphatic transport which resulted in a 3-fold higher oral bio-availability when administered with lipids [108].

One of the most common excipients in lipid-based formulations are natural vegetable oils such as peanut oil and sesame oil. Long chain triglycerides (LCTs), such as those found in natural oils, have been shown to result in better lymphatic uptake compared to medium chain triglycerides (MCTs), despite MCTs improving the emulsification and solubilisation of drug [109]. However, chain length is not the only factor effecting rate of absorption, since lymphatic transport with natural oils is superior to a pure long chain triglycerides [109]. In addition, since long chain triglycerides undergo digestion into fatty acids and monoglycerides prior to absorption, it was hypothesised that administration with pre-digested lipids may improve delivery. However, pre-digested lipid formulations were inferior for intestinal lymphatic transport compared to natural sesame oil. Although the specific reasons for this are to be alluded, it has been hypothesised that natural small antioxidants in sesame oil such as lignans may play a role [109].

1.3.3.2. Prodrugs

Few clinically used oral medications are sufficiently lipophilic to undergo significant lymphatic transport in the absence of modification [103, 110]. The design of prodrugs can be used to modify the physiochemical properties and thus alter the bio-distribution of a drug. One approach is to increase drug LogD 7.4 \geq 5 by designing prodrugs which structurally contain long hydrophobic chains, similar to fatty acids. An example of where this approach has been used clinically is the

prodrug of testosterone, testosterone undecanoate. Testosterone undergoes low intestinal lymphatic transport, as therefore has poor oral bioavailability orally [111]. Testosterone undecanoate is an ester of testosterone containing a long hydrocarbon chain and has higher oral bioavailability [112] likely due to enhanced lymphatic transport and has improved androgenic activity clinically [113].

The concept of designing prodrugs for enhanced lymphatic uptake has now also been extended with the aim of treating disorders of the lymphatic system. For example, activated ester prodrugs of bexarotene and retinoid acid for the treatment of NHL were recently shown to increase drug delivery to the MLN relative to parent drug by over 17- and 2- fold respectively [114]. Similarly, the antiretroviral drug lopinavir does not undergo lymphatic transport however, an activated ester prodrug of lopinavir was shown to increase drug concentrations in MLN to 1 $\mu\text{g/g}$ when administered in sesame oil [115]. This has implications for the targeting of HIV reservoirs in MLN. Importantly, concentrations of lopinavir in MLN were over 16 times higher than the protein- adjusted concentration required for 90 % of viral inhibition (PA-IC₉₀).

An alternative approach to activated ester prodrug design for intestinal lymphatic delivery is to synthesise drugs that mimic the structure of triglycerides. Similar to triglycerides, these triglyceride mimetic prodrugs are understood to be digested to fatty acids and prodrug species equivalent to 2-monoglycerides, which are absorbed into enterocytes where they are re-esterified to the TG derivative. The triglyceride mimetic drugs are then understood to enter the intestinal lymphatics through association with chylomicrons. A triglyceride mimetic prodrug of mycophenolic acid, 1,3-dipalmitoyl-2-mycophenoloyl glycerol, was shown to enhance concentrations of parent drug in MLN in both rat [116] and dog [117] when administered in a lipid-based formulation. Critically, targeted delivery to the MLN

using 2-mycophenoloyl glycerol translated to enhanced immunomodulatory efficacy in a mouse model of antigenic challenge [118]. A similar design has also been applied to designing a triglyceride mimetic prodrug of the anticancer agent docetaxel, which had reduced GI toxicity compared with oral and intravenous parent drug [119]. Focus should now turn to confirming the mechanism of prodrug to parent drug conversion as well as beneficial effects in a clinical setting.

1.3.3.3. Other lipid-based drug delivery systems

In addition to chylomicron associated drug uptake, a variety of orally administered lipid based carriers are being explored for intestinal lymphatic drug delivery [102]. These include nanoparticles, emulsions, dendrimers and liposomes [10, 102, 120]. Structurally, these systems all have potential to be beneficial for protecting drugs from harsh gastrointestinal conditions enabling both hydrophobic and hydrophilic drugs to be encapsulated and delivered to the intestinal lymphatics. The potential for nanoparticle drug delivery has received large interest over recently years.

Solid lipid nanoparticles orient drugs between fatty acid chains of glycerides and have been shown to accumulate in the intestinal lymphatics following duodenal administration [121]. Subsequently, solid lipid nanoparticles have been shown to extend the bio-availability of a range of compounds following intraduodenal and oral administration *in vivo* [122-126]. Solid lipid nanoparticles delivery systems however present challenges such as drug loading into a solid matrix and polymorphic changes resulting in drug expulsion during storage [120].

Unlike solid lipid nanoparticles, which generally contain a single lipid such as a triglyceride, nanostructured lipid carriers (NLCs) have been designed to blend solid and liquid lipids allowing for improved drug loading capacity and reduced

susceptibility to gelation [127]. Subsequently, lymphatic transport NLC has been shown to enhance delivery number to the intestinal lymphatic system [128-130]. The use of NLC may therefore provide an alternative to chemical drug modification to allow for delivery of drugs $< \log p 7.4$. In a recent attempt to target drugs specifically to lymph resident immune cells, a two-stage nanoparticle approach was designed [131]. The approach involved intradermal administration of thiolated poly (propylene sulphide) nanoparticles with programmable degradable linkers which accumulated in draining lymph nodes and released dye cargo as a proof of concept. However, lymph node specific drug cargo release mechanisms have not yet been achieved. In addition, instability means nanoparticles have to be administered shortly after formation and local intradermal administration provides access only to the downstream draining lymph nodes. Based on this, in diseases associated with multiple lymph nodes or lymph nodes that are not accessible by injection, delivery will be more challenging [131].

Emulsions such as micellar systems and self-emulsifying drug delivery systems (SEDDs) have also been investigated for increasing lymphatic uptake of drugs. Emulsions, which are generally composed of oil, water and surfactant, can form self -microemulsifying (SMEDDs) or self-nanoemulsifying (SNEDDs) drug delivery systems depending on droplet size. Subsequently a number of groups have used SMEDDs and SNEDDs to encapsulate drugs for oral delivery *in vivo*, leading to lymphatic transport [132-140]. Similarly, liposomes are spontaneously forming closed structures, formed of a bilayer of phospholipids which have been used to encapsulate drugs for lymphatic delivery [141, 142]. Interestingly, both nanoparticles and liposomes may also be adapted to include surface labels which may also call for a more active targeting approach in the future [143-145]. It should be noted that in the majority of these publications, an increase in bioavailability is

assumed to be a result of increased lymphatic uptake, but drug delivery to the lymphatics is seldom confirmed or quantified. Based on this, the uptake mechanisms of these lipid-based drug delivery systems are not fully understood and based on the complexities of gastrointestinal physiology, multiple pathways are likely to be involved.

1.4. Imaging the intestinal lymphatic system

1.4.1. Imaging as a tool in drug development

Understanding drug accumulation within organs, tissues and cells is critical to predicting efficacy, toxicity, dosing and ultimately clinical potential of a pharmaceutical product. Despite this, investigation into localised drug distribution and the impact of formulation has not historically been routinely integrated into the drug discovery process, or was performed late stage. Subsequently, undesirable pharmacokinetic profiles often contribute to late stage attrition [146] which are both highly time and resource consuming.

Ex vivo tissue analysis using highly sensitive techniques such as high-performance liquid chromatography (HPLC) and liquid chromatography-mass spectrometry (LC-MS) can provide vital information about the quantity of drugs in homogenates from different tissues and organs preclinically. However, due to their disruptive nature, these approaches do not inform real-time drug localisation within intact tissue structures and cellular regions. Effective imaging and quantitative analysis should therefore be performed in parallel to provide a more comprehensive understanding of drug biodistribution.

Molecular imaging is the term given to any technique used to visualise and characterise biological processes. The use of molecular imaging has increased

exponentially over the past 3 decades and has provided critical information about physiological and pathophysiological processes and how these are altered following drug administration [147]. Subsequently, imaging has become a fundamental tool in all aspects of drug discovery. Despite the recent advances in targeted drug delivery to the intestinal lymphatic system (see section 1.3), to our knowledge, very few attempts have been made to characterise drug distribution. Subsequently, critical questions remain around which lymph nodes within the abdomen can be targeted and how, upon entry to lymph nodes, drugs distribute within the organised cellular structures of lymph nodes.

The appropriate imaging technique is dependent on the research question. However, high-resolution analysis of drug distribution has historically relied on the use of radiolabelled tracers which, when undergoing radioactive decay, can be identified by radiation detector. Radiolabels have been used to provide both structural and functional information about the flow of lymph within the extensive network of lymphatic vessels and lymphoid tissues [148, 149].

Almost all visualisation techniques rely on the natural ability of lymphatic vessels to absorb tracers from local interstitial tissues [150, 151]. Tracer administration therefore requires either direct injection into local tissues, or vessel micro cannulation which can be both invasive, difficult and critically inappropriate for imaging lymphatic uptake following oral delivery. Tracers also do not usually allow for distinction between drug and metabolites containing the radioactive label. In addition, the development of new tracers is often challenging, requiring complex chemistry and often limited by the inherent instability of the tracer.

BODIPY dyes are a group of highly lipophilic tracers which may be of interest for imaging the intestinal lymphatics following oral or intraduodenal delivery [118, 152, 153]. However, as with all tracers and labelled moieties there is

always the potential that the distribution of tracer is not representative of the molecule of interest, since they will differ both structurally and chemically. Based on this, there is an unmet need for label-free imaging to answer fundamental questions surrounding drug distribution to the intestinal lymphatic system, information of which could help inform the clinical potential of oral drug delivery for treatment of intestinal lymphatic diseases.

1.4.2. Imaging drug delivery to intestinal lymph nodes

Visualisation of the lymphatic system is commonly performed clinically during diagnosis or treatment of disease. These include locating lymphatic structures so they can be spared during surgical procedures, identifying and monitoring lymphedema but more commonly for the identification of cancerous involvement. Prior to cross-sectional imaging, bipedal lymphography was the standard test for visualising lymph nodes in the abdomen and pelvis [154]. Similar to angiography for imaging blood vessels, the procedure involved direct injection of tracer into lymphatic vessels. However the procedure was invasive, laborious and unreliable for lymph nodes outside the retroperitoneum and above the level of the second lumbar vertebra [154]. In the 1970s and 80s, lymphography was replaced by conventional cross-sectional imaging including computed tomography (CT) and magnetic resonance imaging (MRI). These have the benefit of being non-invasive, have a high patient acceptance and require short examination time.

The assessment of lymph nodes using cross-sectional imaging modalities usually rely on anatomy rather than function and physiology, where enlargement of nodes is considered the primary diagnostic criterion for disease [154-156]. One of the first methods for imaging intestinal lymphatics was CT, which uses X-rays which attenuate differently based on tissue density and are reconstructed to form

cross sectional images. Around the same time MRI was also developed. MRI uses magnetic fields which align protons, so when exposed to a radiocurrent pulse they spin out of equilibrium, releasing electromagnetic energy when the pulse is discontinued. Both CT and MRI have the benefit of being completely label-free. However, using CT and MRI alone, it is difficult to establish a threshold value separating benign from malignant nodes. This is because healthy lymph nodes vary largely in their size and morphology. Subsequently, not all enlarged nodes are malignant and not all malignant nodes are enlarged. In addition, it is now understood that changes in the lymphatics can be the cause and subsequence of a range of conditions including inflammation (see section 1.2.1.1 and 1.2.4). Both CT and MRI are now often combined with positron emission tomography (PET) which uses radioactive tracers to provide functional information for example increased uptake of fluorinated glucose by cancerous cells. Unlike CT and PET, MRI has the benefit of not using ionizing radiation and therefore safer for longitudinal imaging.

Imaging of the intestinal lymph nodes poses a number of difficulties including motion due to peristalsis and respiration, their small size and central location inside the body. There is currently no published evidence describing the distribution of drugs between the specific intestinal lymph nodes following oral administration. Improving the understanding of which specific lymph nodes can be targeted would inform the clinical potential of this approach, particularly in primary tumours that can metastasise in specific nodes of the intestine (section 1.2.4).

1.4.3. Imaging drug distribution within intestinal lymph nodes

1.4.3.1. Imaging to inform structure and function

Imaging tissue microenvironments can provide invaluable information surrounding biological processes, how they are altered in disease and the

pharmacological impact of drugs. Confocal microscopy is an optical imaging technique which can be used to image fluorescently labelled entities. Using confocal microscopy for cellular tracking, along with more traditional staining techniques such as immunohistochemistry, the general spatial distribution of immune cell populations within lymph node lobules are now well described [38, 157-159] (Figure 1.3). Combining cell tracking approaches with simultaneous detection of pathogen can provide critical information when designing effective targeted drug approaches. In a recent example, a combination of *in situ* hybridisation and confocal analysis of a lymph node tissue section from an HIV+ patient, showed viral RNA tended to be generally highest in B-cell follicles, more specifically those with lower frequencies of CD4⁺ T-cells. Interestingly, in the absence of antiviral therapy, viral RNA was higher in extra-follicular spaces relative to follicles [160]. Confocal microscopy was also utilised in one of the only examples of evidence of drug distribution within lymph nodes following oral delivery. In this work, a model prodrug was shown to co-localise with both CD4⁺ T-cells and B220⁺ B-cells within individual mesenteric lymph nodes following oral delivery [118].

Intravital microscopy is a technique for imagining real-time *in vivo* processes in living animals and can be performed using several light microscopy techniques including confocal, widefield fluorescence and multiphoton. Intravital microscopy techniques have advanced our understanding of cell interactions within lymph nodes during antigen presentation and infection [47, 161]. Intravital microscopy also has the potential to indirectly measure drug delivery within tissues [162]. However, since few molecules have sufficient intrinsic fluorescence, confocal microscopy and intravital microscopy generally are limited by their reliance on labelling which as mentioned ultimately can lead to artefacts.

1.4.3.2. *Label-free imaging*

Raman spectroscopy is a label free non-disruptive vibrational technique that was recently used to image structural elements of lymph nodes [163] and has potential for molecular imaging of drug distribution [164]. However, perhaps the most promising and actively progressing field for molecular tissue imaging is mass spectrometry imaging (MSI). MSI is a microscopy technique that can be used to detect unlabelled molecules, without the need to destroy sample integrity. In addition, the non-targeted approach means the technique has the potential to simultaneously image drugs, associated metabolites and biomolecules of interest including histological markers indicating pharmacology, toxicity and disease biomarkers.

All MSI-based techniques function by continuously applying desorption and ionisation probes across the surface of the sample. Through the analysis of individual pixels, mass spectrometry imaging has the capabilities of forming a chemical map of the surface of a sample, which can be expressed in relative intensities to provide information about the spatial localisation of molecules of interest. Subsequently, over the past decade, the application of MSI in drug discovery had become an active area of research [165]. In addition to aiding the chemical characterisation of both healthy and diseased tissue, MSI has successfully been employed to image the spatial distribution of drugs and metabolites within complex biological samples.

The main ionisation techniques employed for MSI include matrix assisted laser desorption ionisation (MALDI), desorption electrospray ionisation (DESI), laser absorption electrospray ionisation (LAESI) and secondary ion mass spectrometry (SIMS). MALDI is one of the most common MSI techniques used in clinical and preclinical research [166, 167]. For MALDI, the matrix is crystallised during the

ionisation process and as the matrix crystallises, analytes are extracted and co-crystallised. For some low molecular weight species, fixation wash, for example using ammonium citrate, and pre-spraying with solvent are necessary for ionisation. Based on this, the choice of matrix, method of application have impacts on the ionisation process. Although both methods are limited by the production of singly charged ions, compared to SIMS, MALDI is superior for the detection of high molecular weight species such as proteins. However, for the purposes of imaging the distribution of small molecules, such as drugs and their metabolites, potential interference from the matrix itself makes detections of lower molecular mass ions (<500 m/z), harder to detect.

1.4.3.3. Time of flight secondary ion mass spectrometry (ToF-SIMS)

SIMS is one of the oldest MSI modalities and was first developed in the 1950s and 1960s [168]. In short, SIMS analysis utilises a beam of accelerated and focused primary ions which collide with the surface of the sample. This causes the generation of secondary ions which are extracted, accelerated and separated based on mass to charge ratio (m/z). An electron flood gun is also used to charge compensate the sample surface by neutralising positive charged resulting from primary ion beams. A sputter gun can also be used to extract material from the sample surface thus allowing for 3D imaging of samples. The analysis is performed under ultra-high vacuum maintained using an airlock system.

The most commonly employed analyser is a time-of-flight (ToF) analyser (Figure 1.6). Using ToF-SIMS, all secondary ions emitted from a single pulse are accelerated to a given potential. The time for the species to drift along a flight tube, or the path length as it is generally referred to, is detected. Subsequently, ions with a higher m/z will have a longer 'time of flight' compared to ions with the same

kinetic energy but lower m/z . The matrix-free nature of ToF-SIMS, along with the ability to focus primary ions emitted in a vacuum using electrostatic lenses, means spatial resolution of ToF-SIMS is superior to MALDI and DESI. In addition, although not optimised for the imaging of large molecules, the absence of a matrix with ToF-SIMS means that there is no associated chemical noise, which might limit analysis of small molecules, as is the case with MALDI [169]. Mass resolution and sensitivity can be further enhanced by hybridisation with other analysers such as was recently described with an orbitrap analyser [170] (Figure 1.6).

SIMS is a good candidate for analysing drug distribution within tissue structures because of its completely matrix and label-free nature and, with the exception of nanoSIMS which is limited to 5 molecular species of interest, SIMS has the capability of identifying an almost infinite number of species within a defined mass range. This allows for the potential for simultaneous imaging of drug and tissue specific biomolecules in the same analysis. ToF-SIMS has been used to analyse the distribution of biomolecules within a range of tissues, including brain [171], skin [172, 173], GI tract [174, 175], eye [176, 177], liver [178], kidney [179], bone [180]. Commonly, this includes sectioning of tissue under cryoconditions followed by a combination of MSI with classical histology, for example Hematoxylin and Eosin (H&E). ToF-SIMS has also been employed to image the distribution of drugs within tissues. However, most examples include high concentrations of topically applied drugs [172, 176, 177, 181], thus neglecting the need for high sensitivity. In a recent publication, the benefits of a hybrid instrument, termed OrbiSIMS, for imaging tissues were described [170]. A schematic of the instrument is provided in Figure 1.6.

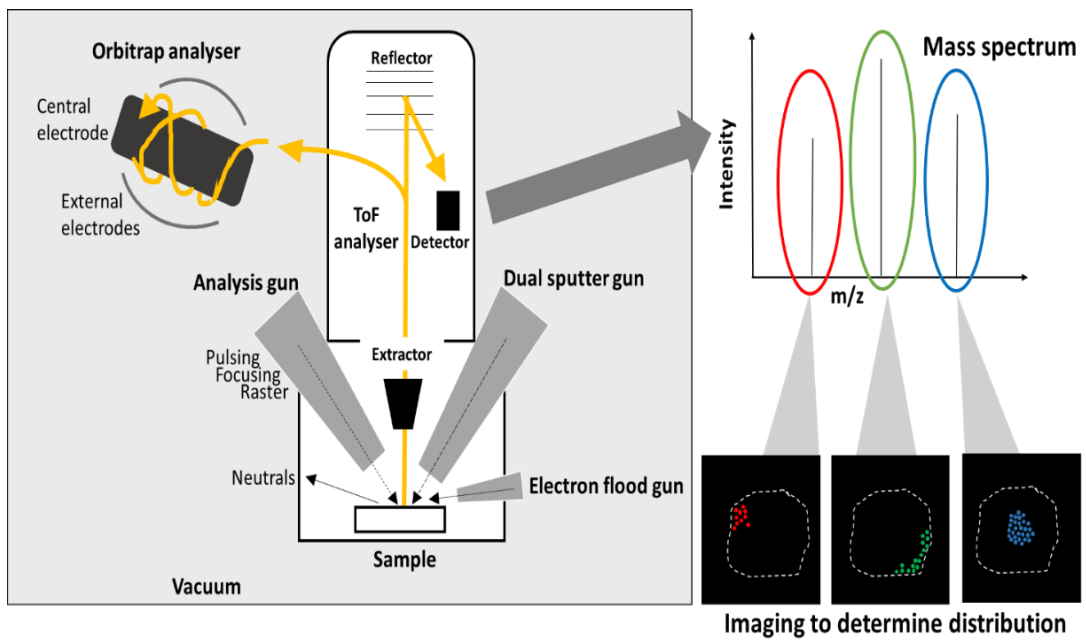


Figure 1.6. Schematic illustrating the primary components of a ToF-SIMS Orbitrap analyser hybrid instrument termed an OrbiSIMS and data processing for imaging.

1.5. Cannabidiol as a model drug for lymphatic delivery

1.5.1. Cannabis as medicine

The cannabis sativa plant has a long history of medicinal use which dates back more than 2000 years [182]. Cannabis was first introduced in Europe in 19th century and became widely used for a range of conditions, with medicinal properties including analgesia, immunomodulation, anticonvulsant properties, muscle relaxation, sedation, hypnosis and increased appetite. Cannabis is the sole source of over 100 naturally-occurring chemical compounds known collectively as phytocannabinoids [183]. Of these, the 2 main components are tetrahydrocannabinol THC and CBD, the ratios of which vary from approximately 1:1 to 80:1 depending on the strain [184]. Despite the long-standing interest for medicinal use, the psychoactive nature of THC meant that cannabis was made illegal to possess, grow, distribute or sell in the UK in 1928 and similarly in the US, possession or transfer was made illegal in 1937. However, widespread recreational and medicinal use continued and a body of anecdotal evidence for the use of cannabis has been gathered. This has refuelled interest in the use of cannabis for medicinal use. Subsequently, increasing public pressure to decriminalise cannabis over the past 10 years has meant medicinal use of cannabis has been legalised in 37 states across the US. In the UK, cannabis remains a Class B drug, possession of which can result in up to 5 years in prison. Although as of November 2018, cannabis based products are now legal for medicinal use in the UK, cannabis based products are still not yet available to patients on the NHS [185]. Subsequently, of the estimated 1.4 million people in the UK were thought to be medical cannabis users in 2020 [186] almost all is sourced on the black market.

1.5.2. Endocannabinoid system

Until the discovery of the endocannabinoid system in the late 1990s, little was known about pharmacodynamics of cannabinoids. The endocannabinoid system is a neuromodulatory system found in most mammals, comprising of cannabinoid receptors, endogenous cannabinoid receptor ligands (endocannabinoids) and the enzymes responsible for the synthesis and degradation of endocannabinoids. Although several endocannabinoids have been described, two of the most well studied are the arachidonic acid derivatives N-arachidonylethanolamine (AEA) and 2-arachidonoylglycerol (2-AG). These are found in all tissues [187]. Endocannabinoids orthosterically modulate the cannabinoid receptors which can be categorised as cannabinoid receptors type 1 (CB1) and type 2 (CB2). Both CB1 and CB2 are structurally similar Gi/Go protein-coupled receptors but differ in their affinities for cannabinoids [188] and expression on different cell types and tissues. CB1 receptors are the most abundant and are primarily distributed in the central nervous system although are also present in the periphery. In contrast, CB2 receptors are found on immune cells including lymphocytes, macrophages, natural killer cells, and microglia and therefore highly abundant within lymphoid tissues [189]. Further research surrounding the endocannabinoid system has supported its involvement in a number of physiological and pathophysiological functions, further fuelling interest in cannabinoids for medical use [190, 191].

1.5.3. Pharmacokinetics of orally administered cannabinoids

Cannabis is most commonly consumed by smoking. The exposure is therefore heavily dependent on the number, duration and frequency, volume and hold time of inhalations [192, 193]. Smoking leads to a rapid onset of effects which is likely to contribute to potential substance abuse. In addition, the negative impact

associated with smoking means that oral administration is the preferred route of administration for medical use. When self-medicating, patients often consume in the form of baked goods such as cakes and cookies.

1.5.3.1. Absorption

Both THC and CBD are structurally very similar (Figure 1.7) and defined as class II Biopharmaceutics Classification System BCS drugs meaning they are poorly soluble in an aqueous environment, but highly permeable across membranes. The $\log D_{7.4}$ values are 7.25 and 6.43 for THC and CBD, respectively [194]. Compared to smoking, oral administration of THC results in a slower absorption with a lower, more delayed peak and is altered by dose, vehicle, physiological factors [195]. Systemic bioavailability of THC and CBD are poor and variable following oral administration, and is thought to be in the regions of 3-10 % and 6% respectively [196-199]. Oral bioavailability of THC was shown to be improved by administration with lipids such as sesame oil, however concentrations were variable [198].

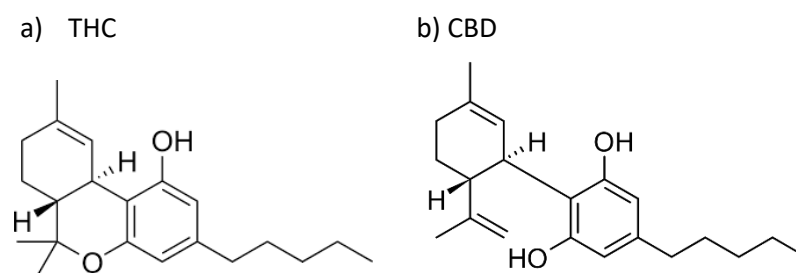


Figure 1.7. Structure of the two major chemical constituents of cannabis; a) THC and b) CBD.

1.5.3.2. Distribution

The lipophilic nature of both THC and CBD mean they accumulate in fatty tissues, such as adipose tissue, lung, brain, heart and liver [200]. As previously mentioned, both THC and CBD were recently shown *in vivo* to undergo lymphatic

transport following oral delivery resulting in high concentrations in the MLN [70]. Concentrations of CBD and THC in the MLN following oral delivery in sesame oil were 250-fold and 100-fold higher relative to plasma. Concentrations of CBD and THC in MLN reached a peak at 2 and 3 hours post administration respectively and were in the region of 10 µg/g [70, 201].

1.5.3.3. Metabolism

The major rate limiting step for CBD and THC metabolism is redistribution from lipid depots into blood. Both drugs undergo significant first pass hepatic metabolism. Phase I metabolism by cytochrome P450 enzymes results in the production of oxidised metabolites, for THC predominantly hydroxylation at C9 producing 11-OH-THC. Similarly, for CBD the main metabolic route involves hydroxylation of the 7-Meth group producing 7-OH-CBD. Subsequent oxidation to corresponding carboxylic acids then occurs. Common Phase 2 reactions include conjugation of oxidised metabolites with glucuronides, which aids water solubility and ultimately excretion. Although the major metabolites are thought to be the same, there is some evidence of interspecies differences in metabolic rates and products which may be attributed to different cytochrome P450 isoenzymes [202, 203]. There is also evidence that genetic polymorphisms in genes encoding cannabinoid metabolising enzymes may alter their efficiency [204]. To a lesser extent, extrahepatic metabolism has also been described in *in vivo* models, in the brain, intestine, heart and lung [205].

1.5.3.4. Excretion

Metabolites of both THC and CBD are largely excreted in the faeces and urine. In humans, the time between consumption and no metabolites being

detected in urine was shown to vary between 3-77 days depending on frequency and extent of use [206]. For CBD, more than 30 metabolites can be detected in urine [207].

1.5.4. Real world-data

As of 1960s, both THC and CBD can be chemically synthesised [208-210]. Due to the non-psychoactive nature of CBD, CBD products containing less than 0.2% or 1 mg THC are legal in the UK. A growing interest in the medicinal properties of cannabinoids including CBD have led to a huge number of CBD products being commercially available. Products range anywhere from food and drinks, to topical creams and lotions and vaporised products such as vaping cartridges. The fashionable nature of these self-medicated products now means that they are widely used, with a reported 6 million people in the UK using CBD based products [211]. Subsequently, CBD products are now amongst the fastest growing well-being sectors in the UK. The clinical applications for which CBD are used are extensive and include chemotherapy induced pain and nausea, multiple sclerosis related spasms, epileptic seizures, appetite stimulation, sleep disorders and anxiety [212]. Despite this, there is a significant lack of real world data surrounding safety and efficacy, meaning there is a call for tighter regulations on CBD in the UK.

Oral solutions of both CBD and THC are clinically available under the brand names Epidiolex® and Marinol® respectively. Epidiolex® is administered as a solution, whereas Marinol® is marketed as a capsule, however both contain sesame oil as an excipient. Currently, in the UK, Epidiolex® is approved by the MHRA for the treatment and prevention of seizures associated with Lennox-Gastaut syndrome and Dravet syndrome. Epidiolex® is also approved for the same indication by the

FDA in the US. Oral CBD showed promise in recent clinical trials for other forms of epilepsy also [213, 214].

Investigation into the potential of oral CBD for a number of other applications is ongoing. A summary of recent trials is given in Table 1. A large body of evidence of the potential of CBD as an immunomodulatory compound has been gathered. Although the specific mechanisms for immunoregulation not yet clear, and are likely to be complex, CBD has been shown to suppress lymphocyte proliferation and production of proinflammatory cytokines [215, 216]. Subsequently CBD has demonstrated efficacy in animal models of MS [217]. An oral-mucosal spray containing CBD and THC branded Sativex® at a ratio of approximately 1:1 and is approved by the MHRA by prescription only for severe spasticity due to multiple sclerosis having showed good efficacy in clinical trials [218]. However, oral CBD was disappointing in clinical trials for MS [219, 220]. Similarly, oral CBD showed efficacy for animal models of ulcerative colitis [221], however little efficacy was shown in a recent clinical trial [222]. One explanation is poor lymphatic delivery, resulting in insufficient interaction with lymph node resident immune cells and low bioavailability. It is not yet clear whether methods to enhance lymphatic delivery of CBD in animal models [70] can be applied to improve clinical efficacy.

Marinol® (dronabinol) has also been approved by FDA as an antiemetic for patients receiving cancer chemotherapy. However marinol® is not currently approved for any indication by MHRA in UK. CBD has also received interest as an anticancer agent [223, 224]. For example, CBD was shown to exhibit activation of autophagy in human glioma, melanoma, pancreatic and hepatic cancer cell lines [225-228]. Focus so far has been for glioblastoma, with Sativex® being well tolerated as an adjuvant therapy with temozolomide [229]. A subsequent Phase II

trial is due to begin recruitment this year. The anticancer potential of CBD for cancers of the lymphatics are yet to be investigated.

Table 1.1. Summary of recent clinical trials involving oral CBD.

Dosing strategy	Disease application	Primary outcome described in study
CBD 20 mg/kg/day (double blind placebo controlled)	Drug resistant Dravet syndrome associated seizures	The median frequency of convulsive seizures per month decreased from 12.4 to 5.9 with cannabidiol, as compared with a decrease from 14.9 to 14.1 with placebo. There was no significant reduction in nonconvulsive seizures [213].
CBD 5 mg/kg/day (open label)	Severe childhood-onset epilepsy (CDKL5 deficiency disorder, Aicardi, Dup15q and dose syndromes)	The percent change in median convulsive seizure frequency for all patients taking CBD in the efficacy group decreased from baseline [n = 46] to week 12 (51.4% [n = 35] [214].
CBD 400 or 800 mg/day for 3 consecutive days	Cue-induced craving and anxiety in drug-abstinent heroin dependent subjects	CBD significantly reduced both craving and anxiety induced by the presentation of salient drug cues compared with neutral cues. [230]
Epidiolex oral solution maximum dose 25-50 mg/kg/day and concomitant medications (open label)	Treatment-resistant seizure disorders (Lennox-Gastaut or Dravet syndrome) (paediatric patients)	At 12 weeks, add-on CBD reduced median monthly major motor seizures by 50% and total seizures by 44%, with consistent reductions in both seizure types through 96 weeks. Twenty-eight percent of LGS/DS patients withdrew, primarily owing to lack of efficacy (20%) [93].
CBD-rich botanical extract (double blind placebo controlled)	Ulcerative colitis	End of treatment remission rates were similar for CBD-rich botanical extract (28%) and placebo (26%) however patients were less tolerant of CBD-rich botanical extract compared with placebo, taking on average one-third fewer capsules, and having more compliance-related protocol deviations [222].
CBD in sesame oil with anhydrous ethanol with added sweetener 5-25 mg/kg/day	Parkinson's disease	10 that completed the study had improvement in total and motor Movement Disorder Society Unified Parkinson Disease Rating Scale scores of 7.70 (9.39, mean decrease 17.8%, $p=0.012$) and 6.10 (6.64, mean decrease 24.7%, $p=0.004$), respectively. Night-time sleep and emotional/behavioural dyscontrol scores also improved significantly. All participants reported mild adverse effects [231].
CBD 600 mg/day for 6 weeks (placebo controlled)	Cognitive dysfunction in chronic schizophrenia	At the dose studied, CBD augmentation was not associated with an improvement in MCCB or PANSS scores in stable antipsychotic-treated outpatients with schizophrenia [224].

1.6. Scope of thesis

The overall aim of this PhD project is to determine the bio-distribution of small molecule drugs and associated pharmaceutical excipients to the intestinal lymphatics following oral delivery. This is necessary for a better understanding of which diseases may best be treated by this approach. CBD will be used as a model drug as it has been shown to undergo lymphatic transport and has clinical potential in diseases of the intestinal lymphatics.

The work in this thesis can be divided into two overarching hypotheses with corresponding research aims which can be further divided into specific objectives;

- **Overarching hypothesis 1: Following oral administration and lymphatic uptake, drug distribution within the structures of the lymph node will be non-uniform.**
- **Overarching aim 1: Determine where drugs distribute within the organised structure of lymph nodes:**
 - Development of a sensitive and label-free *ex vivo* technique for imaging the distribution of CBD, lipid-based vehicles and excipients inside lymph nodes.
 - Application of the technique image CBD, lipid-based vehicles and excipients distribution within sectioned MLN tissue.
 - Application of method to identify Pharmacodynamic changes in lymph node induced by drug and formulation.
 - Determination to what extent this method can be used to quantify drug levels in regions of lymph nodes.

- **Overarching hypothesis 2: Following oral administration and lymphatic uptake, drugs will distribute at varying concentrations amongst the MLN and RPLN.**
- **Overarching aim 2: Determine which individual lymph nodes within the abdomen can be targeted by drugs following oral administration with lipids:**
 - Use of animal models to quantify CBD in individual lymph nodes *ex vivo* following oral administration.
 - Determination of how drug concentrations in individual lymph nodes changes over time and compare with different formulations in an animal model.
 - Development of a robust label-free and non-invasive MRI method for imaging the distribution of lipids in the abdominal lymph nodes of human volunteers over time.
 - Application of the MRI method to identify lipid uptake into intestinal lymph nodes and thus predict the distribution of lipophilic pharmaceutical molecules such as drugs, vehicles and excipients.

2. Development of a Mass spectrometry imaging method for determining the distribution of cannabidiol in lymph nodes

2.1. Introduction

Historically, one major drawback of Secondary ion mass spectrometry (SIMS) for complex biological sample analysis, compared to other mass spectrometry imaging (MSI) techniques such as matrix assisted laser desorption/ionisation (MALDI), has been fragmentation of large secondary ions [232]. This results in hampered detection and identification of intact biomolecules such as lipids, peptides and pharmaceutical compounds. However, over the past two decades a number of advances in SIMS instrumentation, aiding biological sample analysis, have been made. The earliest primary ion beams employed for SIMS consisted of monoatomic species such as Ga^+ and Cs^+ [233]. However, the development of polyatomic or cluster ion beam sources were shown to significantly reduce damage to the sample and enhance ion yield [234]. Polyatomic ion sources include liquid metal ion guns (LMIG) such as bismuth, Bi_n^+ [235], which are now commonly employed for tissue analysis. Large cluster ion beams including gas cluster ion beams (GCIB) can be employed for 'sputtering' material to remove it from the sample surface, thus allowing for depth profile analysis. However, more recently, the application of GCIB sources, such as Argon, Ar_n^+ , as primary analysis beams have become increasingly popular. The use of a single GCIB analysis beam can increase the amount of material analysed and by preventing the loss of material during dual beam analysis, boost ionic yield and sensitivity [236]. Relative to LMIG, GCIB sources also cause lower impact energies and thus further reduce

fragmentation, providing increased yield of higher mass species such as biological macromolecules [236]. The use of GCIB can result in spatial resolution of 2 μm [170] which although inferior to the potential sub 100 nm with LMIG, is superior to many MALDI and DESI systems [237]. Ultimately, GCIB primary analysis beams offer an optimal label-free approach for biomedical imaging.

In addition to advances in primary ion beams, a range of accompanying mass analysers are now available. Notably, a hybrid instrument was recently developed combining the high spatial resolution of SIMS (under 200 nm for inorganic species and under 2 μm for biomolecules) with the high mass-resolving power of an Orbitrap mass spectrometer (>240,000 at m/z 200 and mass accuracy of <2 ppm) [170] (see Chapter 1, Figure 1.5 for a schematic of the instrument). Tandem MS (MS/MS) capabilities also inform fragmentation patterns and assignment. The speed of analysis is also a benefit for acquisition of large images, compared to FT-ICR MS. The capabilities of OrbiSIMS for tissue analysis were demonstrated in a recent publication [170] where the distribution of intact neurotransmitter and lipid molecules within samples of rat brains was imaged. In addition, the instrument demonstrated sufficient sensitivity to obtain metabolomic profiles on single cells. Recent progress was made in the use of this instrument for imaging intact protein structures in biological samples [236].

The importance of appropriate preparation of biological samples for MSI has also been the subject of recent investigation [238-240]. As with many analytical techniques, the ability of a fragment of interest to be detected against a complex matrix using SIMS is directly related to the suitability of the sample preparation. This is particularly true when attempting to obtain high spatial resolution within intact tissues. In addition, cryo functionality has been developed to allow for sustained sample cooling to -170 $^{\circ}\text{C}$ for sustained periods of time [241]. Notably, it

was found that analysis at these temperatures avoids the need for fixation and drying which protects samples from degradation and molecular redistribution under the high vacuum operating conditions of SIMS [239, 242]. Using this method, frozen hydrated samples of bacterial biofilms were successfully analysed for nucleobases and bacterial membrane [241]. In addition, the use of an inert embedding material, called optimal cutting temperature compound (OCT) resulted in less contamination and a reduction in suppression of lipid signals compared to traditional paraffin embedding [238].

2.2. Chapter aims and objectives

The aim of this chapter is to develop a MSI method with sufficient sensitivity, mass and spatial resolution to image CBD in rat lymph node tissues at concentrations relevant to *in vivo* conditions. This work requires the optimisation of several instrumental parameters, including sample preparation, primary analysis beam and analyser combinations and analysis temperature. Once established, the method will then be applied to image the distribution of CBD in rat intestinal lymph nodes following oral administration in a lipid-based formulation. By combining knowledge of the major cellular regions of lymph nodes structures, this work will then inform which cell types CBD may interact with whilst undergoing intestinal lymphatic transport. Estimations about how the distribution of CBD applies to other compounds of interest will also help inform the wider clinical potential of targeted drug delivery to the intestinal lymphatics. A schematic describing the workflow in this chapter is provided below (Figure 2.1).

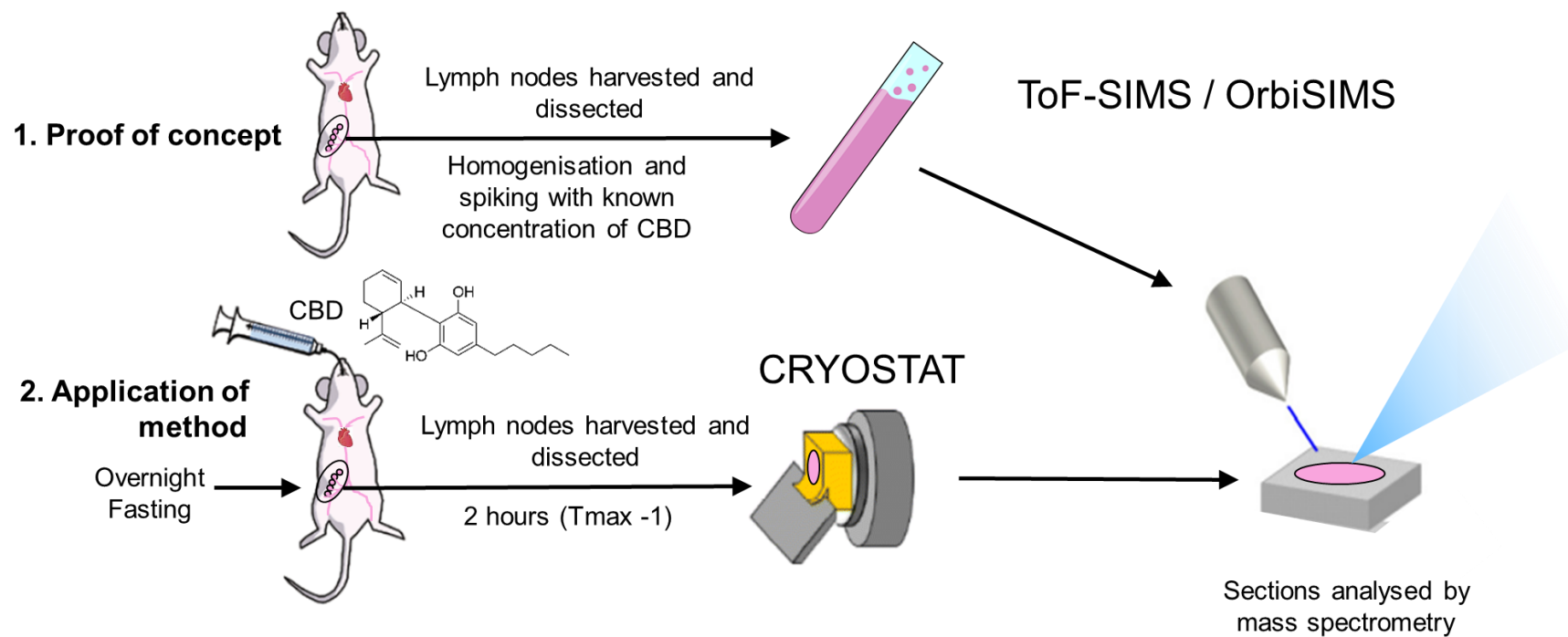


Figure 2.1. Schematic showing the experimental workflow for Chapter 2.

2.3. Materials and Methods

2.3.1 Materials

Plant-derived CBD was purchased from THC Pharm GmbH (Frankfurt, Germany) (98-99 % purity indicated by provider). Linoleic acid, sesame oil, histological grade xylene, haematoxylin, eosin, trifluoroacetic acid (TFA), DPX synthetic resin slide mounting medium and methanol were purchased from Sigma Aldrich (Gillingham, UK). OCT was purchased from VWR International Ltd. (Leuven, Belgium). Acid alcohol and Scott's tap water were purchased from Leica Biosystems (Welzar, Germany). Industrial methylated spirit (IMS), Acetonitrile (ACN) and dimethyl sulfoxide (DMSO) was purchased from Thermo Fischer Scientific (Horsham, UK). CBD was dissolved in ACN for stock and working solutions.

2.3.2 Animals

All experiments and procedures were approved by the UK Home Office in accordance with the Animals [Scientific Procedures] Act 1986. Experiments were performed using male Sprague-Dawley rats (Charles River Laboratories) weighing 300–349 g. The rats were housed in the University of Nottingham Bio Support Unit, and kept in a temperature-controlled and 12 hours light-dark cycle environment with free access to water and food. All experiments were performed in accordance with the approved protocols.

To avoid the wastage of sectioned MLN tissue from dosed animals, in accordance of the 3Rs principles of research involving laboratory animals, initial method development was performed on homogenised MLN tissue spiked with known concentrations of CBD. For the generation of these samples, MLN tissues were collected from animals that were not fasted or dosed.

Sections of MLN tissue from dosed animals for imaging were obtained from animals acclimatized for 5 days and fasted overnight with free access to water. CBD in sesame oil was administered via oral gavage (12mg/ml, 12mg/kg) as previously described [201]. Animals were euthanized by CO₂ asphyxiation two hours post dosing, one hour prior to t_{max} . This is when concentrations in the MLN collectively are highest (Chapter 4, [70, 109]).

In this chapter, homogenised tissues from dosed animals were also acquired as part of another experiment by a colleague (Wanshan Feng). For this experiment, the animals, housing, drug administration and method of euthanasia was the same as for the generation of tissue sections from dosed animals, except the vehicle was linoleic acid instead of sesame oil. Samples were collected 4 hours post dosing.

2.3.3 Tissue collection and preparation

Animal carcasses were laid in a supine position and the ventral abdominal wall was incised to expose the intestine. Individual MLN were removed from the abdominal cavity and gently dissected from surrounding tissue as previously described [201]. Where lymph nodes were used for sectioning, care was taken to maintain tissue in the same orientation as was positioned inside the body and avoiding rotation in either plane, with the aim of having a consistent and comparable imaging plane between samples. Tissue was stored at – 80 °C until needed.

2.3.3.1. Spiked MLN tissue homogenates

Tissue homogenates spiked with CBD were used to obtain an understanding of the ionisation behaviour of CBD against the matrix of MLN tissue. The imaging method developed using these samples could later be applied to sections of MLN from animals administered with CBD. The relative sensitivity of the

method for CBD detection could also be determined. Concentrations of CBD in MLN have been reported in the region of 2- 14 $\mu\text{g/g}$ (Chapter 4, [70, 109]).

Previous in- house preparation of homogenate tissue for MSI included suspension of tissue in solvent, homogenisation, air drying to remove solvent and tissue water content and subsequent resuspension of dried homogenate tissue in solvent. The benefit of this is that tissue drug content can be expressed as a ratio of solid mass, independent of tissue water content. However, since previous work used to quantify CBD in tissues was performed using HPLC and hydrated tissue [4] this initial drying stage was deemed unnecessary.

DMSO was previously shown to cause signal suppression for a range of drugs in tissue homogenates when compared to methanol [243]. Based on this, all homogenates were diluted in methanol.

Dissected MLN tissue added to methanol at a ratio of 1:2 (w/v) and homogenised (POLYTRON® PT 10–35 GT, Kinematica AG, Luzern, Switzerland) at 18000 rpm for 3 minutes on an ice bath. Samples were then spiked with CBD at concentrations ranging from 5000 $\mu\text{g/g}$ – 5 $\mu\text{g/g}$ (weight drug / weight tissue). Spots of 1-2 μl of homogenate were placed on a non-gelatinised glass slide and samples were stored at -80 °C until analysed.

2.3.3.2. Assessment of ion yield following exposure to reactive vapour

In an attempt to optimize the yield of CBD ions during analysis, glass slides containing homogenate samples from tissues that had been spiked with CBD were placed in a petri dish and exposed to TFA vapour for 10 minutes.

2.3.3.3. MLN homogenates from dosed animals

Homogenate MLN tissues from animals dosed orally with CBD were acquired from another study by a colleague (Wanshan Feng) has been diluted at a

ratio of 1:2 (w/w) in HPLC grade water and prepared in the same way as spiked tissue homogenates.

2.3.3.4. High pressure freezing

Where tissue homogenates were high pressure frozen, 2 μ l of suspension was placed into a 0.01 mm depth planchette and frozen using a Leica EM ICE (Leica, Germany) as previously described [244]. Samples were then stored in liquid nitrogen until transfer into the Cryo-OrbiSIMS system.

2.3.3.5. Sample drying

Where tissue homogenates were dried prior to analysis, samples were left at room temperature (laboratory bench) for 2 – 3 hours.

2.3.3.6. Tissue sectioning

Lymph node samples were embedded using the inert support medium, OCT which rapidly solidifies once cooled below -10 °C. Samples were either frozen at -20 °C or dipped in liquid isopentane cooled to -160 °C for 1-2 seconds. Samples were then stored at -80 °C until sectioning.

Sectioning was performed using a cryostat (Leica CM2018, Leica Biosystems, Germany) at a thickness of 16 μ m and a chamber temperature and object temperature of -20 °C and -25 °C respectively. Samples were then thaw-mounted onto non gelatinised polysine microscope adhesion slides (ThermoFisher Scientific) as previously described [22].

H&E staining of tissues helps to aid microscopic imaging of tissue structure and orientation. For lymph node tissue, this can include identification of the outer capsule, sinuses, B-cell follicles and the T-cell paracortex. Sections adjacent to those used for SIMS analysis were stained with haematoxylin and eosin (H & E). In short, glass slides containing sectioned tissue were immersed in haematoxylin for 5 minutes and rinsed in tap water. Samples were then exposed to acid alcohol for 30

seconds, rinsed again in water and emerged in Scott's tap water for a further 30 seconds. Slides were immersed in 1% Eosin for a further 5 minutes and rinsed in 90%, 100% IMS and finally Xylene. DPX synthetic resin slide mounting medium was used to secure a glass cover slip. Optical images of H & E stained tissue sections were obtained using a light microscope (Zeiss Axioplan 2, Carl Zeiss Microscopy, USA).

2.3.4. Analytical methods

2.3.4.1 Time of flight-secondary mass spectrometry (ToF-SIMS)

Due to ease of use and familiarity with the running of the instrument, initial work aimed to determine whether analysis could be performed with using ToF-SIMS. Based on the theoretical benefits of the OrbiSIMS instrument (see section 2.1) if the ToF-SIMS instrument proved incapable future work would use the OrbiSIMS.

For initial ToF-SIMS work, analysis was conducted using a ToF-SIMS IV instrument (IONTOF, GmbH) equipped with a single-stage reflectron analyser. A low energy (<20 eV) electron flood gun was used to charge compensate by neutralising any positively charged regions as a result of bombardment of the sample surface with a positively charged primary ion beam.

2.3.4.1.1. Static SIMS

Static SIMS refers to the process by which a sufficiently low primary ion dose ($\leq 10^{12}$ ions per cm^2) is used to allow mass spectral data to be acquired faster than the lifetime of the surface layer. This means that no area on the sample will be impacted twice during the acquisition time and has the benefit of being completely non-disruptive to the sample surface. Static analysis was performed using a bismuth LMIG, with Bi_3^+ clusters chosen as the primary ion source as

previously described [173]. The primary ion source had a 20 keV beam energy and the primary ion dose density was always maintained at $\leq 1 \times 10^{12}$ ions/cm² to ensure static conditions. For most samples, data was acquired over 500 $\mu\text{m} \times 500 \mu\text{m}$ area at a resolution of 256 pixels / mm unless stated otherwise. Each area was scanned using a random raster pattern. Data was collected at a mass range of 0-825.

2.3.4.1.2. Dual beam dynamic SIMS

Dynamic SIMS is a term used to describe the operation of the primary ion beam at a dose which exceeds the 'static' limit, hence causing the removal of fragments from the sample surface. This mode therefore allows for the collection of material from the underlying sample and the potential for an improvement in secondary ionic yield from the sample. For the purposes of tissue analysis dynamic SIMS also has the potential to allow for 3D imaging of drug distribution although to date this has only been used for single cell analysis not sectioned tissue and was not performed in this work.

Dual beam dynamic SIMS was performed using a Bi₃⁺ analysis beam as described in 2.3.4.1.1. For the process of sputtering, an argon GCIB was used with Ar₁₇₀₀ beam used at a beam energy of 10 keV and a current of 10 nA. Data was collected in a non-interlaced mode with 1 frame analysis, 3 frame sputter. Sputter area was 500 $\mu\text{m} \times 500 \mu\text{m}$ and analysis area using Bi₃⁺ was 200 $\mu\text{m} \times 200 \mu\text{m}$. Data was collected at a mass range of 0-3500.

1.3.4.1.3. Primary ion focusing beam

The spatial resolution achievable is dependent on the primary ion focusing mode. Two primary ion focussing modes are commonly employed for ToF-SIMS; High current-bunched (HC-BU) and burst alignment (BA), each with advantages and

disadvantages depending on the analysis priority. The two methods differ in their primary ion pulse duration; HC-BU uses a device called a buncher, which reduces the primary ion pulse width (typically to <1 ns). The result is that the primary ions of each pulse impact the sample surface in quick succession and energy deposition at the surface is reduced. This results in an increased particle ejection reducing the extraction and detection times for ions of the same m/z . Subsequently high mass resolution can be achieved ($M/\Delta M = 7000$ (FWHM) at $m/z = 29$), but at the expense of the ability of the beam to focus, reducing spatial resolution ($> 2 \mu\text{m}$). In contrast, BA does not use a buncher, meaning the pulse width is longer and total ion count mass resolution is impaired. However, because a high focus beam can be employed, a much higher spatial resolution can be achieved (< 500 nm). For this reason, BA mode is more commonly utilised for the purposes of ToF-SIMS imaging and since this is the ultimate aim of this work, BA was used.

2.3.4.2. *OrbiSIMS*

The 3D OrbiSIMS instrument used in this study is a hybridisation of a TOFSIMS 5 platform (ION-TOF GmbH, Germany) and a Q Exactive HF Orbitrap™ mass spectrometer (Thermo Fischer Scientific, Germany). A similar set up has been described previously [170, 236, 244]. Prior to analysis, mass calibration of the Q exactive instrument was performed using silver cluster ions.

Charge compensation was optimised in the centre of the tissue sample using an electron flood gun with an energy of 21 eV and a current of $-10 \mu\text{A}$ and argon gas flooding. The total primary ion dose was preserved below 1×10^{12} as to ensure static conditions. Data was collected in the negative mode at a mass range of 75-1125 and a random raster mode. Imaging of sectioned tissue was performed using an Ar_{3000}^+ primary ion source at a primary ion energy of 20 keV unless otherwise stated. The time taken to collect images of each node was approximately

3 hours. The area scanned for each lymph node was $2.5 \times 2.5 \text{ mm}^2$ at a pixel size of $20.0 \text{ }\mu\text{m}$.

To investigate the effect of sample temperature on sensitivity of the instrument to detect CBD in tissue samples, analysis was performed at both ambient temperatures and under cryo conditions. The OrbiSIMS instrument is equipped with a fully proportional–integral– derivative (PID) temperature controller and a liquid nitrogen closed loop circulation cooling stage as previously described [244]. Where homogenate samples were high pressure frozen, samples were transferred to the main chamber for analysis using a shuttle chamber Leica EM VCT500 (Leica, Germany) [244]. Where sectioned, tissue samples were stored at $-80 \text{ }^\circ\text{C}$ prior to analysis, samples were allowed to equilibrate to room temperature prior to stage mounting. This was an attempt to avoid the formation of frost. Samples were then cooled in the loading chamber prior to transfer into the analysis chamber. All cryo analysis was performed at $< -130 \text{ }^\circ\text{C}$.

2.3.5 Data processing and analysis

All ToF-SIMS and OrbiSIMS data was collected and interpreted using SurfaceLab 7 (ION-TOF GmbH). All exported peak intensities were normalised to the total ion count of the spectra. All figures and statistical analysis were performed in GraphPad Prism (version 7.03). Peaks were assigned using SurfaceLab 7 functionalities. A deviation of 1 ppm from the assignment was deemed acceptable.

To compare intensities of species in different samples, multiple groups were compared using a one-way analysis of variance (ANOVA) with Tukey's multiple comparisons tests were performed. Where only two groups were being compared, an unpaired, two-tailed t-test was performed. A p value of <0.05 was considered

statistically significant. The relationship between concentration and peak intensity was analysed using linear regression analysis and expressed using the R^2 value.

2.4. Results and Discussion

2.4.1. Method development for ToF-SIMS detection of CBD in lymph node tissue

2.4.1.1 Static SIMS

Preliminary work began by investigating the use of static SIMS for the detection of CBD in tissue homogenates. Despite the discussed benefits of GCIB as a primary ion source (section 2.1.), initial work was performed with an LMIG primary ion source due to its associated superior spatial resolution.

CBD undergoes metabolism in the liver by Cytochrome P450 enzymes [245] which is initially bypassed through uptake into the intestinal lymphatics (see Chapter 1, section 1.5.3.3). Subsequently, the parent molecule of CBD can be readily detected by HPLC in MLN samples from animals dosed orally with CBD (Chapter 4, [70, 109, 201]). Based on this, initial work aimed to characterise the ionisation and any potential fragmentation behaviour of the parent molecule of CBD. The presence of these species could then be determined in tissue samples.

Intact molecular species are often present in at a higher abundance compared to fragments and are so are the most reliably detected. Both the $[M-H]^-$ ($C_{21}H_{29}O_2^-$, $m/z = 313$) and $[M+H]^+$ ($C_{21}H_{31}O_2^+$, $m/z = 315$) species could be identified in samples of powdered CBD in the positive and negative polarity data respectively (Figure 2.2). However the $[M-H]^-$ species was detectable at a higher yield relative to $[M+H]^+$ (Figure 2.2) suggesting CBD is more ionisable in the negative polarity. In addition to the molecular ions, fragment ions are usually formed through collision of molecular ions with primary ions of energetic ions in the samples [246]. Several

fragments of CBD have been described [247, 248] and could be identified in CBD powder (Table 2.1). The proposed fragmentation pattern for fragments at m/z 179, 191 and 245 are shown in Figure 2.3. These species were all present at a lower abundance relative to the $[M-H]^-$ species (Table 2.1). Based on this, majority of future work was performed in the negative mode, unless stated otherwise. The abundance of these ions was consistent in samples of CBD diluted in ACN, DMSO and methanol, suggesting no suppressive solvent effect on CBD ionisation.

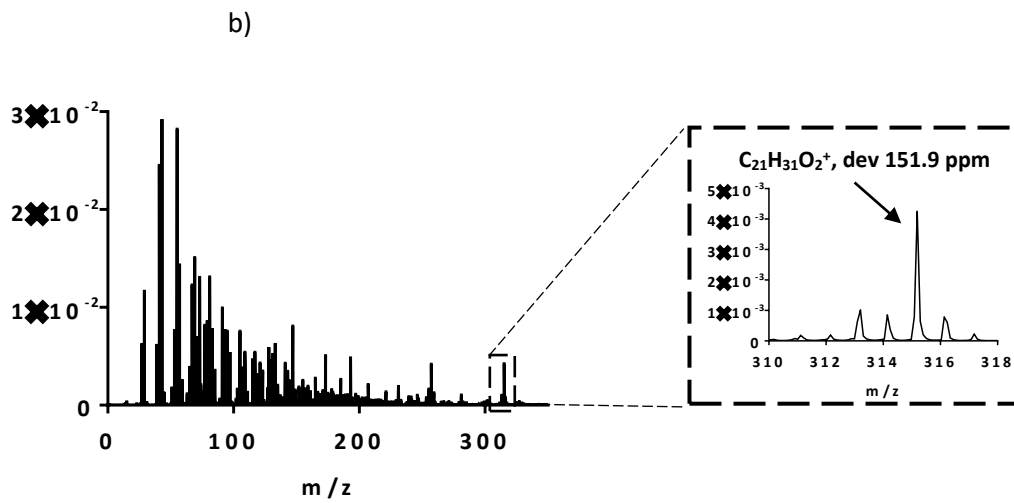
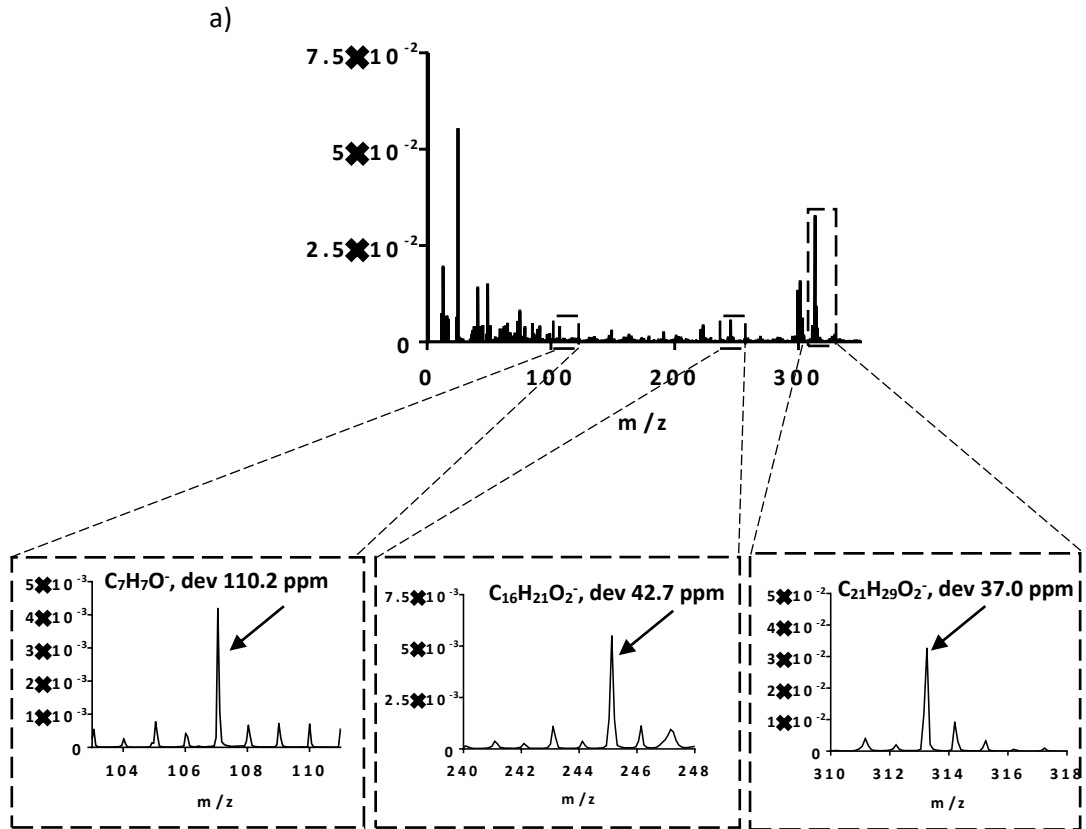


Figure 2.2. Static ToF-SIMS spectra of CBD powder in a) negative mode and b) positive mode.

Table 2.1. CBD fragments and their relative abundance in CBD powder in the negative mode analysed by static SIMS.

m/z	Intensity (normalised to total counts)	Relative abundance (%)
107.0620	5.55E-03	6.42
129.0778	3.74E-05	0.04
137.1113	3.92E-04	0.45
171.0506	8.91E-04	1.03
173.0593	1.95E-03	2.26
179.1069	1.84E-03	2.13
183.0531	8.33E-04	0.96
191.1070	3.16E-03	3.66
201.0840	2.17E-03	2.51
205.1437	1.60E-03	1.85
229.1201	1.34E-03	1.55
245.1438	8.65E-03	10.02
264.7747	3.40E-04	0.39
269.1431	1.95E-03	2.26
277.1901	2.45E-04	0.28
295.0681	1.68E-03	1.94
311.1845	7.87E-03	9.11
313.2289	4.59E-02	53.11

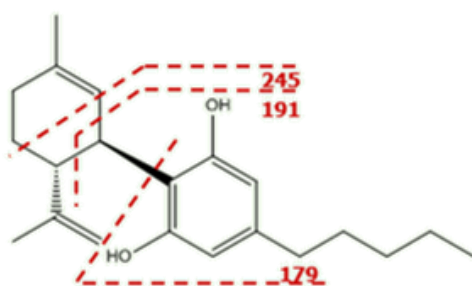


Figure 2.3. Proposed fragmentation patterns for CBD.

Having identified ions that are diagnostic to the presence of CBD, the aim was to assess the ability to identify them within a relevant matrix: in this case MLN tissue homogenate. Analysis of tissue homogenate spiked with CBD demonstrated

that using static SIMS no ions related to CBD could be detected in tissue (Figure 2.4). This was likely a combination of insufficient sensitivity as well as interfering peaks in the tissue which could not be well resolved, even at 5 mg/g, which is sufficiently higher concentrations than physiologically relevant (Chapter 4. [70, 109]). Comparison of the spectra from spiked and blank tissue homogenates did not suggest the presence of any other CBD fragments.

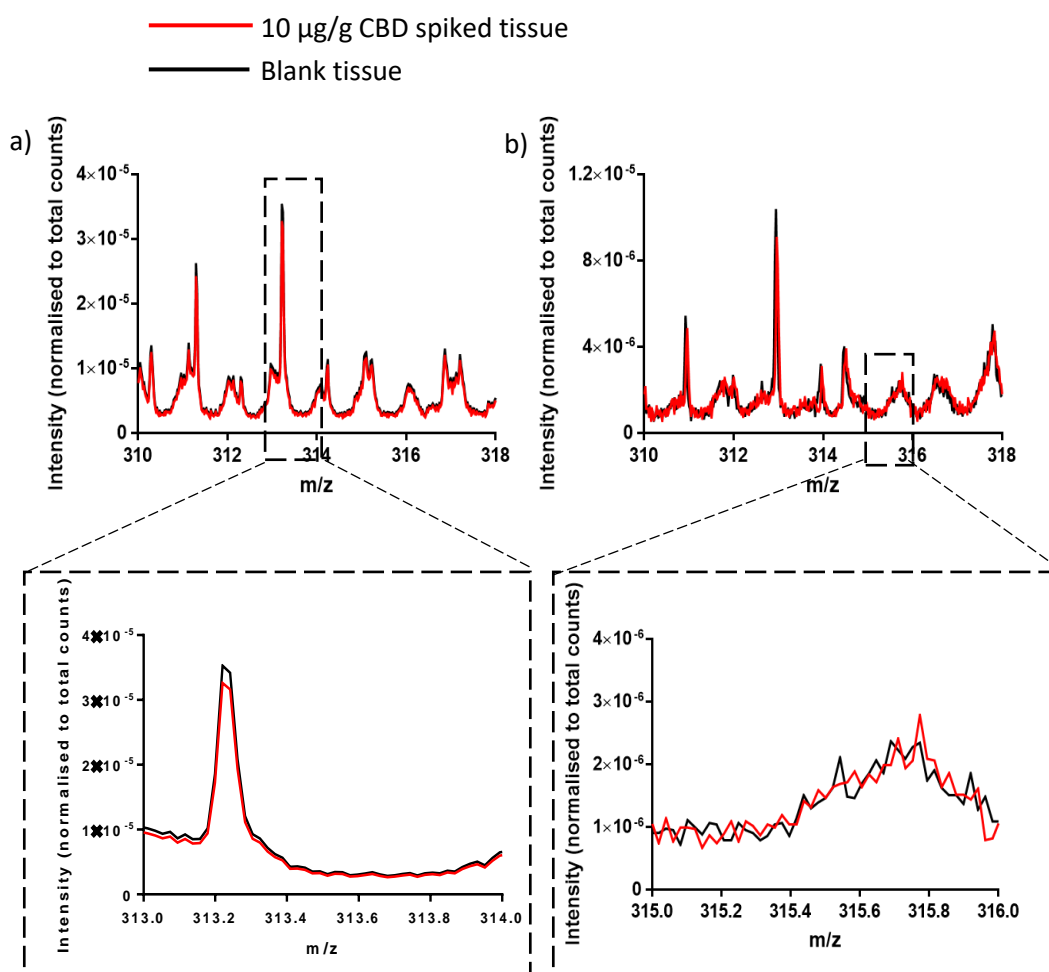


Figure 2.4. Overlaid static ToF-SIMS spectra of blank MLN tissue homogenate (black) and MLN tissue homogenate spiked with 5 mg/g CBD (red) in the a) negative spectra and b) positive spectra.

2.4.1.2 Dynamic SIMS for yield optimisation

The surface of biological samples can become contaminated which can mask the detection of underlying species of interest. Sputtering can be used to remove material from the sample surface thus cleaning it of contaminants and improving the ionic yield of underlying material [249]. Based on this, it was hypothesised that the use of dynamic SIMS may improve the detection and sensitivity for CBD in tissue homogenates. Depth profiling showed that there was an enhancement in ion yield for the $[M-H]^-$ species with increased sputter time (Figure 2.5). Subsequently, dynamic SIMS analysis of CBD spiked tissue homogenates showed that sensitivity could be improved compared to static SIMS (Figure 2.6). Peak intensity was higher in samples spiked with higher concentrations of CBD (Figure 2.7). However, the analytical method was still not sufficient to detect the molecular ion of CBD at *in vivo* relevant concentrations (Figure 2.7). This was in part due to an interfering peak as a similar m/z to CBD in the blank tissue sample which could not be resolved. Poor mass resolution of CBD was also reflected in images of the homogenates (Figure 2.8).

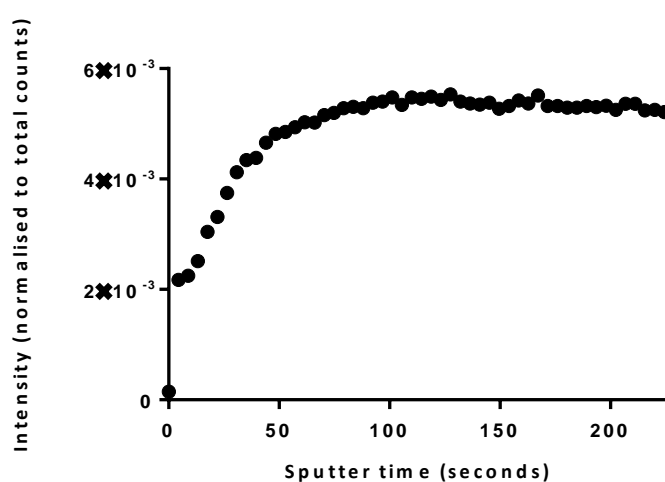


Figure 2.5. Dynamic SIMS negative mode depth profile data of MLN tissue homogenate spiked with 5 mg/g CBD.

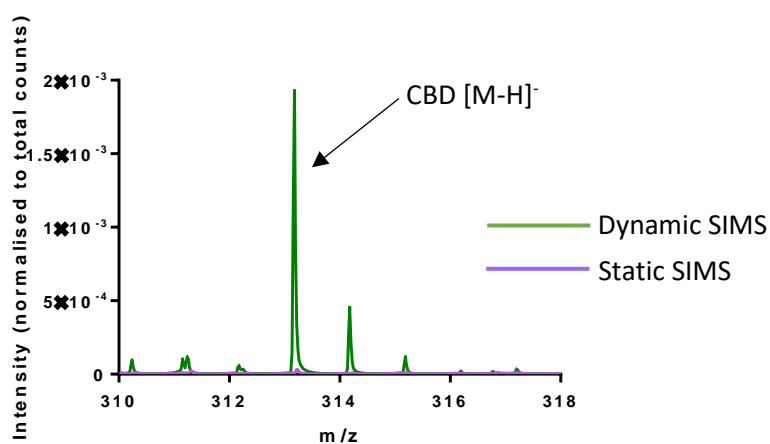


Figure 2.6. ToF-SIMS spectra of MLN tissue homogenate spiked with 5 mg/g using static SIMS (purple) and dynamic SIMS (green). Data shown in the negative mode.

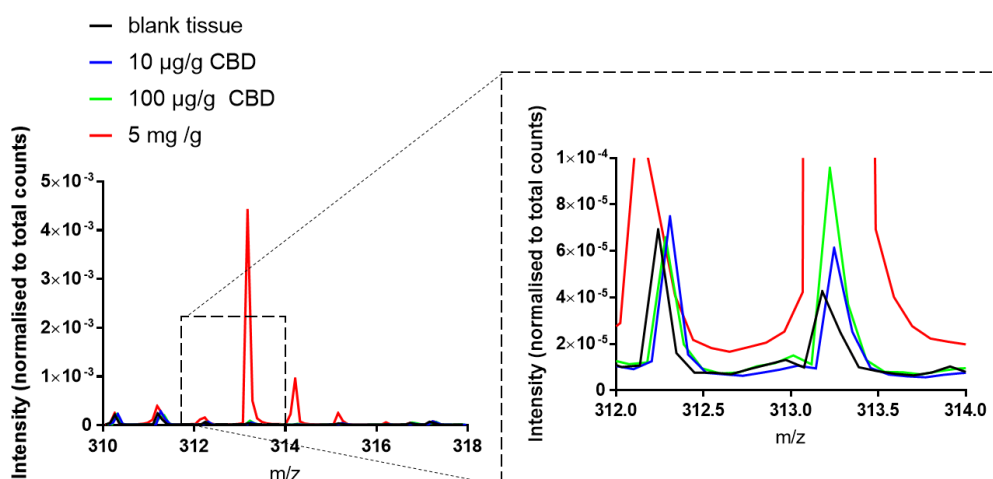


Figure 2.7. Overlaid Dynamic ToF-SIMS spectra of blank MLN tissue homogenate (black) and MLN tissue homogenate spiked with 10 µg/g CBD (red) CBD cannot be deciphered against the matrix of homogenised MLN tissue at *in vivo* relevant concentrations. Data shown in the negative mode.

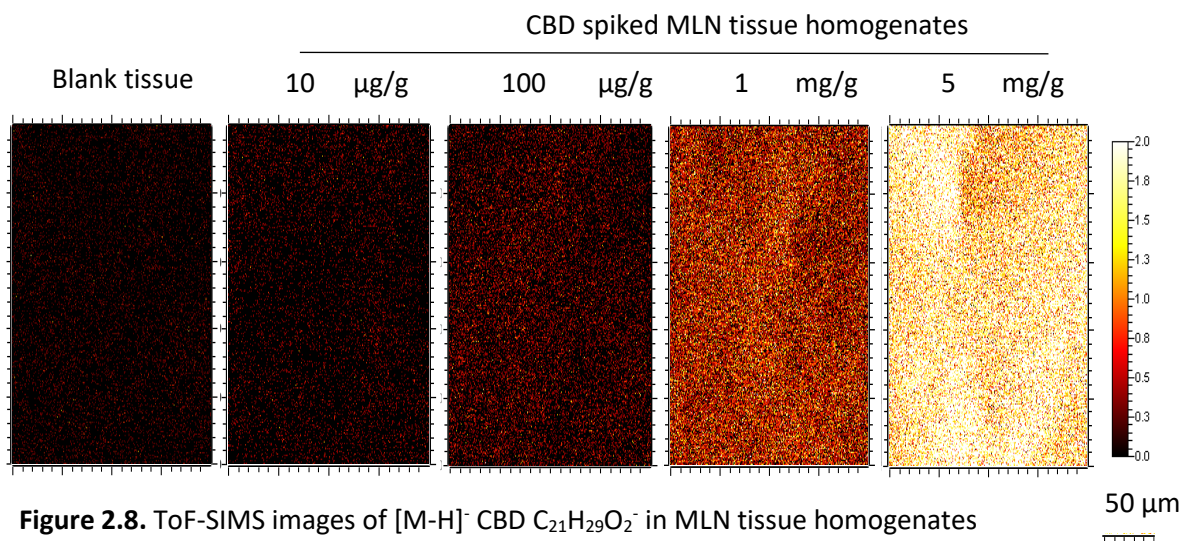


Figure 2.8. ToF-SIMS images of $[M-H]^-$ CBD $C_{21}H_{29}O_2^-$ in MLN tissue homogenates spiked at a range of concentrations.

Poor sensitivity for CBD in spiked homogenate tissues using ToF-SIMS correlated to an inability to detect any CBD related species in sectioned samples from dosed animals using an LMIG primary ion source (Figure 2.9). Development of the tissue sectioning method is described in section 2.4.3. The lack of sensitivity at concentrations as high as 10 µg/g perhaps was not surprising since this concentration is significantly lower than previously described studies looking at drug distribution where high concentrations of drug were applied topically [172, 250]. In addition, whilst samples were held in the main chamber for analysis, it was observed that the intensity of CBD decreased over time. The vapour pressure for CBD at ambient conditions is approximately 3.2×10^{-7} mbar [251]. Based on this, it was hypothesised that main chamber pressure could have exceeded the vapour pressure for CBD, causing sublimation. The impact of temperature on this phenomenon is explored in section 2.4.2.3.

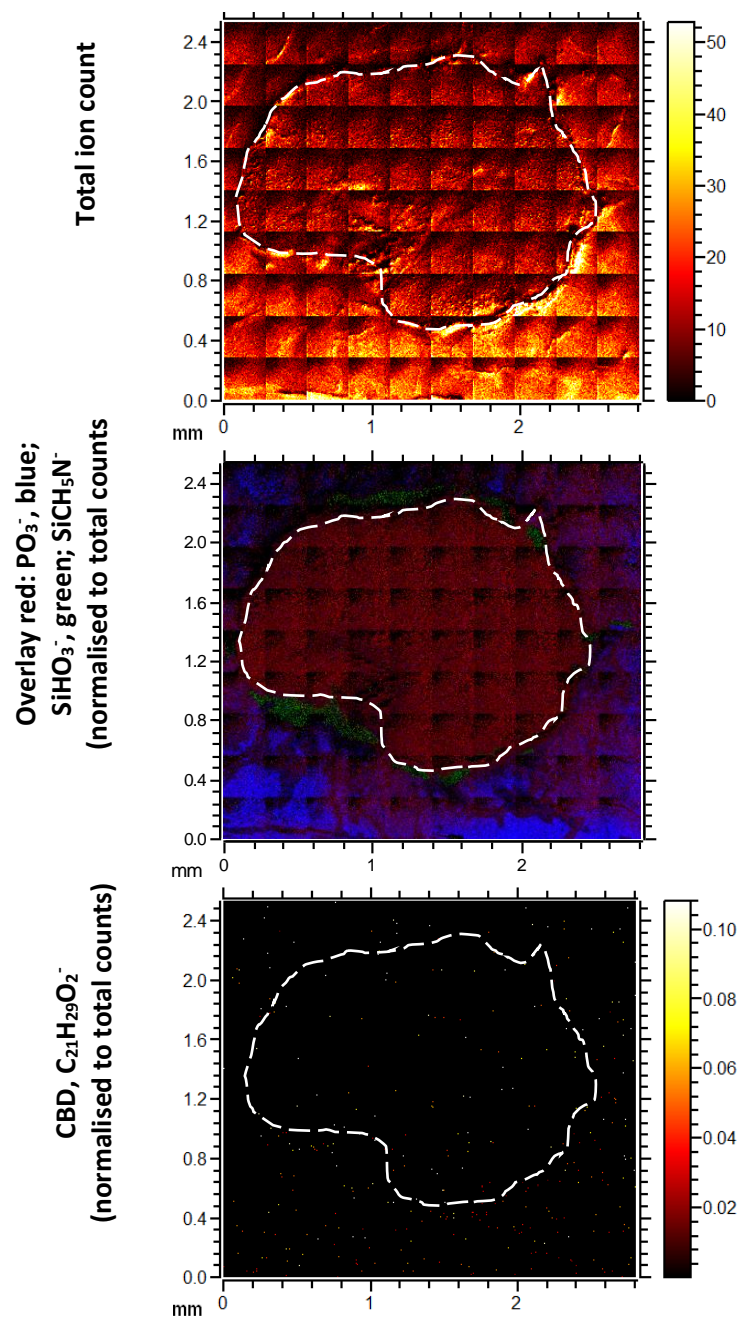


Figure 2.9. ToF-SIMS images of sectioned lymph nodes from animals dosed with CBD. a) total ion counts, b) Overlay red, PO_3^- a tissue fragment, blue, SiHO_3^- OCT, green SiCH_5N^- glass, c) $\text{C}_{21}\text{H}_{29}\text{O}_2^-$ [M-H] $^-$ CBD. The outline of the node is indicated in each image by a dashed white line.

ToF-SIMS is as a semi-quantitative technique. One reason for this is the presence of matrix effects. This phenomenon is well described [252, 253] and refers to the impact that the matrix, in this case chemical components of tissue, have on the electron exchange process and subsequently ionisation of the species of interest, in this case CBD. Despite this, work with both SIMS and MALDI have shown a linear relationship between molecular ion intensity and concentration of drug within tissue homogenate samples [243, 254]. Figure 2.8. indicates a uniform distribution of CBD in tissue homogenate. The relationship between CBD [M-H]⁻ intensity as a function of concentration is shown in Figure 2.10. Some deviation from a linear relationship was observed at lower concentrations. Caution should also be taken when using the calibration curve in the absence of repeats, accuracy and precision assessments and without sufficient validation including determination of the lower limit of quantification (LLOQ). This assessment of relationship between ion abundance and concentration is therefore preliminary and highly exploratory.

Utilisation of this calibration curve can therefore estimate concentrations of CBD in different regions of sectioned tissue from dosed animals as was previously performed for lactate in sections of mouse tumour [254]. Knowledge of the immunomodulatory threshold of CBD can then be used to estimate which cells CBD exerts its pharmacodynamics effects on. However, it should be noted because the calibration curve has been produced in homogenised tissue, where any matrix effects of the tissue on CBD detection would be exerted equally, investigation into potential matrix effects of regions of intact sectioned tissue was also necessary (see Chapter 3 section 3.4.5).

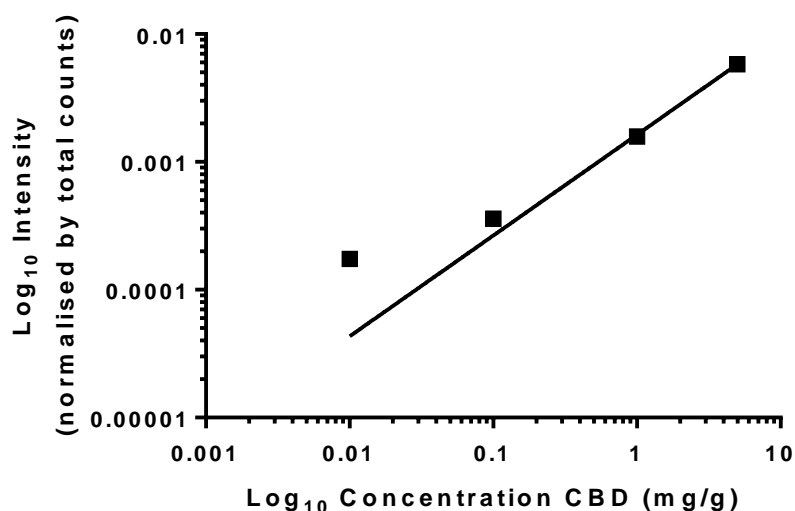


Figure 2.10. Calibration curve showing the intensity of the $[M-H]^-$ for CBD spiked at various concentrations in homogenised MLN tissue using dynamic SIMS ($n=1$).

Data is presented using a log scale.

2.4.1.4 Reactive vapour exposure for yield optimisation

Initial work using ToF-SIMS instrumentation indicated an insufficient ion yield for CBD and *in vivo* relevant concentrations. It was previously shown that exposure of tissue to reactive TFA could improve yield of biologically relevant fragments [255]. It was therefore hypothesised that this may also apply to the molecular ion for CBD through the donation of protons, thus increasing ionisation efficiency. In an attempt to optimise sensitivity to CBD using ToF-SIMS, homogenised tissues were exposed to TFA. However, yield of the molecular ion was not significantly improved compared to untreated tissue homogenate systems in either mode (Figure 2.11).

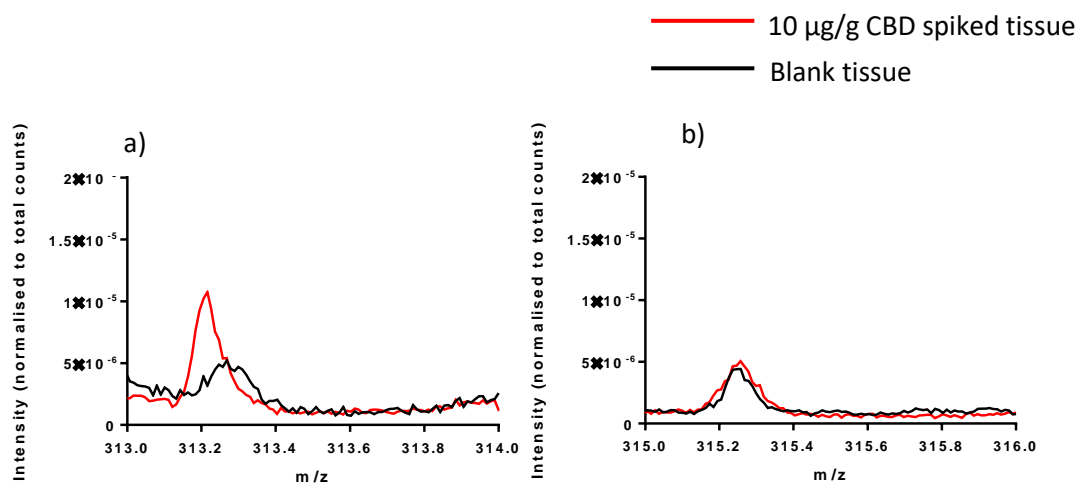


Figure 2.11. Overlaid dynamic ToF-SIMS spectra of blank MLN tissue homogenate (black) and MLN tissue homogenate spiked with 10 µg/g CBD (red) CBD in following exposure to TFA in the a) negative and b) positive mode.

Taken together, the data presented in section 2.4.1. indicate that that using the ToF-SIMS approach specifically utilising the LMIG / ToF combination ion beam / analyser combination could not provide sufficient sensitivity and/or mass resolving power to detect CBD against the matrix of tissue at relevant concentrations for the delivery of CBD.

2.4.2 Method development for OrbiSIMS detection of CBD in lymph node tissue

2.4.2.1 OrbiSIMS Sensitivity relative to ToF-SIMS

A number of potential benefits of OrbiSIMS instrumentation for the analysis of biological samples relative to conventional ToF-SIMS instrumentation have been described (See section 2.1.). Improved mass resolution and sensitivity for cholesterol sulphate was shown using OrbiSIMS compared to ToF-SIMS in mesenchymal skins cells in a recent publication [181]. However, a direct

comparison between the two instruments has not yet been made for the detection of an active pharmaceutical ingredients (API) in tissue sections. It was first aimed to compare whether, relative to analysis with the ToF-SIMS instrument, the mass resolution and sensitivity for CBD in tissue homogenates could be improved using OrbiSIMS. In order to make direct comparisons with work performed using ToF-SIMS, initial work with OrbiSIMS was performed at ambient temperatures.

CBD $[M-H]^-$ could not be detected at 10 $\mu\text{g/g}$ in tissue homogenate using an Ar_{5000}^+ . This is likely because the overall TIC was too low (Figure 2.11.) However using an Ar_{3000}^+ the overall TIC was higher compared to when using an Ar_{5000}^+ analysis beam (Figure 2.12). The enhanced ionic yield observed with Ar_{3000}^+ was in agreement with previous work comparing the two analysis beams [256]. Subsequently using an Ar_{3000}^+ analysis beam, Figure 2.13. demonstrates superior mass resolution and sensitivity for CBD of OrbiSIMS relative to dynamic SIMS using ToF-IV. Subsequently, the $[M-H]^-$ species of CBD could be deciphered against the matrix of tissue at *in vivo* relevant concentrations using an Ar_{3000}^+ analysis beam (Figure 2.11).

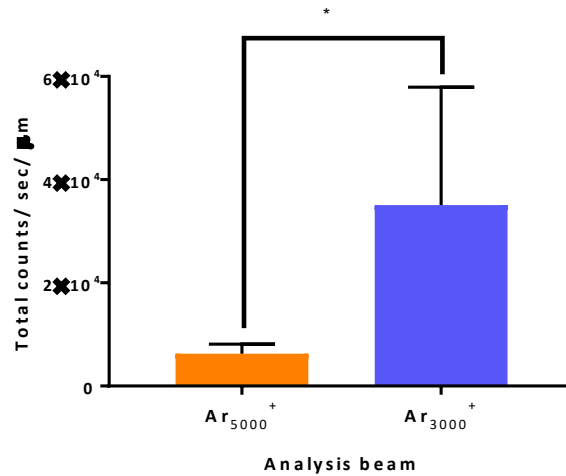


Figure 2.12. Comparison of Total ion counts (TIC) using Ar₅₀₀₀⁺ and Ar₃₀₀₀⁺ beams to analyse MLN tissue homogenates. Data is shown as mean ± SD n = 13 Ar₃₀₀₀⁺ and n = 5 for Ar₅₀₀₀⁺. *Statistically significant, unpaired two-tailed t-test, p < 0.05.

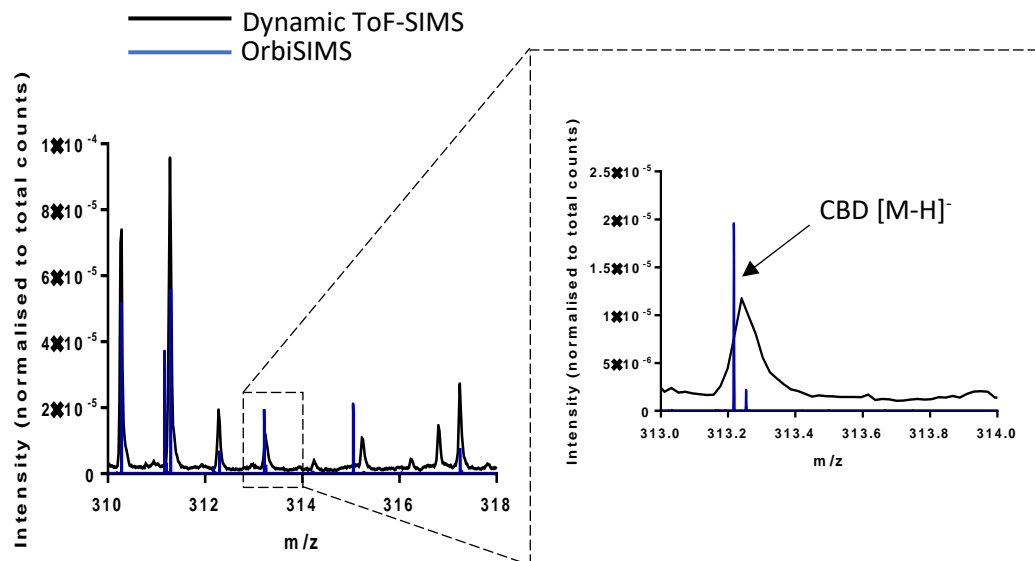


Figure 2.13. Overlaid mass spectra of MLN tissue homogenate spiked with 10 μg/g CBD analysed with dynamic ToF-SIMS (black) and OrbiSIMS (blue).

CBD [M-H]⁻ could be detected within the matrix of tissue homogenate without interfering peaks in blank tissue (Figure 2.14). CBD could also be detected at concentrations of 7.5 µg/g and 5 µg/g although at these concentrations variation in peak intensity was larger. (Figure 2.15). Based on this, the goal of developing a method by which CBD can be detected in tissue at *in vivo* relevant concentrations without the use of labels or matrices has been achieved. To our knowledge, imaging of APIs in tissue has not previously been achievable without the use of labels at concentrations as low as described in this work. The method may be used to image the distribution of CBD in MLN following oral delivery. Again, it should be noted that use of the calibration curve in Figure 2.15 to calculate concentrations of CBD in tissue samples should be done with significant caution in the absence of

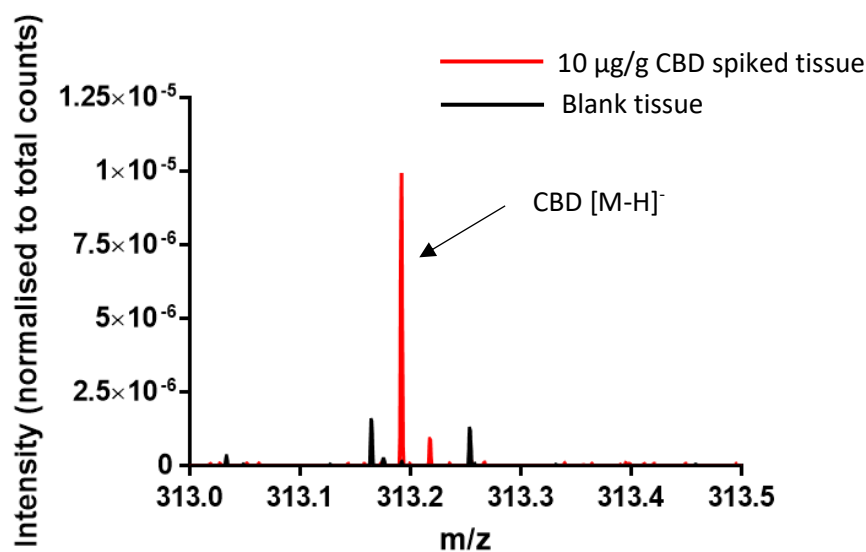


Figure 2.14. OrbiSIMS spectra of blank MLN tissue homogenate (black) and MLN tissue homogenate spiked with 10 µg/g CBD (red). CBD can be clearly deciphered against the matrix of tissue homogenate.

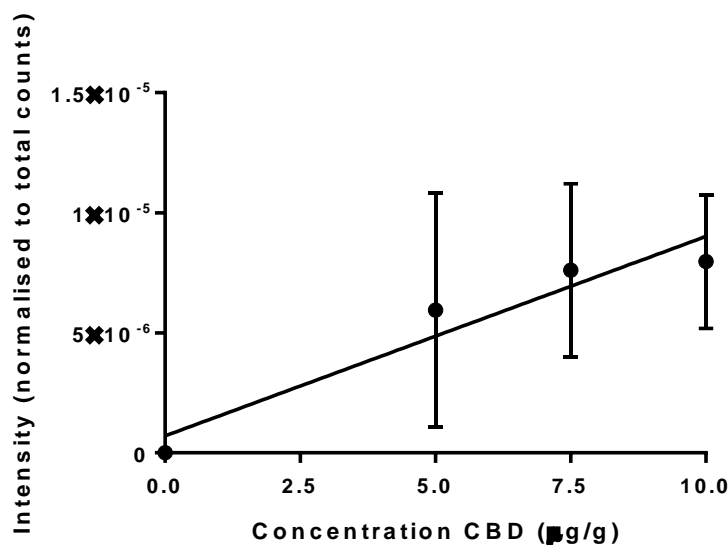


Figure 2.15. Calibration curve showing the intensity of the $[M-H]^-$ for CBD normalised to total counts spiked at various concentrations in homogenised MLN tissue using OrbiSIMS. Data is presented as mean \pm SD, $n=3$. $R^2 = 0.922$.

2.4.2.2. OrbiSIMS analysis of lymph node homogenates from dosed animals

OrbiSIMS analysis of homogenate samples from animals dosed with CBD showed that the CBD $[M-H]^-$ fragment could be detected in all 4 animals with good mass resolution. In addition, the intensity was significantly higher than for 10 $\mu\text{g/g}$ spiked homogenates, suggesting analysis of spiked homogenates represent an underestimate for CBD sensitivity (Figure 2.16). This may be the result of a sample preparation effect and correlated with CBD being clearly visible in an OrbiSIMS image of tissue homogenate from a treated animal (Figure 2.17).

It is important to note that solvent used for homogenisation of tissue was not the same in spiked homogenates and samples from animals. Although there is no reason to hypothesise that either solvent should have a matrix effect on the fragments since theoretically both are removed through the drying process as part

of sample preparation and under vacuum conditions, samples should not be directly compared. Future work with homogenate systems should therefore be homogenised in water to better mimic samples acquired from dosed animals. In addition, the animals dosed with CBD were also dosed with a linoleic acid vehicle. The animals from which tissue homogenates spiked with CBD were obtained were not fasted, however large amounts of linoleic acid in the lymph nodes from these animals are unlikely. Therefore, the tissue matrices are also not completely comparable. Despite these variables, the data in Figure 2.16 further supports the evidence that CBD should be detectable in sectioned tissue from animals dosed orally with CBD.

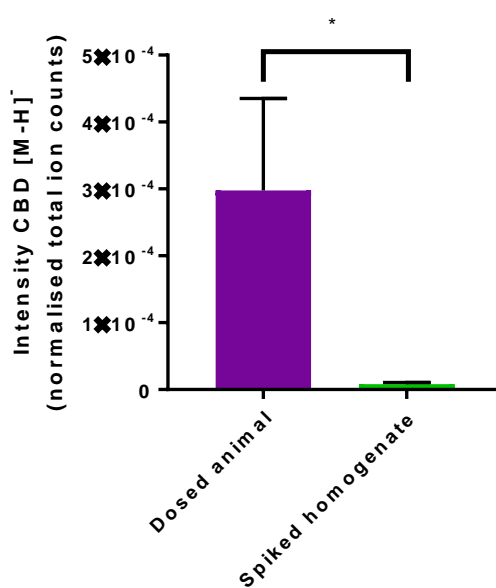


Figure 2.16. Relative intensities of the CBD [M-1]⁻ fragment in homogenates from dosed animals and homogenates spiked with 10 µg/g CBD. Error bars represent mean +/- SD. For dosed animals n represents samples from 4 separate animals and for spiked homogenates n represents 3 spiked systems. *Statistically significant, unpaired two-tailed t-test, p < 0.05.

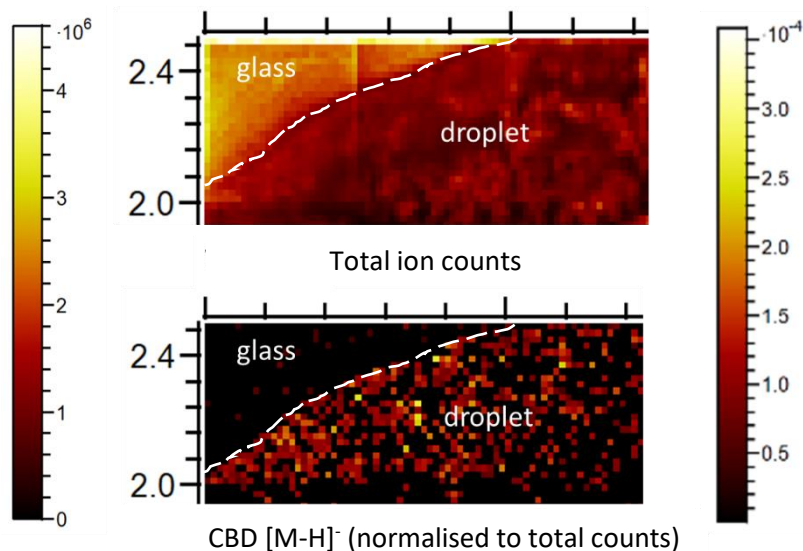


Figure 2.17. OrbiSIMS Image of droplet of MLN tissue homogenate from an animal dosed with CBD. The periphery of the homogenate droplet is indicated by a dashed white line.

A number of CBD fragments identified using static ToF-SIMS analysis of CBD powder were also present in OrbiSIMS analysis of homogenates from treated animals (Table 2.2). Fragments at m/z 205, 229 and 245 were however absent in homogenate samples. There was a highly abundant peak at m/z 269 in tissue homogenates which was initially thought to be related to CBD. However, based on its very high abundance compared to other CBD related ions, it was hypothesised that this species may actually be an interfering peak. Margaric acid is a fatty acid with an $[M-H]^-$ fragment at $C_{17}H_{33}O_2^-$, and is the likely cause, since lipids are also likely to be highly abundant in these samples. The low deviation also provides confidence in this assignment. A fragment at m/z 264 was also highly abundant and this should be monitored alongside the $[M-H]^-$ species in future analysis of sectioned lymph nodes from CBD dosed animals.

Table 2.2. CBD fragments and their relative abundance in tissue homogenates from CBD dosed animals in the negative mode analysed by OrbiSIMS.

m/z	Intensity (normalised to total counts)	Relative abundance (%)
107.0503	1.21E-04	0.68
129.0291	6.00E-06	0.03
137.0972	1.08E-05	0.06
171.1027	2.70E-06	0.02
173.0971	9.22E-06	0.05
179.1078	4.38E-05	0.25
183.1390	8.26E-05	0.47
191.0575	1.40E-06	0.01
201.1124	3.58E-04	2.02
205.1962	4.58E-07	0.00
229.1234	4.03E-07	0.00
245.1171	0.00E+00	0.00
264.7154	1.67E-03	9.39
269.2492	1.52E-02	85.48
277.2181	9.51E-05	0.54
295.2279	7.17E-05	0.40
311.2019	1.08E-04	0.61
313.2176	1.21E-04	0.68

2.4.2.3 Impact of analysis temperature

As mentioned, a decrease in the abundance of CBD fragments was observed whilst samples were held in the main chamber for analysis. Previous reports have described the undesired migration of semi volatile analytes such as cholesterol to the sample surface at room temperature that was prevented under cryogenic conditions [239, 257]. It was hypothesised that at ambient temperatures the vapour pressure for CBD had been exceeded [258] resulting in migration and ultimately sublimation of CBD from the sample. The abundance of CBD in samples was therefore analysed at room temperature and under cryo conditions. To also

compare what effect dehydration had on the abundance of these samples, a comparison with samples that were dried prior to cryo analysis was included. Figure 2.17 demonstrates that when analysed as soon as the vacuum in the main chamber is achieved, CBD intensity is highest in samples at room temperature. In addition, intensity was lowest when analysed under cryo-hydrated conditions. One reason for this may be that in the presence of water, the sample is essentially more dilute, resulting in less tissue material being collected. Interestingly, although higher than the cryo hydrated sample, CBD was less abundant in cryo dried samples compared to RT dried samples. It was hypothesised that, as was described with cholesterol [239, 257] this is also a result of CBD migration towards the surface of the sample. Cholesterol sulphate appeared to behave similarly to CBD. However, interestingly, the increase in intensity at RT was not consistent for all biomolecules, as adenine was most abundant in samples analysed under cryo-hydrated conditions. In addition, Serine was more abundant under cryo dried conditions. Total ion count was also comparable at room temperature and cryo-conditions for dried samples (Figure 2.18). However, since determination of CBD distribution was the ultimately the main goal of this work, it was decided that imaging of sectioned tissue should be performed under cryo conditions following drying.

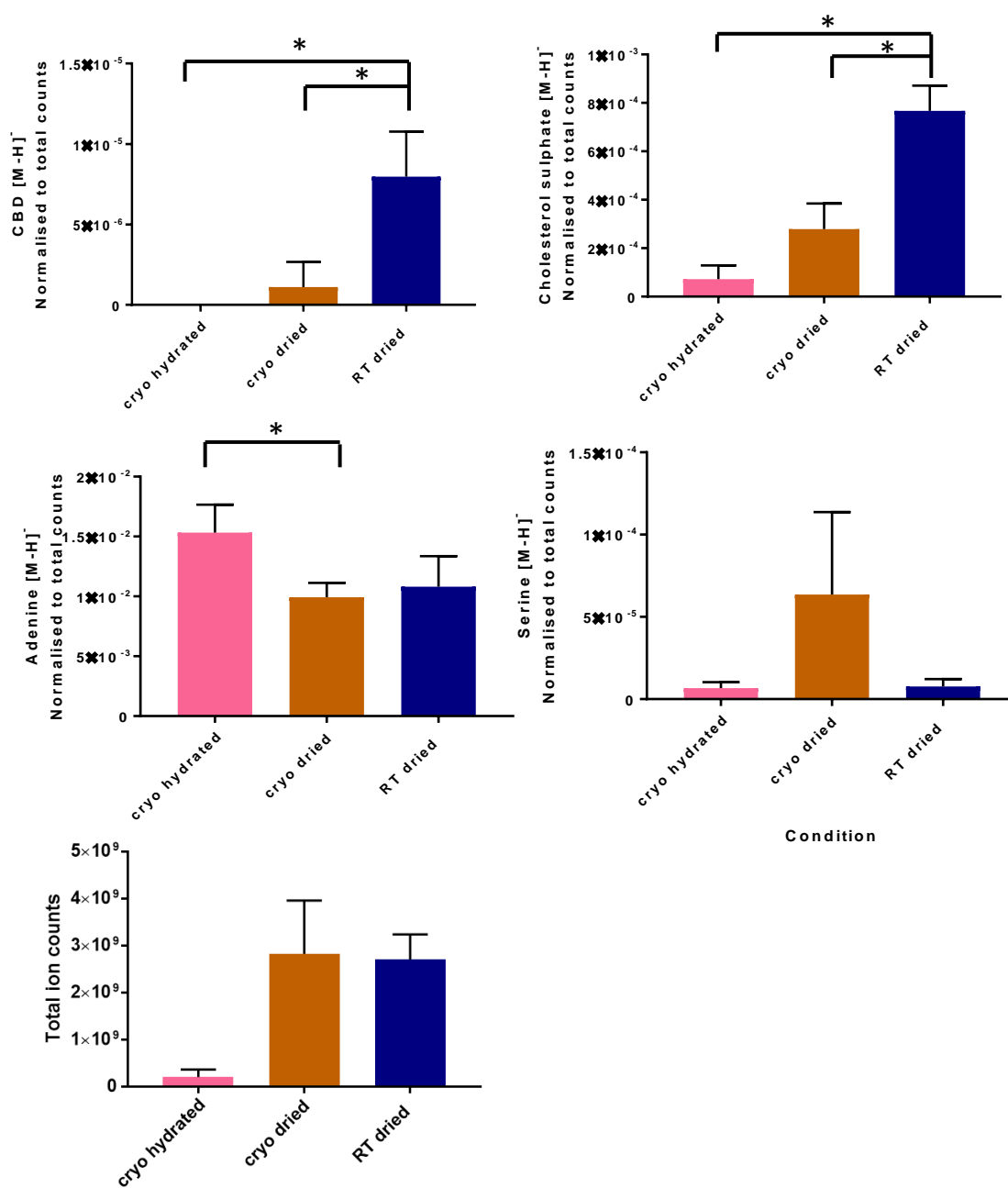


Figure 2.18. Average peak intensities for samples analysed under different conditions. Data is displayed as mean \pm SD. n=4 *statistically significant p < 0.05.

One- way ANOVA, with Tukey's multiple comparisons test.

2.4.3 Optimising tissue sectioning

Having optimised instrumental parameters, the final method development step was to ensure tissue integrity when sectioning. Paraffin embedding is commonly used in histology to support tissue to prevent tearing and damage during sectioning. However, as previously mentioned (Section 2.1) it was shown that it can result in contamination and the need to wash with hexane can affect the integrity of the tissue, especially to lipid species [238]. Based on this, optimal cutting temperature (OCT), an inert polymer based support medium was used. In addition, snap or flash freezing of samples using liquid nitrogen or isopentane has been described as a way of freezing samples at a fast rate to prevent the formation of ice crystals which impact tissue integrity [259]. Despite this, Figure 2.19 shows the integrity of tissue was worse when tissues were snap frozen compared to slow frozen at -20 °C. For this reason, sectioned tissues were slow frozen prior to analysis.

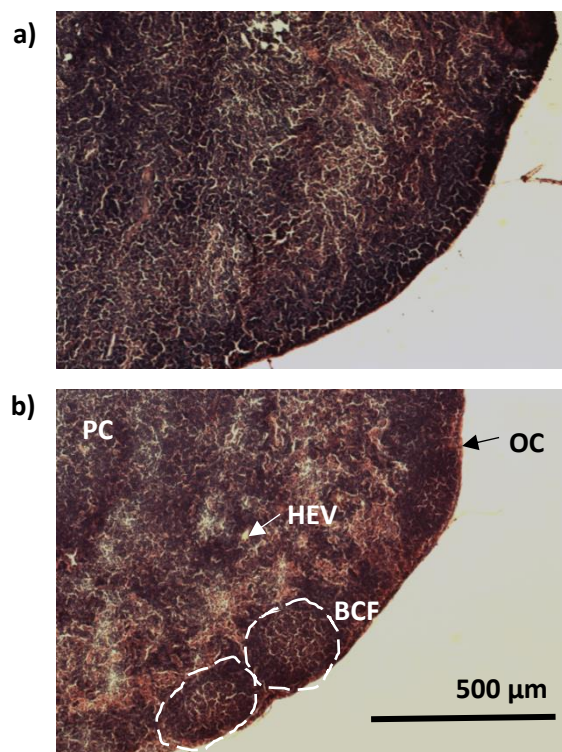


Figure 2.19. 5x magnification light microscope images showing a comparison of the integrity of sectioned MLN following different methods of freezing following H&E staining. Samples were frozen using a) liquid isopentane, b) freezing at -20 °C. Some of the major cellular regions can be deciphered in b) and are indicated; P, paracortex; HEV, high endothelial venule; BCF, B-cell follicle; OC, outer cortex.

2.5. Conclusions

This chapter describes the development of a MSI method that can be applied for the determination of CBD distribution in sectioned MLN tissue. Initial work using a conventional ToF-SIMS instrument and LMIG analysis beam demonstrated that static SIMS provided insufficient sensitivity and mass resolution to detect CBD against the matrix of homogenised MLN tissue. Use of a dynamic SIMS approach allowed for the detection of CBD in homogenates, however sufficient mass resolution or sensitivity at *in vivo* relevant concentrations was not

achieved. This was not improved by exposure to reactive vapour. Correspondingly, CBD could not be detected in sections of lymph node from animals dosed with CBD using LMIG analysis. Based on this, LMIG analysis using conventional ToF-SIMS was deemed inappropriate for the imaging of CBD in lymph node tissue.

As predicted, both mass resolution and sensitivity were superior using a hybrid OrbiSIMS instrument and GCIB analysis beam, compared to ToF-SIMS and LMIG analysis beam. Furthermore, a major finding was that using OrbiSIMS, the molecular ion for CBD in the negative mode, as well as a number of fragment species of CBD, could be resolved at *in vivo* relevant concentrations. However, at lower concentrations reported *in vivo*, (5 – 10 µg/g) large variability in abundance of these ions was observed. As a way of confirming the sensitivity of the developed method, a spot of MLN homogenate from a dosed animal was also imaged and showed CBD was consistently detectable and at higher intensity than predicted using 10 µg/g CBD spiked homogenate. This work therefore represents the lowest concentrations of drug in tissue samples detection using a SIMS method.

The impact of analysis temperature on the detection of CBD was also compared and it was demonstrated that RT analysis results in the highest intensity of $[M-H]^-$. Longitudinal analysis showed reduction in CBD detection over time the reasons for which are sublimation under ultra-high vacuum conditions. Under cryo conditions, dried samples resulted in a better yield of CBD compared to hydrated samples, which is likely due to a dilution of molecules of interest in hydrated samples. For this reason, it was concluded that analysis of sectioned tissue should be performed under cryo conditions. In conclusion, the developed OrbiSIMS method can now be applied to image the distribution of CBD in sections of lymph nodes from orally dosed animals as part of subsequent work. This work also

highlights the potential of OrbiSIMS technology for the analysis of drug in tissue following non-topical administration.

3. Distribution of cannabidiol and other lipophilic molecules within intestinal lymph nodes

3.1. Introduction

Lymph nodes contain well described, distinct cellular regions (section 1.1.1.4.1.). A number of drugs, including Cannabidiol (CBD), can be targeted to the mesenteric lymph nodes (MLN) following oral delivery (section 1.3.1.). However, the distribution of these compounds, within the lymph node structure remains unclear. Subsequently, little is known about the way in which pharmaceutical components interact with different classes of cells within lymph nodes, knowledge of which could have major implications in drug design.

There have been few attempts to image drug distribution in lymph nodes. In one example, a model fluorescent prodrug of the immunomodulatory compound, mycophenolic acid was shown to accumulate in both the cortex and paracortex of MLN at 5 and 10 hours after oral delivery [260]. However, one major drawback of this work, as with any fluorescent label, is that there can be no guarantee that the distribution of the fluorescently labelled prodrug is representative of the drug itself.

Infrared matrix-assisted laser desorption electrospray ionization (IR-MALDESI) imaging has been used to image the distribution of several antiretrovirals (ARV) within lymph nodes following oral delivery [261, 262]. In one example, two orally administered ARV drugs were imaged in MLN following 8 to 10 days' treatment and were shown to have widespread distribution across the node, despite one drug being present in low abundance. In addition, complementary methods were successfully used to demonstrate that HIV reservoirs within the

lymph were poorly exposed to these ARV [261]. However, how drugs distribute in MLN following targeted lymphatic transport, and how distribution compares for different drugs remains unclear.

ToF-SIMS imaging has previously been used to demonstrate the distribution of drug in tissues. However, the only examples have been following topical delivery or direct injection, where concentrations are high (50 – 100 mg/ml) [172, 176, 177]. OrbiSIMS has a number of advantages over ToF-SIMS for biological sample analysis [181] (section 2.4.2.1.). To date only one example of the tissue imaging capabilities of OrbiSIMS has been described. Different anatomical regions of sectioned brain tissue could be distinguished through imaging the distribution of various lipid species [170]. The suitability of OrbiSIMS for the determination of drug distribution in tissues is yet to be determined.

In addition to the understanding of drug distribution, little is known about the innate chemistry of lymph node tissue. By determining the distribution of innate biomolecules within lymph node tissue, Pharmacodynamic changes to these molecules as well as the synthesis and release of additional molecules can, in theory, be identified. Some attempts have been made to identify pathophysiological changes in lymphoid tissue using SIMS imaging. These include studies of cancer [263, 264] and infection [265, 266]. Lymph nodes are largely populated by immune cells, although few examples of immune cell analysis with SIMS exist. In one of the few examples of mass-spectrometry analysis of tissue-resident immune cells, MALDI mass spectra differed among immune cells and these species could be localised to sections of lymph nodes in human colon tissue [267]. But, mass resolving power was poor, meaning no peak assignments could be made. Spatial resolution was also insufficient to localise different immune cell types within the lymph node structure. Subsequently, a label-free method for the simultaneous

imaging of drug molecules, native tissue molecules and detectable markers of drug induced pharmacodynamic changes to tissue chemistry are needed.

3.2. Chapter aims and objectives

The primary aim of this chapter is to determine the distribution of CBD in sectioned lymph nodes following oral delivery using the OrbiSIMS method described in Chapter 2. Using this method, the suitability of OrbiSIMS for a number of other aims can also be assessed. Specific objectives include:

- Exploratory characterisation of the innate chemical composition of lymph node tissue including identification of any markers of the distinct cellular regions. These include the T-cell rich paracortex and peripheral B-cell follicles.
- Determination of the distribution of a model drug of interest, CBD, in sectioned MLN tissue following oral delivery.
- Determination of the distribution of components of the lipid-based formulation in which CBD was administered, in sectioned MLN tissue following oral delivery.
- Determination of any chemical markers of pharmacodynamic changes in innate tissue chemistry as a result of CBD or formulation delivery.

3.3. Materials and methods

3.3.1. Sectioned MLN tissue

3.3.1.1. Materials

As described in Chapter 2 (section 2.3.1), plant-derived CBD was purchased from THC Pharm GmbH (Frankfurt, Germany). Sesame oil was purchased from

Sigma Aldrich (Gillingham, UK). All other solvents and reagents were of HPLC grade and were purchased from Fisher Scientific (Loughborough, UK).

3.3.1.2. *Animals*

Sections of MLN tissue for the determination of CBD distribution following oral delivery were acquired from animals dosed orally with CBD via a sesame oil vehicle (n=3 nodes from 3 animals). Details of the animals, husbandry and maintenance for the studies in this chapter are as described in Chapter 2, section 2.3.2. and 2.3.3. Following 5 days of acclimatisation, rats were fasted overnight with free access to water. CBD in sesame oil was administered via oral gavage (12mg/ml, 12mg/kg) as previously described [7]. Animals were euthanized by CO₂ asphyxiation two hours post dosing, one hour prior to t_{max} and MLN collected. One lymph node from an animal not dosed or fasted was also acquired as a control against which the samples from dosed animals could be compared. A total of 4 nodes were therefore analysed.

3.3.1.3. *Tissue collection and handling*

Tissues were collected, sectioned and stored prior to imaging using the method described in Chapter 2 section 2.3.3.6. For the purposes of determining basic tissue histology, H&E stained images were acquired using the method also described in section 2.3.3.6. For each node approximately 10 sections were acquired and the most integral sample selected for analysis.

3.3.2. Analytical methods

The OrbiSIMS method used in this chapter to image sectioned MLN was described in detail in section 2.3.4.2. Briefly, all data was acquired using an Ar₃₀₀₀⁺ 20keV analysis beam. Ion images containing 409600 pixels were acquired over an

area of 2500 μm x 2500 μm (pixel size 20 μm). The patch FoV was 500 μm , collected in a random raster mode. The Orbitrap analyser was operated in negative mode at the 240,000 at m/z 200 mass resolution setting as previously described [170]. Mass spectra was collected for a mass range of 75-1125. The main chamber was maintained at approximately -140 °C and 9.0E-07 mbar throughout analysis and the total ion image - acquisition time was approximately 2 hours and 10 minutes.

3.3.2.1. *Multivariate analysis*

In samples of sectioned tissue, the presence, abundance and distribution of a number of secondary ions peaks of interest were assessed. These include secondary ions known to be associated with CBD (Table 2.2) and ions assigned as elements of formulation derived chylomicrons. A typical OrbiSIMS spectra from biological sample analysis contains hundreds of thousands of peaks. Manual assessment of all these secondary ion peaks was therefore not feasible. Multivariate analysis (MVA) is a statistical tool can be used to find patterns and relationships in data containing several interdependent simultaneously measured variables. MVA can therefore be used to elucidate the degree of variation between sample types and the identity of the secondary ions which contribute most to this variation. Although no published examples of an OrbiSIMS dataset exist yet, MVA has become a commonly used tool for the assessment of ToF-SIMS data [268].

In this instance, MVA was utilised to identify the secondary ions which differed between the major cellular regions of lymph nodes. These could then in theory be used as markers of these regions. In addition, comparisons of these regions in sections from animals dosed with CBD and animals not dosed were made. This information can subsequently be used to identify any additional markers of CBD distribution or potential markers of CBD induced pharmacodynamic effects.

Principal component analysis (PCA) is one of the most commonly used MVA methods for SIMS data. The principles of PCA are described in depth elsewhere [269]. In short, the data set, which for SIMS is the spectra, is defined as the matrix. Within the matrix, the rows contain different samples and the columns contain variables. For SIMS, the variables are measured intensities of species with varying m/z values. PCA is an axis rotation that aligns each set of axes, or principal components (PCs) with the maximal directions of variance within a data set. PCA then generates the scores and the loadings, which taken together can then be used as a summary to describe the original data set and therefore aid data interpretation. More specifically, the score plot is used to indicate the projection of the data point on the given principal component axes. The loadings highlight which variables, or ions, are responsible for the separation between samples as highlighted in the scores plot. The variables furthest away from the plot origin are described as the most significant contributors to the variance.

As part of this chapter, all PCA was performed using *simsMVA* (version 2, Gustavo Trindade Ph.D., University of Surrey, UK) [270] which operates using MATLAB (Mathworks, Natick, USA). Regions of interest (ROI) were drawn using the *polyline* function within *SurfaceLab 7*, avoiding any areas of tissue damage as indicated by the presence of markers of OCT or glass. To account for the higher yield of smaller fragments, the spectra from each total image was divided into 3 regions from m/z 75-300, 300-700 and 700-1125. An automatic secondary ion peak search was performed at each mass range and approximately the same number of secondary peaks from each region were combined to form one peak list. The intensities for each secondary ion peak in the list were then determined for each region of interest after being normalised to the total counts in the ROI respectively. Data were pre-processed by Poisson scaling and mean centring before PCA.

3.3.3. Determination of tissue matrix effects

A comparison of the matrix effects of underlying sectioned MLN tissue regions on the ionisation efficiency of CBD were assessed. The absence of any matrix effects would imply that any differences in distribution of CBD across tissue sections was not an analytical artefact but instead a true reflection of differences in distribution throughout the lymph node.

3.3.3.1. Tissue preparation

For the determination of matrix effects, sections of MLN were prepared from animals not dosed or fasted. As with samples generated for the purposes of imaging, lymph node tissues were dissected and sectioned as per Chapter 2 section 2.3.3.6.

3.3.3.2. Matrix application

Theoretically, if the matrix effect of different regions of tissue is identical, then the ionisation and detectable abundance of a molecule, present at the same concentration should also be identical. To assess this, an even distribution of CBD was applied to the surface of the sample. This was achieved using a NexDep PVD coater and performed by a colleague (Wenshi He). Samples were loaded into the coater sample holder which was kept at a constant temperature of 10 °C. CBD deposition was carried out in a sequential manner using two coaters and the sample holder was also rotated at 30 rpm to improve the uniformity of material deposition. Six layers of CBD were deposited at a concentration of 0.02 mg/ml CBD in 60% ethanol, 20 z/mm, spray speed 800 mm/min, flow rate 10 µl/min and line distance 2 mm. The final deposition of CBD was 0.75 µg/mm². Deposition rates

were monitored via Quartz crystal microbalance (QCM) sensors inside the coating chamber.

3.3.3.4. Analysis

As previously described (section 1.1.3.2), lymph node tissues can be crudely divided into a central paracortex and periphery containing B-cell follicles. Analysis was performed at varying locations across the lymph node and the intensity of CBD compared at locations on the periphery and at the centre of the node respectively. The analysis parameters using OrbiSIMS are as described in section 2.3.4.2, with a 200 μm x 200 μm FoV size. For the purposes of this analysis, 6 locations in the centre of the node and 6 locations around the periphery of the node were compared across 2 nodes.

3.4. Results and Discussion

3.4.1. Characterisation of innate lymph node tissue using OrbiSIMS imaging

3.4.1.1. Tissue imaging

All lymph nodes are comprised of the same functional units called lobules. However the number of lobules in each node can vary (section 1.1.3.2). In addition, the specific phenotypes of specific cellular populations within different lymph nodes is likely to differ based on the pathogenic environment they are exposed to [19, 20]. The initial aim of this chapter was to provide a preliminary understanding of the distribution of native biomolecules within sections of lymph node tissue. The

reproducibility of imaging between sections from the same node and between different lymph nodes could later be assessed.

A preliminary and exploratory assessment of the capabilities of OrbiSIMS for imaging sectioned MLN tissue was assessed using 2 sections of tissue from a single lymph node taken from an animal not dosed with CBD (Figure 3.1.). An initial observation was that the total ion count for both sections appeared variable across the images (Figure 3.1). This was likely a result of differences in charge compensation across the tissue. However, to account for differences in total ion count across the image, in subsequent images of specific ions of interest, each pixel was normalised to total ion count. Analysis of section 1 was stopped prior to completion, due to a software error. Despite this the majority of the node could be visualised.

H&E images of corresponding sections were also acquired (Figure 3.1.). A densely stained region in the centre of each section corresponding with the T-cell rich paracortex could be observed. In addition, several darker stained round structures could be observed around the periphery of the node, likely to be B-cell follicles.

By assessing the mass spectrum, a highly abundant secondary ion peak could be observed at 885.55 in both sections. This could be assigned as the $[M-H]^-$ species of phosphatidylinositol 38:4 ($C_{47}H_{82}O_{13}P^-$) (deviation 1.1ppm). The abundance of this secondary ion is not surprising since phosphatidylinositols are key constituents in cell membranes and essential metabolic processes in all cells. The tissue perimeter could be identified by overlaying images of phosphatidylinositol 38:4 with makers for glass (m/z 136.94, $Si_2O_5H^-$, deviation 0.7 ppm) and OCT (m/z 105.06 $C_4H_9O_3^-$, deviation 0.2 ppm) (Figure 3.1). No major tears or damage was evident in the tissue.

Interestingly, it was observed that phosphatidylinositol appeared to be distributed more abundantly in a localised region on the periphery on one of the sections (Figure 3.1). However, since this distribution of the phosphatidylinositol species was not mirrored in both sections, the biological significance of this is unclear. As demonstrated in Figure 3.2, several highly abundant secondary ion peaks present in the sectioned tissue appeared to have non-uniform distribution within sections. These included secondary ions at m/z 465.30 (assigned as cholesterol sulphate, $C_{27}H_{45}SO_4^-$, deviation 0.3 ppm) m/z 241.01 (assigned as Phosphoinositide head group, $C_6H_{10}PO_8^-$, deviation 0.8 ppm), and m/z 107.04 (assigned as diaminomaleonitrile $C_4H_3N_4^-$, deviation 0.8 ppm) (Figure 3.2.). Cholesterol sulphate and Phosphoinositol are both components of cell membranes which previously have been shown to have non-uniform distribution following SIMS analysis in skin [173] and brain sections respectively [170]. It is not clear why diaminomaleonitrile was present in high abundance but it possibly a fragment of a larger molecule. Moreover, distribution of these secondary ions differ to each other, suggesting differing chemistries of the tissue. Although the biological rationale for the differences in distribution observed is not clear, differing underlying chemistries of regions of lymph node tissue may indicate a difference in matrix effects. An assessment of matrix effects of the ionisation and detection of CBD in different regions of lymph node tissue are described in section 3.4.4.

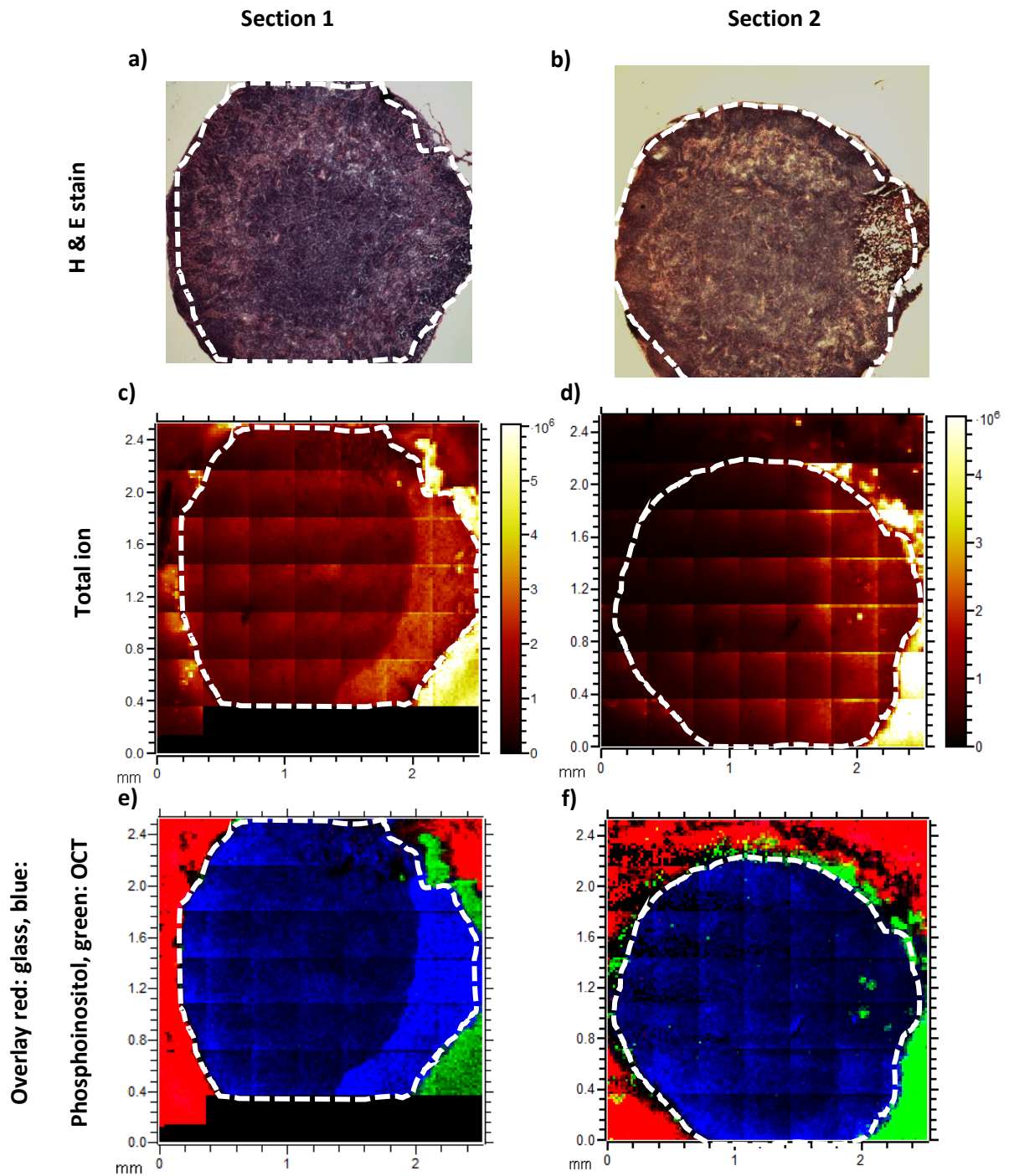


Figure 3.1. H&E stained images from a) Section 1 and b) Section 2 of MLN tissue.

OrbiSIMS images showing total ion for c) Section 1 and d) Section 2, and overlays

of $\text{Si}_2\text{O}_5\text{H}^-$, (red), $\text{C}_4\text{H}_9\text{O}_3^-$ (green) and $\text{C}_{47}\text{H}_{82}\text{O}_{13}\text{P}^-$ (blue) for e) Section 1 and f)

Section 2. The 2 sections were generated from the same lymph node. The

periphery of the tissue is indicated by a white dashed line.

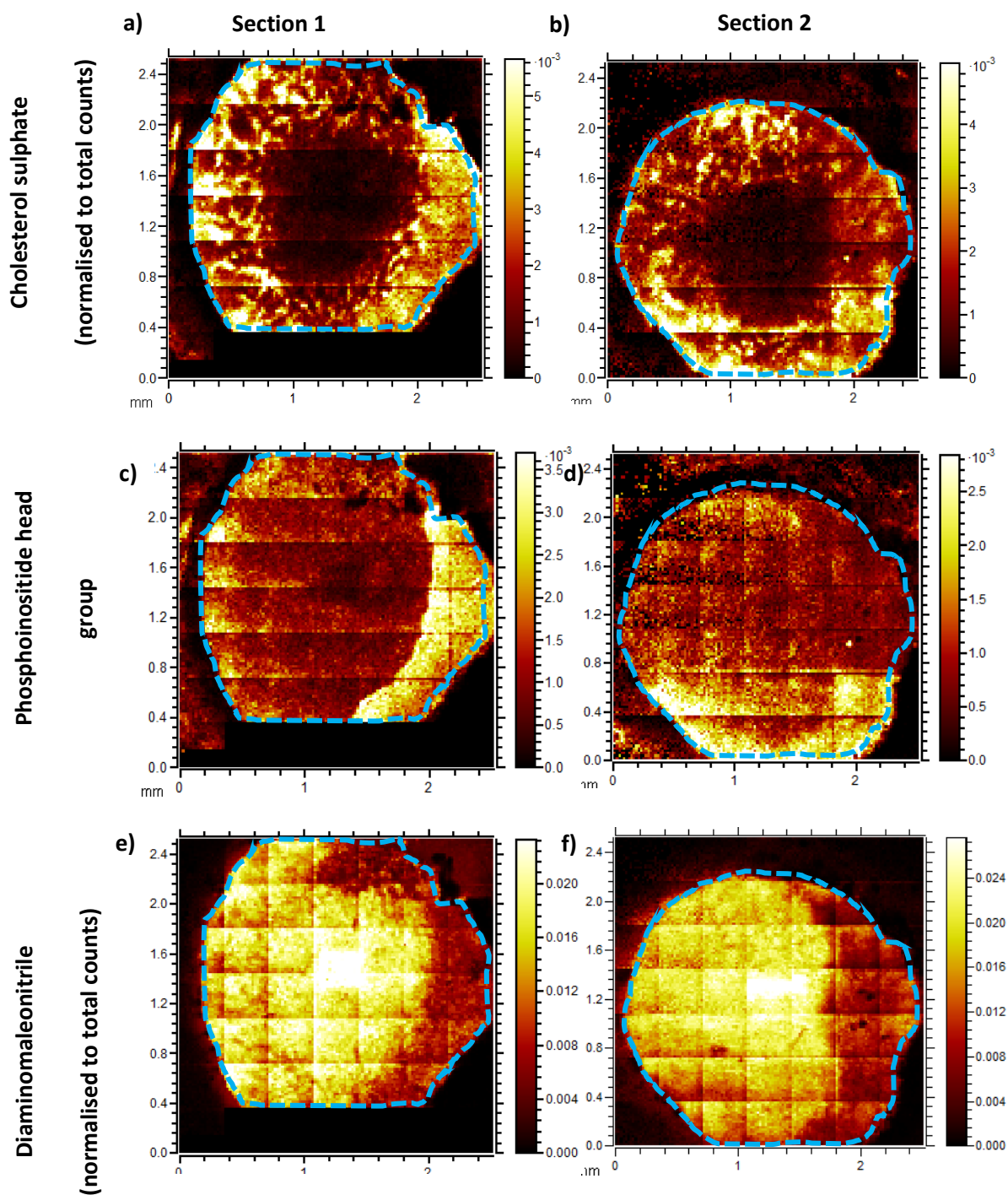


Figure 3.2. OrbiSIMS images showing the spatial distribution of a) and b) Cholesterol sulphate $C_{27}H_{45}SO_4^-$, c) and d) Phosphoinositide head group $C_6H_{10}PO_8^-$ and e) and f) Diaminomaleonitrile $C_4H_3N_4^-$ in 2 sections of MLN tissue respectively. The sections imaged are the same as that in Figure 3.1. The periphery of the tissue is indicated by a blue dashed line.

3.4.1.2. *Defining cellular regions*

Cells of the lymph node are most commonly identified and differentiated by the presence, or absence, of different receptors on the cell surface, for example using immunohistochemistry [271]. However, receptors, including the T-cell co-receptor, CD3 are large G-protein coupled receptors, which cannot currently be identified intact through SIMS. The identification of smaller immune cell markers poses a number of challenges. For example, cells are heterogeneous and chemically diverse and cellular metabolites undergo high dynamic fluctuations. Species such as cytokines, which are secreted by different immune cells, are present at extremely low concentrations and are themselves small proteins which cannot be identified intact. Despite this, some markers of cytokines have been identified by mass spectrometry [272-275]. Imaging of cytokines in tissues is yet to be undertaken. There are very few examples of tissue resident immune cell imaging using mass spectrometry. PCA was previously shown to differentiate different groups of B-cells following isolation from bone marrow [276]. However, many of the secondary ion peaks identified are related to a number of biomolecular macromolecules including phosphocholine, fatty acids and amino acids making them individually non-distinct.

The aim of this highly exploratory work was to determine if OrbiSIMS imaging could be used to identify novel markers of different lymph node cellular regions. PCA was used to identify species, of which the distribution corresponds with the different cellular regions identified in H&E stained sections. These could then be used as markers of these regions in subsequent images. The distribution of specific species of interest, including those related to CBD, could then be compared to that of these markers of cellular distribution. 4 regions of interest were drawn in

the centre of the node, corresponding to the T-cell rich paracortex and 4 were drawn around the periphery of the node corresponding to the B-cell follicles. Although subjective, the drawing of regions of interest (ROI) to be compared by PCA was informed by the differing chemistries observed in Figure 3.2. and by corresponding H&E images, which indicated the boundaries of the cellular regions.

ROIs drawn for the purposes of PCA are shown in Figure 3.3. The secondary ion peak list generated contained a total of 988 secondary peaks, with 317 secondary peaks from m/z 75-300, 331 secondary peaks from m/z 300-700 and 338 secondary ion peaks from m/z 700-1125. Relatively high intensity secondary ions at m/z 79.96 (PO_3H) and 78.96 (PO_3) were removed prior to PCA as it was believed they would dominate PCA and be responsible for the main variability thus dissembling any other variables.

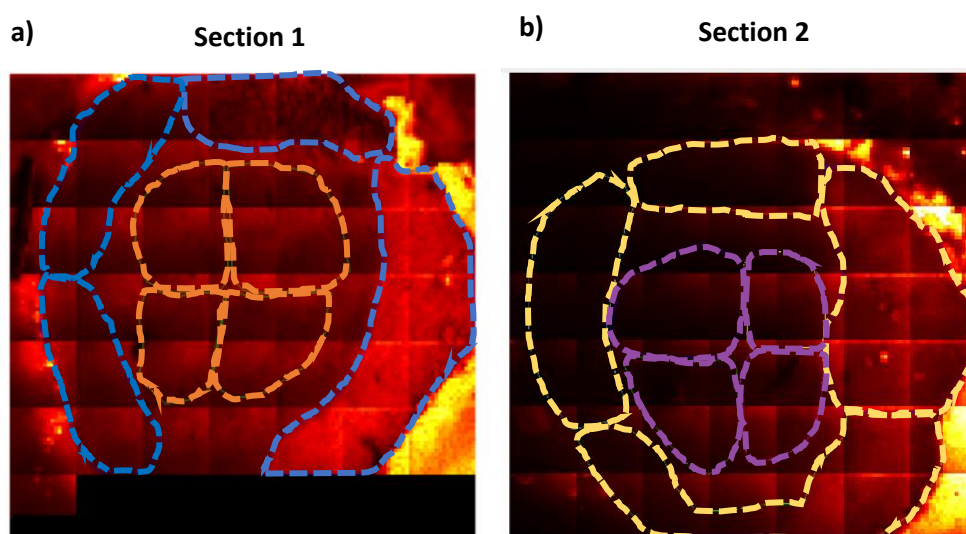


Figure 3.3. Total ion count OrbiSIMS image showing the selected ROI compared by PCA for a) Section 1 and b) Section 2. The sections shown are the same as that in

Figure 3.1. and Figure 3.2.

PC1 was responsible for 69.82% of the variance and most efficiently described differences in peripheral B-cell regions and central T-cell regions in the 2 sections from the animal not dosed, as demonstrated by the scores plot shown in Figure 3.4. Despite this not all B- and T-cell regions were well separated using this component. However, other components did not separate the different ROIs of interest clearly.

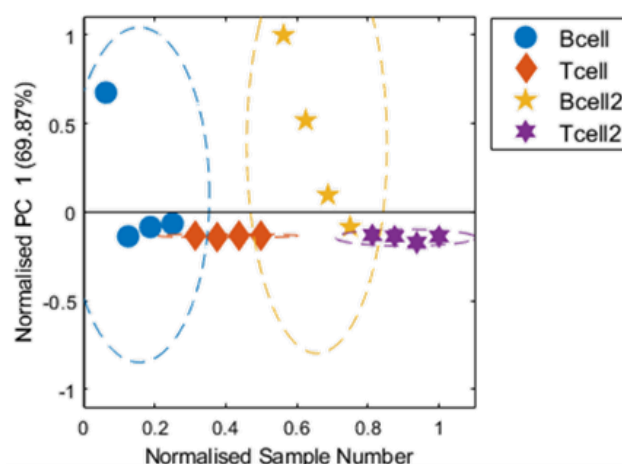


Figure 3.4. Scores plot for PC 1 generated from ROIs of sectioned lymph nodes tissue. The colours of the ROIs correspond with those in Figure 3.3.

Variation between ROIs was largely described by the presence of secondary ions at m/z 279.23, 281.25 and 255.23 which can be assigned as the $[M-H]^-$ species for the fatty acids linoleic, oleic and palmitic acids respectively. Fatty acids are highly ionisable and their distribution has previously been described in a number of tissues using SIMS [173, 174, 277, 278]. The distribution of fatty acids is shown and discussed in more detail in section 3.4.3.1, however in brief, the fatty acids in PC1 (Figure 3.5) were all highly abundant in the ROI located on the right-hand side periphery. The same region also showed different distribution of other secondary ions relative to the rest of the node (Figure 3.2). The reason for distinct chemistry in this peripheral region is unclear. Although efforts were made to keep tissue

orientation consistent, one hypothesis may be an inconsistency in orientation between nodes during sectioning. Subsequently this region may in fact not only contain B-cell follicles, as in the rest of the periphery, but a high proportion of medullary venules draining lipid rich lymph out of the node (see Chapter 1, Section 1.1.1.4.1, Figure 1.1). Alternatively, a region in the periphery of the node with distinct chemistry could correlate with an abnormality such as a reactive hyperplastic lesion, which are common in rodent mesenteric nodes as a result of antigenic stimulation [92].

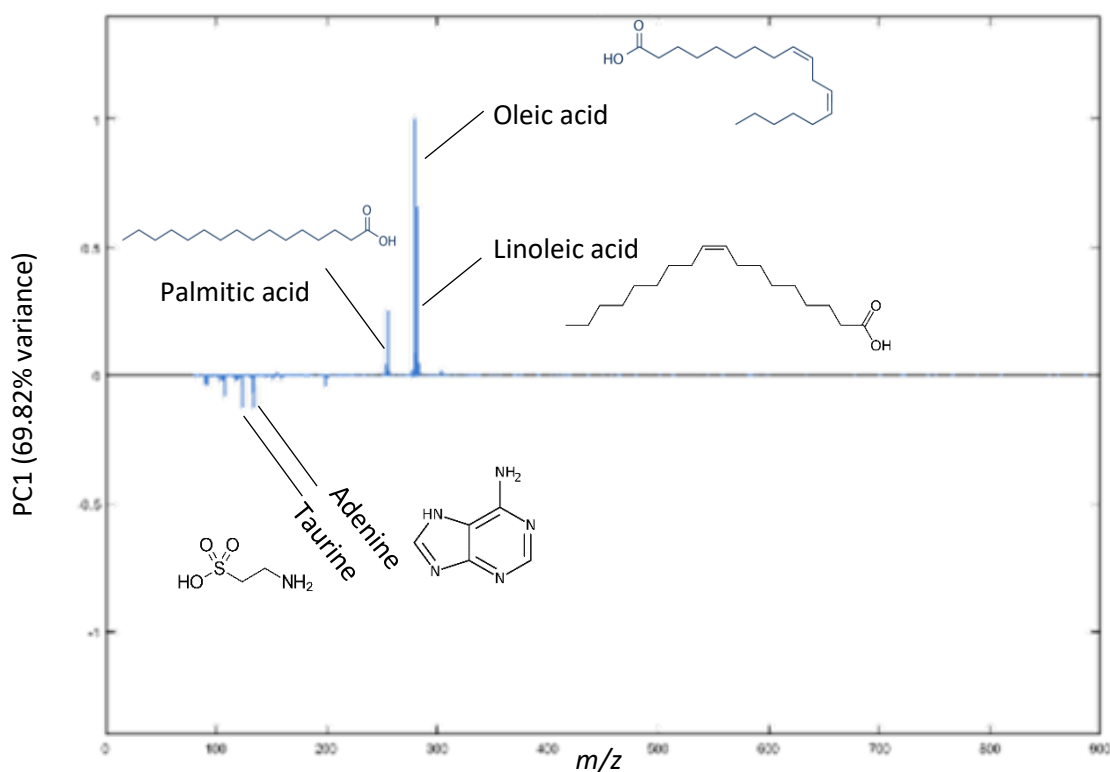


Figure 3.5. Loadings plot for PC 1 generated from PCA of ROIs from sectioned lymph node tissue. The loadings plot corresponds to the score plot in figure 3.4 and ROIs in Figure 3.3.

Secondary ions at m/z 124.01 and 134.05 relating to the $[M-H]^-$ species of the amino acid taurine and the nucleobase adenine were present in the negative

loadings plot (Figure 3.5). This means these secondary ions were less abundant in the B-cell rich periphery. Although not obviously demonstrated in the secondary ions images of taurine in Figure 3.6, high abundance of taurine in T-cell regions would correlate with previous reports of taurine accumulation in these cells [279]. A comparison between the abundance of taurine in tissue resident T- and B-cell regions had not previously been made however. It should be noted taurine also appeared to be highly abundant in the area surrounding the node and although not clear why, this should not affect the analysis done since ROIs were only drawn within the node. Adenine appeared to be less abundant in the area of the periphery on the right-hand side of the node (Figure 3.6). Since adenine is a nuclear marker, this may be indicative of a region of tissue less densely populated with immune cells, which would support the previous hypothesis that this region contains medullary venules. A matrix effect from species more abundant in this region, such as lipids (Figure 3.2. and Figure 3.13) is also possible.

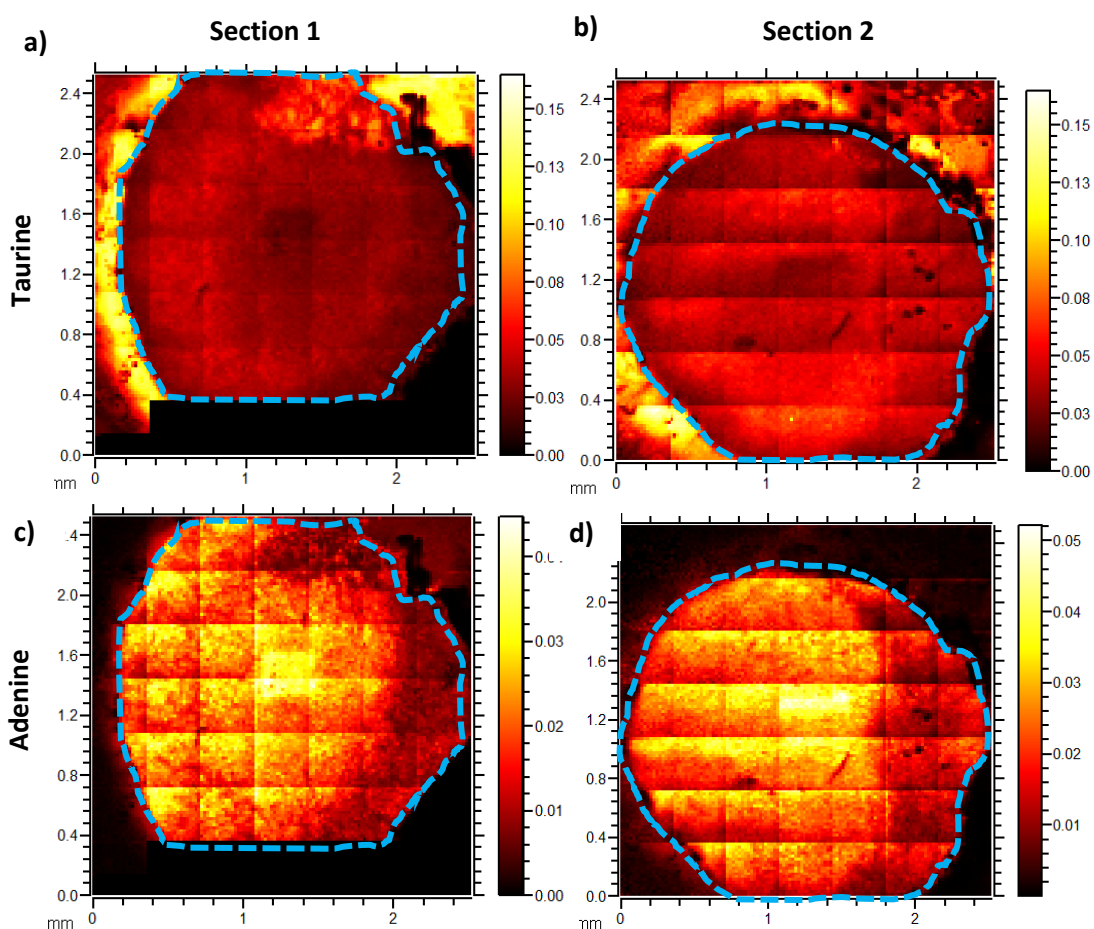


Figure 3.6. OrbiSIMS images showing the spatial distribution of a) and b) taurine, $C_2H_6NO_3S^-$, deviation -0.2 ppm; and c) and d) adenine, $C_5H_4N_5^-$, deviation 0.0 , in 2 sections of MLN respectively. The periphery of the tissue is indicated by a blue dashed line.

Using OrbiSIMS, this work has demonstrated an unsupervised examination of healthy native lymph node sections and provided a novel understanding of the chemical differences defining different regions of healthy lymph node. This knowledge was next applied in an attempt to identify any chemical differences in lymph node tissue resulting from CBD administration.

3.4.2. Imaging the distribution of CBD in sectioned lymph nodes

3.4.2.1. CBD distribution

Having provided some preliminary understanding of the distribution of innate lymph node tissue biomolecules, the imaging capabilities of OrbiSIMS for determination of CBD distribution was assessed. In total, 3 lymph nodes from animals dosed with CBD were analysed. To maximise consistency, all lymph nodes were collected from the apex of the mesenteric chain. Species relating to $\text{Si}_2\text{O}_5\text{H}^-$, $\text{C}_{47}\text{H}_{82}\text{O}_{13}\text{P}^-$ and $\text{C}_4\text{H}_9\text{O}_3^-$ were again used to identify the periphery of the tissue (Figure 3.7). Some damage in one of the sections was identified which was considered minor (Figure 3.7). Generally, the quality of the images for one of the sections was worse compared to the other images acquired (Figure 3.7.c) although it is not clear why.

Several of the CBD species identified in powdered CBD as part of work described in the previous chapter could be identified in sections from dosed animals (Table 3.1.). These included species at m/z 313, 311 and 245, which were also amongst some of those abundant in pure CBD powder (Table 2.1.). An ion at m/z 179 was in powdered CBD and highly abundant in samples from dosed animals. However this ion was largely absent in the tissue and present mainly in the surrounding area. The ion at m/z 179 was also present in the image of sectioned MLN from the animal not dosed and distributed similarly. Based on this, it was concluded that the fragment at m/z 179 was not related to CBD.

The distribution of CBD in sections of MLN is shown in Figure 3.7. The distribution was comparable for all CBD molecular species further indicating these are all fragments of the same parent molecule, CBD. Critically, in one OrbiSIMS image (Figure 3.7a.), species related to CBD were highly abundant and clearly

visible. Moreover, the distribution of CBD within the tissue appeared to be non-uniform. More specifically, CBD was highly abundant in the centre of the lymph node and largely absent around the periphery of the node. As discussed previously, the centre of the node, or paracortex, is dominated by densely packed, homogeneously distributed T-cells, which make up more than 95% of the cellular mass [280]. This is in contrast to the periphery which is populated by follicles of B-cells (see Introduction Chapter, section 1.1.3.2). This image would therefore suggest that the B-cell rich follicles of the lymph node are exposed to much lower concentrations of CBD compared to T-cells. Localisation of CBD to the paracortex of the node would contrast to previous work where orally administered drugs were shown to have widespread distribution across intestinal lymph nodes [118, 261]. It should be noted that from Figure 3.7. it would appear that a small signal, allocated to CBD, was positioned outside of the periphery of the tissue. The reason for this was unclear but may indicate either a contamination of CBD into the OCT during sectioning or more likely the presence of another molecule with a similar m/z which cannot be deciphered from CBD. This further highlights the need for repeat imaging in order to draw confident conclusions about CBD distribution.

Small molecule drugs such as CBD are likely to enter the conduits of the paracortex through gaps in lymphatic endothelial cells (LECs) [37, 44, 280]. Fibroblastic reticular cells (FRCs) line the conduits of the paracortex and have intercellular junctions which contain lymph-borne solutes in the conduit system and thus limit access to T-cells [37]. It has also been suggested that a lack of interstitium with the T-cell region contributes to excluding the majority of lymph soluble molecules from T-cells [280]. The specific characteristics required to access paracortex resident T-cells is not yet clear and there have been conflicting reports surrounding the ability of fluorescent tracers to escape the conduit system [41, 44,

118, 281-283]. However, a recent study using flow cytometry analysis of mesenteric lymph-node resident immune resident cells, including T-cells, showed association with an orally administered fluorescent probe [118].

Both cannabinoid receptors are found on most immune cells, with the expression levels of CB₂ 10–100 times greater than CB₁ [284-286]. Interestingly, both analysis of circulating immune cells and immunochemical staining of lymphoid tissues have indicated a higher expression of CB₂ receptor on B-cell containing follicles compared to T-cells [189, 287-289]. Paradoxically, previous work has suggested that CBD exerts its immunomodulatory effects *in vivo* primarily via T-cells through reduction of inflammatory cytokines [70, 217, 290, 291] which may highlight the role of receptor independent mechanisms [292]. In addition to FRCs, up to 5% of conduit is lined by hematopoietic cells, such as dendritic cells (DCs), which are believed to be involved in sampling the contents of the conduit for soluble antigens and extracellular signalling molecules [44, 293]. Conduit dendritic cells subsequently undergo extensive cross-talk with paracortex resident T-cells [47, 50, 51, 294]. Lymphoid tissue resident dendritic cells have previously been shown to express CB₂ receptors [295, 296] and it has been suggested that endocannabinoids modulate DC- T-cell stimulatory capacity by reducing DC surface expression of major histocompatibility complex class II molecules (MHC-II) [297]. Although significant caution should be taken with a lack of repeats, the image shown in figure 3.7 may support the notion that following oral administration, CBD is directed to the conduit system, and via activity on DCs modulates the immunological activity of paracortex resident T-cells.

The distribution of species related to CBD could not be so effectively visualised in subsequent images of sectioned MLN from dosed animals, as demonstrated in Figure 3.7b &c. In order to understand the discrepancies between

ability to image species related to CBD in each section from dosed animals, as well as homogenate tissues from a dosed animal in Chapter 2 (Figure 2.1.6) the counts for each CBD species and total ion counts were compared. It was hypothesised that the relative counts for the CBD related species would be reflected in the total ion counts. As echoed in the OrbiSIMS images, the counts for all CBD species were highest in section 3 (Figure 3.7a, Table 3.1.). However, total ion count was comparable between sections 3 and 4 (Figure 3.7a & b) as was the intensity of the [M-H]⁻ species for cholesterol sulphate. This indicates concentrations of CBD in section 4 were actually lower compared to section 3 and this reduced concentration explains the inability to image CBD in section 4. Total ion count for section 5 (Figure 3.7c) was approximately 5 times lower compared to that of the other sections from dosed animals. This reduction in overall ionic yield was reflected in a reduction in intensity of all CBD related species at a similar degree to that of section 3. The intensity of cholesterol sulphate was also reduced by approximately 4 times (Table 3.1). Based on this, it may be hypothesised that concentrations of CBD were actually similar in sections 3 and 5 but an overall reduction in ionic yield prevented imaging over CBD.

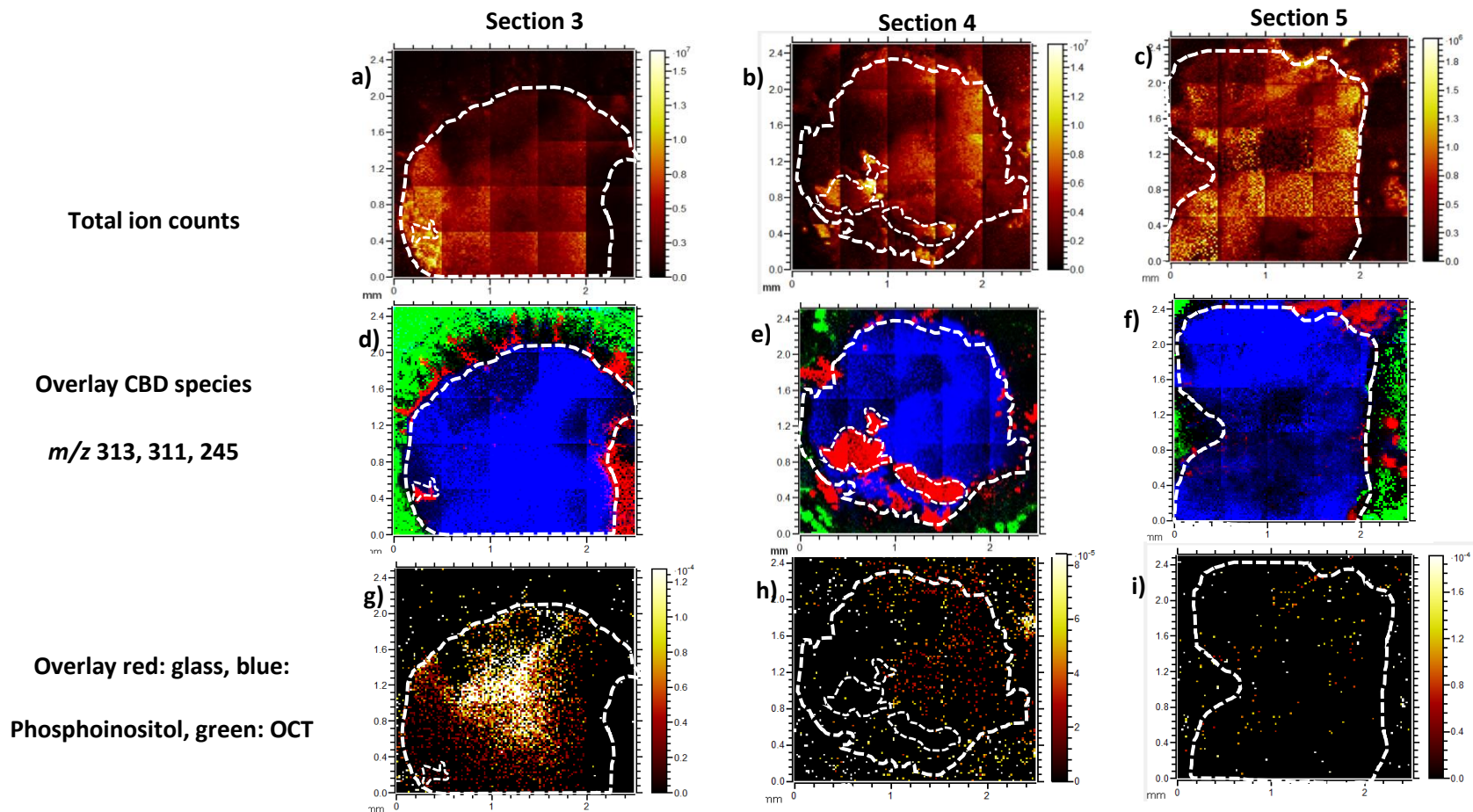


Figure 3.7. OrbiSIMS images of sectioned MLN tissue from animals dosed with CBD. Total ion counts for a) section 3, b) section 4, c) section 5. Overlays of $\text{Si}_2\text{O}_5\text{H}^-$ (red), $\text{C}_4\text{H}_9\text{O}_3^-$ (green) and $\text{C}_{47}\text{H}_{82}\text{O}_{13}\text{P}^-$ (blue) for d) section 3, e) section 4 and f) section 5. Overlays of CBD species $\text{C}_{21}\text{H}_{29}\text{O}_2^-$, $\text{C}_{21}\text{H}_{27}\text{O}_2^-$ and $\text{C}_{16}\text{H}_{21}\text{O}_2^-$ for g) section 3, h) section 4, i) section 5. The periphery of the tissue is indicated by a white dashed line.

Table 3.1. Relative abundances of CBD fragments and cholesterol sulphate in MLN sections.

		CBD fragment			Cholesterol sulphate	Total ion counts
		m/z	245.1549	311.2018	313.2175	
Animal not dosed	Intensity in section 1	N/A	N/A	N/A	61292090	1.89E+10
	Intensity in section 2	N/A	N/A	N/A	14130312	8.48E+10
Animals dosed with CBD	Intensity in section 3	933460	566500	1592747	129170315	1.55E+11
	Intensity in section 4	281645	36764	225096	193426847	1.78E+11
	Intensity in section 5	65356	2830	45923	43374862	2.97E+10
	Relative abundance in sections (% of fragments combined)	46.43 ± 11.70	9.19 ± 6.69	44.39 ± 5.05	N/A	N/A

3.4.2.2. Further tissue characterisation

Many of the markers of CBD activity are cytokines. For example a reduction in IL-2 and GM-CSF expressing T-cells have been described [70]. However as previously discussed, cytokine analysis using SIMS is not readily achievable. This is because SIMS is not optimal for the analysis of intact proteins. Two approaches to identify molecular species that may indicate pharmacodynamic activity of CBD were made. Firstly, using section 3, an ROI was drawn around the centre of the node where CBD was clearly visible (Figure 3.7). The spectra generated from this ROI was compared with that of the entire lymph node. Species that were present in higher abundance were therefore likely to be distributed with CBD in the centre of the node.

Interestingly, the distribution of CBD observed in section 3 (Figure 3.7) was not mirrored by many other species. However, one highly abundant species with a similar distribution of CBD was the [M-H]⁻ for cholesterol (C₂₇H₄₅O⁻, m/z 385.3479, deviation 0.7 ppm) (Figure 3.8). The reason for this is unclear especially considering cholesterol was previously shown to have widespread distribution across the entire MLN [261].

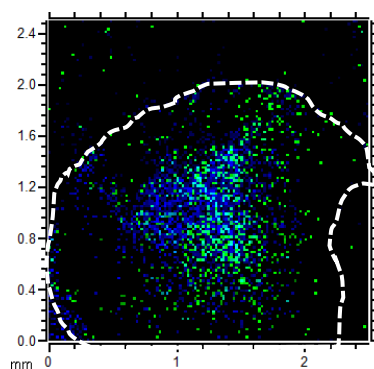


Figure 3.8. OrbiSIMS image of sectioned MLN from a dosed animal (section 3) showing CBD, blue and cholesterol, green. The periphery of the tissue is indicated by a dashed white line.

The second approach to identify chemical markers of CBD activity was to use PCA to compare spectra from cellular regions of lymph nodes from animals dosed with CBD and with those not dosed. As the imaging quality of section 5 was poor (Figure 3.7), it was excluded from this analysis. The ROI for analysis of sections from the animals not dosed were as in Figure 3.3. The ROI for samples from dosed animals is shown in Figure 3.9. The secondary ion list was generated from section 3 as this is the section with the highest abundance of CBD and contained a total of 988 secondary ion, with 339 secondary ions from m/z 75-300, 344 secondary ions from m/z 300-700 and 335 secondary ion peaks from m/z 700-1125.

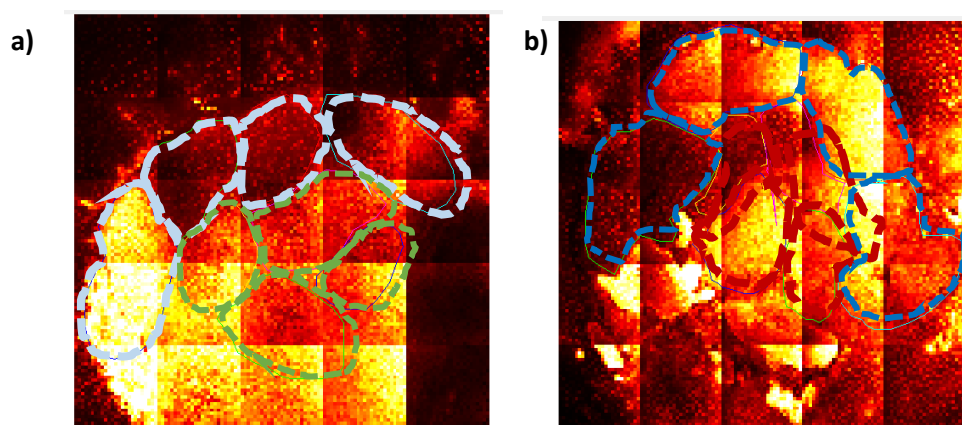


Figure 3.9. Total ion count OrbiSIMS image showing the selected ROI which were compared by PCA. The sections shown are the same as that in Figure 3.7.

PC1 was responsible for 75.88 % of the variance, and as demonstrated by the scores plot (Figure 3.10), shows good separation between regions from samples from CBD dosed and non-dosed animals. The loadings illustrated in Figure 3.11 show that the species most responsible for these differences include the fatty acids oleic, linoleic and palmitic acid. This is likely because of the high abundance of these lipids in the sesame oil formulation in which CBD was administered and not a marker of pharmacodynamic activity. The relative abundancies of these fatty acids

in dosed and not dosed samples and their distribution is shown in Table 3.3 and Figure 3.14.

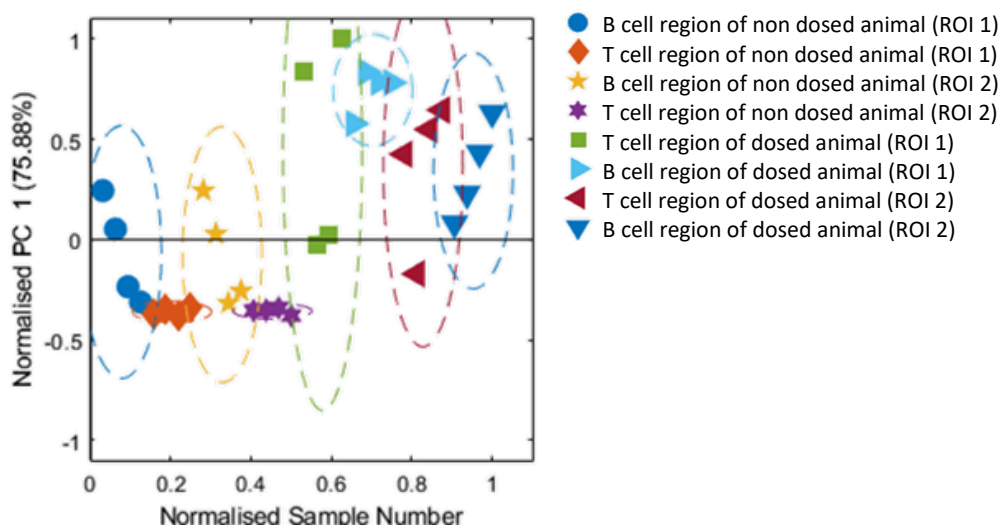


Figure 3.10. Scores plot for PC 1 generated from ROIs of sectioned lymph nodes tissue from CBD dosed and not dosed animals. The colours of the ROIs correspond with those in Figure 3.3 for not dosed animals and Figure 3.9 for dosed animals.

Interestingly, the $[M-H]^-$ species for taurine and adenine were present in the negative loadings plot. In which case, this means these molecules were less abundant in lymph nodes from animals dosed with CBD than those not dosed. It is not clear why this is, but, since analysis of samples from the animals not dosed indicated adenine and taurine to be potential markers of T-cell regions, it could be hypothesised that treatment with CBD results in a reduction of these molecules in T-cells. Suppressive effects of CBD on T-cell functions and proliferation are well described; however, the exact mechanisms are not yet well understood. It should be noted, for the case of taurine, fluctuations of lymph node amino acid content have been described as part of a daily rhythm and one explanation may therefore be the potential different times at which animals were sacrificed [298].

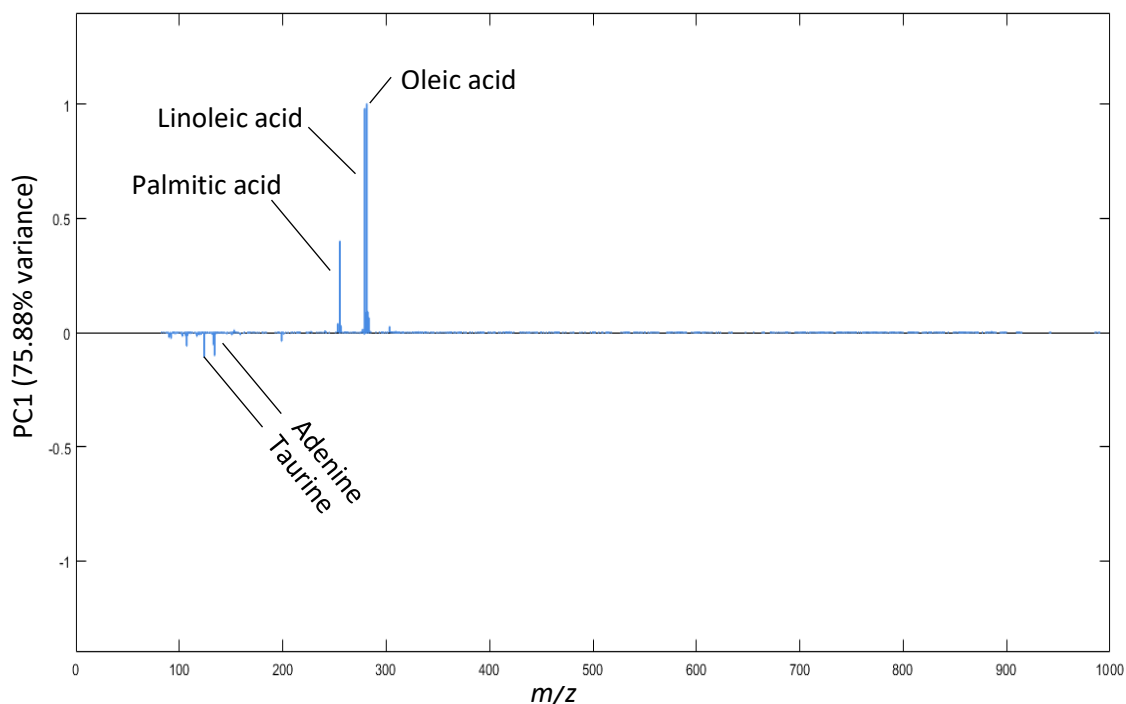


Figure 3.11. Loadings plot for PC 1 generated from PCA of ROIs from sectioned lymph nodes tissue from animals dosed and not dosed with CBD. The loadings plot corresponds to the score plot in Figure 3.9.

The non-uniform, patchy distribution of a range of biomolecules in sections from an animal not dosed (Figure 3.2) was reflected in sections from dosed animals (Figure 3.12). However, distributions of these biomolecules appeared to be inconsistent between sections and without a clear pattern. The reason for this is unknown but the distribution of these biomolecules may simply reflect the natural heterogeneity between different lymph node tissues. Alternatively, as previously alluded to, despite attempts to control for orientation it is possible that this was inconsistent throughout the sample preparation process, thus resulting in different sectioning planes. However, the non-uniform nature of these species further highlights the requirement for an investigation into the matrix effects of these tissues (section 3.4.4.)

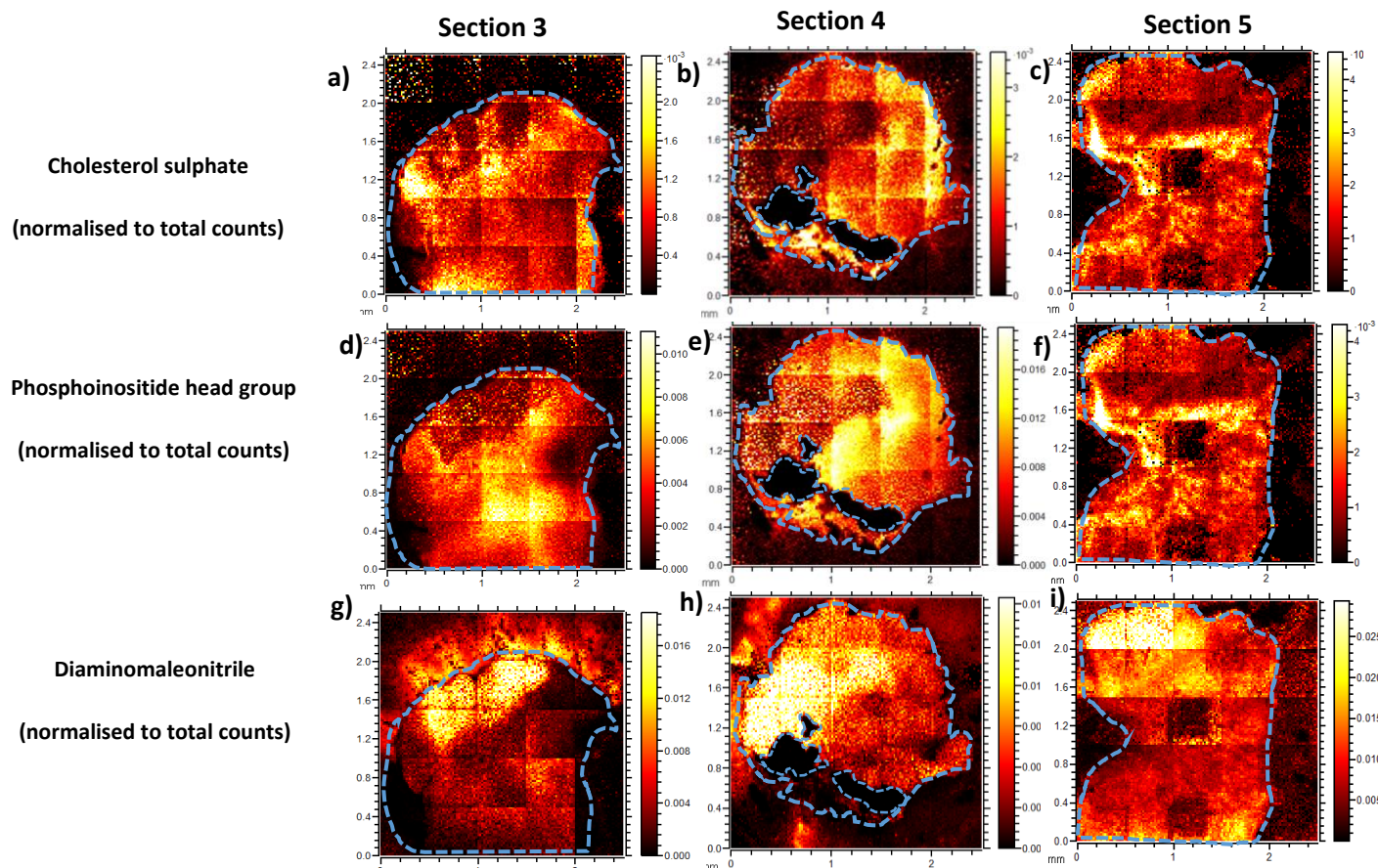


Figure 3.12. OrbiSIMS images of 3 sections of MLN tissue from dosed animals. Images show the distribution of cholesterol sulphate $C_{27}H_{45}SO_4^-$ in a) section 3, b) section 4 and c) section 5; Phosphoinositide head group $C_6H_{10}PO_8^-$ in d) section 3, e) section 4 and f) section 5 and Diaminomaleonitrile $C_4H_3N_4^-$ in g) section 3, h) section 4 and i) section 5. The sections imaged are the same as that in Figure 3.6. The periphery of the tissue is indicated by a blue dashed line.

3.4.2.3. CBD quantification using SIMS

SIMS has been described as a semi quantitative method, however SIMS has not previously been utilised to quantify any species of interest in *ex vivo* tissue samples without the use of a label. The potential of SIMS to quantify CBD concentrations in tissue was assessed using the calibration curve generated in Chapter 2 (Figure 2.14). The concentrations of CBD in sectioned tissue from CBD dosed animals were calculated (Table 3.2.). The concentrations indicated by SIMS were similar to those described as part of a previous publication which used HPLC to quantify CBD in MLN collectively at 2 hours post dosing via oral gavage in a sesame oil vehicle [70, 109]. In addition, the concentrations calculated in sections 4 and 5 were lower than for section 3, which may explain why CBD could not be imaged in these sections. This work represents the first evidence that SIMS may be applied to quantify drug concentrations in tissues.

Table 3.2. Concentrations of CBD in sectioned of MLN as estimated by SIMS data.

Section	Estimated CBD concentration ($\mu\text{g/g}$)
3	11.52
4	0.61
5	1.01

3.4.3. Investigation of tissue matrix effects on CBD ionisation

The ionisation of an ion will, in part, depend on the interaction of that ion with the surrounding material. As mentioned in section 2.4.1.2., this phenomenon, termed the

matrix effect, can impact both the ion formation and yield [252]. In figure 3.7, section 3 appeared to have a higher abundance of CBD in the centre of the node. In order to confirm drug accumulation in the centre of the node, the absence of a matrix effect in the peripheral regions of the node needed to be confirmed. Subsequently, the potential underlying chemistries of different cellular regions in sectioned MLN having a matrix effect on the ionisation of CBD was investigated. As previously discussed, the major cellular regions within the lymph can be crudely divided into the T-cell rich paracortex in the centre of the node and the B-cell rich follicle around the periphery. An even distribution of CBD was applied to the surface of 2 nodes and the ionisation of CBD in the periphery and centre of the node were compared. If the peripheral region of the node was exerting a greater matrix effect compared to the centre of the node, the abundance of CBD would be less on the periphery. Figure 3.13 shows the intensities of CBD in central and peripheral locations in two lymph nodes. The average abundance of CBD was similar across the regions analysed. Based on this, there was no clear evidence of a suppressive or enhanceive matrix effect of the underlying tissue on the intensity of CBD detected. There was however large variability in the ion intensities per region, as indicated by the large standard deviations. Based on the ion intensities in Figure 3.13, and calibration curves produced as part of Chapter 2, it may be assumed that the amount of CBD deposited was lower than analysed in samples in spiked homogenates in Chapter 2. Caution should therefore be taken when making definitive conclusions about the matrix effects of different tissue regions on CBD ionisation. However, this data may provide some preliminary evidence to support findings from section 3.4.2.1 that suggest the differences

in distribution observed in section 3 (Figure 3.6). were a true reflection of differences in distribution of CBD.

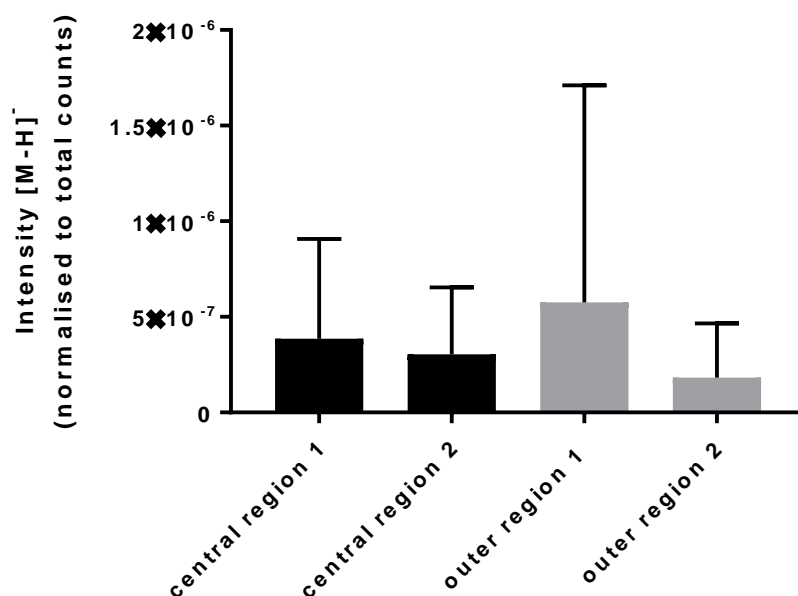


Figure 3.13. Intensity of CBD in 2 sections of MLN tissue sprayed with CBD. 6 locations per region were analysed.

3.4.4. Imaging the distribution of components of the orally administered lipidic formulation in sectioned lymph nodes

3.4.4.1. Fatty acid abundance

In the intestinal lumen, triglycerides are digested into monoglycerides and fatty acids prior to absorption into enterocytes. Here they are resynthesized and packaged into chylomicrons (see Introduction Chapter, section 1.2.2., section 1.3.1). A number of studies have described the composition of lymph and plasma chylomicrons [299-301]. The most abundant lipid classes were triglycerides, free cholesterol and phospholipids including

phosphatidylcholine, phosphatidylethanolamine and sphingomyelin. In addition, the composition of chylomicrons have been shown to be similar across a range of species including humans and rats [302]. The composition of triglycerides in plasma and lymph were generally very similar [303]. Although there have been conflicting reports on the extent to which the composition of lymph and plasma chylomicrons are influenced by the composition of dietary lipids [300, 304-308], they are generally understood to be largely similar. The distribution of chylomicrons and the individual chemical components of chylomicrons within lymph nodes have not previously been described. However, since the lipid compositions of both sesame oil [309] and chylomicrons following oral administered lipids have been described, the abundance and distribution of a range of lipids in lymph nodes could be investigated in this work.

Fatty acids are components of a number of biomolecules including glycerides and phospholipids. The relative abundance of a range of long, medium and short and saturated and unsaturated fatty acids in MLN sections from animals dosed and not dosed with CBD in sesame oil are shown in Table 3.3. There was generally there was a trend towards a higher abundance of total fatty acids in the samples from dosed animals (Table 3.3). However, fatty acids were generally present in high abundance in both samples from dosed and non-dosed animals. Some fatty acids present in the node of the animal that was not dosed are likely to be from the diet, as the animal was not fasted. Based on this, lipids in native tissue cannot be easily deciphered from those specific to formulation based chylomicrons.

The proportions of each individual fatty acid as a percentage of the total fatty acid abundance in each section were generally similar across all sections, both from dosed and

non-dosed animals (Table 3.3). This was with the exception of linoleic acid, which was variable in the sections from the undosed animal, despite being from the same node. The most abundant fatty acids in all sections were oleic, linoleic and palmitic acids which were present in similar abundancies and significantly higher than all other fatty acids. Interestingly, proportions of linoleic acid were significantly higher than previously described in human and sheep intestinal lymph node tissues respectively [310, 311]. Linoleic, oleic and palmitic acids are also the most abundant fatty acids in sesame oil [309] and in lymph, independent of the dietary lipid source [308]. Taken together, this may indicate that the high proportions of linoleic in sectioned MLN tissue, is largely a result of sesame oil derived lymph. Interestingly, sesame oil contains more than double the linoleic acid relative to palmitic acid [309]. However in sections from dosed animals, linoleic and palmitic acid were present in similar profusion. This may indicate that palmitic acid is preferentially absorbed into the lymphatics, although this would require further analysis to confirm. (Table 3.3). Data from a previous publication indicated that differences in abundance of ingested lipid and chylomicron lipid content were only observed for shorter fatty acids, such as myristic and lauric acid [307]. However, myristic acid was present in similar proportions to that previously described in sesame oil [309]. Interestingly, many of the less abundant fatty acids described such as capric and lauric acid have not previously been described in lymph node tissue and were not detected in Gas-cluster mass spectrometry analysis of chylomicrons collected from rat lymph nodes following oral administration of sesame oil and analysis with GC-MS (Feng *et al.*, unpublished). A better understanding of individual fatty acid uptake and chylomicron formation may be required as part of future work.

Arachidonic acid is a precursor for eicosanoids, including leukotrienes. Leukotrienes are synthesised by leukocytes, highly present in lymph nodes. Leukotrienes act as key inflammatory mediators and are therefore essential for immune regulation. As with several of the fatty acids, arachidonic acid was higher in dosed animals compared to the non-dosed animal, despite not being present in sesame oil. This supports hypothesis that arachidonic acid is synthesised from other fatty acids as part of chylomicron assembly, as indicated in previous work showing presence of arachidonic acids in chylomicrons in rats dosed with sesame oil (Feng *et al.*, unpublished).

Table 3.3. Relative abundances of fatty acids in MLN sections from animals dosed with CBD in sesame oil (n=3 sections from 3 animals) and an animal not fasted or dosed (n=2 sections from 1 animal), as determined by OrbiSIMS. The relative abundances of fatty acids in sesame oil and chylomicrons from rats following oral administration of sesame oil were generated by a colleague using GC-MS analysis (n=4 samples from 4 animals) (Wanshan Feng, unpublished).

Fatty acid	[M-H] ⁻ formula	[M-H] ⁻ m/z	Mass deviation (ppm)	Abundance in sesame oil (% of total fatty acids) (mean ± SD)	Abundance in chylomicrons (% of total fatty acids) (mean ± SD)	Intensity in dosed animals (normalised to total counts) (mean ± SD)	Intensity in dosed animals (% of total fatty acids) (mean ± SD)	Intensity in not dosed animal (normalised to total counts) (mean ± SD)	Intensity in not dosed animal (% of total fatty acids) (mean ± SD)
Linoleic (C18:2)	C ₁₈ H ₃₁ O ₂ ⁻	279.2334	1.5	30.42±0.64	38.3 ±2.26	9.88E-02 ±6.63E-02	29.20 ±2.81	3.61E-02 ±3.31E-02	21.12 ±16.43
Oleic (C18:1)	C ₁₈ H ₃₃ O ₂ ⁻	281.2483	-1.0	44.27±0.09	39.52 ±2.08	1.04E-01 ±6.70E-02	31.37 ±1.90	3.84E-02 ±1.50E-02	32.60 ±3.66
Palmitic (C16:0)	C ₁₆ H ₃₁ O ₂ ⁻	255.2332	1.1	12.9±0.33	13.13 ±0.29	6.92E-02 ±3.08E-02	25.55 ±6.61	2.81E-02 ±6.94E-02	25.84 ± 6.84
Stearic (C18:0)	C ₁₈ H ₃₅ O ₂ ⁻	283.264	-0.9	8.09±0.60	0.3 ±0.31	1.76E-02 ±1.13E-02	5.01 ±2.74	7.91E-03 ±2.35E-04	8.38 ±4.21
Linolenic (C18:3)	C ₁₈ H ₂₉ O ₂ ⁻	277.2181	0.7	0.31±0.06	N/A	5.14E-03 ±3.36E-03	1.47 ±0.28	3.94E-03 ±1.60E-03	3.31 ±0.30

Arachidonic (C20:4)	$C_{20}H_{32}O_2^-$	303.2333	1.0	N/A	2.74 ± 0.68	$5.76E-03$ $\pm 6.07E-03$	1.53 ± 0.83	$5.43E-04$ $\pm 4.11E-05$	0.59 ± 0.32
Margaric (C17:0)	$C_{17}H_{33}O_2^-$	269.2491	1.8	0.17 ± 0.02	N/A	$1.07E-03$ $\pm 3.96E-04$	0.43 ± 0.16	$4.85E-04$ $\pm 1.26E-04$	0.44 ± 0.11
Arachidic (C20:0)	$C_{20}H_{39}O_2^-$	311.2956	0.2	1.15 ± 0.01	N/A	$3.12E-04$ $\pm 8.41E-05$	0.15 ± 0.08	$8.94E-05$ $\pm 1.80E-06$	0.09 ± 0.04
Behenic (C22:0)	$C_{22}H_{43}O_2^-$	339.3268	-0.2	0.96 ± 0.04	N/A	$8.19E-05$ $\pm 2.88E-05$	0.04 ± 0.02	$2.90E-05$ $\pm 5.32E-06$	0.03 ± 0.02
Lignoceric (C24:0)	$C_{24}H_{47}O_2^-$	367.3582	0.0	0.92 ± 0.18	N/A	$6.70E-05$ $\pm 4.66E-05$	0.03 ± 0.02	$4.27E-05$ $\pm 1.15E-05$	0.05 ± 0.03
Palmitoleic (C16:1)	$C_{16}H_{29}O_2^-$	253.2179	2.2	0.17 ± 0.01	N/A	$1.15E-02$ $\pm 8.43E-03$	3.36 ± 0.51	$5.99E-03$ $\pm 2.48E-03$	5.01 ± 0.41
Heptadecenoic (C17:1)	$C_{17}H_{31}O_2^-$	267.2332	0.8	0.08 ± 0.01	N/A	$5.69E-04$ $\pm 3.53E-04$	0.20 ± 0.07	$3.65E-04$ $\pm 1.63E-04$	0.30 ± 0.01
Paullinic (C20:1)	$C_{20}H_{37}O_2^-$	309.2802	0.9	0.36 ± 0.02	N/A	$2.51E-03$ $\pm 1.49E-03$	0.76 ± 0.13	$2.19E-04$ $\pm 1.66E-04$	0.31 ± 0.28
Erucic (C22:1)	$C_{22}H_{41}O_2^-$	337.3113	0.3	0.19 ± 0.02	N/A	$1.09E-04$ $\pm 4.84E-05$	0.04 ± 0.01	$1.03E-04$ $\pm 7.07E-05$	0.07 ± 0.02
Caprylic (C8:0)	$C_8H_{15}O_2^-$	143.1076	-0.8	N/A	N/A	$8.62E-05$ $\pm 2.85E-05$	0.04 ± 0.02	$6.85E-05$ $\pm 1.52E-05$	0.08 ± 0.05
Capric (C10:0)	$C_{10}H_{19}O_2^-$	171.139	-0.4	N/A	N/A	$4.69E-05$ $\pm 1.04E-05$	0.02 ± 0.01	$1.49E-04$ $\pm 7.14E-05$	0.12 ± 0.00
Lauric (C12:0)	$C_{12}H_{23}O_2^-$	199.1703	-0.4	N/A	N/A	$1.03E-04$ $\pm 4.09E-05$	0.04 ± 0.02	$4.14E-04$ $\pm 1.95E-04$	0.33 ± 0.00
Myristic (C14:0)	$C_{14}H_{27}O_2^-$	227.2019	1.0	N/A	N/A	$2.68E-03$ $\pm 2.34E-03$	0.76 ± 0.24	$1.56E-03$ $\pm 6.13E-04$	1.33 ± 0.14

It is also of note that the sum of the abundances of all fatty acids, once normalised to total counts, was highest in section 3 (0.56), compared to section 4 (0.31) and section 5 (0.085) which correlates with estimated CBD concentrations in these sections. In Section 5, the proportions of fatty acids to CBD were similar to that of Section 3. This observation supports the theory that the inability to image the distribution of CBD in this sample is the result of an overall reduced ionic yield rather than poor delivery of CBD to the node.

It should be noted that formal statistical analysis was not performed to compare the lipid abundance between samples from treated and untreated animals since the n number was low. Any comparisons made are therefore speculative and would need to be supported with statistical analysis of more data as part of future work to confirm.

3.4.4.2. Fatty acid distribution imaging

In addition to CBD, the OrbiSIMS images of tissue from CBD dosed animals could also be utilised to determine the distribution of elements of chylomicrons and associated small molecules formed from the lipid-based formulation, in this case sesame oil, in which CBD was administered. Comparisons of the distribution of these molecules with CBD may then provide novel insights into the mechanisms by which orally administered compounds undergoing lymphatic transport, such as CBD, are distributed in lymph nodes.

Although CBD distribution could only be clearly imaged in one sample, fatty acids could be clearly imaged across all sections from dosed animals (Figure 3.14). No formal analysis of distribution was performed, however all individual fatty

acids within individual lymph nodes appeared to be distributed in the same way. All individual fatty acids are shown overlaid in a single image per section. Similar distributions of each fatty acid within lymph node sections suggest they are fragments of the same larger parent molecules, such as triglycerides or phospholipids.

In a recent publication investigating dietary lipid distribution, following a prolonged high fat diet in mouse MLN, lipid droplets were shown to be present in macrophages of the subcapsular sinus and interfollicular region, both on the periphery of the node [312]. Moreover, in this same publication, stained lipid droplets were absent from the paracortex, in the centre of the node. However, lipid distribution in the lymphatics at the time of peak absorption was not demonstrated as part of this publication. In images from fasted animals in this thesis (Figure 3.14 a & b), fatty acids were also highly abundant in the periphery of the node and largely absent in the centre. This may explain the presence of these species in the positive loadings plot for B-cell regions on the periphery of the node when compared by PCA with central T-cell regions (Figure 3.4. and 3.5.). This would also correlate with previous suggestions that because of their size, lipid droplets are isolated to the sinuses and unable to enter the conduit system through gaps in LECs [280]. It was not clear why fatty acids specifically were visible on one side of the node (the left of Figure 3.14 a and b), or why some fatty acids could be imaged around the periphery of the tissue, in what was believed to be OCT.

It is of note, in contrast to sections from fasted animals, fatty acid distribution in tissues from dosed animals was significantly more widespread across the node (Figure 3.14 c, d & e). In section 3, where CBD was shown to localise in the centre of the node (Figure 3.6) the fatty acid distribution did not therefore directly mirror the distribution of CBD, as might be expected if the fatty acids were present

in chylomicrons and CBD was associated with these chylomicrons in the lymph node. Again, from these images it cannot be determined which specific cells of the lymph node molecules are associated with. However, these images suggest for the first time that lipids distribute differently within the lymph node at peak absorption.

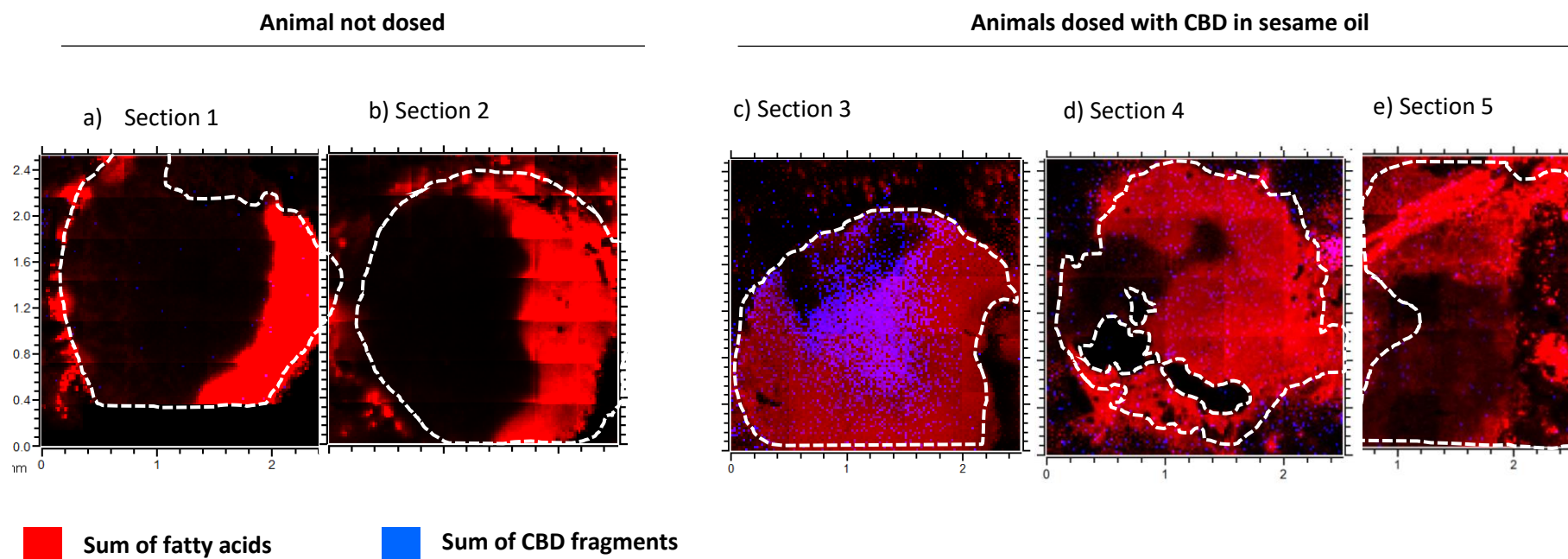


Figure 3.14. OrbiSIMS images of sectioned MLN tissue from an animal not dosed (a&b) and animals dosed with CBD in sesame oil (c-e).

Red is the sum of the $[M-H]^-$ fatty acids shown in Table 3.2 and blue is the sum of the fragments of CBD in Table 3.1. The periphery of each node is demonstrated using the dashed white line. Images are normalised by total ion counts.

3.4.4.3. *Acylglycerides imaging and abundance*

In a previous study by Seyer *et al.*, lipid droplets in duodenal enterocytes with size and density corresponding to that of chylomicrons were shown to contain a range of mono, di and triacylcerides following oral administration of sunflower oil [313]. The relative abundance of the glycerides described in this work are shown in Table 3.4. The abundance of free fatty acids was higher than that of glycerides (Table 3.3., Table 3.4.). This was despite reports that free fatty acids are present in low concentrations in chylomicrons [299]. The distribution of intact glycerides mirrored that of the fatty acids, which likely indicates that the fatty acids, at least in part, originate from fragmentation of glycerides rather than free molecules. Glycerol, which is also a building block for acylglycerides, was however present in low abundance. It should be noted that many acylglycerides identified were present in low and variable abundance, making reliability poor.

3.4.4.4. *Phospholipids and sterols imaging and abundance*

In addition to fatty acids and acylglycerides, a number of other lipids have been described in chylomicrons. These include phospholipids, cholesterol and cholesterol esters [299]. Of these, the [M-H]⁻ ions of a number of phosphatidyl ethanolamines, several phosphatidylcholine species and lysophosphatidyl cholines were detected in all sections. Similar to fatty acids and acylglycerides, these were all also present in samples from the animal not dosed. Distribution of all these lipids also mirrored that of the fatty acids, shown in Figure 3.14.

Table 3.4. Relative abundances of acylglycerides in MLN sections from animals dosed with CBD in sesame oil (n=3 sections from 3 animals) and an animal not dosed or fasted (n=2 sections from 1 animal), as determined by OrbiSIMS. Data is presented as mean \pm SD.

Lipid class	[M-H] ⁻ formula	[M-H] ⁻ m/z	Mass deviation (ppm)	Intensity in MLN from dosed animals (normalised to total counts)	Intensity in MLN from an animal not dosed (normalised to total counts)
Triacylglycerols	C ₅₃ H ₉₅ O ₆ ⁻	827.714	0.8	2.43E-06 \pm 2.62E-06	6.90E-07
	C ₅₃ H ₉₇ O ₆ ⁻	829.7300	1.2	8.80E-06 \pm 5.48E-06	2.62E-06
	C ₅₃ H ₉₉ O ₆ ⁻	831.7457	1.2	3.28E-06 \pm 2.12E-06	9.50E-07
	C ₅₅ H ₉₇ O ₆ ⁻	853.7301	1.2	3.87E-05 \pm 2.35E-05	5.13E-06
	C ₅₅ H ₉₉ O ₆ ⁻	855.7458	1.3	2.11E-05 \pm 1.44E-05	5.56E-06
	C ₅₅ H ₁₀₁ O ₆ ⁻	857.7613	1.1	5.92E-06 \pm 3.89E-06	1.50E-06
	C ₅₅ H ₁₀₃ O ₆ ⁻	859.7747	-1.5	2.73E-07 \pm 1.97E-07	0.00E+00
	C ₅₇ H ₉₇ O ₆ ⁻	877.7300	1.1	6.83E-06 \pm 7.01E-06	1.91E-06
	C ₅₇ H ₁₀₁ O ₆ ⁻	881.7613	1.1	1.02E-05 \pm 8.37E-06	2.39E-06
	C ₅₇ H ₉₉ O ₆ ⁻	879.7458	1.2	1.42E-05 \pm 1.30E-05	3.48E-06
	C ₅₇ H ₁₀₃ O ₆ ⁻	883.7763	1.3	2.48E-06 \pm 1.96E-06	6.49E-07
Diacylglycerides	C ₃₇ H ₆₅ O ₅ ⁻	589.4842	0.8	1.76E-07 \pm 5.75E-08	0.00E+00

	$C_{37}H_{67}O_5^-$	591.5001	1.2	$1.62E-07 \pm 3.87E-08$	2.28E-08
	$C_{37}H_{69}O_5^-$	593.517	3.3	$2.28E-08 \pm 3.23E-08$	2.52E-08
	$C_{39}H_{67}O_5^-$	615.4998	0.7	$1.16E-06 \pm 7.10E-07$	2.47E-07
	$C_{39}H_{69}O_5^-$	617.5155	0.7	$3.75E-07 \pm 2.42E-07$	8.42E-08
	$C_{39}H_{71}O_5^-$	619.5313	0.9	$4.91E-08 \pm 4.07E-08$	0.00E+00
Monoacylglycides	$C_{19}H_{35}O_4^-$	327.2541	0.2	$1.24E-06 \pm 4.98E-07$	3.75E-07
	$C_{19}H_{37}O_4^-$	329.2702	1.3	$7.27E-08 \pm 2.41E-08$	0.00E+00
	$C_{21}H_{37}O_4^-$	353.2699	0.5	$3.38E-06 \pm 1.23E-06$	1.19E-06
	$C_{21}H_{39}O_4^-$	355.2855	0.3	$1.35E-06 \pm 6.25E-07$	2.25E-07
Glycerol	$C_3H_7O_3^-$	91.0399	-1.9	$4.99E-08 \pm 2.63E-08$	3.15E-07

3.4.4.5. Polyphenol imaging and abundance

In addition to lipids, sesame oil also contains a number of other small molecules. These include, but are not limited to, phytoestrogens and phytosterols [309]. Several phytoestrogens and phytosterols present in sesame oil have antioxidant properties [314].

Understanding the distribution of these molecules within the lymph node, and how this compares to the distribution of CBD, may shed light on whether CBD is distributed via passive or active mechanisms. Firstly, the most commonly found phytoestrogen in vegetable oils are lignans. Sesame oil contains two major groups of lignans; lipid soluble lignans, and glycosylated water soluble lignans. The lipid soluble lignans include sesamin ($C_{20}H_{18}O_6$), seamolin ($C_{20}H_{18}O_7$) and sesaminol ($C_{20}H_{18}O_7$), sesamolol ($C_{20}H_{20}O_7$) and pinoresinol ($C_{20}H_{22}O_6$) [309]. Concentrations of sesamin specifically can reach above 10 mg/g in sesame oil [315]. Other abundant plant lignans include matairesinol ($C_{20}H_{22}O_6$) and secoisolariciresinol ($C_{20}H_{26}O_6$) [316]. However, the $[M-H]^-$ species of these compounds was not detected in any sections from dosed animals. It was hypothesised that the reason for this may be due to metabolism by gut bacteria into enterolignans, as in humans [317]. These include enterolactone ($C_{18}H_{18}O_4$) and enterodiol ($C_{18}H_{22}O_4$). It should be noted that, neither enterolactone nor enterodiol could be detected in any sections. One reason may be because the LogP for the molecules (3.2 and 2.6 respectively), which is a good predictor of extent of lymphatic transport [104] was too low for association with chylomicrons and subsequent lymphatic transport.

3.4.4.6. Lipid soluble vitamins imaging and abundance

A number of natural oils also contain lipid soluble vitamins including tocopherols. Tocopherols represent a group of low molecular weight molecules, with high LogP. γ -tocopherol was previously shown to be present in sesame oil at concentrations of up to 0.5 mg/g [318]. The absorption of α -tocopherol and γ -tocopherol from the small intestine was shown to be similar to that of lipids [319, 320]. Both α -tocopherol ($[M-H]^-$ $C_{29}H_{49}O_2^-$, m/z 429.3740) and γ -tocopherol ($[M-H]^-$ $C_{28}H_{47}O_2^-$, m/z 415.3585) were present in high abundance in sections from dosed animals ($9.98E-05 \pm 1.09E-04$ and $4.37E-06 \pm 6.77E-07$ respectively). However, both α - and γ -tocopherol were also equally as prevalent in the lymph node from the animal not dosed ($2.95E-05$ and $1.28E-05$ respectively). As a result, conclusions about the distribution of sesame oil derived tocopherols specifically are difficult to draw. Despite this, the distribution of α - and γ -tocopherol mirrored that of fatty acids and acylglycerides and was widespread across the node in animals dosed with sesame oil and CBD, but more localised to one side of the periphery in animals not dosed (Figure 3.14).

Sesame oil also contains vitamin K1 [321], which has a LogP of 9.7 and has also been shown to undergo lymphatic transport following duodenal infusion [322]. The $[M-H]^-$ ($C_{31}H_{45}O_2^-$) species for vitamin K1 was not identified in any section of lymph node analysed. None of the phenolic compounds such as flavonoids described in sesame oil were identified in sections [323]. Other lipid soluble vitamins (A and D) are known not to be present in sesame oil and so were not the subject of analysis.

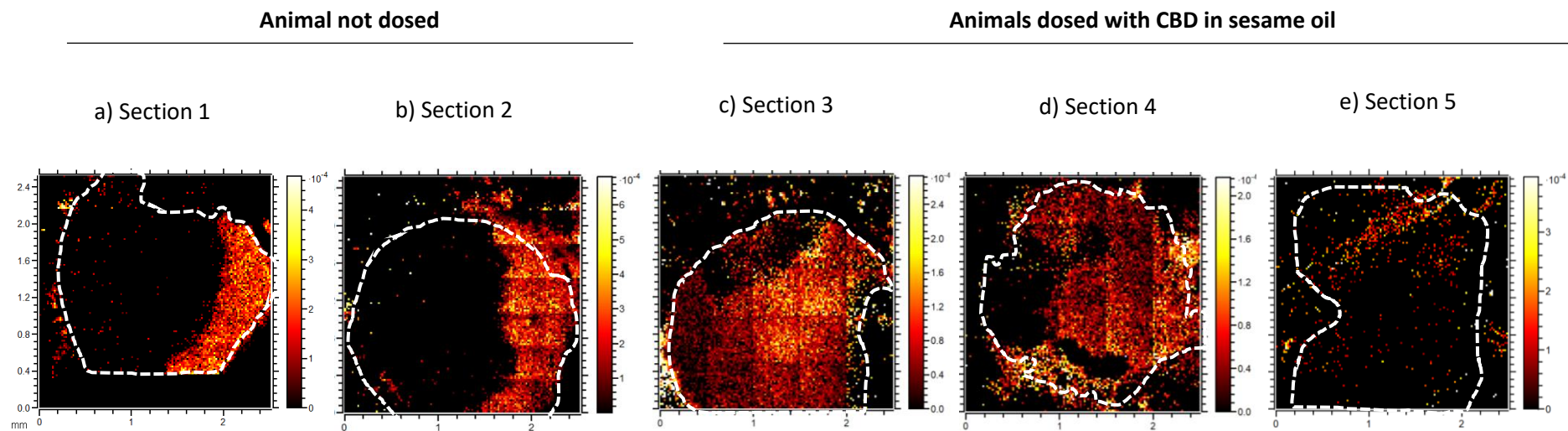


Figure 3.15. OrbiSIMS images showing the distribution of the sum of alpha tocopherol, $C_{29}H_{49}O_2^-$ and gamma tocopherol, $C_{28}H_{47}O_2^-$ in sectioned MLN tissue from an animals not dosed (a & b) and animals dosed with CBD in sesame oil (c- e). The periphery of the node is indicated by the dashed white line.

3.5. Conclusions

The work in this Chapter utilises the method described in Chapter 2 and represents the evidence of drug distribution in intestinal lymph nodes at peak absorption, following oral delivery. Images from this thesis act as the first evidence that at peak absorption, CBD may distribute primarily in the T-cell rich paracortex, thus supporting the hypothesis that CBD exerts immunomodulatory effects through these cells. There was no evidence of a matrix effect that would distort the visualisation of CBD in sectioned tissue. In addition, using the calibration curve generated in Chapter 2, ion abundance using OrbiSIMS correlated to concentrations previously reported *in vivo*. Based on the work in this chapter, it may also be hypothesised that other small molecule drugs undergoing lymphatic transport following oral delivery could also distribute in the T-cell paracortex. If further work confirms drug association with lymph node resident T-cells this could have considerable future clinical implications for diseases where lymph resident T-cells are implicated.

The work in this chapter also represents the first label and matrix free imaging and use of OrbiSIMS to image drug distribution in tissue samples following oral delivery as well as the initial evidence of SIMS to analyse lymphatic tissue. It is however important to acknowledge that a major limitation of this work was that CBD could not be clearly imaged in 2 of the 3 sections imaged. This means strong caution should be used when drawing conclusions without sufficient replicates. By comparing the abundance of other molecules between samples, it is not clear if this was an analytical issue, or whether concentrations in these samples were lower than estimated in previous publications using quantitative analysis, or a combination of both these factors. Although sesame oil remains the most superior

known formulation for lymphatic delivery, it has been associated with considerable inter-animal variability [109]. Based on this, it is possible that in some samples, concentrations were lower than estimated based on previous *in vivo* data. This is also supported by extrapolations from the calibration curves generated from homogenised tissue as part of Chapter 2.

Secondary ions relating to a range of biomolecules could also be identified and imaged in sectioned lymph nodes. These included fatty acids known to be present in sesame oil formulation. Fatty acids were responsible for chemical differences between lymph nodes from animals dosed with CBD in sesame oil and those not dosed. This may indicate they were present in the formulation. However, critically, many lipid species were also highly evident in samples from an animal not dosed, which hindered conclusions about formulation derived chylomicron distribution specifically. Acylglycerides, phospholipids and sterols as well as lipid-soluble vitamins known to undergo lymphatic transport were also identified and imaged. In samples from dosed animals, these biomolecules showed a widespread distribution across the node, which was in contrast to the centrally localised distribution of CBD. This may indicate an independent mechanism of distribution compared to CBD although concluding this would require further investigation.

It was noted, when PCA was applied to identify fatty acids, taurine and adenine as potential chemical markers that this could be used to differentiate different cellular regions within tissue. This may be useful in the characterisation of lymphatic tissue in future work. Finally, a lower abundance of potential T-cell markers in tissue from animals dosed with CBD may support the role of these cells in CBD induced immunoregulatory effects *in vivo*.

4. Determination of which individual lymph nodes can be targeted following oral administration of drugs using an animal model

4.1. Introduction

The superior mesenteric lymph nodes (MLN), make up a large group of between 100-150 nodes which can be further subcategorised into the mesenteric, mesocolic and ileocolic nodes (Section 1.1.3.2.). Rats have fewer lymph nodes compared to humans, however the basic morphologic structure and rates of lipid transport to the MLN are comparable [6, 7]. A number of studies in rats have shown that the MLN collectively can be targeted by a range of different compounds using orally administered lipid- based formulations [70, 114, 115, 118] (section 1.3). Studies have also indicated that lipid absorption varies along the small intestine [20] and that the intestinal lymph nodes drain distinct segments of the gastrointestinal tract [20]. However, potential segregation of lymphatic drainage from different parts of the GI tract into these nodes has been largely overlooked in previous studies. Based on this, the distribution of drugs into individual lymph nodes and how this compares to pharmacological thresholds remains unknown.

Following collection into the superior MLN, lymph draining from the duodenum, small bowel and ascending and transverse colon then enters the superior mesenteric duct [4]. Lymph from the superior MLN is then directed through the pre-aortic nodes (part of retroperitoneal lymph nodes (RPLN)) which lie in front of the aorta before entry into the cisterna chyli and thoracic duct [4]. (Chapter 1, section 1.1.3.2, Figure 1.3.). It can therefore be hypothesised that the RPLN may also be targeted by lipophilic compounds undergoing intestinal

lymphatic transport, although perhaps less efficiently than MLN due to a dilution factor. Despite this, RPLN have to date been largely overlooked in terms of lymphatic delivery research and little is known about how efficiently they can be targeted via the oral route.

Recently, nodes draining different regions of the gastrointestinal track were shown to be immunologically distinct [19] with differing immune cell populations and subsequently differing immunological functions [20]. Based on this, knowledge of which specific intestinal lymph nodes can be targeted has particular importance in inflammatory disorders where specific regions of the bowel are implicated, such as Ulcerative Colitis. In addition, as well as being implicated as primary tumour sites in lymphoma (section 1.2.4.1), specific groups of intestinal and retroperitoneal lymph nodes are also differently implicated in metastasis from a range of primary tumours (Chapter 1, section 1.2.4.2). Effective targeting of the RPLN could be particularly important, since RPLN metastasis has a poor prognosis [324]. With a growing interest surrounding lymphatic targeting using lipid based formulations in the literature [10-12], knowledge of which specific nodes can be targeted is therefore essential for determining the clinical potential of intestinal lymphatic drug targeting.

4.2. Chapter aims and objectives

The aim of this chapter was to use an animal model to improve the understanding of which specific lymph nodes receive chylomicron-associated drugs draining from the gastrointestinal track following oral administration. This can then inform which nodes can be targeted using lipid-based formulations and

subsequently the clinical potential of lipid-based formulations for lymphatic targeting.

For this chapter, an *in vivo* bio-distribution model in rats was used to quantify the delivery of CBD as a model compound in individual lymph nodes of the mesentery and retroperitoneum.

Specific objectives include:

- Quantification of CBD distribution into individual MLN and RPLN in rats at various time points post oral administration.
- A comparison of CBD concentrations in intestinal lymph nodes following administration in a range of lipid- based vehicles.

4.3. Methods and materials

4.3.1 Detection and quantification of CBD in rat lymphatic tissue

The method used to quantify CBD in individual lymph nodes was a modification of a previously reported method [215] and is described below.

4.3.1.1 Materials

Plant-derived CBD was purchased from THC Pharm GmbH (Frankfurt, Germany). Sesame oil was purchased from Sigma Aldrich (Gillingham, UK). All other solvents and reagents were of HPLC grade and were purchased from Fisher Scientific (Loughborough, UK).

4.3.1.2 Animals

Animal husbandry and maintenance for the studies in this chapter are as described in Chapter 2, section 2.3.2. and 2.3.3.

4.3.1.3 Bio-distribution studies

Following 5 days of acclimatization, animals were fasted overnight with free access to water. CBD in lipid-based vehicle (sesame oil, coconut oil or rapeseed oil) was administered via oral gavage (12mg/ml, 12mg/kg) as previously described [7].

Following oral administration in sesame oil, CBD reaches highest concentrations in MLN one hour prior to maximum concentrations being measured in the plasma (t_{max-1}) at 2 hours post dosing [70, 109, 201, 325]. In addition, the t_{max} of rapeseed oil and coconut oil is 5 hours (Feng et al, manuscript in preparation). Since it was hypothesised that CBD would enter RPLN after MLN, it was sensible to assume that CBD would reach peak concentrations in RPLN at time points at or later than 2 hours post administration. Based on this, following administration of CBD, tissues were collected at 2, 3, 5 and 8 hours post administration. 3 animals per time point per vehicle were euthanized via carbon dioxide gas. Individual lymph nodes were dissected and separated from the surrounding tissue. The anatomical location of the nodes dissected and analysed are depicted in Figure 4.1. and 4.2. Four individual lymph nodes collected across the mesenteric chain were collected, with position 1 being at the top of the chain, and position 4 at the bottom. RPLN collected at position 5 & 6 were the iliac/caudal lymph nodes and para-aortic nodes, respectively.

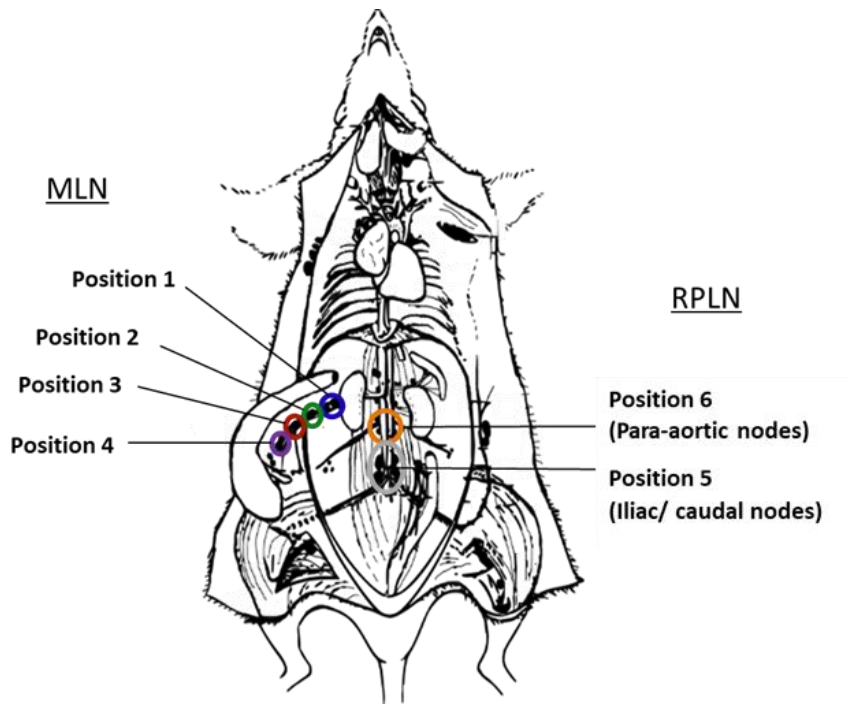


Figure 4.1. Anatomical localisation of the mesenteric lymph nodes and retroperitoneal lymph nodes collected as part of the bio-distribution study.

Modified from [4].

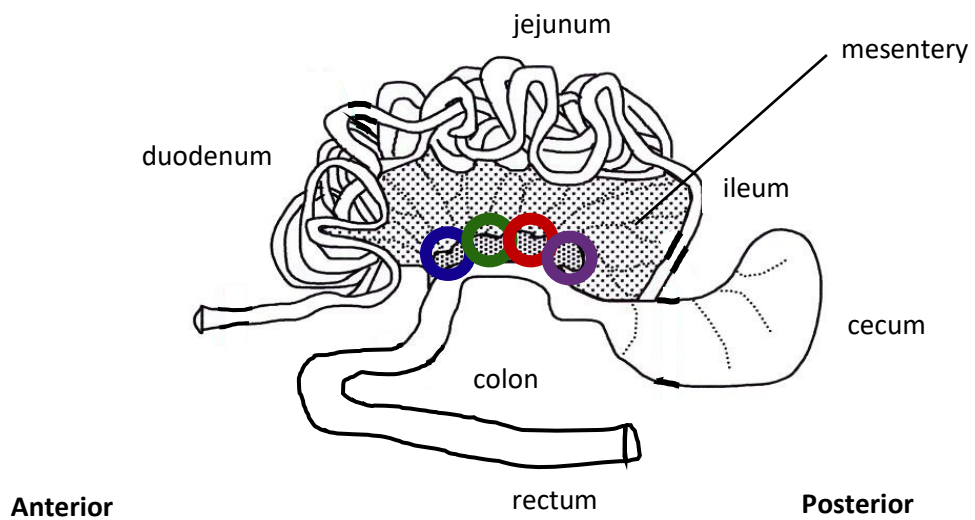


Figure 4.2. Schematic of the rat intestines and mesentery. The lymph nodes collected in this study are depicted by the coloured circles. Blue, position 1; Green, position 2; Red, position 3 & purple, position 4. The anterior and posterior of the body are also indicated. Modified from [5].

4.3.1.4. Sample preparation

For the purpose of comparing drug concentrations, singular lymph nodes were analysed individually. Individual lymph node samples were added to 1.5ml green RINO bead lysis tubes (WebScientific, Crewe, UK) in 175 μ l water and homogenised using Bullet Bender Gold 24 Tissue Homogeniser (Next Advance, USA) at 4 °C. Dichlorodiphenyltrichloroethane at a final concentration of 5 μ g/ml was used as an internal standard. Following homogenisation, 100 μ l suspension was prepared for protein precipitation and liquid – liquid extraction. Cold acetonitrile was added (600 μ l) and the sample vortexed for 1 minute. Water (450 μ l) was then added followed by 3 ml n-Hexane. Samples were vortexed for a further 5 minutes and centrifuged at 4000 g at 10 °C for 10 minutes. The upper organic layer was removed and evaporated under nitrogen at 35 °C (Techne DRI-Block type DB-3D). Dry residue was reconstituted in 100 μ l mobile phase. The final concentrations in tissue samples were calculated according to the weight of the tissue and expressed as μ g/g.

Calibration curves were prepared by diluting MLN tissue from non-dosed animals in water at a ratio of 1:2 (w/v) and homogenising (POLYTRON® PT 10-35 GT, Kinematica AG, Luzen, Switzerland) at 18000 rpm for 3 minutes on an ice bath. Samples were then spiked with CBD at final concentrations of 0.02, 0.05, 0.1, 0.5, 1 and 10 μ g/ml CBD and prepared in the same way as described for single lymph nodes.

4.3.1.5 Chromatographic conditions

A Waters Alliance 2695 separations module equipped with a Waters 996 photodiode array ultraviolet (UV) detector was used for sample analysis.

Separation was achieved using an ACE C18-PFP 150 mm × 4.6 mm, 3 µm particle size column (Hichrom Ltd., Reading, UK), protected by an ACE C18-PFP 3 m guard cartridge. The mobile phase was a mixture of acetonitrile and water in a ratio of 62:38 (v/v) at a flow rate of 1 ml/min. Samples were stored at 4 °C during analysis and the column was maintained at 55 °C. Injection volume was 40 µl and CBD was detected at a wavelength of 220 nm. Data collecting and processing was carried out by the Empower™ 2 software (Waters).

4.3.1.6. HPLC data analysis

The lower limit of quantification (LLOQ) for CBD using this method is 10 ng/ml. All data are presented as mean ± standard error of the mean (SEM). One way analysis of variance (ANOVA) followed by Tukey's multiple comparisons test was used to assess significance of differences between individual lymph nodes at different time points. A *p* value <0.05 was considered statistically significant. All figures and statistical tests were generated in GraphPad Prism (version 7). Potential outliers were excluded using a Grubb's test where alpha = 0.05 was deemed significant.

4.4. Results and Discussion

4.4.1. Bio-distribution of CBD into different lymph nodes following oral administration in lipidic vehicles in rats

4.4.1.1. Bio-distribution of CBD into individual MLN at different time points following oral administration in sesame oil vehicle

The aim of this work was firstly to assess how distribution of CBD compares within the individual lymph nodes of the mesentery at various time points post oral

administration. For this work, sesame oil was used as a vehicle as it was shown to be highly efficient for delivery of CBD to MLN [70]. The concentrations of CBD in individual MLN and RPLN at 2, 3, 5 and 8 hours post oral administration are shown in Figure 4.3. At 2 hours post administration, concentrations of CBD were significantly higher in the lymph nodes positioned second from the apex of the chain (position 2), when compared to lymph nodes at the bottom of the chain (position 4). Based on the positioning of lymphatic vessels that drain lymph from the gut tissues into the MLN, it was hypothesised that the upper nodes in the chain drain lymph from the duodenum and upper jejunum whereas the lower nodes drain the ileum, caecum and partially the colon [4] (Figure 4.1 & 4.2). Data from this work describing the distribution of a lipophilic drug are therefore in agreement with previous studies that suggested the majority of dietary lipid absorption occurs in the duodenum and jejunum [20]. Concentrations in the MLN collectively in this work were comparable to concentrations previously reported in MLN post oral administration in sesame oil [70].

At 3 hours post administration, concentrations in MLN at position 1, 2 and 3 appeared to be higher compared to position 4, however this was not statically significant. At 5 and 8 hours post administration concentrations in MLN at all positions were comparable. The average concentration of CBD across all MLN from animals dosed with sesame oil was $8.3 \pm 1.8 \mu\text{g/g}$, $7.8 \pm 2.2 \mu\text{g/g}$, $3.6 \pm 0.4 \mu\text{g/g}$ and $2.2 \pm 0.4 \mu\text{g/g}$ for 2, 3, 5 and 8 hours post administration respectively.

Using the same data as presented in Figure 4.3, the concentrations in each lymph node over time were also compared (Figure 4.4). For all lymph nodes, concentrations of CBD were not statically different at 2, 3, 5 & 8 hours following administration. Data from this work therefore suggest that exposure to CBD is widespread across lymph nodes positioned throughout the mesenteric chain. In

addition, based on current understanding of lymph drainage, the fact that CBD is present at substantial levels in the lymph nodes positioned lower in the chain may also indicate that some absorption occurs in the lower GI tract. Confirmation of drug absorption from the lower GI tract would however require future work.

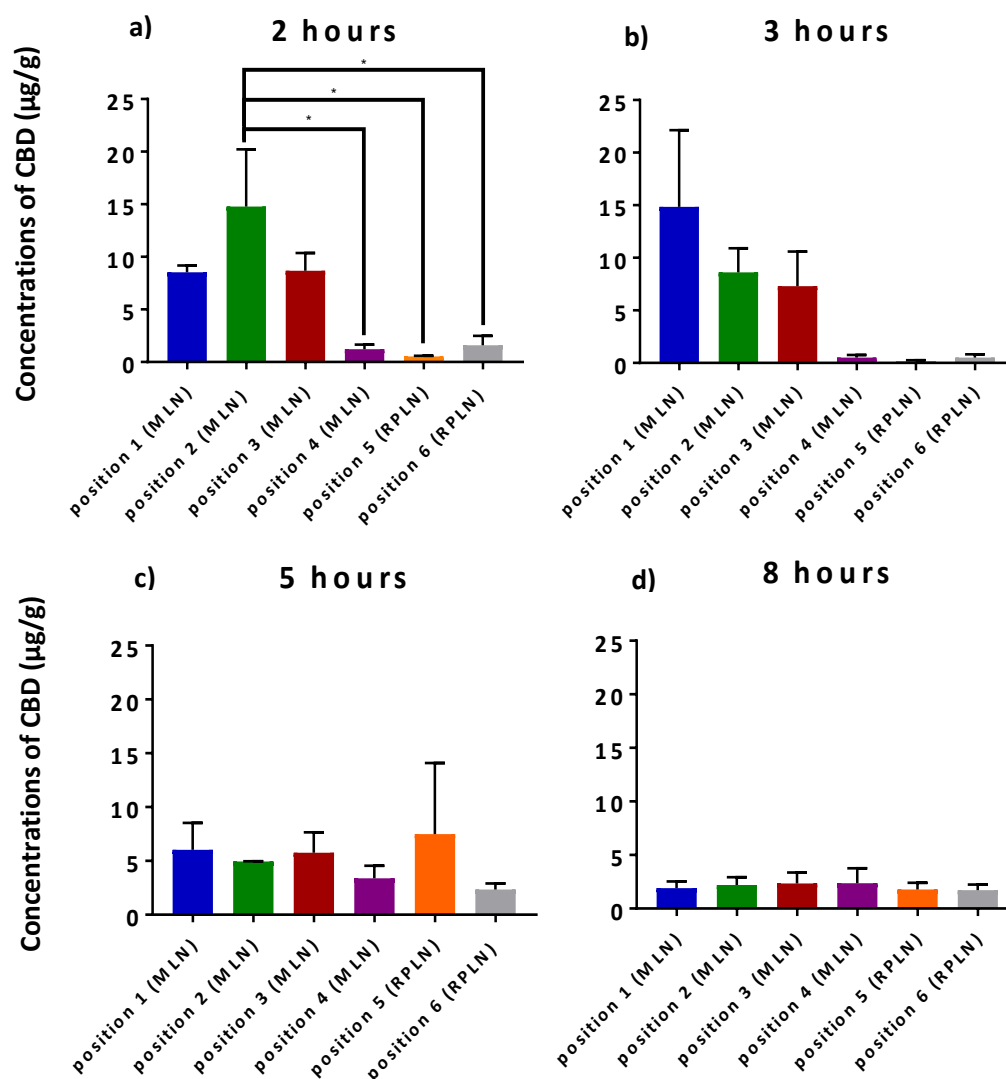


Figure 4.3. Distribution of CBD in MLN and RPLN at various time points post oral administration in sesame oil. The bar colours in this figure correspond to the positions of lymph nodes collected in Figures 4.1 & 4.2. All data are presented as mean \pm SEM, $n = 3$. Statistical analysis was performed using one-way ANOVA with Tukey's multiple comparisons test. * $P < 0.05$. No outliers were identified (Grubb's test, $\alpha = 0.05$).

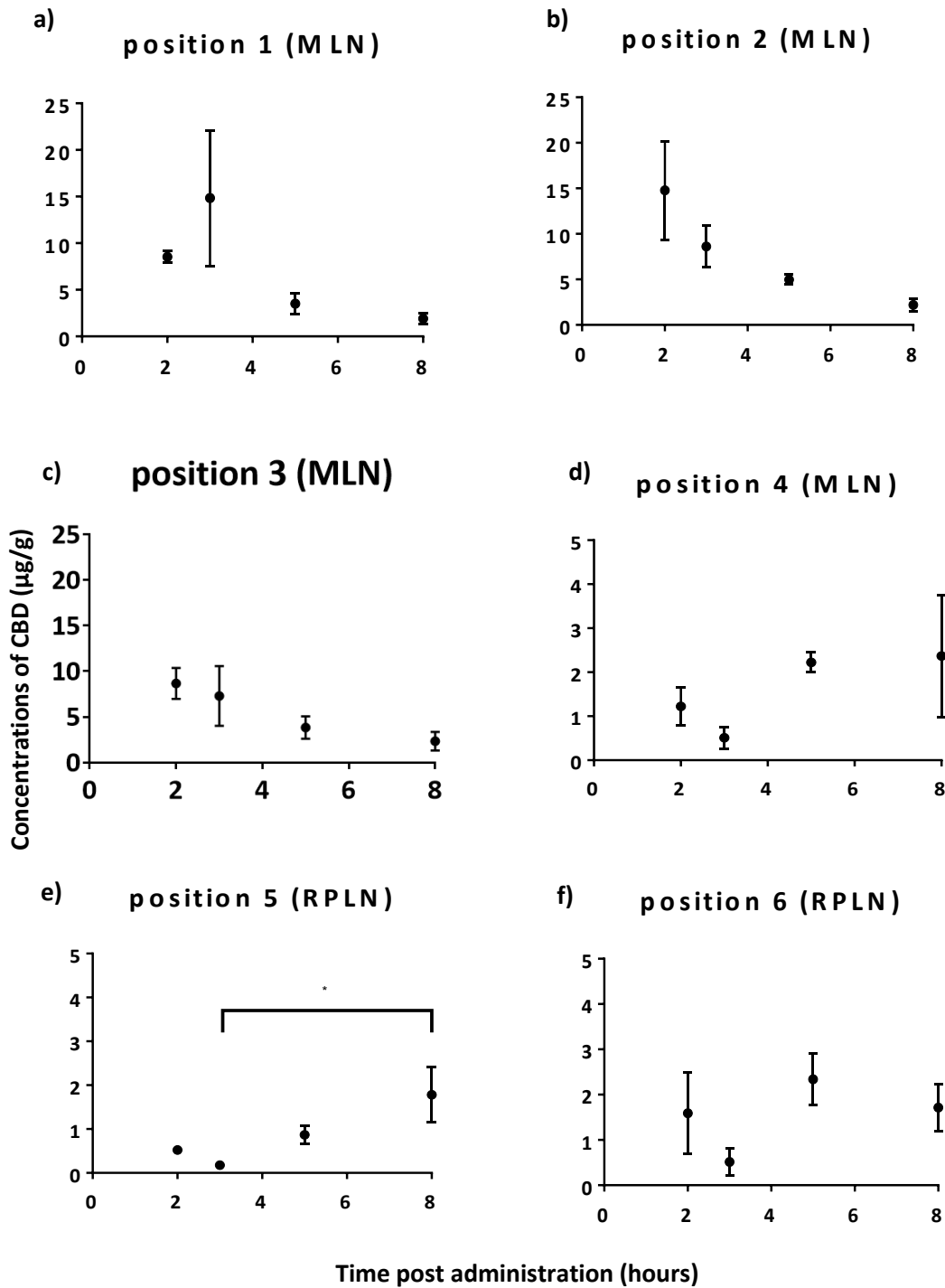


Figure 4.4. Distribution of CBD at various time points post oral administration in sesame oil in MLN and RPLN at various positions (a-f). The data in this figure is the same as the data in Figure 4.3, presented differently. All data are presented as mean \pm SEM, $n = 3$. Statistical analysis was performed using one-way ANOVA with Tukey's multiple comparisons test. * $P < 0.05$. No outliers were identified (Grubb's test, $\alpha = 0.05$).

4.4.1.2. Bio-distribution of CBD into individual RPLN at different time points following oral administration in sesame oil vehicle

It was also aimed to assess whether the RPLN could also be targeted using orally administered lipid-based formulations, and how the concentrations are compared to that of the MLN at various time points post dosing. At 2 hours post administration, MLN at position 2 contained significantly higher concentrations of CBD compared to both the iliac and para-aortic lymph nodes at position 5 and 6 respectively (Figure 4.3). Concentrations at position 5 and 6 were similar to those previously shown in plasma [70]. Relatively low concentrations in the RPLN 2 hours post administration are consistent with previous reports which showed no uptake of dye into the iliac or caudal nodes following injection into the small intestine and colon shortly after administration [19].

At 3 hours post administration, concentrations in RPLN were lower than in MLN however this was not significantly different. However, at both 5 and 8 hours post administration, concentrations of CBD were comparable in the MLN and RPLN at all positions (Figure 4.3). In addition to widespread drug delivery to MLN at multiple positions, this data demonstrates that the RPLN can therefore also be targeted through oral administration in lipidic vehicles. Importantly, at 5 and 8 hours post administration, concentrations of CBD in the RPLN were more than 20 times higher than concentrations previously reported in plasma [70]. Based on this, the accumulation of CBD in RPLN is not likely to be a result of redistribution from plasma following entry into systemic circulation. When comparing the differences in concentrations of CBD in the iliac / caudal nodes at position 6, at each time point, concentrations were not significantly different. However, at position 5 concentrations were significantly higher 8 hours post administration compared to

3 hours (Figure 4.4). Increasing drug concentrations over time may also indicate a delayed uptake as a result of lymph being directed from the MLN into the RPLN.

It should be noted that the concentrations observed in the RPLN at 3, 5 and 8 hours post administration were above the immunomodulatory threshold as previously determined [70]. CBD is likely therefore to exert pharmacological effects on the cells of RPLN, in addition to the MLN. It can also be hypothesised that through the mechanism of association with chylomicrons and lymphatic transport, other highly lipophilic compounds may be distributed in a similar way. This has relevance for metastatic cancers, in particular testicular and colon cancers, where RPLN are involved and avoidance of invasive lymph node dissection would be beneficial.

4.4.1.3. Bio-distribution of CBD into individual MLNs and RPLN at different time points following oral administration in different lipid-based formulations

To assess the impact that formulation has on the distribution of CBD in individual intestinal lymph nodes, concentrations were also compared following administration in other natural oils. Sesame oil contains high proportions of unsaturated long chain fatty acids [309] (Chapter 3, section 3.1.2.1). The fatty acid composition of rapeseed oil is very similar to that of sesame oil [326] and so any differences in distribution may be attributed to other components such as small molecules like lignans. In contrast, coconut oil contains a more varied mixture of fatty acids, including shorter chain fatty acids and saturated fatty acids, such as lauric acid [327]. It was therefore included so the impact of fatty acid composition on distribution could be assessed.

The concentrations of CBD in individual MLN and RPLN at 2, 3, 5 & 8 hours post administration following oral administration in coconut oil and rapeseed oil are shown in Figure 4.5 & 4.6, respectively. Unlike following administration in sesame oil, there was no statistical differences between concentrations of CBD in MLN individual lymph nodes at any time point when administered in coconut or rapeseed oil. In addition, concentrations in RPLN were comparable to that of MLN at all time points in both formulations. Concentrations of CBD in all nodes were generally lower at 2, 3 and 5 hours when formulated in coconut and rapeseed oil compared to sesame oil. At 8 hours post administration concentrations across all lymph nodes were comparable in all formulations. The reason for this is unclear, however is consistent with previous work showing sesame oil to be superior for delivery of CBD to MLN relative at a range of other lipid-based vehicles [109, 325]. There are several possible explanations for this. Firstly, natural oils such as sesame, coconut and rapeseed oils contain triglycerides with a range of chain lengths and degrees of saturation. It is possible that the triglyceride composition of sesame oil is more favourable for the formation of chylomicrons and subsequent lymphatic transport. In addition, natural oils contain a number of minor constituents (section 3.4.3.4. and 3.4.3.5) which may have bioactive properties which effect lymphatic transport including acting as co-factors during lipid absorption.

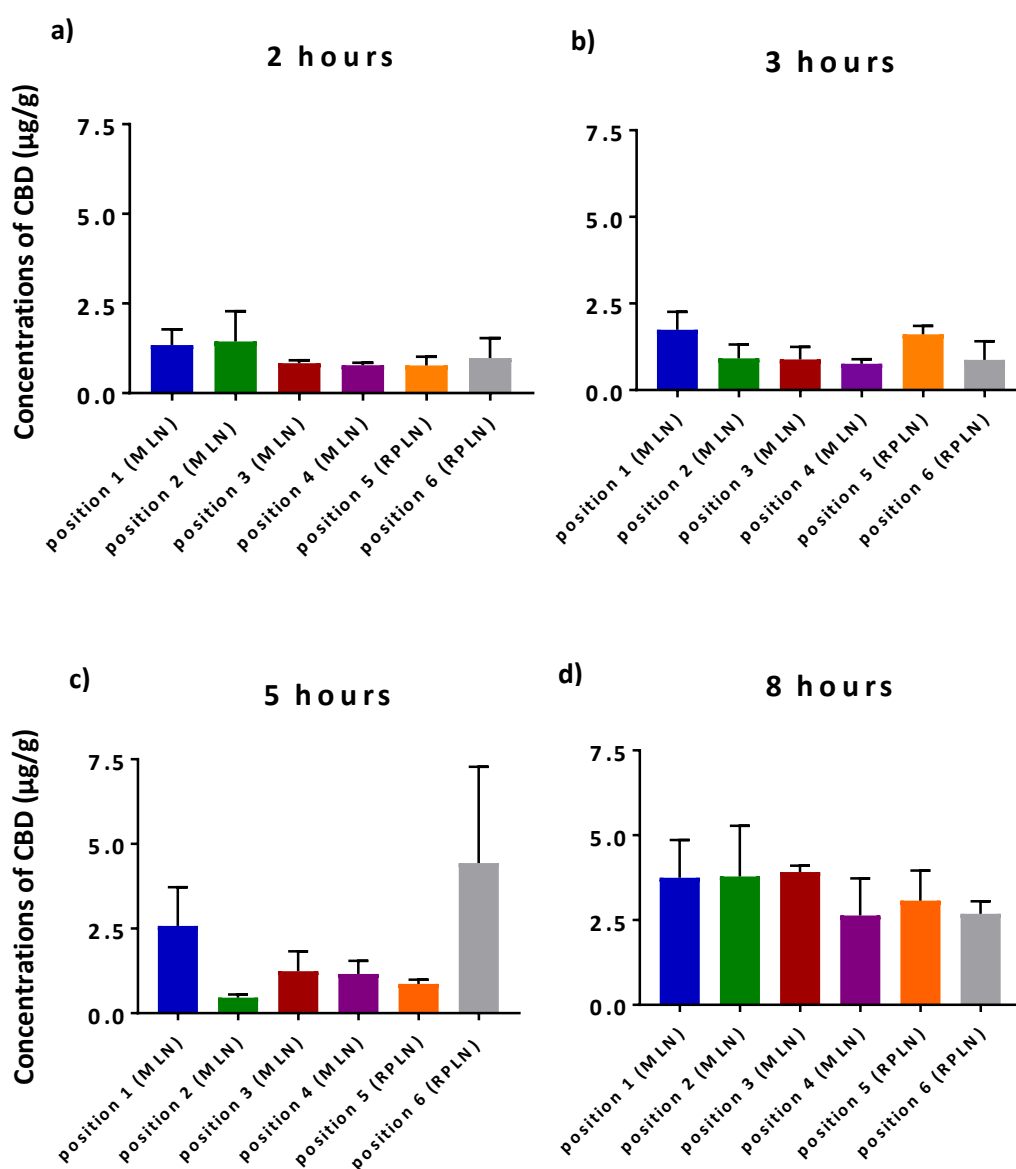


Figure 4.5. Distribution of CBD in MLN and RPLN at various time points post oral administration in coconut oil. The bar colours in this figure correspond to the positions of lymph nodes collected in Figures 4.1 & 4.2. All data are presented as mean \pm SEM, $n = 3$. Statistical analysis was performed using one-way ANOVA with Tukey's multiple comparisons test. * $P < 0.05$. No outliers were identified (Grubb's test, $\alpha = 0.05$).

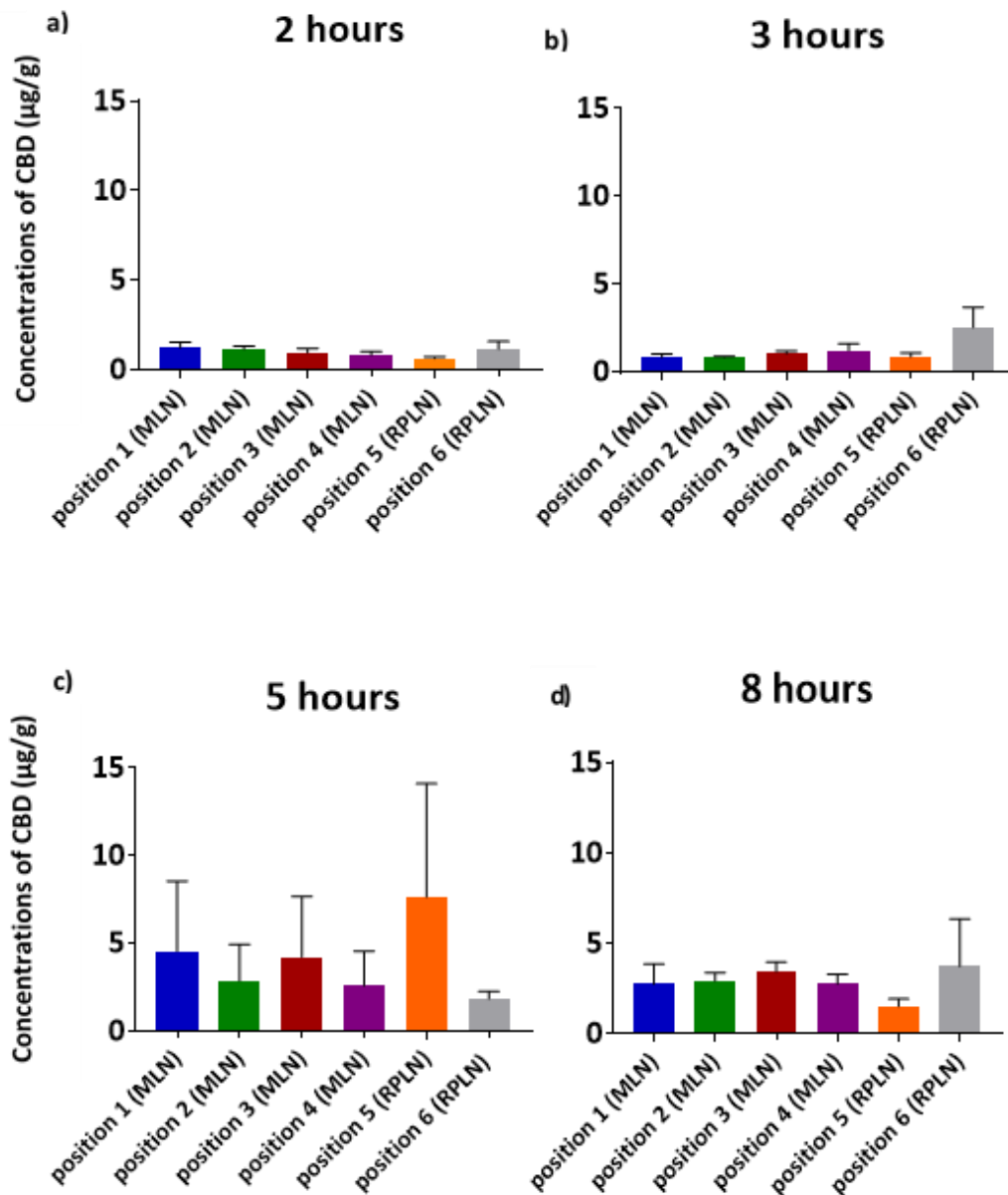


Figure 4.6. Distribution of CBD in MLN and RPLN at various time points post oral administration in rapeseed oil. The bar colours in this figure correspond to the positions of lymph nodes collected in Figures 4.1 & 4.2. All data are presented as mean \pm SEM, $n = 3$. Statistical analysis was performed using one-way ANOVA with Tukey's multiple comparisons test. * $P < 0.05$. No outliers were identified (Grubb's test, $\alpha = 0.05$).

Using the same data as presented in Figure 4.5 & 4.6, the concentrations in each lymph node over time were also compared (Figure 4.7 & 4.8). There was a trend towards increasing concentrations in all nodes at 8 hours post administration in coconut oil and rapeseed oil. Statistically significant increases in concentrations 8 hours post administration were seen at positions 3 and 5 for coconut oil (Figure 4.7) and positions 2, 3 and 4 for rapeseed oil (Figure 4.8). This delay in uptake into intestinal lymph nodes compared to sesame oil correlates with a later t_{max} with coconut and rapeseed oils (Feng *et al.*, unpublished data).

A one-way multiple comparisons ANOVA was also performed to compare exposure at different nodes at each time point across the 3 formulations. Concentrations of CBD were significantly higher with a sesame oil vehicle compared to rapeseed and coconuts oil at position 1 and 3, 2 hours post administration, position 2, 3 hours post administration and position 2, 5 hours post administration. Concentrations were also significantly higher with sesame oil compared to rapeseed oil at position 5, 5 hours post administration, and compared to coconut oil at position 5, 3 hours post administration. This supports previous work which showed CBD lymphatic drug delivery was superior with sesame oil compared to other formulations (Feng *et al.*, unpublished data).

Overall, the data from this section imply that using lipid-based vehicles, drug distribution to the individual nodes of the mesentery is widespread but variable with time. In addition, the RPLN can be targeted using several lipid-based formulations and concentrations above immunomodulatory thresholds can be achieved in these nodes.

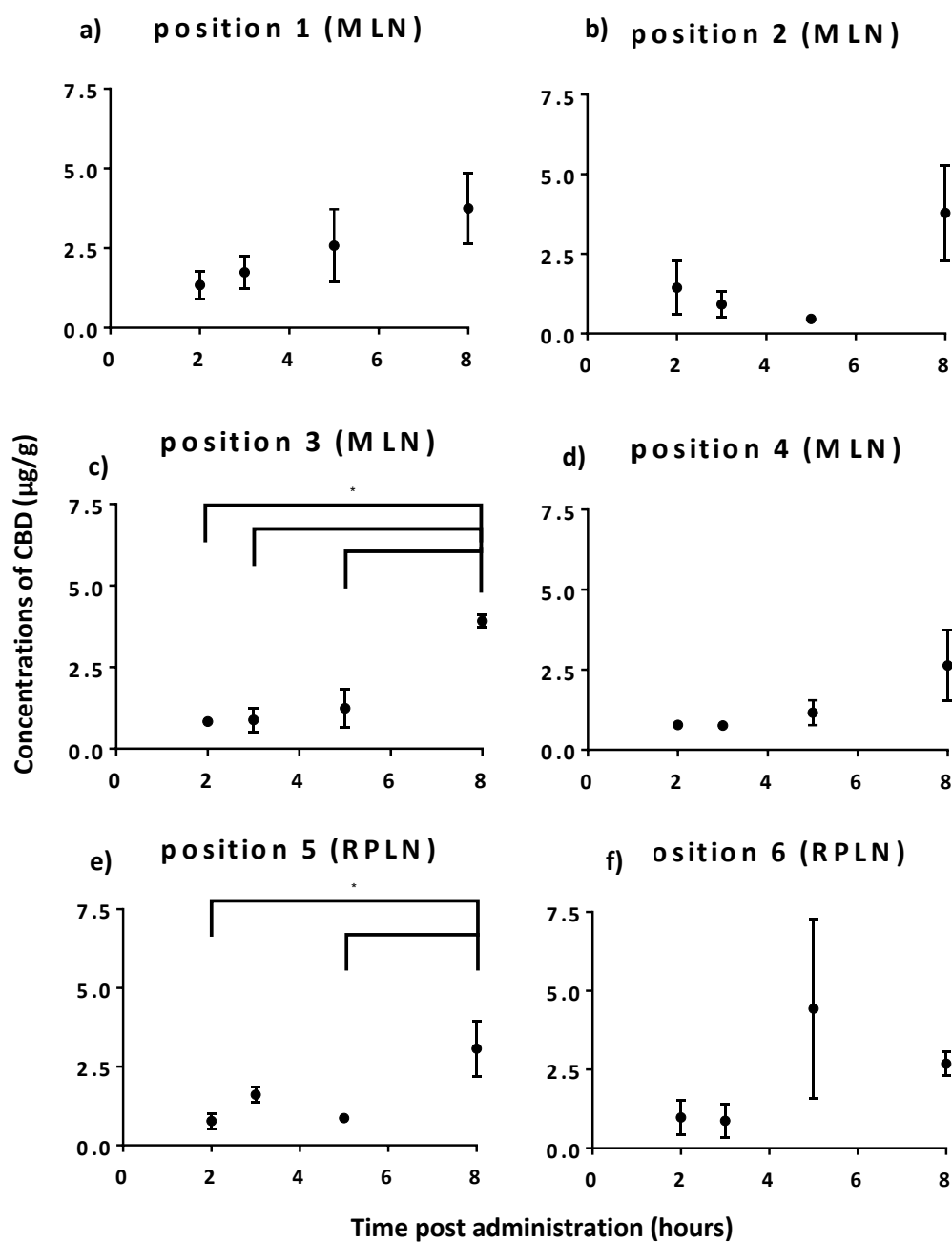


Figure 4.7. Distribution of CBD at various time points post oral administration in coconut oil in MLN and RPLN at various positions (a-f). The data in this figure is the same as the data in Figure 4.5, presented differently. All data are presented as mean \pm SEM, $n = 3$. Statistical analysis was performed using one-way ANOVA with Tukey's multiple comparisons test. * $P < 0.05$. No outliers were identified (Grubb's test, $\alpha = 0.05$).

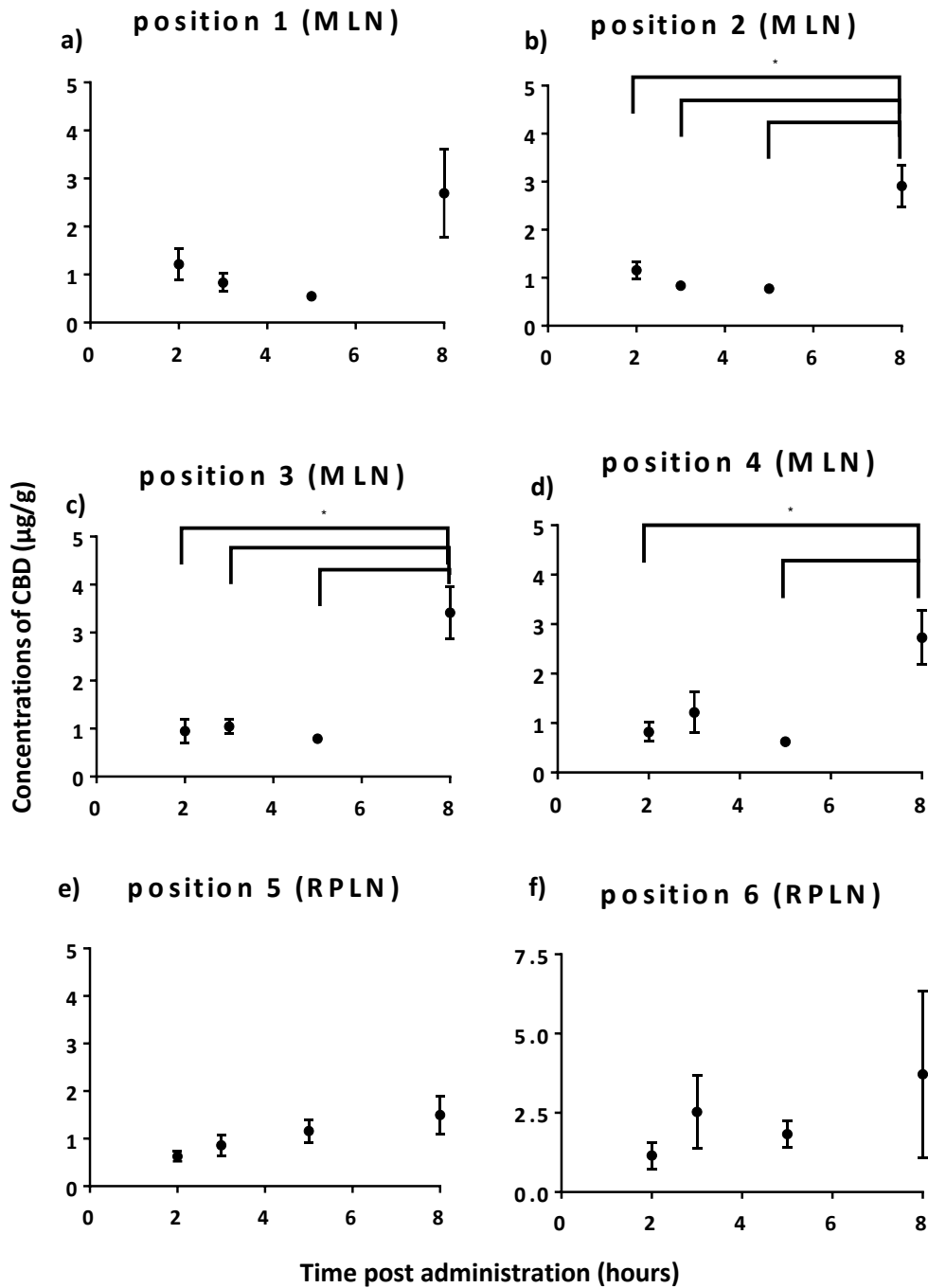


Figure 4.8. Distribution of CBD at various time points post oral administration in rapeseed oil in MLN and RPLN at various positions (a-f). The data in this figure is the same as the data in Figure 4.6, presented differently. All data are presented as mean \pm SEM, $n = 3$. Statistical analysis was performed using one-way ANOVA with Tukey's multiple comparisons test. * $P < 0.05$. No outliers were identified (Grubb's test, $\alpha = 0.05$).

4.5 Conclusions

In this Chapter an animal model was used to provide information on which specific lymph nodes can be targeted using orally administered lipid- based formulations. Firstly, when administered orally in sesame oil, CBD was shown to be delivered a higher concentrations into lymph nodes positioned second from the apex of the chain of mesenteric nodes 2 hours after administration in animal models. However, at later time points, drug exposure across the MLN was widespread and similar concentrations were observed throughout. When administered in other natural lipidic vehicles, drug delivery to the MLN was less efficient and concentrations were similar throughout all MLN. These findings indicate that drug concentrations in individual MLN vary with time and vehicle, however MLN throughout the mesenteric chain are exposed to orally administered drugs undergoing intestinal lymphatic transport.

It was also demonstrated for the first time that the RPLN can be targeted as well as the MLN. At 2 hours post administration in sesame oil concentrations of CBD in the RPLN were also significantly lower compared to the MLN second from the apex of the chain of nodes. However, at all later time points concentrations in the RPLN were similar to that of the MLN. When administered in rapeseed and coconut oil, concentrations in RPLN were consistently comparable to that of the MLN between 2 and 8 hours post administration. Therefore, in addition to the MLN, the RPLN may also be targeted by oral route of administration, which may have further implications for treatment of a range of diseases.

5. Assessing lymphatic uptake of lipids in healthy human volunteers using Magnetic Resonance Imaging

5.1. Introduction

Very few attempts have been made to quantify drug delivery to the intestinal lymphatic system in human volunteers. In one of the only examples in the literature, radioactivity following oral administration of radiolabelled testosterone was quantified. This however required a hugely invasive thoracic duct catheter following neck surgery [328]. Imaging the lymphatic system has the potential to inform which lymph nodes can be targeted using orally delivered drugs (section 1.4.2.).

A label-free Magnetic Resonance Imaging (MRI) method was recently described for the imaging of the intestinal lymph nodes in healthy human volunteers [18]. In this work, several parameters were measured, including lymph node major and minor axis length and Apparent Diffusion Coefficient (ADC), a measure of the extent of water diffusion. Large lipid droplets have been observed in MLN as a result of a high fat diet [19].

It has been widely observed that shortly after oral administration of lipids, intestinal lymph nodes swell as they receive lipid rich lymph draining from the intestine. Based on this, it was hypothesised that lymph nodes may increase in size as they receive lymph containing dietary lipids. As the composition of lymph draining into lymph nodes becomes more lipid rich, it was also hypothesised that the ADC may also change. Using these parameters as indications of lipid uptake, the MRI methodology previously described may thus be adapted to allow for the

identification of nodes involved in lymphatic uptake of dietary lipids, lipid excipients and co-administered drugs.

5.2. Chapter aims and objectives

Using an MRI method previously developed for the imaging of intestinal lymph nodes, the feasibility of MRI for imaging and quantifying the uptake of lipids into lymph nodes in humans was assessed. Specific aims include:

- Assessment of the feasibility of MRI methodology for repeated longitudinal imaging of the intestinal lymphatics in healthy human volunteers.
- Application of the MRI method to image the intestinal lymphatics pre and post high fat meal
- Determination of potential measurable changes in various parameters identified in individual lymph nodes indicating uptake of lipids.

5.3. Methods and materials

5.3.1. Magnetic resonance imaging in human volunteers

The study protocol was approved by the University of Nottingham School of Medicine and Health Sciences Research Ethics Committee, Queens Medical Centre, Nottingham, University Hospitals, Nottingham, UK. (ref no. 358-1906). All subjects gave written informed consent and had no contraindications to MRI.

5.3.1.1. Study participants

All three participants were healthy male volunteers aged 25-30 years with no history of underlying cardiac or gastrointestinal disorders or symptoms. All

participants had a healthy BMI (between 18.5 and 24.9) and no food intolerances or allergies and were not known to be taking any medication.

5.3.1.2. Study Design

Participants were asked to fast from 10 pm the evening prior to the MRI study day. Water was allowed up until 2 hours prior to scanning. Participants were scanned in the supine position at fasted baseline and then 120, 180, 240 and 300 minutes after the consumption of a high fat content meal. The meal was consumed directly after the baseline scan was performed. The meal consisted of 300 g creamed rice pudding uniformly mixed with 25 g seedless raspberry jam and 30 g double cream, and a drink of 100 ml orange juice with 240 mL of water (total energy content 518.8 kcal, fat content 18.5 g and approximately 25 % energy from fat, with a known median gastric half-emptying time of 80 minutes [329]). No additional food or water consumption was permitted throughout the duration of the imaging.

5.3.1.3. MRI acquisition

All images were acquired using a Philips 3T Ingenia (Best, the Netherlands) with a 32 channel dStream torso coil (Philips Healthcare). The scanning process was performed in my presence by Hannah Williams. Anatomical imaging planes are depicted in Figure 5.1.

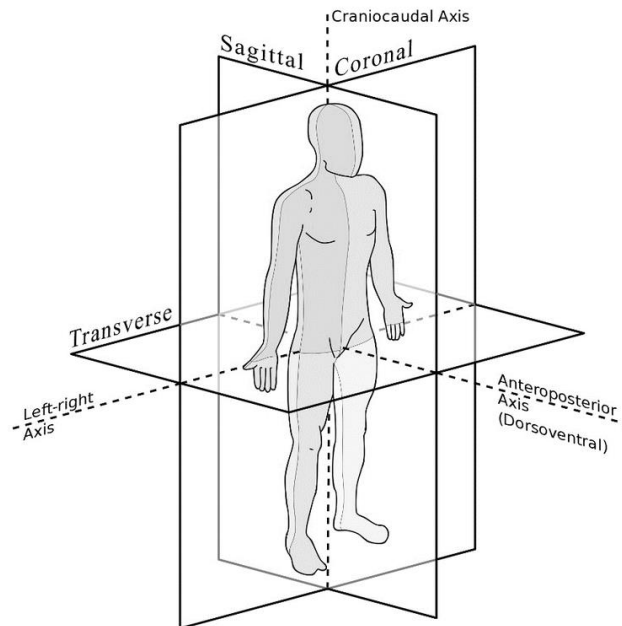


Figure 5.1. Anatomical planes of the human body [6].

5.3.1.4. Lymph node imaging

The Diffusion-weighted whole-body imaging with background suppression (DWIBS) sequence was used to highlight the lymph nodes within the abdomen (pre inversion, $T_I=260$ ms, for background suppression). A free breathing coronal DWIBS was first acquired to gain a general idea of where nodes were located. Following this, a respiratory triggered DWIBS was performed in the sagittal plane, to reduce through plane motion. Eight imaging slices of the abdomen were acquired at each time point, with $2.5 \times 2.5 \times 4.68$ mm³ voxels, reconstructed to 1.56×1.56 mm² in-plane resolution and a slice thickness of 4.68 mm with 0 mm gap between them (Time to Echo (TE)= 75 ms, Inversion time (TI)= 260 ms, Repetition time (TR_{min})=3000 ms, Sensitivity Encoding (SENSE) factor 2.3).

It was hypothesised that the lymph nodes that receive lipids from the meal would physically swell causing an increase in size. Three parameters (area, major axis and minor axis) were recorded in an attempt to characterise any changes in lymph node size following the high fat meal. The number of lymph nodes visible at

each time point was also compared in order to assess whether some lymph nodes which in the fasted state are not initially visible then become visible as they receive lipids.

It was also hypothesised that ADC may change as the lymph nodes receive lipid rich lymph from the intestine. Two diffusion weightings ($b=0,600 \text{ s/mm}^2$) were used to measure ADC across the 8 slices.

5.3.1.5. Gastric volume (T2)

Gastric emptying and small bowel water were also measured to monitor the progression of lipids through the GI system. Gastric volumes were determined using a coronal Half-Fourier Acquisition Single-shot Turbo spin Echo (HASTE) sequence. Twenty- eight slices were acquired at each time point with $1.4 \times 1.7 \times 5 \text{ mm}^3$ voxels reconstructed to $1 \times 1 \text{ mm}^2$ in plane resolution with a slice thickness of 5mm and slice gap of 1 mm (TE=96 ms, TR=1262, SENSE factor 2.0).

5.3.1.6. Small bowel water content (SBWC)

SBWC was determined using a single shot, fast spin echo sequence (Rapid Acquisition with Relaxation Enhancement, RARE) as previously described [330]. Briefly, 20 coronal slices (7 mm slice thickness, no gaps in-between slices, $0.78 \text{ mm} \times 0.78 \text{ mm}$ in-plane reconstructed resolution) were acquired in a single breath hold (TR = 1169 ms, TE = 400 ms, acquired resolution = $1.4 \text{ mm} \times 1.76 \text{ mm}$, SENSE factor 2).

5.3.1.7. MRI data analysis

For each lymph node a region of interest (ROI) was drawn around the periphery of the node on the two diffusion weighted images using Medical Image

Processing, Analysis and Visualization software (Version 9.0.0, National Institutes of Health) [331]. Area, major and minor axis were calculated. The signals from the two b value images were used to calculate ADC using the formula $ADC = -1/b_{600} \ln(S(b_{600})/S(b_0))$. Where a lymph node could be consistently imaged across all time points, the % change in each parameter relative to baseline per lymph node was calculated. This allowed for changes in smaller lymph nodes to be equally represented. The position of each lymph node in terms of vertebra level was also recorded in an attempt to assess which lymph nodes were being imaged [28]. The gastric volumes were calculated by drawing a region of interest around the bright content of the stomach in MIPAV on the T2 weighted dataset. The total volume was a sum of the volumes measured from each of the image slices. SBWC measurement was analysed with in-house software which was previously described and validated [332].

The reproducibility of data acquired from ROIs drawn in MIPAV was determined by drawing ROIs around the same randomly selected 15 nodes 3 times respectively (1 node per time point per participant). Relative Standard Error (RSD) and Relative Error (RE) were calculated as a measure of accuracy and precision respectively. All repeats were performed by the same observer. All data are presented at mean \pm standard error of the mean (SEM). A one- way ANOVA followed by Tukey's multiple comparisons test was used to compare the mean % change from baseline of nodes in all slices at each time point. The same nodes were compared at each time point. A *p* value <0.05 was considered statistically significant. All figures and statistical tests were generated in GraphPad Prism (version 7).

5.4. Results and Discussion

5.4.1. Assessment of lymphatic uptake of lipids using MRI in healthy human volunteers

In addition to the bio-distribution studies in rats described in Chapter 4, assessment of the feasibility of a non-invasive longitudinal imaging method to determine the uptake of lipids in the intestinal lymphatics following oral administration was performed. Specifically, the aim of this study was to establish whether MRI could be utilized to image the intestinal lymph nodes of healthy human volunteers at multiple time-points pre and post meal. Through repeat measurements of various parameters such as lymph node size and ADC, the feasibility of this method to identify changes in intestinal lymph nodes following the ingestion of a fatty meal was also assessed. Measurable changes in lymph nodes following lipid uptake could then be exploited to track the movement of lipids and drugs through the lymphatic system and inform which lymph nodes could be targeted using orally administered lipid-based formulations.

5.4.1.1. Gastric volume and SBWC to inform MRI scanning intervals in human volunteers

Gastric volume and SBWC were measured at several time points following the high fat meal in order to predict when lipids may be entering the intestinal lymphatics for each individual. This could then be used to inform scanning intervals. In one participant, gastric volume was largely unchanged across all time points, the reason for which is unclear. However, in the other 2 participants an increase in gastric volume was observed at 120 minutes post meal (Figure 5.2). Gastric volume appeared to then be reduced to approximately baseline equivalent volumes at 180

minutes post meal (Figure 5.2). Similarly, SBWC, appeared to decrease in all subjects as a result of nutrient-driven fluid absorption [24]. This was followed by an increase at 180 – 120 minutes post meal (Figure 5.2). Based on this, it was predicted that lipid uptake into the lymphatics would be the greatest after 120 minutes post meal. Postprandial human plasma triglyceride concentrations have been shown to increase after 1 hour, reaching a peak between 3-4 hours [333, 334]. Since lipid-rich lymph will ultimately collect in the thoracic duct prior to entering the systemic circulation, the majority of lipids were predicted to have left the intestinal lymphatic system by 300 minutes post meal. Subsequently scanning intervals after baseline were 120, 180, 240 & 300 minutes post meal.

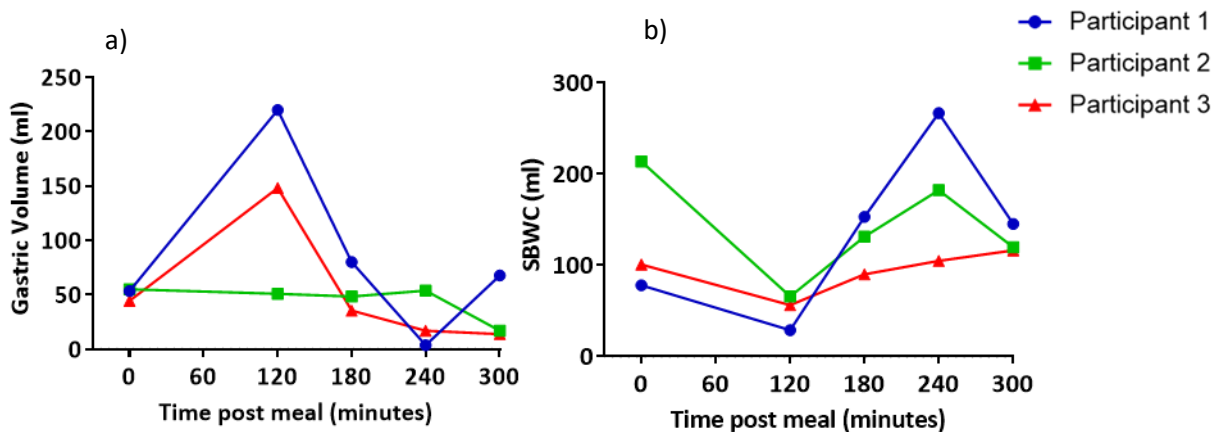


Figure 5.2. a) Gastric volume and b) small bowel water content (SBWC) post high fat meal. Each line represents data from an individual participant.

5.4.1.2. Number of lymph nodes

The number of abdominal lymph nodes visible at each time point was also compared in order to assess whether some lymph nodes which in the fasted state are not visible then become visible as they receive lipids-rich lymph.

The number of nodes visible in each scan at each time point ranged from 39 to 94 with an average of 61 nodes visible per time point per participant (mean \pm SEM 4.27) (Figure 5.3). In two out of three participants, more lymph nodes were visible at 180, 240 & 300 minutes post meal relative to baseline (Figure 5.3).

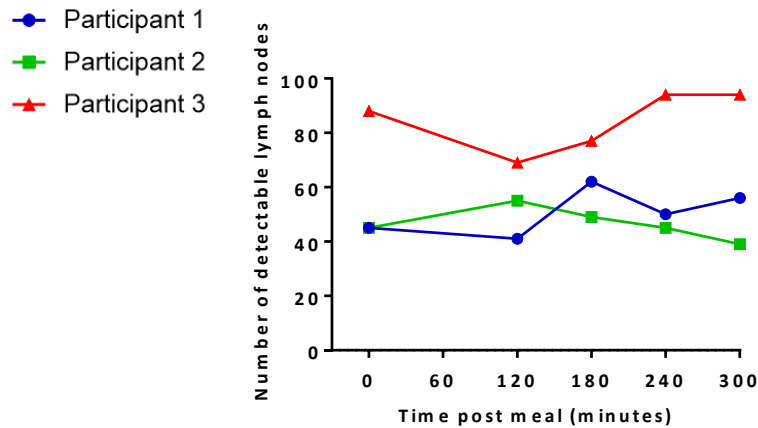


Figure 5.3. Number of lymph nodes visible at each time point post meal. a) Data represents the combined total of nodes across all slices. Each line represents data from an individual participant.

In order to compare the same individual lymph nodes at each scanning time point, imaging planes needed to be consistent. To ensure comparisons of “like for like” slices, the vertebrae of the spine were used as an anatomical marker. Using this approach, the same lymph nodes could be identified across different scanning time points (Figure 5.4).

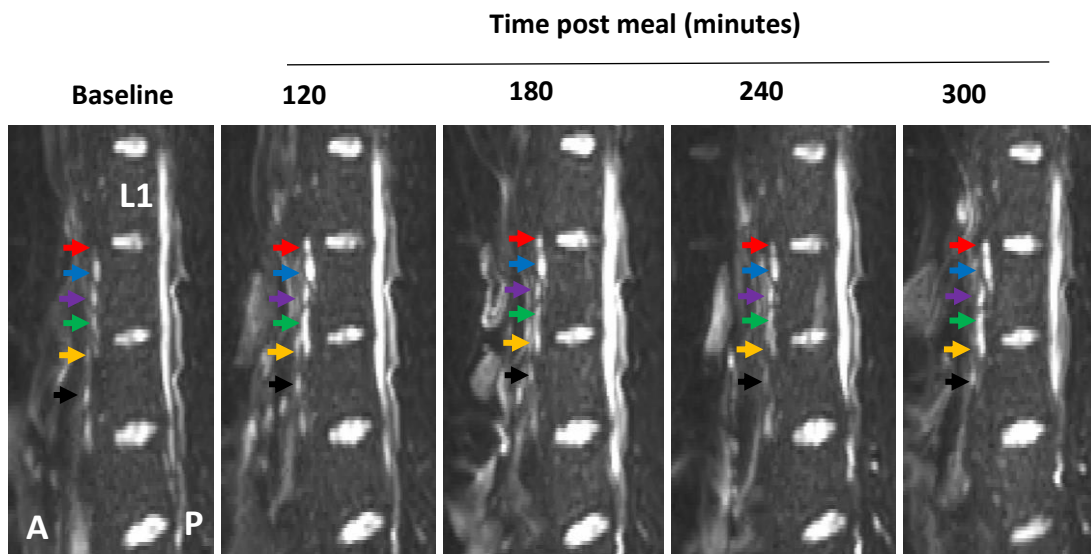


Figure 5.4. Example Diffusion Weighted Image (DWI) showing how the vertebra of the spine can be used as an anatomical marker to allow for the same lymph nodes to be consistently imaged at multiple time-points pre and post meal. The first lumbar vertebra is indicated (L1) and lymph nodes are indicated by coloured arrows. Colours represent the same individual lymph at each time point. The anterior side (A) of the body is to the left of each image and the posterior side (P) is on the right.

The number of nodes consistently imaged across all time points were 11 for participant 1, 22 for participant 2 and 33 for participant 3 respectively. Lymph nodes that could be consistently imaged across all scanning time points were then analysed and compared at each time point relative to baseline in an attempt to identify changes following intake of the high fat meal.

Table 5.1. Vertebral level of nodes imaged across all time points. Data

represents the mean across all participants \pm SEM.

	Vertebra L1-2	Vertebra L2-3	Vertebra L3-4	Vertebra L4 & below
Number of nodes visible across all time points	5 \pm 1	11 \pm 3	4 \pm 1	1 \pm 1
As a percent of nodes visible across all time points	24 %	52 %	18%	6%

5.4.1.3. Grouping of imaged lymph nodes

Few examples in the literature describe the intestinal lymph nodes in the sagittal plane. Abdominal lymph nodes are often distinguished by their location relative to major blood vessels (Section 1.1.3.2). However, since the blood vessels of the mesentery were not distinguishable in the images collected in this work, lymph nodes could only be grouped by their anatomical location on the craniocaudal and anteroposterior axis (Figure 5.1, 5.5). More specifically, because the vertebra of the spine were clearly visible lymph nodes were first grouped by their position of the craniocaudal axis in relation to the vertebra.

The majority of the nodes imaged were positioned slightly anterior to the centre of the spine between the second and third lumbar vertebra (Table 5.1). Based on their location, these nodes are most likely to be retroperitoneal nodes, more specifically the preaortic nodes. In some scans, nodes were visible closer to the spine (Figure 5.5) and therefore more likely to be the retroaortic nodes. In addition, a small number of nodes were located between the fourth and fifth vertebra and likely to be the iliac nodes.

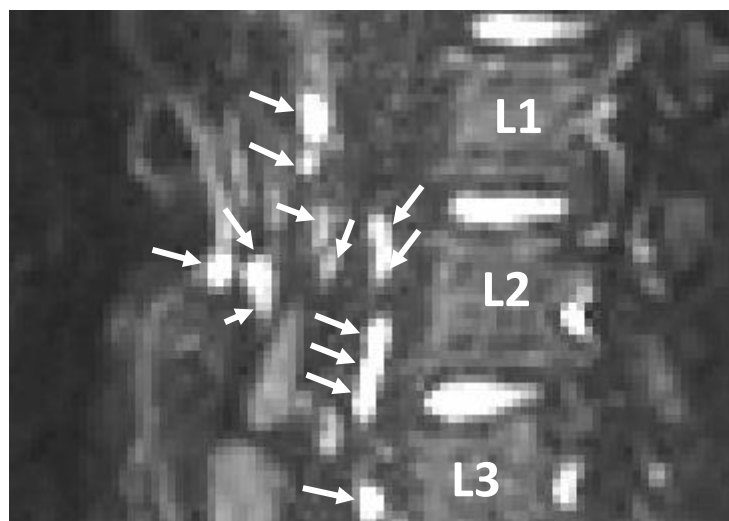


Figure 5.5. Example Diffusion weighted Image (DWI). Lymph nodes can be seen along the spine at various distances from the spine. Lymph nodes are indicated with white arrows. The lumbar vertebra (L1-3) are also indicated.

5.4.1.4. Lymph node size

It was hypothesised that as lymph nodes receive lipids from the meal, they would physically swell causing an increase in size. Three parameters (area, major axis and minor axis) were recorded in an attempt to characterise any changes in lymph node size following the high fat meal.

Where a lymph node could be consistently imaged across all time points, the percentage change in each parameter relative to baseline per lymph node was calculated. This allowed for changes in smaller lymph nodes to be equally represented. One node was excluded from the data set based on fluctuations of over 200% change area at adjacent scanning time points, which was deemed physiologically impossible and likely to be the result of a partial volume error.

For each parameter, data are first presented as the mean of individual changes in individual lymph nodes for all consistently imaged lymph nodes per participant. Minor axis length only increased above baseline in one participant. However, in two out of three participants, mean node area and major axis lengths increased at both 120 and 180 minutes post meal relative to baseline (Figure 5.6). The largest increases relative to baseline were seen in lymph node area, which was higher both at 120 minutes and 180 minutes post meal in two out of three participants (Figure 5.6). For participant 2, % change in area was statistically significant at 180 and 300 minutes post meal relative to baseline (Figure 5.6). Area may therefore be a more sensitive measure for monitoring lipid uptake than axis length. This could be because both changes in major and minor axes lengths are simultaneously reflected in the area.

In order to compare whether changes were more pronounced in some lymph nodes relative to others, data is then also presented with nodes subcategorised into changes in individual lymph nodes at each vertebra level for each participant. For participant 2, lymph nodes positioned between lumbar vertebrae 1-2 appeared to have the most pronounced increases in area, major and minor axis relative to baseline, however this was not statistically significant. Change in area was significantly higher at 180 compared to 300 minutes post meal in participant 3 for lymph nodes positioned between lumbar vertebrae 3-4. Generally,

there was no clear trend indicating a correlation between lymph node positioning relative to a vertebra level and change in size at each time point (Figure 5.7).

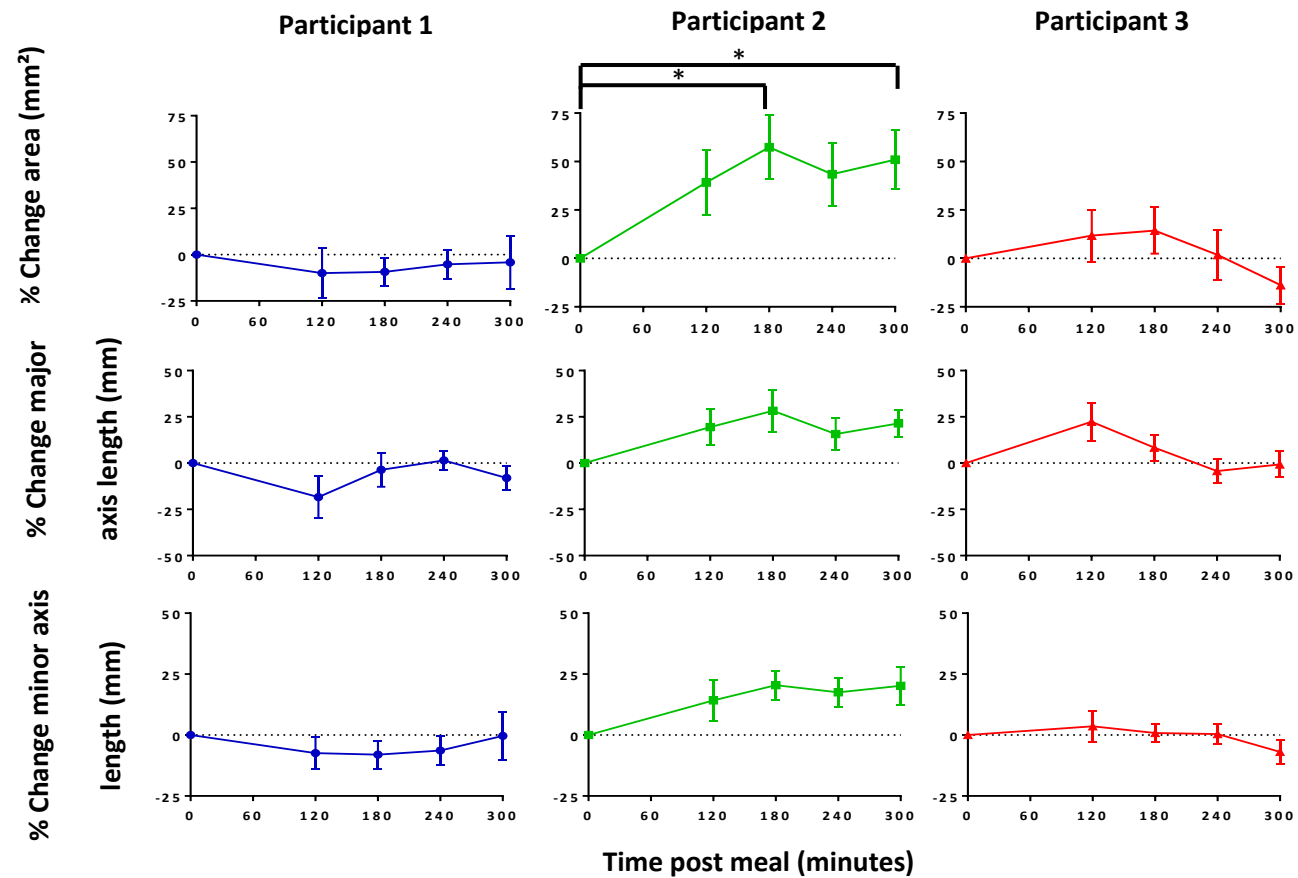


Figure 5.6. Change in lymph node area, major and minor axis length relative to baseline post high fat meal. Data represents mean \pm SEM of all nodes that were consistently imaged across all time points. $n=11$ for participant 1, $n=22$ for participant 2 and $n=33$ for participant 3.

Statistical analysis was performed using one-way ANOVA with Tukey's multiple comparisons test. $*p<0.05$.

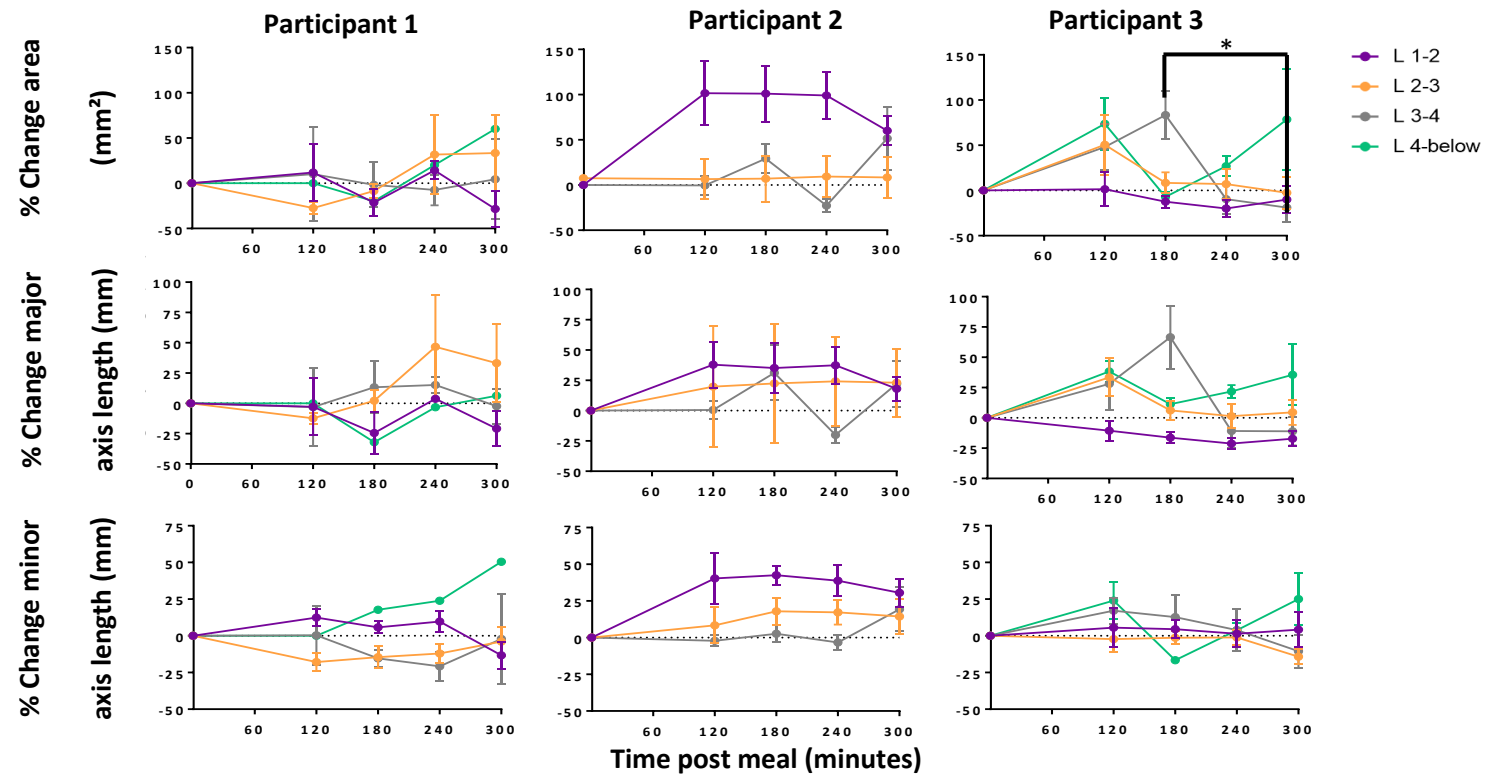


Figure 5.7. Change in lymph node area, major and minor axis length relative to baseline post high fat meal. Data represents the average difference between individual lymph nodes at each vertebra level (mean \pm SEM). L = lumbar vertebra. The data in this figure is the same as in Figure 5.6, displayed differently. Statistical analysis comparing change in area, major and minor axis length at each time point was performed using one-way ANOVA with Tukey's multiple comparisons test. * $p < 0.05$.

5.4.1.5. ADC

It was also hypothesised that ADC may change as the lymph nodes receive lipid-rich lymph from the intestine. Two diffusion weightings ($b=0,600 \text{ s/mm}^2$) were used to measure ADC across the 8 slices. In all three participants, there was an increase in mean lymph node ADC post-meal relative to baseline (Figure 5.8.). Increases in ADC appeared to be highest at 120 and 180 min post-meal, which encouragingly correlated with time scale predictions on gastric volume and SBWC. However, this was not statistically significant.

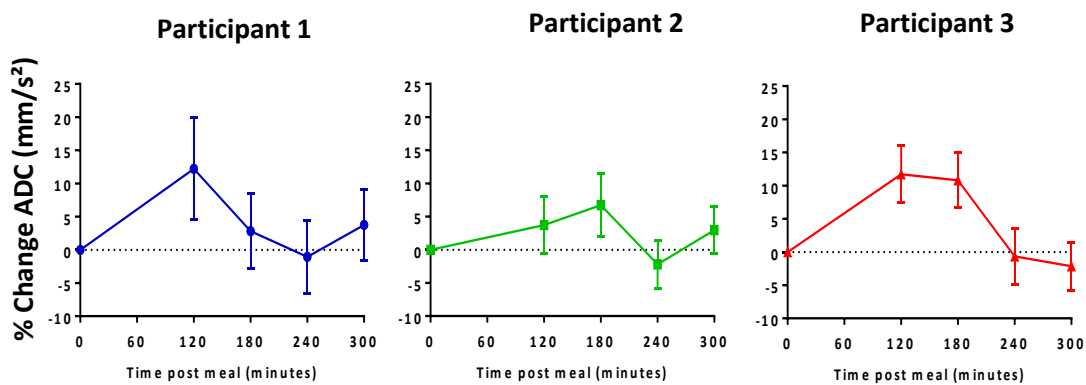


Figure 5.8. Change in lymph node Apparent Diffusion Coefficient post high fat meal.

Data represents the average difference between individual lymph nodes (mean \pm SEM).

b). $n=11$ for participant 1, $n=22$ for participant 2 and $n=33$ for participant 3.

Largest increases in ADC appeared to be in nodes located between the first and second, and second and third lumbar vertebra (Figure 5.9). However, no increases in ADC were statistically significant compared to baseline. In participant 3, a peak increase in ADC

was observed at 180 minutes post meal and was significantly higher compared to 300 minutes post meal, at which ADC was similar to baseline.

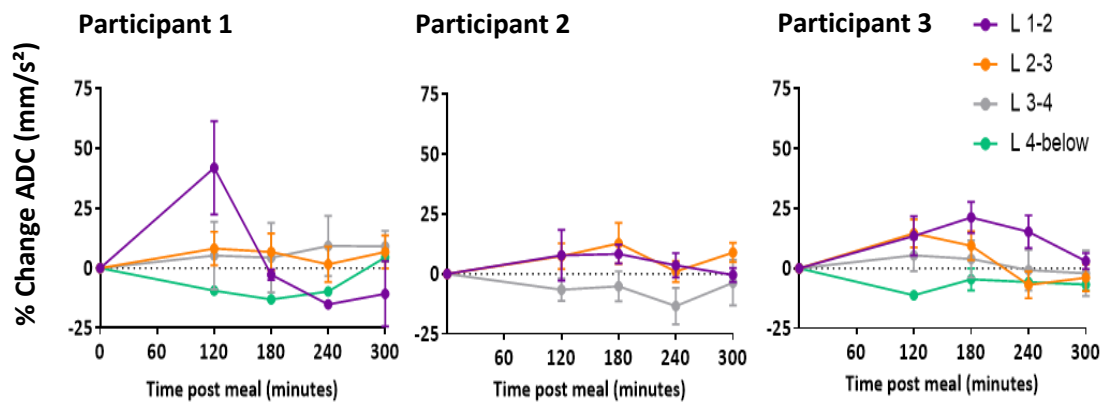


Figure 5.9. Change in lymph node Apparent Diffusion Coefficient post high fat meal.

Data represents the average difference between individual lymph nodes at each vertebra level (mean \pm SEM). L = lumbar vertebra. The data in this figure is the same as in Figure 5.8. displayed differently. Statistical analysis comparing change in ADC at each time point was performed using one-way ANOVA with Tukey's multiple comparisons

test. * $p < 0.05$.

5.4.1.6. Reproducibility.

The reproducibility of ROI drawing in MIPAV for 15 randomly selected nodes is demonstrated in Table 5.2. In some cases, inconsistency in ROI drawing resulted in a large error, which may account for some of the variability in data observed. ADC was the parameter in which reproducibility was the most consistent.

Table 5.2. Relative standard deviation (RSD) and Relative Error (RE) for 15 nodes (n=3).

Node	Area		Major axis		Minor axis		ADC	
	RSD	RE	RSD	RE	RSD	RE	RSD	RE
1	20.20	11.66	15.12	8.73	16.74	9.67	17.60	10.16
2	8.17	4.71	5.70	3.29	5.13	2.96	0.67	0.39
3	0.00	0.00	1.29	0.75	1.30	0.75	0.67	0.38
4	14.39	8.31	3.96	2.29	17.99	10.38	3.22	1.86
5	29.99	17.32	18.38	10.61	17.02	9.83	3.09	1.79
6	14.89	8.59	3.67	2.12	17.99	10.39	0.73	0.42
7	8.41	4.85	5.07	2.93	22.43	12.95	0.98	0.56
8	13.61	7.86	12.55	7.25	4.95	2.86	1.58	0.91
9	6.43	3.71	3.79	2.19	2.58	1.49	1.10	0.64
10	11.66	6.73	4.31	2.49	7.81	4.51	12.11	6.99
11	16.23	9.37	10.03	5.79	8.68	5.01	1.18	0.68
12	44.04	25.43	35.89	20.72	8.41	4.85	6.57	3.79
13	9.94	5.74	10.05	5.80	3.89	2.24	5.18	2.99
14	25.12	14.50	10.77	6.22	19.27	11.12	4.19	2.42
15	12.86	7.42	8.61	4.97	13.90	8.02	18.96	10.94

5.5. Conclusions

To compliment bio-distribution experiments in animals, the feasibility of a previously developed MRI method for imaging abdominal lymph nodes in healthy human volunteers was assessed for imaging the uptake of dietary lipids. Data collected as part of this chapter could then model the potential lymphatic uptake of orally administered lipid-based formulations.

Individual lymph nodes could be repeatedly imaged at multiple time points. Postprandial increases in lymph node size and ADC could be observed. Larger changes relative to baseline were observed when comparing lymph node area than when comparing major and minor axes lengths. However, ADC was the only parameter to consistently change across all participants and so may show the most promise for tracking the movements of lipids through the intestinal lymphatic system and interaction with immune cells. Based on this, the MRI methodology described represents a safe and label-free approach which may be used to inform which lymph nodes can be targeted using orally delivered lipid-based formulations. Future work should focus on ensuring the reproducibility in a larger participant cohort, as well as optimisation of the methodology to reduce variability.

6. General Discussion and Further Work

6.1. Key findings and implications

Taken collectively, the work in this thesis has provided novel insights into distribution of small molecule drugs in the intestinal lymphatic system following oral administration. This has included highly exploratory feasibility assessments of a range of techniques for imaging the intestinal lymphatics. For much of this work, Cannabidiol (CBD) was used a model drug, on which assumptions about lipophilic small molecule distribution generally were made.

The initial work described focussed on the adaptability of Secondary ion mass spectrometry (SIMS) analysis for determining drug distribution within the defined cellular compartments of lymph nodes. More specifically, suitability of a recently developed hybrid instrument, termed OrbiSIMS, was assessed.

The superior sensitivity and mass resolution power of OrbiSIMS compared to conventional ToF-SIMS for detection of CBD in tissue samples was demonstrated. Data suggested that sensitivity was reduced under cryo conditions, however these temperatures were necessary to prevent CBD sublimation under high pressures. Although a formal investigation into the limit of detection of the method used was not performed, it was shown that previously determined *in vivo* relevant concentrations of CBD (5-10 μg) [70, 109, 325] could be detected in MLN tissues. To our knowledge, this work represents the lowest reported concentrations of exogenous drug detected in tissue using SIMS instrumentation. However at lower concentrations, large variability in ion abundance was observed, suggesting the limit of the sensitivity of the instrument was reached. Although the ionisation and subsequent ion detection of different drug molecules will ultimately differ to CBD,

this work may indicate that lack of sensitivity may impede the use of OrbiSIMS for imaging drug distribution in other *ex vivo* samples, where concentrations are lower.

Application of the OrbiSIMS method allowed for an image of CBD distribution in a MLN to be obtained. CBD distribution appeared primarily in the paracortex of the node. This work represents the first entirely label and matrix free visual evidence of drug distribution in lymph nodes at peak lymphatic absorption following oral delivery. In addition, distribution primarily in the paracortex has not been previously reported and may therefore provide an insights into the mechanisms by which CBD exerts its immunomodulatory effects *in vivo*. However, generation of conclusions about CBD distribution was significantly hindered by the inability to reproduce images of CBD in lymph nodes, which again may be a limitation of the method. A calibration curve generated from homogenates spiked with known concentrations of CBD was used to calculate CBD concentrations in sections from dosed animals. Concentrations were in the physiological ranges previously determined *in vivo*, however the method was not fully validated. Although there was no evidence to support the presence of a matrix effect, there was again some variability in the data which reduces the confidence behind it, therefore further work should be used to confirm CBD distribution.

In further exploratory work, multi-variate analysis (MVA) was employed to compare spectra from different cellular regions of interest (ROI) in lymph node tissue. In addition to CBD, a number of biomolecules including fatty acids, phosphoinitiol and cholesterol sulphate could be imaged and assigned. Fatty acids such as oleic acid, linoleic acid and palmitic acid were more abundant in the periphery of the node, however were mainly isolated to one ROI. Again the lack of repeated imaging limits the ability to make conclusions about the relevance of this finding. The simultaneous localisation of CBD with an immune cell marker, which

would aid conclusions about drug cell interactions, therefore remains yet to be achieved. A comparison of tissue sections from animals dosed with CBD and not dosed with CBD was hindered by the fact that non-dosed animals were not fasted. In terms of tissue analysis, SIMS is limited by its inability to detect intact polypeptides such as cytokines. The identification of specific immune cell markers using SIMS therefore remains a challenge which may be better addressed using alternative techniques. Furthermore, the interaction of CBD with the T-cells of the paracortex would require confirmation with different techniques as part of future work.

Generalised delivery of drugs to all lymph node resident immune cells has been the rationale for targeting lymph nodes [10, 118, 131, 346, 347]. Confirmation that small molecule drugs such as CBD interact with lymph node resident T-cells would have large clinical indications in diseases where these cells play a central pathophysiological role. MLN contribute to pro-inflammatory Th17-cell generation during inflammation of the small intestine [348]. Delivery of immunoregulatory compounds such as CBD could therefore be effective treatment for Crohn's disease. In addition, many T-cell lymphomas affect MLNs, either directly in the case of intestinal T-cell lymphomas such as enteropathy-associated T-cell lymphoma or metastatically such as systemic panniculitis-like T-cell lymphoma and cutaneous T-cell lymphoma [349]. In addition, the lack of selectivity for cancer cells of many anticancer chemotherapeutic drugs means targeted distribution is critical to improving efficacy and reducing side effects. Interestingly, a prodrug of bexarotene, which is approved for T-cell lymphomas, was shown to deliver high concentrations of parent drug to the MLN following oral delivery in sesame oil [114]. By suggesting potential interaction of lipid based molecules with lymph node resident T-cells, this work may therefore further support the potential of bexarotene prodrugs for

treatment of T-cell lymphoma. Finally, CD4+ T-cells are known latent reservoirs of HIV even during prolonged dosing of ARV therapy [73, 350, 351]. A prodrug approach was also shown to deliver high concentrations of lopinavir to MLN [115] and may therefore have great therapeutic potential for the abolition of lymph node reservoirs of HIV.

The major second part of this thesis provided evidence of which specific intestinal lymph nodes can be targeted following oral delivery and co-administration with dietary lipids. This work included two complementary approaches. The MLN comprise a large group of nodes, which previous work has shown can be targeted by a range of drugs [70, 114, 115, 118]. Using a previously established highly sensitive HPLC method, work in this thesis showed for the first time that although drug was present throughout the individual nodes of the mesenteric chain at peak absorption, the concentrations of CBD were not uniform. Specifically, lymph nodes located towards the upper middle part of the mesenteric chain were shown to contain the highest concentrations of CBD. These nodes are thought to drain the duodenum and jejunum (Chapter 1, Figure 1.1.) which aligns with previous work suggesting these are the major locations of dietary lipid uptake from the small intestine [20, 353]. Although not specifically assessed in rats, a recent study in mice indicated that duodenum draining lymph nodes played a critical role in gut derived infection and overall systemic tolerance to gut antigens [20]. This further highlights the clinical potential of targeted drug delivery of immunomodulatory drugs to these nodes for diseases such as Crohn's disease.

Another key finding, was that in addition to the MLN, the retroperitoneal lymph nodes (RPLN), more specifically the para-aortic and iliac/ caudal nodes, could also be targeted following oral delivery. Moreover, at later time points, concentrations were similar to that of the MLN. The delayed increase in drug

concentrations in the para-aortic nodes may indicate that, as hypothesised, lymph flows from the MLN to the para-aortic nodes [4, 28]. Interestingly, based on current understanding of lymphatic flow in both rats and humans (see Chapter 1, section 1.1.3.1) the route of drug delivery into iliac and caudal lymph nodes is less clear. Real-time imaging may be used to provide a better understanding of this. CBD concentrations in the RPLN were significantly higher than previously reported in plasma at the same time points [70] thus indicating CBD is not redistributed from systemic circulation. Based on this, work in this thesis has provided evidence for widespread lymphatic drug delivery following oral administration. Again, assuming similar distribution of other chylomicron associated drugs undergoing lymphatic delivery, this could have implications for diseases where retroperitoneal nodes are particularly affected. More specifically, a number of cancers initiate in [354] and metastasise to [79, 324, 355, 356] these nodes, and currently have poor prognosis, likely due to low exposure to chemotherapeutic drugs.

Finally, to complement quantitative drug analysis in animal models, the feasibility of a non-invasive approach for imaging the lymphatic uptake of orally administered lipids in human volunteers was assessed. Again, as part of a highly exploratory piece of work, using a modification of a previously described MRI method, repeated imaging confirmed for the first time the feasibility of the method for longitudinal imaging of intestinal lymph nodes in healthy human volunteers. Although the drawing of ROIs around individual lymph nodes was somewhat subjective and likely contributed to the observed variability in the data, imaging performed before and after high fat meal indicated for the first time that a number of changes in lymph nodes could be detected using MRI, including size and area. Of note, apparent diffusion coefficient (ADC) was consistently higher across all 3 participants and correlated with time scale predictions based on gastric volume and

SBWC. However, significant changes in ADC could only be observed when all nodes were considered collectively, which impeded the identification of individual nodes receiving lipids. There was also large variability in the number and distribution between volunteers, which makes identification of specific groups of nodes challenging with the limited images generated. However, this work has confirmed MRI as a suitable, non-invasive approach by which the distribution of lipids and lipid-based formulations may be tracked throughout the human intestinal lymphatic system.

6.2. Future work

6.2.1. Confirmation of drug distribution within lymph nodes

While the results collected as part of this thesis provide a novel insight into the lymphatic distribution of a clinically relevant study drug, CBD, further research should be undertaken to confirm the wider clinical potential of targeted drug delivery to the intestinal lymphatics following oral administration. Firstly, immediate future work should include analysis of more samples to ensure the reproducibility of the findings presented. One approach to maximise drug concentrations in samples, and therefore the probability of imaging CBD using the OrbiSIMS method described, may be to select samples acquired towards the upper middle region of the mesenteric chain, where concentrations were shown to be highest.

Although the use of other mass spectrometry imaging (MSI) techniques was not investigated as part of this thesis, the non-destructive nature of SIMS analysis means that in future work, there is the potential to perform additional imaging in parallel using complementary techniques. This may provide information to further supplement evidence of drug Pharmacology *in vivo*. More specifically,

whilst several publications have described superiority of SIMS relative to other mass spectrometry imaging techniques for imaging small molecules, matrix assisted laser desorption / ionisation (MALDI) results in less ion fragmentation and therefore is widely understood to be superior to SIMS for the analysis of intact biomolecules such as proteins. Subsequently, MALDI has been utilised for imaging the spatial distribution different immune cell markers within tissue sections [267] including CD3+ T-cells. Corresponding localisation of CBD and markers of T-cells and DCs would therefore help to further elucidate remaining questions surrounding potential interaction with these cells within the paracortex and ultimately the mechanisms by which CBD exerts its immunomodulatory effects *in vivo*. A MATLAB based quantitative imaging analysis similar to one previously described could be used to quantify any correlation between specific cell types and CBD [261]. In addition some MALDI methods can be performed at ambient pressures, which may also negate the need to analyse under cryo-conditions and would likely prevent the sublimation of CBD.

A number of recent publications have also indicated the potential of MALDI for cytokine analysis [265, 267, 357]. Cytokines are fundamental to immune cell signalling and subsequent systemic immune control, and changes in immune cell cytokine secretion are known to occur following CBD administration [70, 358-360]. Based on this, comparison with control sections from untreated animals has the potential to demonstrate localised pharmacodynamic activity of CBD within lymph nodes. Additionally, a number of changes in lymph node architecture and functioning have been described as a result of disease states. For example, in inflammatory bowel diseases such as Crohn's disease, lymphangiogenesis, lymphatic enlargement, adipose expansion, granulomatous have been described

[361-364]. Therefore confirmation of CBD distribution in diseased lymph nodes is also important as part of future work.

In addition to tissue imaging, complementary work to confirm CBD association with specific subtypes of lymph node resident immune cells should also feature as part of future work. OrbiSIMS analysis of individual cells may be possible for the imaging of CBD as was previously done for amiodarone in macrophages [170]. Alternatively flow cytometry methods, similar to that previously described [118, 131] may be adapted. This, however, would require the use of a suitable fluorescent label for CBD [365].

As previously mentioned, in addition to CBD a number of other small molecule drugs can be delivered to MLN at similar concentrations [70, 114, 115, 118]. In order to assess the wider indication of drug delivery to the intestinal lymphatics, future work may also look to use MSI to assess distribution of other drugs within lymph nodes. This is particularly important in diseases where specific cell types are implicated. A more general understanding of small molecule distribution in intestinal lymph nodes following oral delivery may therefore also inform novel drug design strategies. Although not always easy to predict, it is possible that unlike CBD, other compounds of interest may not sublime under high pressure at room temperature. Based on this, analysis at room temperature using OrbiSIMS may be more feasible, which could result in improved sensitivity for these compounds, compared to CBD.

6.2.2. Assessing which lymph nodes can be targeted by oral delivery

A key aim in future work should be to compare how the distribution of other drugs known to undergo lymphatic transport compares to CBD. Similar to the method described in this thesis, HPLC analysis of individual lymph nodes following

oral drug administration may be performed. For drugs of interest including bexarotene and lopinavir, validated HPLC methods have been described and could be used in future work [114, 115]. Inferior MLNs are not hypothesised to receive high concentrations of drug following oral administration. However, in order, to gain a wider understanding of global lymphatic delivery, they may also be collected and analysed as part of future work.

Having determined the feasibility of MRI for detecting lipid-induced changes in lymph nodes, several approaches could be implemented to improve the method sensitivity. Firstly, in terms of study design, the preliminary nature of this work means a small cohort of participants were included. More data from a larger number of participants would provide statistical power in future studies and thus aid conclusions about which lymph nodes can be targeted using lipid- based formulations. There is also substantial variability in the data for all parameters measured and although an initial appraisal of this is one of the findings of this feasibility study, future work with larger sample sizes will also allow for a more detailed assessment variability. More specifically, inter-participant differences in gastric emptying times were observed. Based on this, differences in the rates of lipid uptake into the lymphatics are also likely and so more personalised scanning intervals may ensure differences are not being missed. Similarly, combining scanning with simultaneous blood sampling to determine triglyceride content would also provide indications of lipids entry into systemic circulation and subsequent flow out of the lymphatic system. In addition, in an attempt to enhance lipid uptake, the lipid content of the meal or formulation could be adjusted to include a higher lipid content. This may include long-chain triglycerides, which have been shown in preclinical studies to enhance lymphatic uptake [109]. This however

would require additional gastric emptying time data, which would likely be delayed as a result and may pose problems with palatability.

Improvements in imaging quality could also enhance the sensitivity of the proposed MRI imaging approach. Inevitably, as with most imaging techniques, a compromise between resolution and background noise is required. Although more invasive for participants, the use of an intravenous administration of an anticholinergic agent such as butylscopolamine could be utilised to prevent peristaltic movement which is known to decrease image quality [366]. Finally, although the vertebra of the spine was useful in identifying individual lymph nodes across each scan, the use of external markers to ensure consistent imaging planes would also be beneficial in future studies. A control scanning set in the fasted state, following water only, or alternatively following a meal with equal calories but no lipids, could also be useful to determine background fluctuations in lymph node parameters in the absence of lipids.

Radiolabels are often used in the clinic to identify sentinel nodes. The development of a suitable radiolabel to image intestinal lymphatic uptake would complement the work performed in this thesis by providing a whole body real-time picture of lymphatic drug distribution following oral administration. One approach may be to radiolabel lipophilic compounds already known to undergo extensive lymphatic delivery, such as CBD. Fluorine-18 (^{18}F) is the most clinically and preclinically used radioisotope in positron emission tomography (PET). This is because it has near ideal decay, small atomic size and ability to form stable bonds with carbon [367]. However, synthesis of complex PET tracers remains a challenge, especially in the presence of a variety of functional groups [368, 369]. In addition, for the labelling of drug like molecules, there are often few positions available for incorporation of ^{18}F without impairment of reactivity [367]. Subsequently there is no

general method described to radiolabel structurally complex molecules with ^{18}F . For *in vivo* PET applications, the short half-life of ^{18}F (110 minutes) also means radiolabelling must occur at late stage in the synthesis, thus making multistep radiochemical routes impractical.

Synthesis of a fluorinated CBD molecule in a late stage electrophilic fluorination reaction has previously been demonstrated [370] and extent of lipophilicity and subsequent chylomicron association was not predicted to be affected [104]. This method may therefore be adapted to radiolabel CBD for PET imaging. Alternatively, other labelled equivalents of molecules known to undergo lymphatic transport, such as fatty acids, have been described [371, 372], as well as diglycerides which were used to label liposomes [373]. However it should be noted that the use of these radiolabelled molecules to model chylomicron associated drug uptake would require confirmation of stability following oral delivery as well as characterisation of lymphatic uptake.

Finally, as previously mentioned delivery of CBD to the MLN has potential for the treatment of a range of inflammatory diseases. However, to date clinical efficacy of oral cannabinoids for inflammatory disease such as multiple sclerosis (MS) has been poor [219, 220]. Animal models of inflammatory and autoimmune disease can be used to assess the potential therapeutic potential of drug targeting to the intestinal lymphatic system, such as the EAE model of MS [374]. Whilst outside the scope of this thesis, future work should include assessment of to what extent enhanced delivery of the CBD to the intestinal lymph nodes using lipid-based orally delivered formulations improves efficacy for inflammatory diseases. Knowledge of enhanced efficacy could then be used to support in human clinical trials. Ultimately, in addition to the work in this thesis, further work could therefore

provide an undisputed rationale for perusing research into lymphatic drug delivery for the treatment of diseases associated with the intestinal lymphatic system.

References

1. Morón, F.E. and J. Szklaruk, *Learning the nodal stations in the abdomen*. The British Journal of Radiology, 2007. **80**(958): p. 841-848.
2. Willard-Mack, C.L., *Normal Structure, Function, and Histology of Lymph Nodes*. Toxicologic Pathology, 2006. **34**(5): p. 409-424.
3. Lucey, B.C., J.W. Stuhlfaut, and J.A. Soto, *Mesenteric Lymph Nodes Seen at Imaging: Causes and Significance*. RadioGraphics, 2005. **25**(2): p. 351-365.
4. Tilney, N.L., *Patterns of lymphatic drainage in the adult laboratory rat*. Journal of anatomy, 1971. **109**(Pt 3): p. 369-383.
5. Trevaskis, N.L., et al., *A Mouse Model to Evaluate the Impact of Species, Sex, and Lipid Load on Lymphatic Drug Transport*. Pharmaceutical Research, 2013. **30**(12): p. 3254-3270.
6. Pelkey, J., *Upright posture and the meaning of meronymy: A synthesis of metaphoric and analytic accounts*. Cognitive Semiotics, 2018. **11**.
7. Natale, G., G. Bocci, and D. Ribatti, *Scholars and scientists in the history of the lymphatic system*. Journal of anatomy, 2017. **231**(3): p. 417-429.
8. Cueni, L.N. and M. Detmar, *The lymphatic system in health and disease*. Lymphatic research and biology, 2008. **6**(3-4): p. 109-122.
9. Trevaskis, N.L., L.M. Kaminskas, and C.J. Porter, *From sewer to saviour - targeting the lymphatic system to promote drug exposure and activity*. Nat Rev Drug Discov, 2015. **14**(11): p. 781-803.
10. Schudel, A., D.M. Francis, and S.N. Thomas, *Material design for lymph node drug delivery*. Nature Reviews Materials, 2019. **4**(6): p. 415-428.
11. Crivellato, E., L. Travan, and D. Ribatti, *The Hippocratic treatise 'On glands': the first document on lymphoid tissue and lymph nodes*. Leukemia, 2007. **21**(4): p. 591-2.
12. MIURA, S., et al., *Modulation of intestinal immune system by dietary fat intake: Relevance to Crohn's disease*. Journal of Gastroenterology and Hepatology, 1998. **13**(12): p. 1183-1190.
13. Mörbe, U.M., et al., *Human gut-associated lymphoid tissues (GALT); diversity, structure, and function*. Mucosal Immunology, 2021. **14**(4): p. 793-802.
14. Hansen, K.C., et al., *Lymph formation, composition and circulation: a proteomics perspective*. International Immunology, 2015. **27**(5): p. 219-227.
15. Scallan, J.P., et al., *Lymphatic pumping: mechanics, mechanisms and malfunction*. The Journal of physiology, 2016. **594**(20): p. 5749-5768.
16. Cifarelli, V. and A. Eichmann, *The Intestinal Lymphatic System: Functions and Metabolic Implications*. Cellular and Molecular Gastroenterology and Hepatology, 2019. **7**(3): p. 503-513.
17. Zhang, F., et al., *Lymphatic Endothelial Cell Junctions: Molecular Regulation in Physiology and Diseases*. Front Physiol, 2020. **11**: p. 509.
18. Bernier-Latmani, J. and T.V. Petrova, *Intestinal lymphatic vasculature: structure, mechanisms and functions*. Nature

- Reviews Gastroenterology & Hepatology, 2017. **14**(9): p. 510-526.
19. Houston, S.A., et al., *The lymph nodes draining the small intestine and colon are anatomically separate and immunologically distinct*. Mucosal immunology, 2016. **9**(2): p. 468-478.
 20. Esterházy, D., et al., *Compartmentalized gut lymph node drainage dictates adaptive immune responses*. Nature, 2019. **569**(7754): p. 126-130.
 21. Wang, T.Y., et al., *New insights into the molecular mechanism of intestinal fatty acid absorption*. European journal of clinical investigation, 2013. **43**(11): p. 1203-1223.
 22. Black, D.D., *Development and Physiological Regulation of Intestinal Lipid Absorption. I. Development of intestinal lipid absorption: cellular events in chylomicron assembly and secretion*. American Journal of Physiology-Gastrointestinal and Liver Physiology, 2007. **293**(3): p. G519-G524.
 23. Sesorova, I.S., et al., *Structure of the enterocyte transcytosis compartments during lipid absorption*. Histochemistry and Cell Biology, 2020. **153**(6): p. 413-429.
 24. Hussain, M.M., *A proposed model for the assembly of chylomicrons*. Atherosclerosis, 2000. **148**(1): p. 1-15.
 25. Randolph, G.J. and N.E. Miller, *Lymphatic transport of high-density lipoproteins and chylomicrons*. J Clin Invest, 2014. **124**(3): p. 929-35.
 26. Thompson, E.C., *Focus issue: Structure and function of lymphoid tissues*. Trends in Immunology, 2012. **33**(6): p. 255.
 27. Hirosue, S. and J. Dubrot, *Modes of Antigen Presentation by Lymph Node Stromal Cells and Their Immunological Implications*. Frontiers in immunology, 2015. **6**: p. 446-446.
 28. Standring, S., *Gray's anatomy : the anatomical basis of clinical practice*. Forty-second edition. ed. Anatomy : the anatomical basis of clinical practice. 2021, New York: Elsevier.
 29. Smedley, J., et al., *Tracking the luminal exposure and lymphatic drainage pathways of intravaginal and intrarectal inocula used in nonhuman primate models of HIV transmission*. PLoS One, 2014. **9**(3): p. e92830.
 30. Park, J.M., et al., *Pathways of nodal metastasis from pelvic tumors: CT demonstration*. Radiographics, 1994. **14**(6): p. 1309-21.
 31. Mikhael, M. and Y.S. Khan, *Anatomy, Abdomen and Pelvis, Lymphatic Drainage*, in *StatPearls*. 2022, StatPearls Publishing
- Copyright © 2022, StatPearls Publishing LLC.: Treasure Island (FL).
32. Alexander, J.S., et al., *Gastrointestinal lymphatics in health and disease*. Pathophysiology : the official journal of the International Society for Pathophysiology, 2010. **17**(4): p. 315-335.
 33. Van den Broeck, W., A. Derore, and P. Simoens, *Anatomy and nomenclature of murine lymph nodes: Descriptive study and nomenclatory standardization in BALB/cAnNCrl mice*. Journal of Immunological Methods, 2006. **312**(1): p. 12-19.
 34. Willard-Mack, C.L., *Normal structure, function, and histology of lymph nodes*. Toxicol Pathol, 2006. **34**(5): p. 409-24.
 35. Sainte-Marie, G., F.-S. Peng, and C. Bélisle, *Overall architecture and pattern of lymph flow in the rat lymph node*. American Journal of Anatomy, 1982. **164**(4): p. 275-309.
 36. Sainte-Marie, G., C. Bélisle, and F.S. Peng, *The Deep Cortex of the Lymph Node: Morphological Variations and Functional Aspects, in Reaction Patterns of the Lymph Node: Part 1 Cell Types and*

- Functions*, E. Grundmann and E. Vollmer, Editors. 1990, Springer Berlin Heidelberg: Berlin, Heidelberg. p. 33-63.
37. Hons, M. and M. Sixt, *The lymph node filter revealed*. Nature Immunology, 2015. **16**(4): p. 338-340.
 38. Louie, D.A.P. and S. Liao, *Lymph Node Subcapsular Sinus Macrophages as the Frontline of Lymphatic Immune Defense*. Frontiers in Immunology, 2019. **10**(347).
 39. Phan, T.G., et al., *Immune complex relay by subcapsular sinus macrophages and noncognate B cells drives antibody affinity maturation*. Nature Immunology, 2009. **10**(7): p. 786-793.
 40. Heath, T.J. and H.J. Spalding, *Pathways of lymph flow to and from the medulla of lymph nodes in sheep*. Journal of anatomy, 1987. **155**: p. 177-188.
 41. Gretz, J.E., et al., *Lymph-Borne Chemokines and Other Low Molecular Weight Molecules Reach High Endothelial Venues via Specialized Conduits While a Functional Barrier Limits Access to the Lymphocyte Microenvironments in Lymph Node Cortex*. Journal of Experimental Medicine, 2000. **192**(10): p. 1425-1440.
 42. Nolte, M.A., et al., *A conduit system distributes chemokines and small blood-borne molecules through the splenic white pulp*. The Journal of experimental medicine, 2003. **198**(3): p. 505-512.
 43. Roozendaal, R., et al., *Conduits mediate transport of low-molecular-weight antigen to lymph node follicles*. Immunity, 2009. **30**(2): p. 264-276.
 44. Sixt, M., et al., *The conduit system transports soluble antigens from the afferent lymph to resident dendritic cells in the T cell area of the lymph node*. Immunity, 2005. **22**(1): p. 19-29.
 45. Kelch, I.D., et al., *High-resolution 3D imaging and topological mapping of the lymph node conduit system*. PLoS Biol, 2019. **17**(12): p. e3000486.
 46. Brown, F.D. and S.J. Turley, *Fibroblastic reticular cells: organization and regulation of the T lymphocyte life cycle*. Journal of immunology (Baltimore, Md. : 1950), 2015. **194**(4): p. 1389-1394.
 47. Miller, M.J., J.R. McDole, and R.D. Newberry, *Microanatomy of the intestinal lymphatic system*. Annals of the New York Academy of Sciences, 2010. **1207 Suppl 1**(Suppl 1): p. E21-E28.
 48. Mionnet, C., et al., *High endothelial venules as traffic control points maintaining lymphocyte population homeostasis in lymph nodes*. Blood, 2011. **118**(23): p. 6115-6122.
 49. Blanchard, L. and J.-P. Girard, *High endothelial venules (HEVs) in immunity, inflammation and cancer*. Angiogenesis, 2021. **24**(4): p. 719-753.
 50. Castellanos, C.A., et al., *Lymph node-resident dendritic cells drive T_H2 cell development involving MARCH1*. Science Immunology, 2021. **6**(64): p. eabh0707.
 51. Miller, M.J., et al., *Imaging the single cell dynamics of CD4⁺ T cell activation by dendritic cells in lymph nodes*. J Exp Med, 2004. **200**(7): p. 847-56.
 52. Gatto, D., K. Wood, and R. Brink, *EBI2 operates independently of but in cooperation with CXCR5 and CCR7 to direct B cell migration and organization in follicles and the germinal center*. J Immunol, 2011. **187**(9): p. 4621-8.
 53. De Silva, N.S. and U. Klein, *Dynamics of B cells in germinal centres*. Nature Reviews Immunology, 2015. **15**(3): p. 137-148.

54. Tomura, M., et al., *Monitoring cellular movement in vivo with photoconvertible fluorescence protein "Kaede" transgenic mice*. Proc Natl Acad Sci U S A, 2008. **105**(31): p. 10871-6.
55. Miura, S., et al., *Modulation of intestinal immune system by dietary fat intake: relevance to Crohn's disease*. J Gastroenterol Hepatol, 1998. **13**(12): p. 1183-90.
56. Watzl, B., S. Girrbaach, and M. Roller, *Inulin, oligofructose and immunomodulation*. Br J Nutr, 2005. **93 Suppl 1**: p. S49-55.
57. Vojdani, A., L.R. Gushgari, and E. Vojdani, *Interaction between food antigens and the immune system: Association with autoimmune disorders*. Autoimmun Rev, 2020. **19**(3): p. 102459.
58. Sartor, R.B., *Mechanisms of Disease: pathogenesis of Crohn's disease and ulcerative colitis*. Nature Clinical Practice Gastroenterology & Hepatology, 2006. **3**(7): p. 390-407.
59. Guerra, I. and F. Bermejo, *Management of inflammatory bowel disease in poor responders to infliximab*. Clinical and experimental gastroenterology, 2014. **7**: p. 359-367.
60. Bokemeyer, B., et al., *Inadequate Response, Treatment Patterns, Health Care Utilization, and Associated Costs in Patients With Ulcerative Colitis: Retrospective Cohort Study Based on German Claims Data*. Inflammatory Bowel Diseases, 2022.
61. Khoudari, G., et al., *Rates of Intestinal Resection and Colectomy in Inflammatory Bowel Disease Patients After Initiation of Biologics: A Cohort Study*. Clinical Gastroenterology and Hepatology, 2020.
62. Biancone, L., et al., *Cancer Risk in Inflammatory Bowel Disease: A 6-Year Prospective Multicenter Nested Case-Control IG-IBD Study*. Inflammatory Bowel Diseases, 2019. **26**(3): p. 450-459.
63. Guan, Q., *A Comprehensive Review and Update on the Pathogenesis of Inflammatory Bowel Disease*. Journal of immunology research, 2019. **2019**: p. 7247238-7247238.
64. Bsat, M., et al., *Differential Pathogenic Th17 Profile in Mesenteric Lymph Nodes of Crohn's Disease and Ulcerative Colitis Patients*. Frontiers in Immunology, 2019. **10**(1177).
65. Stephens, M., S. Liao, and P.-Y. von der Weid, *Mesenteric Lymphatic Alterations Observed During DSS Induced Intestinal Inflammation Are Driven in a TLR4-PAMP/DAMP Discriminative Manner*. Frontiers in Immunology, 2019. **10**(557).
66. Tsunoda, I., *Lymphatic system and gut microbiota affect immunopathology of neuroinflammatory diseases, including multiple sclerosis, neuromyelitis optica and Alzheimer's disease*. Clin Exp Neuroimmunol, 2017. **8**(3): p. 177-179.
67. Camara-Lemarroy, C.R., et al., *The intestinal barrier in multiple sclerosis: implications for pathophysiology and therapeutics*. Brain : a journal of neurology, 2018. **141**(7): p. 1900-1916.
68. Parodi, B. and N. Kerlero de Rosbo, *The Gut-Brain Axis in Multiple Sclerosis. Is Its Dysfunction a Pathological Trigger or a Consequence of the Disease?* Frontiers in Immunology, 2021. **12**(3911).
69. Francis, A. and C.S. Constantinescu, *Gastrointestinal influences in multiple sclerosis: Focus on the role of the microbiome*. Clinical and Experimental Neuroimmunology, 2018. **9**(S1): p. 2-12.
70. Zgair, A., et al., *Oral administration of cannabis with lipids leads to high levels of cannabinoids in the intestinal lymphatic system and prominent immunomodulation*. Sci Rep, 2017. **7**(1): p. 14542.
71. Cojocaru, M., et al., *Gastrointestinal manifestations in systemic autoimmune diseases*. Maedica, 2011. **6**(1): p. 45-51.

72. Zaiss, M.M., et al., *The gut–joint axis in rheumatoid arthritis*. Nature Reviews Rheumatology, 2021. **17**(4): p. 224-237.
73. Cantero-Pérez, J., et al., *Resident memory T cells are a cellular reservoir for HIV in the cervical mucosa*. Nature Communications, 2019. **10**(1): p. 4739.
74. Pantaleo, G., et al., *Lymphoid organs function as major reservoirs for human immunodeficiency virus*. Proceedings of the National Academy of Sciences, 1991. **88**(21): p. 9838-9842.
75. Giannini, C., et al., *Association between persistent lymphatic infection by hepatitis C virus after antiviral treatment and mixed cryoglobulinemia*. Blood, 2008. **111**(5): p. 2943-2945.
76. Griffin, A.J., et al., *Dissemination of persistent intestinal bacteria via the mesenteric lymph nodes causes typhoid relapse*. Infection and immunity, 2011. **79**(4): p. 1479-1488.
77. Popova, T.G., et al., *Whole proteome analysis of mouse lymph nodes in cutaneous anthrax*. PLoS One, 2014. **9**(10): p. e110873.
78. Nached, M.Z. and L.S. Al-Ozaibi, *Primary Retroperitoneal Filariasis Presenting with Acute Abdomen*. Dubai Medical Journal, 2021. **4**(3): p. 273-275.
79. Luo, C.-H. and B. Zou, *Retroperitoneal Lymph Node Metastases*, in *Retroperitoneal Tumors: Clinical Management*, C.-H. Luo, Editor. 2018, Springer Netherlands: Dordrecht. p. 273-276.
80. Sharma, N. and M.S. Cappell, *Gastrointestinal and Hepatic Manifestations of Ebola Virus Infection*. Digestive Diseases and Sciences, 2015. **60**(9): p. 2590-2603.
81. Estaquier, J. and B. Hurtrel, *[Mesenteric lymph nodes, a sanctuary for the persistence of HIV. Escape mechanisms]*. Med Sci (Paris), 2008. **24**(12): p. 1055-60.
82. Sung, H., et al., *Global Cancer Statistics 2020: GLOBOCAN Estimates of Incidence and Mortality Worldwide for 36 Cancers in 185 Countries*. CA: A Cancer Journal for Clinicians, 2021. **71**(3): p. 209-249.
83. Ciortan, E. and L. Carra, *Abdominal mass as the first sign of follicular lymphoma B of mesentery: Case report*. Journal of ultrasound, 2010. **13**(3): p. 123-125.
84. Salemis, N.S., et al., *Diffuse large B cell lymphoma of the mesentery: an unusual presentation and review of the literature*. J Gastrointest Cancer, 2009. **40**(3-4): p. 79-82.
85. Abdulla, M., et al., *Prognostic impact of abdominal lymph node involvement in diffuse large B-cell lymphoma*. European journal of haematology, 2020. **104**(3): p. 207-213.
86. Chaffer, C.L. and R.A. Weinberg, *A Perspective on Cancer Cell Metastasis*. Science, 2011. **331**(6024): p. 1559.
87. Schmoll, H.J., *AJCC Cancer Staging Manual, 6th edition*. Annals of Oncology, 2003. **14**(2): p. 345.
88. Mehlen, P. and A. Puisieux, *Metastasis: a question of life or death*. Nat Rev Cancer, 2006. **6**(6): p. 449-58.
89. Fares, J., et al., *Molecular principles of metastasis: a hallmark of cancer revisited*. Signal Transduction and Targeted Therapy, 2020. **5**(1): p. 28.
90. Lucey, B.C., J.W. Stuhlfaut, and J.A. Soto, *Mesenteric lymph nodes seen at imaging: causes and significance*. Radiographics, 2005. **25**(2): p. 351-65.
91. Rawla, P., T. Sunkara, and A. Barsouk, *Epidemiology of colorectal cancer: incidence, mortality, survival, and risk factors*. Przegląd gastroenterologiczny, 2019. **14**(2): p. 89-103.

92. Elmore, S., *Histopathology of the Lymph Nodes*. Vol. 34. 2006. 425-54.
93. Su, J.L., et al., *The role of the VEGF-C/VEGFR-3 axis in cancer progression*. Br J Cancer, 2007. **96**(4): p. 541-5.
94. Sato, T., et al., *The Combination of Intralymphatic Chemotherapy with Ultrasound and Nano-/Microbubbles Is Efficient in the Treatment of Experimental Tumors in Mouse Lymph Nodes*. Ultrasound in Medicine and Biology, 2014. **40**(6): p. 1237-1249.
95. García Nores, G.D., et al., *Obesity but not high-fat diet impairs lymphatic function*. International Journal of Obesity, 2016. **40**(10): p. 1582-1590.
96. Mallick, A. and A.R. Bodenham, *Disorders of the lymph circulation: their relevance to anaesthesia and intensive care*. BJA: British Journal of Anaesthesia, 2003. **91**(2): p. 265-272.
97. Ferrell, R.E., et al., *Candidate gene analysis in primary lymphedema*. Lymphat Res Biol, 2008. **6**(2): p. 69-76.
98. Al-Tarrah, K., et al., *Massive Localized Abdominal Lymphedema Treatment Challenges*. Plastic and Reconstructive Surgery – Global Open, 2020. **8**(1).
99. Morgan, P., et al., *Can the flow of medicines be improved? Fundamental pharmacokinetic and pharmacological principles toward improving Phase II survival*. Drug Discov Today, 2012. **17**(9-10): p. 419-24.
100. Sensken, S.C., C. Bode, and M.H. Graler, *Accumulation of fingolimod (FTY720) in lymphoid tissues contributes to prolonged efficacy*. J Pharmacol Exp Ther, 2009. **328**(3): p. 963-9.
101. Chu, Y., et al., *Oral administration of tipranavir with long-chain triglyceride results in moderate intestinal lymph targeting but no efficient delivery to HIV-1 reservoir in mesenteric lymph nodes*. Int J Pharm, 2021. **602**: p. 120621.
102. Zhang, Z., et al., *An update on oral drug delivery via intestinal lymphatic transport*. Acta Pharmaceutica Sinica B, 2021. **11**(8): p. 2449-2468.
103. Gershkovich, P. and A. Hoffman, *Uptake of lipophilic drugs by plasma derived isolated chylomicrons: linear correlation with intestinal lymphatic bioavailability*. Eur J Pharm Sci, 2005. **26**(5): p. 394-404.
104. Gershkovich, P., et al., *The role of molecular physicochemical properties and apolipoproteins in association of drugs with triglyceride-rich lipoproteins: in-silico prediction of uptake by chylomicrons*. Journal of Pharmacy and Pharmacology, 2010. **61**(1): p. 31-39.
105. Trevaskis, N.L., et al., *Intestinal Lymph Flow, and Lipid and Drug Transport Scale Allometrically From Pre-clinical Species to Humans*. Frontiers in Physiology, 2020. **11**(458).
106. Trevaskis, N.L., W.N. Charman, and C.J.H. Porter, *Lipid-based delivery systems and intestinal lymphatic drug transport: a mechanistic update*. Advanced drug delivery reviews, 2008. **60**(6): p. 702-716.
107. Caliph, S.M., W.N. Charman, and C.J. Porter, *Effect of short-, medium-, and long-chain fatty acid-based vehicles on the absolute oral bioavailability and intestinal lymphatic transport of halofantrine and assessment of mass balance in lymph-cannulated and non-cannulated rats*. J Pharm Sci, 2000. **89**(8): p. 1073-84.
108. Gershkovich, P., et al., *Different impacts of intestinal lymphatic transport on the oral bioavailability of structurally similar synthetic*

- lipophilic cannabinoids: dexanabinol and PRS-211,220*. Eur J Pharm Sci, 2007. **31**(5): p. 298-305.
109. Feng, W., et al., *Natural sesame oil is superior to pre-digested lipid formulations and purified triglycerides in promoting the intestinal lymphatic transport and systemic bioavailability of cannabidiol*. European Journal of Pharmaceutics and Biopharmaceutics, 2021. **162**.
 110. Taylor, M.D., S.S. Kim, and L.J. Vaia, *Therapeutic digoxin level in chylous drainage with no detectable plasma digoxin level*. Chest, 1998. **114**(5): p. 1482-4.
 111. Ichihashi, T., et al., *A quantitative concept of the mechanism of intestinal lymphatic transfer of lipophilic molecules*. Pharm Res, 1994. **11**(4): p. 508-12.
 112. Shackelford, D.M., et al., *Contribution of lymphatically transported testosterone undecanoate to the systemic exposure of testosterone after oral administration of two andriol formulations in conscious lymph duct-cannulated dogs*. J Pharmacol Exp Ther, 2003. **306**(3): p. 925-33.
 113. Skakkebaek, N.E., et al., *Androgen replacement with oral testosterone undecanoate in hypogonadal men: a double blind controlled study*. Clin Endocrinol (Oxf), 1981. **14**(1): p. 49-61.
 114. Lee, J.B., et al., *Lipophilic activated ester prodrug approach for drug delivery to the intestinal lymphatic system*. Journal of controlled release : official journal of the Controlled Release Society, 2018. **286**: p. 10-19.
 115. Qin, C., et al., *Targeted delivery of lopinavir to HIV reservoirs in the mesenteric lymphatic system by lipophilic ester prodrug approach*. Journal of Controlled Release, 2020. **329**.
 116. Han, S., et al., *Targeted delivery of a model immunomodulator to the lymphatic system: comparison of alkyl ester versus triglyceride mimetic lipid prodrug strategies*. J Control Release, 2014. **177**: p. 1-10.
 117. Han, S., et al., *Lymphatic Transport and Lymphocyte Targeting of a Triglyceride Mimetic Prodrug Is Enhanced in a Large Animal Model: Studies in Greyhound Dogs*. Mol Pharm, 2016. **13**(10): p. 3351-3361.
 118. Kochappan, R., et al., *Targeted delivery of mycophenolic acid to the mesenteric lymph node using a triglyceride mimetic prodrug approach enhances gut-specific immunomodulation in mice*. J Control Release, 2021. **332**: p. 636-651.
 119. Tian, C., et al., *Efficient Intestinal Digestion and On Site Tumor-Bioactivation are the Two Important Determinants for Chylomicron-Mediated Lymph-Targeting Triglyceride-Mimetic Docetaxel Oral Prodrugs*. Adv Sci (Weinh), 2019. **6**(24): p. 1901810.
 120. Ali Khan, A., et al., *Advanced drug delivery to the lymphatic system: lipid-based nanoformulations*. International journal of nanomedicine, 2013. **8**: p. 2733-2744.
 121. Bargoni, A., et al., *Solid lipid nanoparticles in lymph and plasma after duodenal administration to rats*. Pharm Res, 1998. **15**(5): p. 745-50.
 122. Manjunath, K. and V. Venkateswarlu, *Pharmacokinetics, tissue distribution and bioavailability of clozapine solid lipid nanoparticles after intravenous and intraduodenal administration*. J Control Release, 2005. **107**(2): p. 215-28.

123. Chalikwar, S.S., et al., *Formulation and evaluation of Nimodipine-loaded solid lipid nanoparticles delivered via lymphatic transport system*. *Colloids Surf B Biointerfaces*, 2012. **97**: p. 109-16.
124. Zara, G.P., et al., *Pharmacokinetics and tissue distribution of idarubicin-loaded solid lipid nanoparticles after duodenal administration to rats*. *J Pharm Sci*, 2002. **91**(5): p. 1324-33.
125. Paliwal, R., et al., *Effect of lipid core material on characteristics of solid lipid nanoparticles designed for oral lymphatic delivery*. *Nanomedicine*, 2009. **5**(2): p. 184-91.
126. Bargoni, A., et al., *Transmucosal transport of tobramycin incorporated in solid lipid nanoparticles (SLN) after duodenal administration to rats. Part II--tissue distribution*. *Pharmacol Res*, 2001. **43**(5): p. 497-502.
127. Müller, R.H., M. Radtke, and S.A. Wissing, *Solid lipid nanoparticles (SLN) and nanostructured lipid carriers (NLC) in cosmetic and dermatological preparations*. *Adv Drug Deliv Rev*, 2002. **54 Suppl 1**: p. S131-55.
128. Muchow, M., et al., *Production and characterization of testosterone undecanoate-loaded NLC for oral bioavailability enhancement*. *Drug Dev Ind Pharm*, 2011. **37**(1): p. 8-14.
129. Zhuang, C.Y., et al., *Preparation and characterization of vinpocetine loaded nanostructured lipid carriers (NLC) for improved oral bioavailability*. *Int J Pharm*, 2010. **394**(1-2): p. 179-85.
130. Zhou, L., et al., *Preparation of tripterine nanostructured lipid carriers and their absorption in rat intestine*. *Pharmazie*, 2012. **67**(4): p. 304-10.
131. Schudel, A., et al., *Programmable multistage drug delivery to lymph nodes*. *Nature Nanotechnology*, 2020. **15**(6): p. 491-499.
132. Holm, R., et al., *Examination of oral absorption and lymphatic transport of halofantrine in a triple-cannulated canine model after administration in self-microemulsifying drug delivery systems (SMEDDS) containing structured triglycerides*. *Eur J Pharm Sci*, 2003. **20**(1): p. 91-7.
133. Kommuru, T.R., et al., *Self-emulsifying drug delivery systems (SEDDS) of coenzyme Q10: formulation development and bioavailability assessment*. *Int J Pharm*, 2001. **212**(2): p. 233-46.
134. Yao, J., Y. Lu, and J.P. Zhou, *Preparation of nobiletin in self-microemulsifying systems and its intestinal permeability in rats*. *J Pharm Pharm Sci*, 2008. **11**(3): p. 22-9.
135. Dixit, A.R., S.J. Rajput, and S.G. Patel, *Preparation and bioavailability assessment of SMEDDS containing valsartan*. *AAPS PharmSciTech*, 2010. **11**(1): p. 314-21.
136. Chen, Y., et al., *Self-microemulsifying drug delivery system (SMEDDS) of vinpocetine: formulation development and in vivo assessment*. *Biol Pharm Bull*, 2008. **31**(1): p. 118-25.
137. Li, X., et al., *Development of silymarin self-microemulsifying drug delivery system with enhanced oral bioavailability*. *AAPS PharmSciTech*, 2010. **11**(2): p. 672-8.
138. Sun, M., et al., *Intestinal absorption and intestinal lymphatic transport of sirolimus from self-microemulsifying drug delivery systems assessed using the single-pass intestinal perfusion (SPIP) technique and a chylomicron flow blocking approach: linear correlation with oral bioavailabilities in rats*. *Eur J Pharm Sci*, 2011. **43**(3): p. 132-40.

139. Singh, B., et al., *Development of optimized self-nano-emulsifying drug delivery systems (SNEDDS) of carvedilol with enhanced bioavailability potential*. *Drug Deliv*, 2011. **18**(8): p. 599-612.
140. Beg, S., et al., *Development, optimization, and characterization of solid self-nanoemulsifying drug delivery systems of valsartan using porous carriers*. *AAPS PharmSciTech*, 2012. **13**(4): p. 1416-27.
141. Ling, S.S., et al., *Enhanced oral bioavailability and intestinal lymphatic transport of a hydrophilic drug using liposomes*. *Drug Dev Ind Pharm*, 2006. **32**(3): p. 335-45.
142. Guan, P., et al., *Enhanced oral bioavailability of cyclosporine A by liposomes containing a bile salt*. *Int J Nanomedicine*, 2011. **6**: p. 965-74.
143. Pridgen, E.M., et al., *Transepithelial Transport of Fc-Targeted Nanoparticles by the Neonatal Fc Receptor for Oral Delivery*. *Science Translational Medicine*, 2013. **5**(213): p. 213ra167-213ra167.
144. Anderson, K.E., et al., *Formulation and Evaluation of a Folic Acid Receptor-Targeted Oral Vancomycin Liposomal Dosage Form*. *Pharmaceutical Research*, 2001. **18**(3): p. 316-322.
145. Anderson, K.E., B.R. Stevenson, and J.A. Rogers, *Folic acid-PEO-labeled liposomes to improve gastrointestinal absorption of encapsulated agents*. *Journal of Controlled Release*, 1999. **60**(2): p. 189-198.
146. Parasrampur, D.A., L.Z. Benet, and A. Sharma, *Why Drugs Fail in Late Stages of Development: Case Study Analyses from the Last Decade and Recommendations*. *The AAPS Journal*, 2018. **20**(3): p. 46.
147. Willmann, J.K., et al., *Molecular imaging in drug development*. *Nature Reviews Drug Discovery*, 2008. **7**(7): p. 591-607.
148. Kosaka, N., et al., *In vivo real-time lymphatic draining using quantum-dot optical imaging in mice*. *Contrast media & molecular imaging*, 2013. **8**(1): p. 96-100.
149. Zheng, Q., M. Itkin, and Y. Fan, *Quantification of Thoracic Lymphatic Flow Patterns Using Dynamic Contrast-enhanced MR Lymphangiography*. *Radiology*, 2020. **296**(1): p. 202-207.
150. Munn, L.L. and T.P. Padera, *Imaging the lymphatic system*. *Microvascular research*, 2014. **96**: p. 55-63.
151. Barrett, T., P.L. Choyke, and H. Kobayashi, *Imaging of the lymphatic system: new horizons*. *Contrast Media Mol Imaging*, 2006. **1**(6): p. 230-45.
152. Kassis, T., et al., *Dual-channel in-situ optical imaging system for quantifying lipid uptake and lymphatic pump function*. *Journal of biomedical optics*, 2012. **17**(8): p. 086005-086005.
153. Paulus, A., et al., *[(18)F]BODIPY-triglyceride-containing chylomicron-like particles as an imaging agent for brown adipose tissue in vivo*. *Sci Rep*, 2019. **9**(1): p. 2706.
154. Torabi, M., S.L. Aquino, and M.G. Harisinghani, *Current Concepts in Lymph Node Imaging*. *Journal of Nuclear Medicine*, 2004. **45**(9): p. 1509.
155. Luciani, A., et al., *Lymph node imaging: basic principles*. *Eur J Radiol*, 2006. **58**(3): p. 338-44.
156. Mao, Y., S. Hedgire, and M. Harisinghani, *Radiologic Assessment of Lymph Nodes in Oncologic Patients*. *Current Radiology Reports*, 2013. **2**(2): p. 36.
157. Rezende, R., et al., *Visualizing Lymph Node Structure and Cellular Localization using Ex-Vivo Confocal Microscopy*. *Journal of Visualized Experiments*, 2019: p. 59335.

158. Salmon, H., et al., *Ex vivo imaging of T cells in murine lymph node slices with widefield and confocal microscopes*. Journal of visualized experiments : JoVE, 2011(53): p. e3054-e3054.
159. Rezende, R.M., et al., *Visualizing Lymph Node Structure and Cellular Localization using Ex-Vivo Confocal Microscopy*. J Vis Exp, 2019(150).
160. Moysi, E., et al., *In Situ Characterization of Human Lymphoid Tissue Immune Cells by Multispectral Confocal Imaging and Quantitative Image Analysis; Implications for HIV Reservoir Characterization*. Frontiers in Immunology, 2021. **12**(2058).
161. Stein, J.V. and F.G. S, *Dynamic intravital imaging of cell-cell interactions in the lymph node*. J Allergy Clin Immunol, 2017. **139**(1): p. 12-20.
162. Amornphimoltham, P., A. Masedunskas, and R. Weigert, *Intravital microscopy as a tool to study drug delivery in preclinical studies*. Advanced Drug Delivery Reviews, 2011. **63**(1): p. 119-128.
163. Suo, Y., et al., *Label-free imaging of lymph nodes with stimulated Raman scattering microscopy*. SPIE/COS Photonics Asia. Vol. 11190. 2019: SPIE.
164. Kumamoto, Y., et al., *Label-free Molecular Imaging and Analysis by Raman Spectroscopy*. Acta histochemica et cytochemica, 2018. **51**(3): p. 101-110.
165. Castellino, S., N.M. Lareau, and M.R. Groseclose, *The emergence of imaging mass spectrometry in drug discovery and development: Making a difference by driving decision making*. Journal of mass spectrometry : JMS, 2021. **56**(8): p. e4717-e4717.
166. Zhao, Y.S. and C. Li, *Mass Spectrometry Imaging: Applications in Drug Distribution Studies*. Curr Drug Metab, 2015. **16**(9): p. 807-15.
167. Nilsson, A., et al., *Mass Spectrometry Imaging in Drug Development*. Analytical Chemistry, 2015. **87**(3): p. 1437-1455.
168. Herzog, R.F.K. and F.P. Viehböck, *Ion Source for Mass Spectrography*. Physical Review, 1949. **76**(6): p. 855-856.
169. Trim, P.J. and M.F. Snel, *Small molecule MALDI MS imaging: Current technologies and future challenges*. Methods, 2016. **104**: p. 127-41.
170. Passarelli, M.K., et al., *The 3D OrbiSIMS—label-free metabolic imaging with subcellular lateral resolution and high mass-resolving power*. Nature Methods, 2017. **14**: p. 1175.
171. Touboul, D. and A. Brunelle, *TOF-SIMS imaging of lipids on rat brain sections*. Methods Mol Biol, 2015. **1203**: p. 21-7.
172. Starr, N.J., et al., *Enhanced vitamin C skin permeation from supramolecular hydrogels, illustrated using in situ ToF-SIMS 3D chemical profiling*. International Journal of Pharmaceutics, 2019. **563**: p. 21-29.
173. Starr, N.J., et al., *Age-Related Changes to Human Stratum Corneum Lipids Detected Using Time-of-Flight Secondary Ion Mass Spectrometry Following in Vivo Sampling*. Analytical Chemistry, 2016. **88**(8): p. 4400-4408.
174. Brulet, M., et al., *Lipid mapping of colonic mucosa by cluster TOF-SIMS imaging and multivariate analysis in cfr knockout mice[S]*. Journal of Lipid Research, 2010. **51**(10): p. 3034-3045.
175. Seyer, A., et al., *Lipidomic and spatio-temporal imaging of fat by mass spectrometry in mice duodenum during lipid digestion*. PLoS One, 2013. **8**(4): p. e58224.

176. Mains, J., C. Wilson, and A. Urquhart, *ToF-SIMS analysis of ocular tissues reveals biochemical differentiation and drug distribution*. *Eur J Pharm Biopharm*, 2011. **79**(2): p. 328-33.
177. Mains, J., C.G. Wilson, and A. Urquhart, *ToF-SIMS Analysis of Dexamethasone Distribution in the Isolated Perfused Eye*. *Investigative Ophthalmology & Visual Science*, 2011. **52**(11): p. 8413-8419.
178. Debois, D., et al., *In situ lipidomic analysis of nonalcoholic fatty liver by cluster TOF-SIMS imaging*. *Anal Chem*, 2009. **81**(8): p. 2823-31.
179. Nygren, H., et al., *Imaging TOF-SIMS of rat kidney prepared by high-pressure freezing*. *Microsc Res Tech*, 2005. **68**(6): p. 329-34.
180. Kern, C., et al., *New insights into ToF-SIMS imaging in osteoporotic bone research*. *Biointerphases*, 2020. **15**(3): p. 031005.
181. Hodgkinson, T., et al., *The use of nanovibration to discover specific and potent bioactive metabolites that stimulate osteogenic differentiation in mesenchymal stem cells*. *Science Advances*. **7**(9): p. eabb7921.
182. Zias, J., et al., *Early medical use of cannabis*. *Nature*, 1993. **363**(6426): p. 215.
183. Rock, E.M. and L.A. Parker, *Constituents of Cannabis Sativa*. *Adv Exp Med Biol*, 2021. **1264**: p. 1-13.
184. Madras, B.K., *Tinkering with THC-to-CBD ratios in Marijuana*. *Neuropsychopharmacology*, 2019. **44**(1): p. 215-216.
185. Nutt, D., et al., *So near yet so far: why won't the UK prescribe medical cannabis?* *BMJ Open*, 2020. **10**(9): p. e038687.
186. Cannabis, C.f.M. *LEFT BEHIND: THE SCALE OF ILLEGAL CANNABIS USE FOR MEDICINAL INTENT IN THE UK*. 2020, January; Available from: <https://static1.squarespace.com/static/60f5a46e59bd9b68f91bb25f/t/610520aab98b2c457c35c591/1627725998567/Left+Behind+.pdf>.
187. Hillard, C.J., *Circulating Endocannabinoids: From Whence Do They Come and Where are They Going?* *Neuropsychopharmacology*, 2018. **43**(1): p. 155-172.
188. Reggio, P.H., *Endocannabinoid binding to the cannabinoid receptors: what is known and what remains unknown*. *Current medicinal chemistry*, 2010. **17**(14): p. 1468-1486.
189. Gallègue, S., et al., *Expression of central and peripheral cannabinoid receptors in human immune tissues and leukocyte subpopulations*. *Eur J Biochem*, 1995. **232**(1): p. 54-61.
190. Micale, V., et al., *Endocannabinoid system and mood disorders: priming a target for new therapies*. *Pharmacol Ther*, 2013. **138**(1): p. 18-37.
191. Meccariello, R., *Endocannabinoid System in Health and Disease: Current Situation and Future Perspectives*. *Int J Mol Sci*, 2020. **21**(10).
192. Azorlosa, J.L., et al., *Marijuana smoking: effect of varying delta 9-tetrahydrocannabinol content and number of puffs*. *J Pharmacol Exp Ther*, 1992. **261**(1): p. 114-22.
193. Perez-Reyes, M., *Marijuana smoking: factors that influence the bioavailability of tetrahydrocannabinol*. *NIDA Res Monogr*, 1990. **99**: p. 42-62.
194. Brutlag, A. and H. Hommerding, *Toxicology of Marijuana, Synthetic Cannabinoids, and Cannabidiol in Dogs and Cats*. *Vet Clin North Am Small Anim Pract*, 2018. **48**(6): p. 1087-1102.

195. Huestis, M.A., *Human cannabinoid pharmacokinetics*. Chemistry & biodiversity, 2007. **4**(8): p. 1770-1804.
196. Ohlsson, A., et al., *Plasma delta-9 tetrahydrocannabinol concentrations and clinical effects after oral and intravenous administration and smoking*. Clin Pharmacol Ther, 1980. **28**(3): p. 409-16.
197. Wall, M.E., et al., *Metabolism, disposition, and kinetics of delta-9-tetrahydrocannabinol in men and women*. Clin Pharmacol Ther, 1983. **34**(3): p. 352-63.
198. Perez-Reyes, M., et al., *Pharmacology of orally administered 9 - tetrahydrocannabinol*. Clin Pharmacol Ther, 1973. **14**(1): p. 48-55.
199. Perucca, E. and M. Bialer, *Critical Aspects Affecting Cannabidiol Oral Bioavailability and Metabolic Elimination, and Related Clinical Implications*. CNS Drugs, 2020. **34**(8): p. 795-800.
200. Grotenhermen, F., *Pharmacokinetics and Pharmacodynamics of Cannabinoids*. Clinical Pharmacokinetics, 2003. **42**(4): p. 327-360.
201. Zgair, A., et al., *Dietary fats and pharmaceutical lipid excipients increase systemic exposure to orally administered cannabis and cannabis-based medicines*. Am J Transl Res, 2016. **8**(8): p. 3448-59.
202. Borys, H.K. and R. Karler, *Cannabidiol and delta 9-tetrahydrocannabinol metabolism. In vitro comparison of mouse and rat liver crude microsome preparations*. Biochem Pharmacol, 1979. **28**(9): p. 1553-9.
203. Harvey, D.J. and N.K. Brown, *Comparative in vitro metabolism of the cannabinoids*. Pharmacol Biochem Behav, 1991. **40**(3): p. 533-40.
204. Gasse, A., et al., *Toxicogenetic analysis of Δ 9-THC-metabolizing enzymes*. International Journal of Legal Medicine, 2020. **134**(6): p. 2095-2103.
205. Nakazawa, K. and E. Costa, *Metabolism of delta 9 - tetrahydrocannabinol by lung and liver homogenates of rats treated with methylcholanthrene*. Nature, 1971. **234**(5323): p. 48-9.
206. Ellis, G.M., Jr., et al., *Excretion patterns of cannabinoid metabolites after last use in a group of chronic users*. Clin Pharmacol Ther, 1985. **38**(5): p. 572-8.
207. Harvey, D.J. and R. Mechoulam, *Metabolites of cannabidiol identified in human urine*. Xenobiotica, 1990. **20**(3): p. 303-20.
208. Mechoulam, R. and Y. Gaoni, *A Total Synthesis of dl- Δ 1-Tetrahydrocannabinol, the Active Constituent of Hashish1*. Journal of the American Chemical Society, 1965. **87**(14): p. 3273-3275.
209. Gaoni, Y. and R. Mechoulam, *Isolation, Structure, and Partial Synthesis of an Active Constituent of Hashish*. Journal of the American Chemical Society, 1964. **86**(8): p. 1646-1647.
210. Lago-Fernandez, A., et al., *New Methods for the Synthesis of Cannabidiol Derivatives*. Methods Enzymol, 2017. **593**: p. 237-257.
211. Steenson, S. and L. Chambers, *Cannabidiol: A budding industry!* Nutrition Bulletin, 2019. **44**(3): p. 228-240.
212. Katchan, V., P. David, and Y. Shoenfeld, *Cannabinoids and autoimmune diseases: A systematic review*. Autoimmun Rev, 2016. **15**(6): p. 513-28.

213. Devinsky, O., et al., *Trial of Cannabidiol for Drug-Resistant Seizures in the Dravet Syndrome*. N Engl J Med, 2017. **376**(21): p. 2011-2020.
214. Devinsky, O., et al., *Open-label use of highly purified CBD (Epidiolex®) in patients with CDKL5 deficiency disorder and Aicardi, Dup15q, and Doose syndromes*. Epilepsy Behav, 2018. **86**: p. 131-137.
215. Zgair, A., et al., *Oral administration of cannabis with lipids leads to high levels of cannabinoids in the intestinal lymphatic system and prominent immunomodulation*. Scientific reports, 2017. **7**(1): p. 14542-14542.
216. Atalay, S., I. Jarocka-Karpowicz, and E. Skrzydlewska, *Antioxidative and Anti-Inflammatory Properties of Cannabidiol*. Antioxidants (Basel, Switzerland), 2019. **9**(1): p. 21.
217. Kozela, E., et al., *Cannabidiol inhibits pathogenic T cells, decreases spinal microglial activation and ameliorates multiple sclerosis-like disease in C57BL/6 mice*. Br J Pharmacol, 2011. **163**(7): p. 1507-19.
218. Novotna, A., et al., *A randomized, double-blind, placebo-controlled, parallel-group, enriched-design study of nabiximols* (Sativex®) , as add-on therapy, in subjects with refractory spasticity caused by multiple sclerosis*. Eur J Neurol, 2011. **18**(9): p. 1122-31.
219. Killestein, J., et al., *Immunomodulatory effects of orally administered cannabinoids in multiple sclerosis*. J Neuroimmunol, 2003. **137**(1-2): p. 140-3.
220. Katona, S., et al., *Cannabinoid influence on cytokine profile in multiple sclerosis*. Clin Exp Immunol, 2005. **140**(3): p. 580-5.
221. Borrelli, F., et al., *Cannabidiol, a safe and non-psychotropic ingredient of the marijuana plant Cannabis sativa, is protective in a murine model of colitis*. J Mol Med (Berl), 2009. **87**(11): p. 1111-21.
222. Irving, P.M., et al., *A Randomized, Double-blind, Placebo-controlled, Parallel-group, Pilot Study of Cannabidiol-rich Botanical Extract in the Symptomatic Treatment of Ulcerative Colitis*. Inflamm Bowel Dis, 2018. **24**(4): p. 714-724.
223. Seltzer, E.S., et al., *Cannabidiol (CBD) as a Promising Anti-Cancer Drug*. Cancers, 2020. **12**(11): p. 3203.
224. Bogdanović, V., J. Mrdjanović, and I. Borišev, *A Review of the Therapeutic Antitumor Potential of Cannabinoids*. J Altern Complement Med, 2017. **23**(11): p. 831-836.
225. Galluzzi, L., et al., *Autophagy in malignant transformation and cancer progression*. Embo j, 2015. **34**(7): p. 856-80.
226. Armstrong, J.L., et al., *Exploiting cannabinoid-induced cytotoxic autophagy to drive melanoma cell death*. J Invest Dermatol, 2015. **135**(6): p. 1629-1637.
227. Carracedo, A., et al., *The stress-regulated protein p8 mediates cannabinoid-induced apoptosis of tumor cells*. Cancer Cell, 2006. **9**(4): p. 301-12.
228. Salazar, M., et al., *Cannabinoid action induces autophagy-mediated cell death through stimulation of ER stress in human glioma cells*. J Clin Invest, 2009. **119**(5): p. 1359-72.
229. Twelves, C., et al., *A phase 1b randomised, placebo-controlled trial of nabiximols cannabinoid oromucosal spray with temozolomide in patients with recurrent glioblastoma*. British Journal of Cancer, 2021. **124**(8): p. 1379-1387.

230. Hurd, Y.L., et al., *Cannabidiol for the Reduction of Cue-Induced Craving and Anxiety in Drug-Abstinent Individuals With Heroin Use Disorder: A Double-Blind Randomized Placebo-Controlled Trial*. *American Journal of Psychiatry*, 2019. **176**(11): p. 911-922.
231. Leehey, M.A., et al., *Safety and Tolerability of Cannabidiol in Parkinson Disease: An Open Label, Dose-Escalation Study*. *Cannabis Cannabinoid Res*, 2020. **5**(4): p. 326-336.
232. Porta Siegel, T., et al., *Mass Spectrometry Imaging and Integration with Other Imaging Modalities for Greater Molecular Understanding of Biological Tissues*. *Mol Imaging Biol*, 2018. **20**(6): p. 888-901.
233. Weibel, D.E., N. Lockyer, and J.C. Vickerman, *C60 cluster ion bombardment of organic surfaces*. *Applied Surface Science*, 2004. **231-232**: p. 146-152.
234. *The Magic of Cluster SIMS*. *Analytical Chemistry*, 2005. **77**(7): p. 142 A-149 A.
235. Touboul, D., et al., *Improvement of Biological Time-of-Flight-Secondary Ion Mass Spectrometry Imaging with a Bismuth Cluster Ion Source*. *Journal of the American Society for Mass Spectrometry*, 2005. **16**(10): p. 1608-1618.
236. Kotowska, A.M., et al., *Protein identification by 3D OrbiSIMS to facilitate in situ imaging and depth profiling*. *Nature Communications*, 2020. **11**(1): p. 5832.
237. Buchberger, A.R., et al., *Mass Spectrometry Imaging: A Review of Emerging Advancements and Future Insights*. *Analytical chemistry*, 2018. **90**(1): p. 240-265.
238. Gamble, L.J., et al., *ToF-SIMS of tissues: "lessons learned" from mice and women*. *Biointerphases*, 2015. **10**(1): p. 019008.
239. Shon, H.K., et al., *Molecular depth profiling on rat brain tissue sections prepared using different sampling methods*. *Biointerphases*, 2018. **13**: p. 03B411.
240. Yoon, S. and T.G. Lee, *Biological tissue sample preparation for time-of-flight secondary ion mass spectrometry (ToF-SIMS) imaging*. *Nano Convergence*, 2018. **5**(1): p. 24.
241. Zhang, J., et al., *Cryo-OrbiSIMS for 3D Molecular Imaging of a Bacterial Biofilm in Its Native State*. *Analytical Chemistry*, 2020. **92**(13): p. 9008-9015.
242. Newell, C.L., et al., *Cryogenic OrbiSIMS Localizes Semi-Volatile Molecules in Biological Tissues*. *bioRxiv*, 2019: p. 862391.
243. Vorng, J.L., et al., *Semiempirical Rules To Determine Drug Sensitivity and Ionization Efficiency in Secondary Ion Mass Spectrometry Using a Model Tissue Sample*. *Anal Chem*, 2016. **88**(22): p. 11028-11036.
244. Zhang, J., et al., *Cryo-OrbiSIMS for 3D molecular imaging of a bacterial biofilm in its native state*. *bioRxiv*, 2019: p. 859967.
245. Beers, J.L., D. Fu, and K.D. Jackson, *Cytochrome P450-Catalyzed Metabolism of Cannabidiol to the Active Metabolite 7-Hydroxy-Cannabidiol*. *Drug Metabolism and Disposition*, 2021: p. DMD-AR-2020-000350.
246. Vickerman, J. and I. Gilmore. *Surface analysis : the principal techniques*. 2009.
247. Citti, C., et al., *Cannabinoid Profiling of Hemp Seed Oil by Liquid Chromatography Coupled to High-Resolution Mass Spectrometry*. *Frontiers in Plant Science*, 2019. **10**(120).
248. Berman, P., et al., *A new ESI-LC/MS approach for comprehensive metabolic profiling of phytocannabinoids in Cannabis*. *Scientific Reports*, 2018. **8**(1): p. 14280.

249. Taglauer, E., *Surface cleaning using sputtering*. Applied Physics A, 1990. **51**(3): p. 238-251.
250. Desbenoit, N., et al., *Localisation and quantification of benzalkonium chloride in eye tissue by TOF-SIMS imaging and liquid chromatography mass spectrometry*. Anal Bioanal Chem, 2013. **405**(12): p. 4039-49.
251. Lovestead, T.M. and T.J. Bruno, *Determination of Cannabinoid Vapor Pressures to Aid in Vapor Phase Detection of Intoxication*. Forensic Chem, 2017. **5**: p. 79-85.
252. Jones, E., N. Lockyer, and J. Vickerman, *Suppression and enhancement of non-native molecules within biological systems*. Applied Surface Science - APPL SURF SCI, 2006. **252**: p. 6727-6730.
253. Seah, M.P., et al., *Quantifying SIMS of Organic Mixtures and Depth Profiles-Characterizing Matrix Effects of Fragment Ions*. J Am Soc Mass Spectrom, 2019. **30**(2): p. 309-320.
254. Swales, J.G., et al., *Quantitation of Endogenous Metabolites in Mouse Tumors Using Mass-Spectrometry Imaging*. Anal Chem, 2018. **90**(10): p. 6051-6058.
255. Angerer, T.B., et al., *Improved molecular imaging in rodent brain with time-of-flight-secondary ion mass spectrometry using gas cluster ion beams and reactive vapor exposure*. Anal Chem, 2015. **87**(8): p. 4305-13.
256. Lee, S.J., et al., *Development of an Argon Gas Cluster Ion Beam for ToF-SIMS Analysis*. Bulletin of the Korean Chemical Society, 2019. **40**.
257. Piwowar, A., et al., *Investigating the effect of temperature on depth profiles of biological material using ToF-SIMS*. Surface and Interface Analysis, 2011. **43**: p. 207-210.
258. Lovestead, T.M. and T.J. Bruno, *Determination of Cannabinoid Vapor Pressures to Aid in Vapor Phase Detection of Intoxication*. Forensic chemistry (Amsterdam, Netherlands), 2017. **5**: p. 79-85.
259. Moline, S.W. and G.G. Glenner, *ULTRARAPID TISSUE FREEZING IN LIQUID NITROGEN*. Journal of Histochemistry & Cytochemistry, 1964. **12**(10): p. 777-783.
260. Kochappan, R., et al., *Targeted delivery of mycophenolic acid to the mesenteric lymph node using a triglyceride mimetic prodrug approach enhances gut-specific immunomodulation in mice*. Journal of Controlled Release, 2021. **332**: p. 636-651.
261. Scholz, E.M.B., et al., *Quantitative Imaging Analysis of the Spatial Relationship between Antiretrovirals, Reverse Transcriptase Simian-Human Immunodeficiency Virus RNA, and Collagen in the Mesenteric Lymph Nodes of Nonhuman Primates*. Antimicrob Agents Chemother, 2021. **65**(6).
262. Thompson, C.G., et al., *Mass spectrometry imaging reveals heterogeneous efavirenz distribution within putative HIV reservoirs*. Antimicrobial agents and chemotherapy, 2015. **59**(5): p. 2944-2948.
263. Ellsworth, D.L., et al., *Examining protein expression profiles in axillary lymph nodes using histology directed MALDI-TOF to identify markers of early metastatic breast cancer*. Clinical Cancer Research, 2006. **12**(19 Supplement): p. A112.
264. Abbassi-Ghadi, N., et al., *Imaging of Esophageal Lymph Node Metastases by Desorption Electrospray Ionization Mass Spectrometry*. Cancer Research, 2016. **76**(19): p. 5647-5656.

265. Do, T., et al., *MALDI MSI Reveals the Spatial Distribution of Protein Markers in Tracheobronchial Lymph Nodes and Lung of Pigs after Respiratory Infection*. *Molecules*, 2020. **25**(23).
266. Hulme, H.E., et al., *Mass spectrometry imaging identifies palmitoylcarnitine as an immunological mediator during Salmonella Typhimurium infection*. *Scientific reports*, 2017. **7**(1): p. 2786-2786.
267. Holzlechner, M., et al., *In Situ Characterization of Tissue-Resident Immune Cells by MALDI Mass Spectrometry Imaging*. *Journal of Proteome Research*, 2017. **16**(1): p. 65-76.
268. Graham, D.J. and D.G. Castner, *Multivariate Analysis of ToF-SIMS Data from Multicomponent Systems: The Why, When, and How*. *Biointerphases*, 2012. **7**(1): p. 49.
269. Lever, J., M. Krzywinski, and N. Altman, *Principal component analysis*. *Nature Methods*, 2017. **14**(7): p. 641-642.
270. Trindade, G.F., M.-L. Abel, and J.F. Watts, *simsMVA: A tool for multivariate analysis of ToF-SIMS datasets*. *Chemometrics and Intelligent Laboratory Systems*, 2018. **182**: p. 180-187.
271. Garside, P., et al., *Visualization of specific B and T lymphocyte interactions in the lymph node*. *Science*, 1998. **281**(5373): p. 96-9.
272. Stenken, J.A. and A.J. Poschenrieder, *Bioanalytical chemistry of cytokines--a review*. *Anal Chim Acta*, 2015. **853**: p. 95-115.
273. Izrael-Tomasevic, A., et al., *Targeting Interferon Alpha Subtypes in Serum: A Comparison of Analytical Approaches to the Detection and Quantitation of Proteins in Complex Biological Matrices*. *Journal of Proteome Research*, 2009. **8**(6): p. 3132-3140.
274. Groessl, M., et al., *Profiling of the human monocytic cell secretome by quantitative label-free mass spectrometry identifies stimulus-specific cytokines and proinflammatory proteins*. *Proteomics*, 2012. **12**(18): p. 2833-42.
275. Meissner, F., et al., *Direct proteomic quantification of the secretome of activated immune cells*. *Science*, 2013. **340**(6131): p. 475-8.
276. Frisz, J.F., et al., *Identifying differentiation stage of individual primary hematopoietic cells from mouse bone marrow by multivariate analysis of TOF-secondary ion mass spectrometry data*. *Analytical chemistry*, 2012. **84**(10): p. 4307-4313.
277. Seyer, A., et al., *Lipidomic and spatio-temporal imaging of fat by mass spectrometry in mice duodenum during lipid digestion*. *PLoS one*, 2013. **8**(4): p. e58224-e58224.
278. Sjövall, P., B. Johansson, and J. Lausmaa, *Localization of lipids in freeze-dried mouse brain sections by imaging TOF-SIMS*. *Applied Surface Science - APPL SURF SCI*, 2006. **252**: p. 6966-6974.
279. Kaesler, S., et al., *Effective T-cell recall responses require the taurine transporter Taut*. *European Journal of Immunology*, 2012. **42**(4): p. 831-841.
280. Lämmermann, T. and M. Sixt, *The microanatomy of T-cell responses*. *Immunol Rev*, 2008. **221**: p. 26-43.
281. Gretz, J.E., A.O. Anderson, and S. Shaw, *Cords, channels, corridors and conduits: critical architectural elements facilitating cell interactions in the lymph node cortex*. *Immunological Reviews*, 1997. **156**(1): p. 11-24.
282. Kaldjian, E.P., et al., *Spatial and molecular organization of lymph node T cell cortex: a labyrinthine cavity bounded by an epithelium-like monolayer of fibroblastic reticular cells anchored to basement*

- membrane-like extracellular matrix*. *Int Immunol*, 2001. **13**(10): p. 1243-53.
283. Anderson, A.O. and N.D. Anderson, *Studies on the structure and permeability of the microvasculature in normal rat lymph nodes*. *Am J Pathol*, 1975. **80**(3): p. 387-418.
284. Pacher, P., S. Bátkai, and G. Kunos, *The endocannabinoid system as an emerging target of pharmacotherapy*. *Pharmacol Rev*, 2006. **58**(3): p. 389-462.
285. Graham, E.S., et al., *Detailed characterisation of CB2 receptor protein expression in peripheral blood immune cells from healthy human volunteers using flow cytometry*. *Int J Immunopathol Pharmacol*, 2010. **23**(1): p. 25-34.
286. Han, K.H., et al., *CB1 and CB2 cannabinoid receptors differentially regulate the production of reactive oxygen species by macrophages*. *Cardiovascular Research*, 2009. **84**(3): p. 378-386.
287. Rayman, N., et al., *Distinct Expression Profiles of the Peripheral Cannabinoid Receptor in Lymphoid Tissues Depending on Receptor Activation Status*. *The Journal of Immunology*, 2004. **172**(4): p. 2111.
288. Rayman, N., et al., *The expression of the Peripheral Cannabinoid receptor on cells of the immune system and Non-Hodgkin's lymphomas*. *Leukemia & Lymphoma*, 2007. **48**(7): p. 1389-1399.
289. Lynn, A.B. and M. Herkenham, *Localization of cannabinoid receptors and nonsaturable high-density cannabinoid binding sites in peripheral tissues of the rat: implications for receptor-mediated immune modulation by cannabinoids*. *Journal of Pharmacology and Experimental Therapeutics*, 1994. **268**(3): p. 1612.
290. Siemens, A.J., D. Walczak, and F.E. Buckley, *Characterization of blood disappearance and tissue distribution of [³H]cannabidiol*. *Biochem Pharmacol*, 1980. **29**(3): p. 462-4.
291. Siemens, A.J., D. Walczak, and F.E. Buckley, *Characterization of blood disappearance and tissue distribution of [³H]cannabidiol*. *Biochemical Pharmacology*, 1980. **29**(3): p. 462-464.
292. Springs, A.E.B., et al., *Effects of targeted deletion of cannabinoid receptors CB1 and CB2 on immune competence and sensitivity to immune modulation by Δ^9 -tetrahydrocannabinol*. *Journal of Leukocyte Biology*, 2008. **84**(6): p. 1574-1584.
293. Itano, A.A., et al., *Distinct dendritic cell populations sequentially present antigen to CD4 T cells and stimulate different aspects of cell-mediated immunity*. *Immunity*, 2003. **19**(1): p. 47-57.
294. Kornete, M. and C.A. Piccirillo, *Functional crosstalk between dendritic cells and Foxp3+ regulatory T cells in the maintenance of immune tolerance*. *Frontiers in Immunology*, 2012. **3**.
295. Matias, I., et al., *Presence and regulation of the endocannabinoid system in human dendritic cells*. *Eur J Biochem*, 2002. **269**(15): p. 3771-8.
296. Pandey, R., et al., *Endocannabinoids and immune regulation*. *Pharmacol Res*, 2009. **60**(2): p. 85-92.
297. Wacnik, P.W., et al., *Cannabinoids affect dendritic cell (DC) potassium channel function and modulate DC T cell stimulatory capacity*. *J Immunol*, 2008. **181**(5): p. 3057-66.
298. Bonacho, M.G., et al., *Aging-induced changes in 24-h rhythms of mitogenic responses, lymphocyte subset populations and neurotransmitter and amino acid content in rat submaxillary lymph nodes during Freund's adjuvant arthritis*. *Experimental Gerontology*, 2001. **36**(2): p. 267-282.

299. Wood, P., et al., *THE LIPID COMPOSITION OF HUMAN PLASMA CHYLOMICRONS*. J Lipid Res, 1964. **5**: p. 225-31.
300. Kayden, H.J., A. Karmen, and A. Dumont, *ALTERATIONS IN THE FATTY ACID COMPOSITION OF HUMAN LYMPH AND SERUM LIPOPROTEINS BY SINGLE FEEDINGS*. J Clin Invest, 1963. **42**(9): p. 1373-81.
301. Sakr, S., et al., *Fatty acid composition of an oral load affects chylomicron size in human subjects*. The British journal of nutrition, 1997. **77** **1**: p. 19-31.
302. Zilversmit, D.B., *The composition and structure of lymph chylomicrons in dog, rat, and man*. The Journal of clinical investigation, 1965. **44**(10): p. 1610-1622.
303. Christie, W.W., et al., *The positional distributions of fatty acids in the triacylglycerols and phosphatidylcholines of the intestinal and popliteal lymph and plasma of sheep*. Lipids, 1984. **19**(12): p. 982-6.
304. Dole, V.P., et al., *The fatty acid patterns of plasma lipids during alimentary lipemia*. The Journal of clinical investigation, 1959. **38**(9): p. 1544-1554.
305. Blomstrand, R. and O.L. Dahlback, *The fatty acid composition of human thoracic duct lymph lipids*. The Journal of clinical investigation, 1960. **39**(7): p. 1185-1191.
306. Fernandes, J., J.H. Van De Kamer, and H.A. Weijers, *The absorption of fats studied in a child with chylothorax*. J Clin Invest, 1955. **34**(7, Part 1): p. 1026-36.
307. Bragdon, J.H. and A. Karmen, *The fatty acid composition of chylomicrons of chyle and serum following the ingestion of different oils*. Journal of Lipid Research, 1960. **1**(2): p. 167-170.
308. Jeffery, N.M., et al., *Characteristics of lipid and lymphocytes collected from the lymph of rats fed a low fat diet or high fat diets rich in N-6 or N-3 polyunsaturated fatty acids*. Nutrition Research, 1998. **18**(2): p. 299-308.
309. Pathak, N., et al., *Value addition in sesame: A perspective on bioactive components for enhancing utility and profitability*. Pharmacognosy reviews, 2014. **8**(16): p. 147-155.
310. Christie, W.W. and R.C. Noble, *The lipid composition of the spleen and intestinal and popliteal lymph nodes in the sheep*. Lipids, 1985. **20**(6): p. 389-92.
311. Westcott, E., et al., *Fatty acid compositions of lipids in mesenteric adipose tissue and lymphoid cells in patients with and without Crohn's disease and their therapeutic implications*. Inflamm Bowel Dis, 2005. **11**(9): p. 820-7.
312. Streich, K., et al., *Dietary lipids accumulate in macrophages and stromal cells and change the microarchitecture of mesenteric lymph nodes*. Journal of advanced research, 2020. **24**: p. 291-300.
313. Seyer, A., et al., *Lipidomic and spatio-temporal imaging of fat by mass spectrometry in mice duodenum during lipid digestion*. PLoS One, 2013. **8**(4): p. e58224.
314. Wan, Y., et al., *The relationship of antioxidant components and antioxidant activity of sesame seed oil*. J Sci Food Agric, 2015. **95**(13): p. 2571-8.
315. Wu, W.-H., *The contents of lignans in commercial sesame oils of Taiwan and their changes during heating*. Food Chemistry, 2007. **104**(1): p. 341-344.

316. Moazzami, A.A., S.L. Haese, and A. Kamal-Eldin, *Lignan contents in sesame seeds and products*. European Journal of Lipid Science and Technology, 2007. **109**(10): p. 1022-1027.
317. Borriello, S.P., et al., *Production and metabolism of lignans by the human faecal flora*. J Appl Bacteriol, 1985. **58**(1): p. 37-43.
318. Aued-Pimentel, S., et al., *Composition of tocopherols in sesame seed oil: An indicative of adulteration*. Grasas y Aceites, 2006. **57**.
319. Wang, X.D., et al., *Vitamin E enhances the lymphatic transport of beta-carotene and its conversion to vitamin A in the ferret*. Gastroenterology, 1995. **108**(3): p. 719-26.
320. Nagy, K., et al., *Double-balloon jejunal perfusion to compare absorption of vitamin E and vitamin E acetate in healthy volunteers under maldigestion conditions*. European Journal of Clinical Nutrition, 2013. **67**(2): p. 202-206.
321. Ferland, G. and J.A. Sadowski, *Vitamin K1 (phylloquinone) content of edible oils: effects of heating and light exposure*. Journal of Agricultural and Food Chemistry, 1992. **40**(10): p. 1869-1873.
322. Hollander, D. and E. Rim, *Effect of luminal constituents on vitamin K1 absorption into thoracic duct lymph*. American Journal of Physiology-Endocrinology and Metabolism, 1978. **234**(1): p. E54.
323. Mekky, R.H., et al., *Metabolic Profiling of the Oil of Sesame of the Egyptian Cultivar 'Giza 32' Employing LC-MS and Tandem MS-Based Untargeted Method*. Foods, 2021. **10**(2).
324. Calderillo-Ruiz, G., et al., *Retroperitoneal lymph node metastases as a prognosis factor in overall survival in metastatic colorectal cancer*. Annals of Oncology, 2019. **30**: p. iv72.
325. Feng, W., et al., *Inclusion of Medium-Chain Triglyceride in Lipid-Based Formulation of Cannabidiol Facilitates Micellar Solubilization In Vitro, but In Vivo Performance Remains Superior with Pure Sesame Oil Vehicle*. Pharmaceutics, 2021. **13**: p. 1349.
326. Matthaus, B., M.M. Özcan, and F. Al Juhaimi, *Some rape/canola seed oils: fatty acid composition and tocopherols*. Z Naturforsch C J Biosci, 2016. **71**(3-4): p. 73-7.
327. Azeez, S., *Fatty acid profile of coconut oil in relation to nut maturity and season in selected cultivars/hybrids*. British Food Journal, 2007. **109**: p. 272-279.
328. Horst, H.J., et al., *Lymphatic absorption and metabolism of orally administered testosterone undecanoate in man*. Klin Wochenschr, 1976. **54**(18): p. 875-9.
329. Ng, C., et al., *Postprandial changes in gastrointestinal function and transit in cystic fibrosis assessed by Magnetic Resonance Imaging*. J Cyst Fibros, 2020.
330. Marciani, L., et al., *Postprandial Changes in Small Bowel Water Content in Healthy Subjects and Patients With Irritable Bowel Syndrome*. Gastroenterology, 2010. **138**(2): p. 469-477.e1.
331. McAuliffe, M.J., et al. *Medical Image Processing, Analysis and Visualization in clinical research*. in Proceedings 14th IEEE Symposium on Computer-Based Medical Systems. CBMS 2001. 2001.
332. Hoad, C.L., et al., *Non-invasive quantification of small bowel water content by MRI: a validation study*. Phys Med Biol, 2007. **52**(23): p. 6909-22.
333. Williams, C.M., *Postprandial lipid metabolism: effects of dietary fatty acids*. Proceedings of the Nutrition Society, 2007. **56**(2): p. 679-692.
334. Lopez-Miranda, J., et al., *Dietary Fat Clearance in Normal Subjects Is Modulated by Genetic Variation at the Apolipoprotein B Gene*

- Locus. Arteriosclerosis, Thrombosis, and Vascular Biology*, 1997. **17**(9): p. 1765-1773.
335. Karlsson, O. and J. Hanrieder, *Imaging mass spectrometry in drug development and toxicology*. *Arch Toxicol*, 2017. **91**(6): p. 2283-2294.
 336. Kumamoto, Y., et al., *CD4+ T cells support cytotoxic T lymphocyte priming by controlling lymph node input*. *Proceedings of the National Academy of Sciences of the United States of America*, 2011. **108**(21): p. 8749-8754.
 337. Liao, S. and T.P. Padera, *Lymphatic function and immune regulation in health and disease*. *Lymphatic research and biology*, 2013. **11**(3): p. 136-143.
 338. Soderberg, K.A., et al., *Innate control of adaptive immunity via remodeling of lymph node feed arteriole*. *Proceedings of the National Academy of Sciences*, 2005. **102**(45): p. 16315-16320.
 339. Angelina, A., et al., *Cannabinoids induce functional Tregs by promoting tolerogenic DCs via autophagy and metabolic reprogramming*. *Mucosal Immunology*, 2022. **15**(1): p. 96-108.
 340. Adhikary, S., et al., *Signaling through cannabinoid receptor 2 suppresses murine dendritic cell migration by inhibiting matrix metalloproteinase 9 expression*. *Blood*, 2012. **120**(18): p. 3741-3749.
 341. Gaffal, E., et al., *Cannabinoid Receptor 2 Modulates Maturation of Dendritic Cells and Their Capacity to Induce Hapten-Induced Contact Hypersensitivity*. *International Journal of Molecular Sciences*, 2020. **21**(2): p. 475.
 342. Robinson, R.H., et al., *Cannabinoids inhibit T-cells via cannabinoid receptor 2 in an in vitro assay for graft rejection, the mixed lymphocyte reaction*. *J Neuroimmune Pharmacol*, 2013. **8**(5): p. 1239-50.
 343. Kozela, E., et al., *Cannabidiol inhibits pathogenic T cells, decreases spinal microglial activation and ameliorates multiple sclerosis-like disease in C57BL/6 mice*. *British journal of pharmacology*, 2011. **163**(7): p. 1507-1519.
 344. Kotschenreuther, K., et al., *Cannabinoids drive Th17 cell differentiation in patients with rheumatic autoimmune diseases*. *Cellular & Molecular Immunology*, 2021. **18**(3): p. 764-766.
 345. Eisenstein, T. and J. Meissler, *Effects of Cannabinoids on T-cell Function and Resistance to Infection*. *Journal of neuroimmune pharmacology : the official journal of the Society on NeuroImmune Pharmacology*, 2015. **10**.
 346. Thomas, S.N. and A. Schudel, *Overcoming transport barriers for interstitial-, lymphatic-, and lymph node-targeted drug delivery*. *Current Opinion in Chemical Engineering*, 2015. **7**: p. 65-74.
 347. Porter, C.J.H. and N.L. Trevaskis, *Targeting immune cells within lymph nodes*. *Nature Nanotechnology*, 2020. **15**(6): p. 423-425.
 348. Kawabe, T., et al., *Mesenteric lymph nodes contribute to proinflammatory Th17-cell generation during inflammation of the small intestine in mice*. *Eur J Immunol*, 2016. **46**(5): p. 1119-31.
 349. Lester, L., et al., *Systemic panniculitis-like T-cell lymphoma with involvement of mesenteric fat and subcutis*. *J Cutan Pathol*, 2015. **42**(1): p. 46-9.
 350. Abreu, C.M., et al., *Myeloid and CD4 T Cells Comprise the Latent Reservoir in Antiretroviral Therapy-Suppressed SIVmac251-Infected Macaques*. *mBio*, 2019. **10**(4): p. e01659-19.

351. Aid, M., et al., *Follicular CD4 T Helper Cells As a Major HIV Reservoir Compartment: A Molecular Perspective*. *Frontiers in Immunology*, 2018. **9**.
352. Yang, X., et al., *Cannabidiol Regulates Gene Expression in Encephalitogenic T cells Using Histone Methylation and noncoding RNA during Experimental Autoimmune Encephalomyelitis*. *Scientific Reports*, 2019. **9**(1): p. 15780.
353. Jersild Jr., R.A. and R.T. Clayton, *A comparison of the morphology of lipid absorption in the jejunum and ileum of the adult rat*. *American Journal of Anatomy*, 1971. **131**(4): p. 481-503.
354. Francis, I.R., et al., *Retroperitoneal sarcomas*. *Cancer imaging : the official publication of the International Cancer Imaging Society*, 2005. **5**(1): p. 89-94.
355. Moussa, M. and M.A. Chakra, *Metastatic prostate cancer presenting as a retroperitoneal mass: a case report and review of literature*. *Journal of Surgical Case Reports*, 2019. **2019**(10).
356. Nishiyama, A., et al., *Retroperitoneal Metastasis from Lung Adenocarcinoma Mimics Retroperitoneal Fibrosis*. *Journal of Thoracic Oncology*, 2016. **11**(2): p. 266-267.
357. Ouedraogo, R., et al., *Whole-cell MALDI-TOF mass spectrometry: a tool for immune cell analysis and characterization*. *Methods Mol Biol*, 2013. **1061**: p. 197-209.
358. Henshaw, F.R., et al., *The Effects of Cannabinoids on Pro- and Anti-Inflammatory Cytokines: A Systematic Review of In Vivo Studies*. *Cannabis Cannabinoid Res*, 2021. **6**(3): p. 177-195.
359. Robinson, E.S., et al., *Cannabinoid Reduces Inflammatory Cytokines, Tumor Necrosis Factor- α , and Type I Interferons in Dermatomyositis In Vitro*. *The Journal of investigative dermatology*, 2017. **137**(11): p. 2445-2447.
360. Vuolo, F., et al., *Evaluation of Serum Cytokines Levels and the Role of Cannabidiol Treatment in Animal Model of Asthma*. *Mediators of inflammation*, 2015. **2015**: p. 538670-538670.
361. Liao, S. and P.-Y. von der Weid, *Inflammation-induced lymphangiogenesis and lymphatic dysfunction*. *Angiogenesis*, 2014. **17**(2): p. 325-334.
362. Jiang, X., et al., *Decreased lymphatic HIF-2 α accentuates lymphatic remodeling in lymphedema*. *The Journal of Clinical Investigation*, 2020. **130**(10): p. 5562-5575.
363. Girard, J.P., C. Moussion, and R. Förster, *HEVs, lymphatics and homeostatic immune cell trafficking in lymph nodes*. *Nat Rev Immunol*, 2012. **12**(11): p. 762-73.
364. Zhang, Q., et al., *Increased lymphangiogenesis in joints of mice with inflammatory arthritis*. *Arthritis Res Ther*, 2007. **9**(6): p. R118.
365. Tsujikawa, K., et al., *Development of a novel immunoassay for herbal cannabis using a new fluorescent antibody probe, "Ultra Quenchbody"*. *Forensic Sci Int*, 2016. **266**: p. 541-548.
366. Wagner, M., et al., *High-Resolution T2-Weighted Abdominal Magnetic Resonance Imaging Using Respiratory Triggering: Impact of Butylscopolamine on Image Quality*. *Acta Radiologica*, 2008. **49**(4): p. 376-382.
367. Sander, K., et al., *Sulfonium salts as leaving groups for aromatic labelling of drug-like small molecules with fluorine-18*. *Sci Rep*, 2015. **5**: p. 9941.
368. van der Born, D., et al., *Fluorine-18 labelled building blocks for PET tracer synthesis*. *Chem Soc Rev*, 2017. **46**(15): p. 4709-4773.

369. Halder, R. and T. Ritter, *18F-Fluorination: Challenge and Opportunity for Organic Chemists*. The Journal of Organic Chemistry, 2021. **86**(20): p. 13873-13884.
370. Breuer, A., et al., *Fluorinated Cannabidiol Derivatives: Enhancement of Activity in Mice Models Predictive of Anxiolytic, Antidepressant and Antipsychotic Effects*. PLoS One, 2016. **11**(7): p. e0158779.
371. DeGrado, T.R., et al., *Synthesis and Preliminary Evaluation of 18-^{&sup>&sup>}F-Fluoro-4-Thia-Oleate as a PET Probe of Fatty Acid Oxidation*. Journal of Nuclear Medicine, 2010. **51**(8): p. 1310.
372. Tu, Z., et al., *Synthesis and evaluation of 15-(4-(2-[¹⁸F]Fluoroethoxy)phenyl)pentadecanoic acid: a potential PET tracer for studying myocardial fatty acid metabolism*. Bioconjug Chem, 2010. **21**(12): p. 2313-9.
373. Marik, J., et al., *Long-circulating liposomes radiolabeled with [¹⁸F]fluorodipalmitin ([¹⁸F]FDP)*. Nucl Med Biol, 2007. **34**(2): p. 165-71.
374. Constantinescu, C.S., et al., *Experimental autoimmune encephalomyelitis (EAE) as a model for multiple sclerosis (MS)*. British journal of pharmacology, 2011. **164**(4): p. 1079-1106.